Modeling He-II cryostat performance and characterization of spin manipulation components for a neutron electric dipole moment experiment at TRIUMF

by

Sean Hansen-Romu

A Thesis submitted to the Faculty of Graduate Studies of

The University of Manitoba

in partial fulfillment of the requirements for the degree of

DOCTOR OF PHILOSOPHY

Department of Physics and Astronomy

University of Manitoba

Winnipeg

ABSTRACT

This thesis chronicles measurements of ultracold neutrons (UCN) performed at TRIUMF in fall 2018 and fall 2019. Heat response data of the UCN source bottle was taken by measuring its temperature using the vapour pressure of the ^{4}He. The time-dependence of the He-II bottle temperature is well-described by a model where heat transport is limited by quantum turbulence in the He-II. In addition, measurements of UCN spin manipulation components showed that the adiabatic fast-passage device had a spin flipping efficiency of 0.977 ± 0.008 and 1.007 ± 0.008, and the spin analyzers had a measured polarizing power of 0.650 ± 0.003 and 0.630 ± 0.003. Simulations show that the low spin analyzer efficiency is most likely due to a lower than expected magnetization in the foils, and additional sources of depolarization around the spin-analyzers. The simulations of the analyzer show that the single pass polarizing power of the foil is 0.78 ± 0.08. Under the assumption of no transmission of the wrong spin state through the superconducting magnet, the polarizing power was measured as 0.57 ± 0.05. Simulations reveal that the bore was responsible for some reduction in polarizing power, however better magnetic field gradient control for the spin flipper gradient is required to rule out the possibility of inefficient spin flippers as the cause of the depolarization.

ACKNOWLEDGMENTS

I would like to express my deepest gratitude to Dr. Blair Jamieson for his invaluable mentorship and feed back. This endeavour would not have been possible without my Defence committee: Dr. Jeff Martin, and Dr. Kumar Sharma. generously provided me with expertise and insight.

Extremely grateful to the TUCAN Collaboration without whom I would have no thesis. Special thanks to the late night shift workers during the run, as well as member of the collaboration who helped with installation, data taking with my experiment. Their efforts contributed to my experiment.

I would like to mention my dearest wife, Sasha Ostrowski, and my family. Their belief and words of encouragement have kept my motivation high all throughout this process.

Table of Contents

List of Figures

List of Tables

1. Introduction

This thesis presents progress on two important parts of a neutron electric dipole moment (nEDM) experiment. The first part focuses on the heat response of the vertical cryostat using a heating coil wound onto the ultracold neutron (UCN) production bottle. The second part of the thesis focuses on experimental equipment for the polarization (spin) analysis of the neutrons. In particular, it describes the characterization of the neutron spin manipulating components, including the polarizer, the analyzer, and the spin flipper. Both of these key contributions to the nEDM experiment are related to increasing the UCN statistics. The goal of TRIUMF Advanced Ultracold Neutron (TUCAN) collaboration is to develop the highest density UCN source in the world and measure the nEDM or lower the limit on the nEDM to 10^{-27}e $\cdot$ cm [1]. The TUCAN sources uses superfluid helium (He-II) to convert cold neutrons into UCN.

The heat input provided by a short intense beam or a heating coil produce similar heat loads when their powers are similar. The temperature of the cryostat is measured with a low temperature pressure gauge measuring the helium vapour above the bottle. This pressure is related to the temperature of the helium superfluid. UCN losses after production is strongly related to the ^{4}He temperature go as T^7, measured in Kelvin. This makes the temperature and how the temperature evolves (the heat response) during heating a huge factor in UCN production and statistics. A new technique is developed for calculating the superfluid helium heat response in the vertical cryostat. The results show that when the new TUCAN source is installed and subjected to a higher beam power, the horizontal cyrostat's heat response will be able to handle the higher heat load requirements, because of an innovative new heat exchanger design that is vastly superior to the vertical source.

In the neutron EDM experiment, UCN spin analysis has been shown to have greater statistical sensitivity when counting both spin states of the UCN at the same time, compared to counting the spin states sequentially [2]. The total length of UCN guide between the spin flipper and the spin analyzer is related to losses. Making a compact spin flipper and putting it close to the spin

analyzer can reduce losses in the arms due to transport. Components were designed and tested for a simultaneous spin analyzer that had the magnetic fringe field providing the needed field gradient. The idea is that using the magnetic fringe field from the magnetizing of the iron foil for the field gradient for the spin flipper can reduce the size of the apparatus and provide better statistics overall.

This introductory chapter will present the underlying physics motivation for nEDM searches. It will discuss how finding a non-zero nEDM could provide a mechanism for the matter-antimatter asymmetry of the universe, called baryon asymmetry. Additionally, this chapter will outline the properties of UCN and their basic physical interactions.

Part I (Chapters 2-5) will focus on the UCN production, with Chapter 2 presenting the physics of UCN production as well as an overview of other UCN facilities worldwide. Chapter 3 will discuss TUCANs prototype vertical UCN source. Chapter 4 will highlight temperature measurements of the vertical source and discuss the 1D superfluid heat response model.

Part II, consisting of chapters 5-10, will be related to UCN polarization measurements. Chapter 5 will discuss how the UCN spin is related to the nEDM and how to measure the nEDM by use of the Rasmey Method. Chapter 6 will present the simultaneous spin analyzer design as well as design requirements. Chapter 7 will present measurements of the UCN simultaneous spin analyzer (SSA) components. Chapter 8 will be the analysis and simulation of the UCN spin analyzer setups. Chapter 9 will discuss the final results of the SSA components tests taking the simulations into account. Chapter 10 is a review of the magnetic characterization of the analyzer foils.

Finally, Chapter 11 will provide a conclusion on the measurements presented in this thesis and discuss their impact on the nEDM experiment's design.

1.1 Fundamental Symmetries

Searches for nonzero EDMs are really searches for a violation in the fundamental symmetries in particle physics. The three discrete symmetries we are interested in, in the context of particle physics symmetries, are charge conjugation (C), Parity transformation (P), and time reversal symmetry (T). Charge conjugation symmetry is the idea that physics is unchanged or invariant if all

matter particles are replaced with their anti-matter equivalents and vice versa. Parity transformation symmetry is the idea that the laws of physics are invariant under the inversion of the coordinate system. Time-reversal symmetry is the idea that the laws of physics will remain the same under the reversal of time. In the Standard Model, C, P, and T are individually violated.

The combined symmetry of CPT has so far been observed to be an exact symmetry fundamental to nature. While C, P, and T haven't been found to be exact symmetries, in order for the combined CPT symmetry to hold, a violation of T-symmetry requires an equal and opposite violation of the combined CP-symmetry to hold. CP-violations searches are experiments looking at differences between the properties of particles and anti-particles. In particular, a search for an EDM is a search for a time-reversal violation, and assuming Charge-Parity-Time reversal (CPT) conservation (required by Lorentz invariance), it is a CP violation search.

1.2 nEDM and Symmetry Breaking

Figure 1.1 illustrates the symmetry violation properties of a particle with spin, $\vec{S}$, placed in parallel $\vec{E}$ and $\vec{B}$ fields.

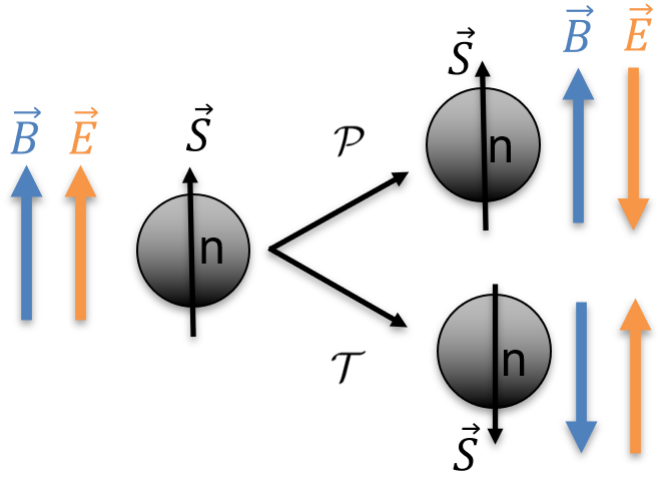

Figure 1.1: Parity transformations $\mathcal{P}$ and time reversal $\mathcal{T}$ operators acting on a neutron, n, in a magnetic field, $\vec{B}$, and electric field $\vec{E}$.

The transformation properties of the Hamiltonian, H under symmetry operators, determine the invariance of the system. Considering the Hamiltonian which defines the equations of motion and defines the evolution of the spin S, with a magnetic moment μ, and electric moment d in an electric field $\vec{E}$ and magnetic field $\vec{B}$:

$$\hat{H} = -\frac{\vec{S}}{|S|} \cdot (\mu\vec{B} + d\vec{E}). \tag{1.1}$$

Under the parity transformation the electric field reverses its direction:

$$P(\hat{H}) = -\frac{(\vec{S})}{|S|} \cdot (\mu(\vec{B}) + d(-\vec{E})). \tag{1.2}$$

For time reversal of the equations of motion, both spin and magnetic moment change sign. The first term of Equation 1.3 is symmetric because both spin and magnetic moment reverse, resulting in an even reversal. Only the spin changes in the second term of:

$$T(\hat{H}) = -\frac{(-\vec{S})}{|S|} \cdot (\mu(-\vec{B}) + d(+\vec{E})). \tag{1.3}$$

The existence of the EDM term violates P and T symmetry, whereas the magnetic dipole moment term is invariant. Looking at the Equations 1.2 and 1.3, a system with the electric field in opposite directions is equivalent to time reversal of the Hamiltonian. Measuring any differences in the equation of motion of 1.1 under an electric field reversal in direction is a test of time reversal symmetry.

1.3 CP violation of nEDM

Calculating the observable EDMs from fundamental CP-violating sources that could exist at high energy scales can be organized by considering the intervening energy scales, as seen in Figure 1.2. The energy scales correspond to the scale of the effective field theories used to calculate them, with the strength of Wilson coefficients encoding information about CP-violation at higher energy scales.

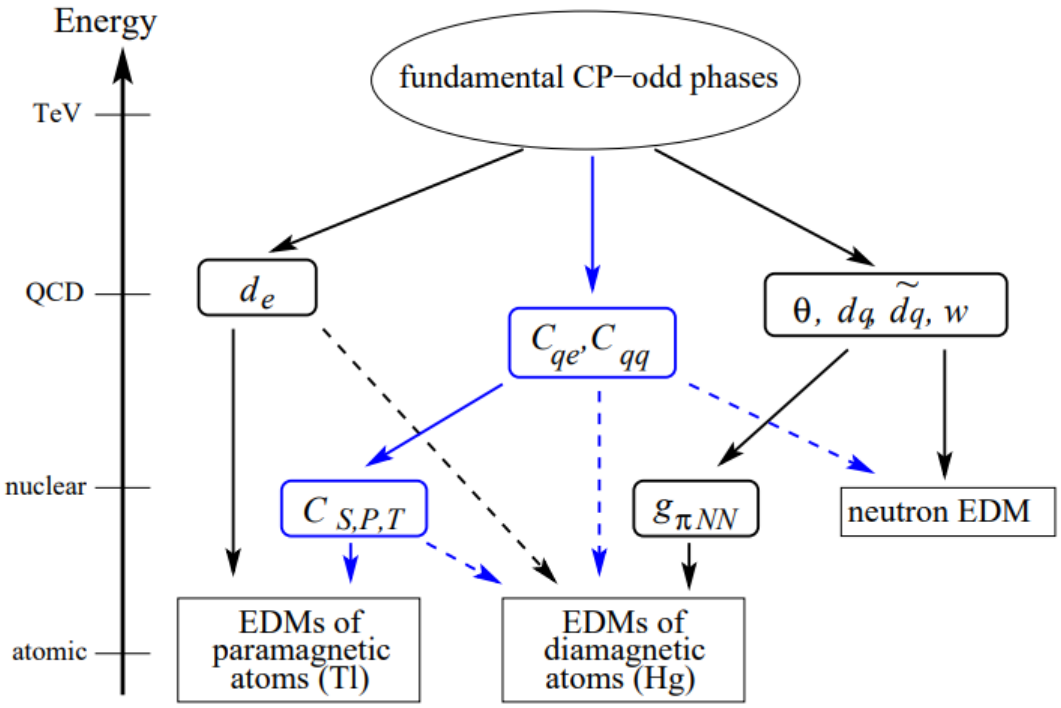

Figure 1.2: Heritage of the EDMs. Dashed lines indicated weaker sensitivity, and the blue line is used for clarity [3]. This diagram is discussed further in the surrounding text.

The left and middle terminus of Figure 1.2 explain atomic EDMs from the source of CP-violation from nuclear sources and above. The right side describes in the neutron EDM, whose contributions are from the θ term in quantum chromodynamics (QCD), quark EDMs d_q, quark chromo-EDMs $\tilde{d}_q$, and a CP-odd three gluon interaction w (sometimes referred to as the Weinberg operator [4]).

Paramagnetic atoms would have EDMs primarily through contributions of the electron EDM d_e and electron nucleon couplings through Wilson coefficients (C_S, C_P, C_T) at the nuclear level. The electron EDM can be measured using paramagnetic atoms such as Tl. Nowadays, molecules can also be used to measure the electron EDM. The world's best limit on the electron EDM has been measured using thallium monoxide ThO [5].

The primary nuclear contributions to the diamagnetic atomic EDM is the result of CP-violating pion nucleon interactions $g_{\pi NN}$, which ultimately arise from the same sources as the neutron EDM.

At QCD confinement energy scales ($\sim$GeV), the electron-quark C_{qe} and quark-quark C_{qq} interactions primarily contribute to the electron nucleon interactions $C_{S,P,T}$. Additionally, small quark-quark contributions can contribute directly to the neutron EDM. The electron and electron-quark interactions can contribute weakly to the EDM of diamagnetic atoms.

The sources of CP violation originate from fundamental theories such as the Standard Model. Some Beyond the Standard Model (BSM) theories predict values of the nEDM that are higher than the SM. Theoretical work surrounding the neutron EDM have connections to three broad categories: 1) new sources of CP violation beyond the standard model [6, 7, 8, 9, 10]; 2) models of baryogenesis requiring new physics, such as electroweak baryogenesis [11]; and 3) the strong CP problem, which in turn is related to the existence of axions [12, 13].

The relationship to baryogenesis is particularly important [14]. The Sakharov Criteria are a set of three conditions that must be fulfilled by the processes involved to result in the observed baryon asymmetry of the present-day universe [15].

1. Baryon number (B) violation

2. C, CP violation

3. lack of thermal equilibrium.

The first criterion of B-violation is needed to create excess baryons compared to anti-baryons. C or CP violation is needed so that interactions of anti-baryons are different from those of baryons. The non-thermal equilibrium is needed so that reverse reactions do not cancel forward reactions, driving the production towards matter.

Electroweak baryogenesis is a scenario based on SM that produces a net baryon number. However, one of its problems is that the SM does not have enough CP violation to account for the baryon asymmetry of our universe [14].

1.4 Ultracold Neutrons

The most precise EDM measurements have been done using ultracold neutrons (UCN). UCN are neutrons that are so slow that they can be trapped in material bottles. They reflect from material surfaces if their energy is less than that of a material-dependent neutron optical potential $\lesssim 300$ neV, sometimes called the Fermi potential.

Free neutrons have a mean lifetime of 878.4 $\pm$ 0.5 s [16]. Neutrons need to be liberated from a nucleus to become free neutrons. Typically, newly liberated free neutrons have a kinetic energy at the energy scale of about a megaelectronvolt ($\sim$ MeV) and need to be moderated to lower energies. This is accomplished by neutron converters that moderated the neutrons with elastic collisions, slowing down the neutrons. Table 1.1 defines these energy ranges, the corresponding velocity ranges in meters per second, and the corresponding neutron wavelength ranges. Efficient methods of converting fast neutrons to UCN are needed so that the properties of UCN can be used for experiments. The ability to store UCN and the neutrons' long lifetime make them prime candidate particles for high precision fundamental physics experiments.

Table 1.1: Common names for different energy ranges of neutrons and their corresponding velocities and wavelengths.

Neutrons	Energy Range E	Velocity v (m/s)	Wavelength λ (Å)
Fast	> 0.8 MeV	$> 12.3 \times 10^6$	< 0.0003
Intermediate	1 eV - 0.8 MeV	13.8×10^3 - 12.3×10^6	0.0003 - 0.28
Epithermal	100 meV - 1 eV	4374 - 13.8×10^3	0.28 - 0.9
Thermal	12 meV - 100 meV	1515 - 4374	0.9 - 2.6
Cold	0.12 meV - 12 meV	152 - 1515	2.6 - 26.1
Very Cold	300 neV - 0.12 meV	7.5 - 152	26.1 - 52.2
Ultracold	≤ 300 neV	≤ 8	≥ 500

1.4.1 Weak Force

The primary weak force interaction of neutrons is neutron decay. Neutrons have a mean lifetime of 878.4 $\pm$ 0.5 s [16] with the decay

$$\mathrm{n} \rightarrow \mathrm{p} + \mathrm{e}^{-} + \bar{\nu} + 782 \ \text{keV}. \tag{1.4}$$

The weak force moderated decay sets timescales of experiments like neutron EDM. Neutrons can be bottled for hundreds of seconds.

1.4.2 Gravity

UCNs experience a gravitational potential given by:

$$V_g = mg\Delta h = (102 \text{ neV m}^{-1})\Delta h \tag{1.5}$$

where m is the mass of the neutron, g is the gravitational acceleration due to Earth, and Δh is the height difference the potential is referencing. UCNs are unique in that their kinetic energy is low enough that gravity has a large effect at the energy on the scale of the experiment. A drop of a meter or two results in a significant kinetic energy gain for UCNs such that they have enough energy to leak out of the guides. A guide that is 3 meters tall will never let UCNs escape from their top, as this represents a 306 neV potential.

1.4.3 Electromagnetism

The charge of a neutron is zero, and it has a magnetic moment $\mu_n = (-1.91304273 \pm 0.00000045)\mu_N$[16], where

$$\mu_N = \frac{e\hbar}{2m_p} = 31.524512550(15) \text{ neV T}^{-1} \tag{1.6}$$

is the nuclear magneton. So that $\mu_n \approx -60$ neV/T.

The magnetic moment $\vec{\mu}$ causes the neutron to feel forces induced by magnetic fields, $\vec{B}$, via the

Hamiltonian $\hat{H}$. So equation 1.1 with negligible electric field and large magnetic field becomes:

$$\hat{H} = -\frac{\vec{S}}{|S|}\mu \cdot \vec{B}. \tag{1.7}$$

This is used in EDM experiments to produce highly polarized UCN, and to analyze their spins.

1.4.4 Strong Force

It is the strong force that gives rise to the property that UCN can be trapped in material bottles. Neutrons interact with the nuclei in materials via the strong force. The neutron wavelength of UCN is so large that it sees the nuclei of solids and liquids as physical surfaces that can be modeled as an effective potential V_F. The effective potential depends on the bound coherent n-nucleus scattering length and density of the material. The best isotopes for holding neutrons in bottles have the largest V_F approximately $\sim$ 300 neV, such as Be 252 neV, Ni 252 neV, ^{58}Ni 335 neV,and BeO 261 neV [17]. This is truly what defines a UCN, the scale of the neutron effective potential for experimentally useful surface coating materials.

1.5 The neutron electric dipole moment

Similar to how a magnetic moment can be thought of as a tiny magnet in the neutron, an EDM can be thought of as a tiny separation of charge. This is useful in describing the effect of the neutron motion in electric and magnetic fields classically, but both the magnetic moment and the EDM are more fundamental properties than a classical description can provide.

The magnetic moment is a fundamental property of quarks and leptons. Another fundamental property is the spin angular momentum, often simply called spin. In a baryon such as the neutron, the spin components of quarks sum together and define the spin axis of the resulting particle. This axis of spin is in the same direction as the magnetic moment. Neutrons are spin 1/2 particles. Similarly to the magnetic moment, the EDM would have to be aligned with the spin as well.

$$\vec{\mu} = \mu\vec{S}. \tag{1.8}$$

The magnetic moment precesses about a magnetic field B_0 with a frequency ω given by:

$$\omega = \gamma B_0. \tag{1.9}$$

Here γ is the gyromagnetic ratio of the particle which relates the frequency of oscillation of the spin vector about a magnetic field due to its magnetic moment, and $\hbar = 1.054571 \times 10^{-34}$ J·s is Planck's constant. This frequency ω is called the Larmor frequency. The action of the magnetic field on the Hamiltonian induces an energy splitting known as Zeeman splitting. The solution for a static magnetic field, B_0 results in solutions, or eigenvalues, for the equation related to the direction of the spin vector, and the magnetic field. The resulting energy splitting is:

$$U = -\mu B_0 \frac{m_S}{S}, \tag{1.10}$$

where $m_S = (-S, -S+1, \ldots, S-1, S)$ is the spin quantum number corresponding to the allowable projections of spin onto the magnetic moment axis. In a spin $S = 1/2$ system the allowable values of $m_S = \pm 1/2$ correspond to the energy splitting $E = \mp \mu B_0$.

There is an analogous splitting in energy due to an EDM in an electric field E_0, called the Stark effect.

$$U = -dE_0 \frac{m_S}{S} \tag{1.11}$$

In a spin $J = 1/2$ system the allowable values of $m_J = \pm 1/2$ correspond to the energy splitting $E = \mp dE_0$.

The equations of motion of a particle with an electric dipole moment d and a magnetic moment μ in a magnetic and an electric field ($\vec{B}$ and $\vec{E}$) is given by the Hamiltonian:

$$\hat{H} = -\mu \frac{\vec{S}}{|\vec{S}|} \cdot \vec{B} - d \frac{\vec{S}}{|\vec{S}|} \cdot \vec{E} \tag{1.12}$$

Here the spin of the particle is $\vec{S}$ and can take values of either spin up or spin down. When the

directions of the magnetic field and the electric field are constrained to be either parallel (↑↑) or anti-parallel (↑↓) with respect to each other, the spin vector of the particle precesses about the collective axes of the fields. The measured Larmor frequency ω of a particle with the Hamiltonian given by Equation 1.12 is:

$$\omega_{\uparrow\uparrow}\hbar = 2|\mu B + dE|,$$
$$\omega_{\uparrow\downarrow}\hbar = 2|\mu B - dE|.$$

Note that the sign of the electric dipole moment d is in reference to the magnetic dipole μ in this equation. The direction of the magnetic field is in the z direction and the electric field is either along $+$z or $-$z-direction.

Solving these two equations for the strength of the EDM, d, yields

$$d = \frac{\hbar(\omega_{\parallel} - \omega_{\nparallel})}{4E_0}. \tag{1.13}$$

This means that the EDM is measured by the difference in the frequency of oscillations when the magnetic field and electric field are parallel to when they are antiparallel.

1.6 Nuclear magnetic resonance and the Ramsey sequence

In the rotating frame of reference, S', of the oscillating magnetic moment, that is rotating about the z-axis with frequency at the Larmor frequency ω_0, the rotating frame coordinates in the static frame S transform according to

$$\begin{aligned} x' &= x\cos\omega_0 t - y\sin\omega_0 t \\ y' &= x\sin\omega_0 t + y\cos\omega_0 t \\ z' &= z. \end{aligned} \tag{1.14}$$

In the frame of reference S', the spins act as if the polarization vector is held in place, and no longer see the static magnetic holding field B_0 at all. If the system is subjected to an oscillating magnetic field $B_1(t)$ perpendicular to z' at the same frequency as that of ω_0 , the magnetic spins will evolve in the rotating frame as if they were only subjected to a magnetic field along the x'-direction. The spins will now start to precess about that new rotating vector with a new frequency $\omega_1 = \gamma B_1$. The amount of rotation that the polarization vector undergoes in frame S' can be set by limiting the time B_1 is on, defining a pulse length in time. A full 2π rotation would have a pulse length of t_1. To undergo a $\pi/2$ rotation, the particle of interest is subjected to a pulse for a time $t_{\pi/2}$ defined by

$$t_{\pi/2} = \frac{1}{4} t_1 = \frac{\pi}{2\gamma B_1}. \tag{1.15}$$

The Ramsey method can be used to determine the frequency of oscillations due to Larmor precession [18]. First, a polarized particle is placed in a static magnetic field. The system is subject to an oscillating magnetic pulse with frequency ω_{RF} for a time τ, allowed a period of free precession T, and then subject to another pulse that is coherent with the original one as shown in Fig. 1.3a. The term RF is borrowed from nuclear magnetic resonance to denote a B_1 transverse pulse, and not to denote its frequency, which is typically tens of Hertz. Doing a Ramsey sequence at another frequency $\omega_{RF} \neq \omega_0$ produces incomplete slip flipping. The probability of the particle being in its original state is given by

$$P = 1 - 4\sin^2\theta \sin^2 \frac{a\tau}{2} \Big[\cos\frac{\lambda T}{2} \cos\frac{a\tau}{2} - \cos\theta \sin\frac{\lambda T}{2} \sin\frac{a\tau}{2} \Big]^2, \tag{1.16}$$

where $\cos\theta = -\omega_{RF}/a$, $\sin\theta = 2b/a$, $a = \sqrt{\omega_{RF}^2 + (2b)^2}$, $b = \omega_0 \frac{B_1}{B_0}$, and $\lambda = \omega_0 - \omega_{RF}$ [18].

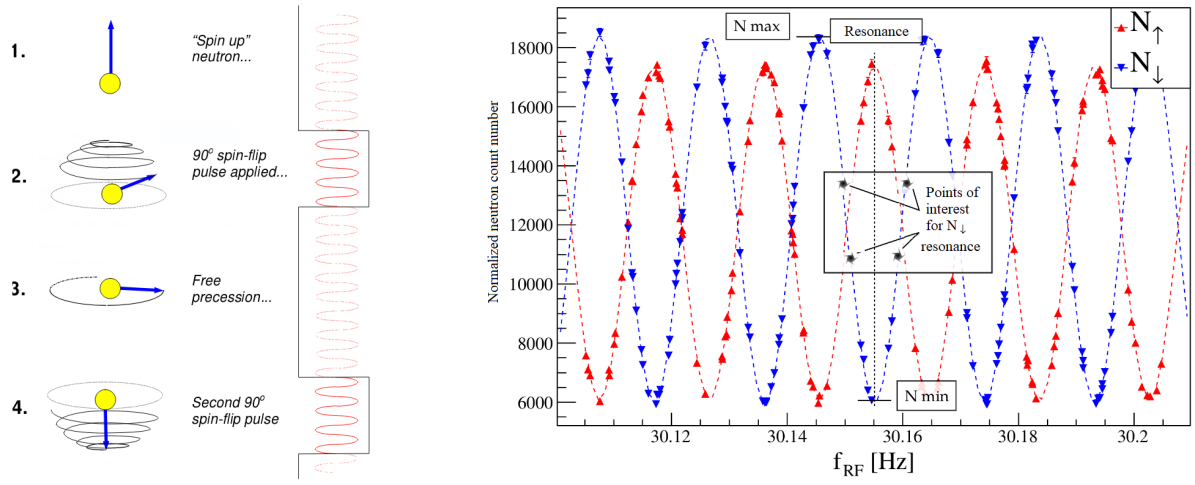

(a) (b)

Figure 1.3: Ramsey technique, shown left (a), is used to measure the oscillating frequency and starts with (1) polarization along one direction, (2) then a cosine pulse is applied to tilt the spins, (3) then spins are allowed to free process (4) an pulse in-phase with the original cosine is applied to tilt the spins again. Figure from [19]. The Ramsey fringe, shown right (b), is a sequence of measurements of the number of neutrons in each of the spin states $N_{\uparrow,\downarrow}$ taken with several different oscillating field frequencies ω_1. $N_\uparrow$ is red and $N_\downarrow$ in blue. The central resonance of the Ramsey field can be determined by the four off-resonance points indicated by the stars. Figure adapted from Victor Hélaine's thesis [20].

The probability distribution function $P(\omega_{RF})$ describes a Ramsey fringe when multiplied by the initial number of neutrons. In Fig. 1.3.b each blue point has a corresponding red point; the pair represents a single experiment pulse with frequency f_{RF}. The Ramsey method is also called the method of separating oscillating fields. Here, instead of sweeping over all frequencies to determine the total signal as done in NMR, we can look at the two contributions making up the signal by using a polarizer capable of looking at the number of UCN with spin up (red) or spin down (blue). The maximal spin flip occurs on resonance, flipping all particles by $\pi/2$ pulse twice. The particle polarization, P, is defined as the fractional population difference between the positive high field seeking state $m_S = +1/2$ and the low field seeking state $m_S = -1/2$ and is given by

$$P = \frac{N_+ - N_-}{N_+ + N_-}, \tag{1.17}$$

where N_+ and N_- are number of particles with spin state of $m_S = +1/2$ and $-1/2$ respectively. Highly polarized systems will have one population of the spin states much greater than that of the other state.

The Ramsey fringe for each of the states are separated by its visibility α. Measuring four points of interest on the blue curve, at frequencies off the resonance allows for a quadratic equation to fit for the resonance. Measuring these points for $E = 0$ and comparing any frequency shifts due to large electric fields that are aligned with the magnetic field.

Measuring the final polarization state of the UCN are related to the frequency of precession of UCN in a magnetic and electric field, through its spin evolution during the Ramsey method.

1.7 Current Searches for the nEDM

The world's leading nEDM measurement was conducted, in 2021, at Paul Scherrer Institue (PSI), Switzerland using an atomic Mercury comagnetometer and an array of optically pumped cesium vapour magnetometers to achieve an upper limit on the magnitude of the nEDM, $|d_n| < 1.8 \times 10^{-26}$ e cm (90% CL) [21].

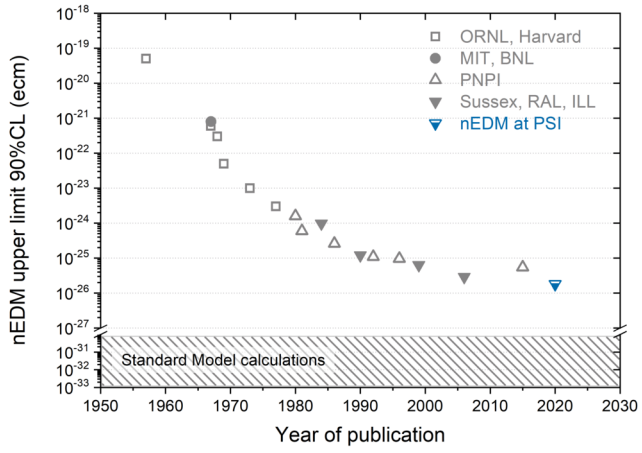

Figure 1.4: History of the nEDM measurements, including the recent PSI measurement [22].

Search for a nEDM has a history dating back the last 1950s (Figure 1.4). The search has pushed

the limits of the nEDM several orders of magnitude in the decades that followed. The search for the nEDM is currently an active field. There are several nEDM searches worldwide with the goal of measuring the nEDM, as summarized in Table 1.2.

Table 1.2: Planned nEDM experiments.

Experiment Group	goal precision nEDM [e cm]	Time frame/goal	location
TUCAN	1×10^{-27}	Installing in 2022-2024, running 2025-2028	TRIUMF, Canada
LANL nEDM	2×10^{-27}	Experiment completed within 5 years of comissioning, currently commissioning	Los Alamos, USA
nEDM@SNS	3×10^{-28}	Within 3 years of 2026-2028 start	Oak Ridge, USA
PanEDM	1×10^{-27}	In first 100 days with potential to upgrade, ongoing installation, UCN production 2023-2024	ILL, France
n2EDM	1×10^{-27}	In 500 days of data, with potential to upgrade, installing	PSI, Switzerland
BeamEDM	5×10^{-28}	Proposed ability of fully upgraded experiment, source complete 2025	ESS, Sweden
PNPI	1×10^{-27}	Between 2023 and 2028	Gatchina, Russia

The LANL nEDM has a goal to reach 2×10^{-27} e cm by 2026 [23]. Their experiment will have a factor of four increase on UCN counts, as well as several upgrades from the previous best

measurement which was done at PSI.

The nEDM@SNS project goal is to reach $\sim 3 \times 10^{-28}$ e cm in 3 years with start time of 2026 to 2028 [24]. Using a measurement cell inside the superfluid helium, the measurement will be conducted with a novel UCN high voltage system.

The PanEDM goal is to reach a sensitivity of mid 10^{-27} e cm in the first 100 days of operation, with hopes to receive UCN soon [25, 26, 27]. Their experiment will have an upgraded UCN source called SuperSUN and dual Cs and Hg magnetometers.

The n2EDM at PSI aims to reach $\sim 1 \times 10^{-27}$ e cm in 500 days of data taking [28, 29].This new measurement is going to use a dual UCN chamber with a larger magnetically shielded room than their previous.

The BeamEDM at ESS [30, 31] is a proof of concept measurement to test the viability of a novel beam Ramsey measurement. The proposed final sensitivity is 5×10^{-28} e cm in the first 100 days of data collection [32].

The PNPI project at PIK has a goal of reaching a sensitivity of 10^{-27} e cm between 2023 and 2028 [33]. This group is developing a high-density UCN horizontal source at the PIK reactor in Gatchina, Russia.

The TUCAN goal is to reach $\sim 1 \times 10^{-27}$ e cm [34] on the nEDM measurement using a new He-II source designed to produce the highest UCN density, with a factor of 100 larger than PSI's measurement. The expected UCN per cycle for the new TUCAN source is 1600000 based on Monte Carlo simulations, compared to PSI nEDM at 15000 UCN per cycle.

As summarized in this section, several groups are working towards leading nEDM measurements. All of these groups use different combinations of techniques, and which ones achieve their goal sensitivities will depend on testing out novel approaches and developing new systems.

1.8 The neutron electric dipole moment experiment

The world's leading nEDM measurement was conducted at PSI, Switzerland using an atomic Mercury comagnetometer and an array of optically pumped cesium vapour magnetometers to achieve an upper limit on the magnitude of the nEDM, $|d_n| < 1.8 \times 10^{-26}$ e cm (90% CL)

[21]. The current nEDM measurement is $d_{\mathrm{n}} = (0.0 \pm 1.1_{\mathrm{stat}} \pm 0.2_{\mathrm{sys}}) \times 10^{-26} e \cdot \mathrm{cm}$ [21].

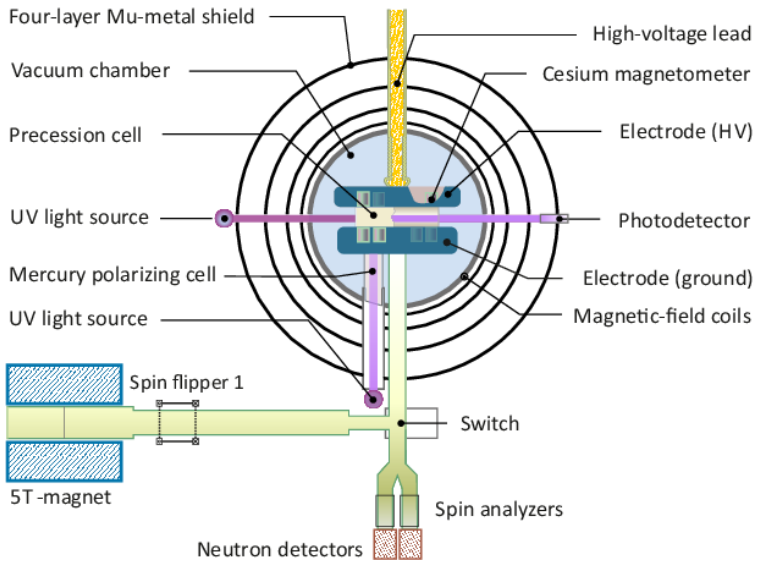

Figure 1.5: Schematic diagram for the neutron electric dipole moment experiment at PSI, Switzerland [35]. UCN enter from a source via a UCN guide located at the bottom left travel through a 5 T super conducting magnet (SCM) on their way to the precession cell and remain aligned to a global B-field. Once there a static E-field is applied parallel or anti-parallel to the B-field, while a transverse RF field produced the pulse necessarily for the Ramsey method of frequency separation.

The nEDM measurement is performed inside a four-layer μ-metal shield. The magnetic shield is required to decrease the magnitude and gradient B-fields that the neutrons see to a level of less than 1 nT/m. By lowering the B-field gradient, false EDMs that can mimic an EDM are reduced. False EDMs appear are systematics that arise that change the frequency with E-feild changes but are from magnetic moment interactions from B-field imhomogenity and E terms.

UCNs from the source are transported into the setup, where they first interact with a UCN polarizing foil. The polarized UCN travel into the storage cell, which contains a cohabiting mercury gas. An ultraviolet mercury lamp below the UCN cell is used to polarize the Hg atoms before UCN filling. Once the pre-polarizing is completed via optical pumping, the Hg gas vapor is leaked into the storage cell to act as a comagnetometer. The mercury co-magnetometer is used to correct the data from false EDMs caused by systematic effects such as magnetic field gradients.

Once in the cell, the UCN undergo a Ramsey sequence as shown in Fig. 1.3. The polarization of the UCN is determined by emptying the cell through an analyzer foil into a UCN detector below. By measuring UCN after different RF frequencies are used, points on the Ramsey fringe curve are used to determine the resonant frequency. The experimental data are taken at four frequencies, two on either side of the resonance frequency, at the maximum slope on either side of the Ramsey central fringe to get the best fit of the Ramsey central fringe. The signature of a neutron EDM is a shift in the frequency in the central fringe under reversal of the E field. Using the polarizer (analyzer) foil only a particular polarization state of UCN is measured at one time. An RF coil in an adiabatic fast passage spin flipper is used to flip the spins allowing the other polarization state to be measured.

The difference between the two frequencies of precession in differing electric field orientations allows us to measure the electric dipole d. The nEDM measurement is then a precision frequency measurement, of the precession of the UCN.

1.9 Statistical Sensitivity

The statistical sensitivity of the nEDM $\sigma(d_n)$ measured by the Ramsey Method is given by:

$$\sigma(d_n) = \frac{\hbar}{2\alpha T E\sqrt{N}}, \tag{1.18}$$

where E is the electric field, T is the free precession time, N is the number of detected UCN, and α is the visibility of the Ramsey Fringe.

The purpose of measuring and improving spin detection is to increase the Ramsey Fringe visibility α. Improving the spin state differentiation, which ultimately determines the frequency that the UCNs experienced during free precession in the experimental cell, increases the statistical sensitivity of the measurement.

Additionally, any decrease in UCN loss probability increases the precision, as it is a net increase in counting N. Minimizing losses through an SSA would increase precision like Victor Hélaine accomplished in his thesis [20]. By using the fringe field of the foil instead of gradient coils, we

hope to further decreases losses by shortening the arms of our SSA.

This thesis aims to improve the neutron counts N by providing calculations of the cryostat needed for the new UCN source. Also, the goal of the thesis is to provide high polarization and high analyzing power of the polarization of neutrons, which is related to the α.

Other work is being done to construct a high field electric conductor capable of producing a large, stable, homogeneous field. The free precession time of the neutron is limited by the spin relaxation of the neutron.

1.10 Systematic Errors

There are various systematic errors that would mimic a false nEDM if they are not identified and properly treated [21]. The contributions to the nEDM are

$$d = d_n + d_n^{false} + d_{quad} + d_{grav} + d_T + d_{Earth} + d_{light} + d_{inc} + d_{other} \tag{1.19}$$

where each term is a contribution from a specific systematic. The $v \times E$ effect from motion mimics an EDM, d_n^{false}. The quadrupole fields and Earth's rotation, d_{quad} and d_{Earth}, induce an effective frequency change as the UCN follow orbital paths in the experimental cell. Transverse corrected fields would induce a systematic, d_T and would need to be accounted for with Hg or Cs co-magnetometers. This is in addition to depolarization due to differences in energies UCN would sample due to average center of mass sampling UCN see in the experimental cells. The rapid change of direction when reflecting in a magnetic field has a larger effect on more energetic UCN. This depolarizing power is enhanced by gravity, d_{grav}. Effects that can mimic an EDM include a mercury light shift, d_{light}, induced scattering from ^{199}Hg, spin dependent incoherent scattering interactions as a result of the pseudo magnetic field from the precessing co-magnetometer Hg atoms d_{inc}, and other non-compensated effects d_{other}.

Using an atomic co-magnetometer to sample the magnetic field during the experiment samples the volume and atoms center of is almost identical to the cell volume, however the low-energy UCNs feel the effects of gravity strongly and are denser in the bottom of the EDM experimental

cell. This means the atomic gas that makes up the co-magnetometer experiences a different magnetic field on average than the UCNs, which mimics a false EDM if the systematic effect is not corrected. To correct for this, precise estimates of the center of mass need to be used. Additionally, the light source used to probe the comagnetometer atoms can cause a shift which directly mimics an EDM, d_{light}. There is also a direct systematic from $v \times E$ which mimics the quadrupole effect and induces a false EDM on the ensemble of UCN.

There are other sources of possible EDMs, such as the large electric field's ability to move the electrodes slightly when flipping the electric field direction between runs, leakage currents, sparks, 0.04% magnitude high voltage ripples can cause AC B fields, artifacts of the measurement process, and the stability of the fields over the experimental run time.

Each systematic needs to be characterized or accurately estimated in order to achieve a precise measurement of the EDM. Usually, the level of systematic needs to match or be better than the level of statistical uncertainty. This means that as the ability to distinguish the polarization states of the UCN goes up, all aspects of the experiment must improve as well.

1.11 Summary

TUCAN's goal is to measure the nEDM to the precise limit of $1 \times 10^{-27}\ e$ cm. The goal of the projects described in this thesis are to characterize improvements to the cooling of the prototype vertical cryostat to inform the new horizontal cryostat design, and to test the neutron spin handling components for the upcoming nEDM measurement.

One of the unique features of the TUCAN nEDM measurements is the design of the He-II UCN source, which is the subject of the following chapter, Chapter 2. It is an accelerator driven spallation neutron source using a horizontal superfluid He-II cryostat UCN converter. Its heat response is crucial for achieving a high density of UCN and I measured the heat response of a UCN source to characterize the validity of a thermal conductivity model for He-II.

Part I

UCN Production

2. Physics of Ultracold neutron production

Ultracold neutrons (UCN) are very slow neutrons that can be stored in material bottles. This makes them excellent subjects to probe the fundamental physical properties of neutrons, such as the lifetime of the neutron, neutron electric dipole moment, and others. Many experimental groups have developed their unique methods of creating UCN.

There are several methods of creating UCN which I will discuss briefly. The two main steps to create UCN are to first liberate neutrons bound in atomic nuclei into free neutrons, and then to moderate them to lower energies by different means to produce UCN.

There are two main methods to liberate large numbers of neutrons efficiently from nuclei. The first is by nuclear fission in a nuclear reactor, and the second is by spallation using energetic protons incident on a high mass number nuclear target.

There are various ways to convert the energetic (MeV) free neutrons into UCN (neV). This chapter will discuss a UCN conversion Doppler shifter and superthermal conversion. More details will be provided on UCN production with superfluid helium (He-II) and solid D_2 converters. The TUCAN source uses He-II, and will be described in detail. Helium-II and neutron interactions are vital to understand how TUCAN's liquid helium moderated spallation driven UCN Source produces UCNs.

2.1 Neutron production

The two main methods of neutron production are nuclear fission and accelerator-driven spallation. In nuclear reactors, the fission of uranium results in neutron-rich nuclei emitting neutrons. The neutrons drive a chain reaction, but some of the freed neutrons may also be used for experiments. In spallation sources, like the one at TRIUMF, a high-energy proton beam initiates the break-up of nuclei, also liberating neutrons. At present, nuclear reactors (e.g. ILL) and accelerator-driven spallation sources (e.g. SNS, J-PARC) are competitive in their ability to generate large numbers of free neutrons for experiments.

Once the neutrons are liberated from nuclei, they have very high energies > 1 MeV. Thermalizing the neutrons to a mean energy of ~ 25 meV is accomplished by bringing them into contact with a neutron moderator at room temperature. Neutron moderators are generally made of materials containing light nuclei. Elastic collisions of neutrons with the nuclei cause the neutrons to lose energy until they come into thermal equilibrium with the surrounding material ($kT \sim 25$ meV for $T = 300$ K). Neutrons emitted from the neutron moderator will have a Maxwell-Boltzmann energy spectrum with a characteristic temperature $T = 300$ K.

2.2 UCN converters

Ultracold neutrons have a kinetic energy $E < 300$ neV. Much lower than room temperature neutrons.

The Maxwell-Boltzmann energy spectrum is a probability spectrum with a maximum near the average and two tails, one that falls off towards infinity and another short tail that diminishes in probability towards lower energies. Thus, the probability of UCN being created with $E < 300$ neV is always nonzero for the process of thermalization, but not in large numbers. The Maxwell-Boltzmann distribution $f(v)$ in terms of velocity v is given by:

$$f(v) = \sqrt{\left(\frac{m}{2\pi k_B T}\right)^3} 4\pi v^2 \exp^{-\left(\frac{mv^2}{2k_B T}\right)}. \tag{2.1}$$

Here m is the mass of the neutron, k_B is the Boltzmann constant, and T is the temperature of the system in Kelvin. Integrating Equation 2.1 over velocity from 0 to 7.6 m/s gives the probability of UCN, for room neutrons neutrons this is 3.01×10^{-8}. Thus the need to convert higher energy neutrons to UCN directly rather than through thermalization.

2.2.1 Superthermal sources

A superthermal converter can be considered as a two-state system whose energy difference Δ, is of order a few meV. Cold neutrons with corresponding energy matching the superthermal system, interacts with the system lose energy by creating excitations in the system. The resulting

neutrons are colder, having had some of their energy removed by the excitation.

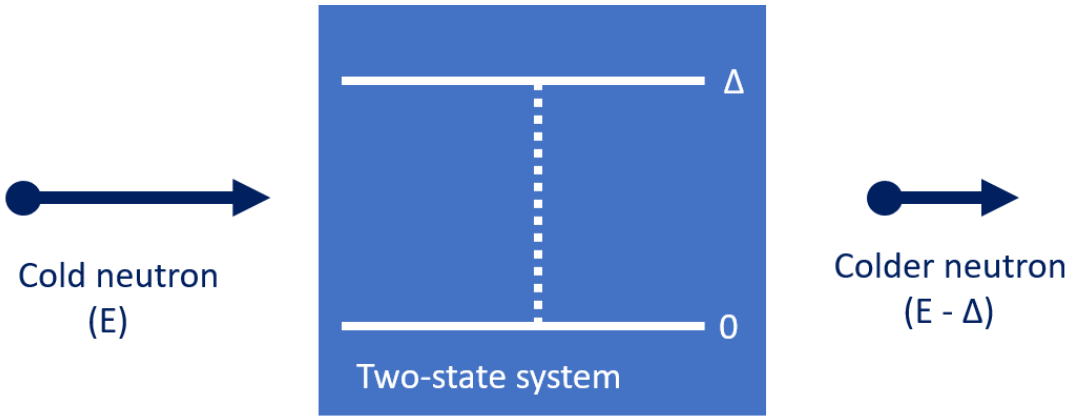

Figure 2.1: A diagram of a two-state superthermal system that cools neutrons by using the neutron's energy to excite the system into its excited state.

In Figure 2.1 the two-state system is initially in the lower state. The cold neutron deposits energy Δ into the system exciting it to the upper state. The exiting neutron is now colder. This process is called downscattering. If the now colder neutron stays in thermal contact with the system, it can easily absorb the energy back, which is called upscattering. Upscattering can be suppressed by cooling the converter, depopulating the excited state.

There are several condensed matter systems where UCN production is large and UCN losses are small. Candidate superthermal converters are solid deuterium (sD_2) and superfluid helium ^{4}He. There are a few other materials such as O_2, CD_2, and $^{15}N_2$ ices for example that could be used. In this thesis I will focus on mainly ^{4}He, but I briefly introduce sD_2 sources because they are our chief competitors.

Solid ortho-deuterium (sD_2) has a high production rate for downscattering cold neutrons to UCNs because of deuterium's large neutron scattering cross-section and the many vibration states of the deuterium crystal that can be excited. However, multiple loss channels means there is no single source of losses for reasonable values of the parameters of the material. The loss rate or

decay constant is given by $1/\tau$ and is a measure of the exponential decay following

$$N(t) = N_0 \exp^{-\frac{1}{\tau}t} \tag{2.2}$$

The overall loss rate $1/\tau_{\mathrm{UCN}}$ is given by the sum of its loss channels:

$$\frac{1}{\tau_{\mathrm{UCN}}} = \frac{1}{\tau_{\mathrm{phonon}}} + \frac{1}{\tau_{\mathrm{para}}} + \frac{1}{\tau_{\mathrm{D,abs}}} + \frac{1}{\tau_{\mathrm{H,abs}}} [36]. \tag{2.3}$$

Here the loss rate through phonon upscattering is given by $1/\tau_{\mathrm{phonon}}$, the loss rate of the para-deuterium is given by $1/\tau_{\mathrm{para}}$, the loss rate for neutron capture by deuterium is $1/\tau_{\mathrm{D,abs}}$, and from hydrogen capture is $1/\tau_{\mathrm{H,abs}}$. In total, these sources make the lifetime of UCN in the crystal about 25 ms at 5 K [36]. After downscattering, if the neutrons linger, they can be lost by any of the mechanisms just described. Therefore, the UCN need to exit the sD_2 within about 25 ms. Furthermore, all the loss rates are similar in magnitude for reasonable experimental parameters, so it is difficult to improve this by much. The main takeaway with solid ortho-deuterium moderation is that the process creates lots of UCNs, but has comparably high losses. Trying to limit these high losses is where some of the engineering challenges lie when using solid D_2 sources. Also, frost on the surface of crystalline sD_2 can cause large losses which evolve over time [37].

2.2.2 Liquid superfluid ^{4}He UCN source

The dispersion curves of free neutrons and superfluid ^{4}He is shown in Fig. 2.2. Referring to the dispersion cure for the elementary excitation in He-II, the linear part near zero momentum is due to excitations called phonons and near and beyond the local minimum excitations are called rotons. The free neutron dispersion curve crosses the He-II dispersion curve at an energy of 1 meV on the vertical axis. This means that a neutron near 1 meV can scatter from He-II producing exactly one phonon, while conserving both energy and momentum in the scattering process. The resultant neutron will be reduced to near zero energy. A large number of 1 meV neutrons impinging on He-II will make a very efficient UCN source. Higher energy neutrons can lose energy by multi-phonon

production [38].

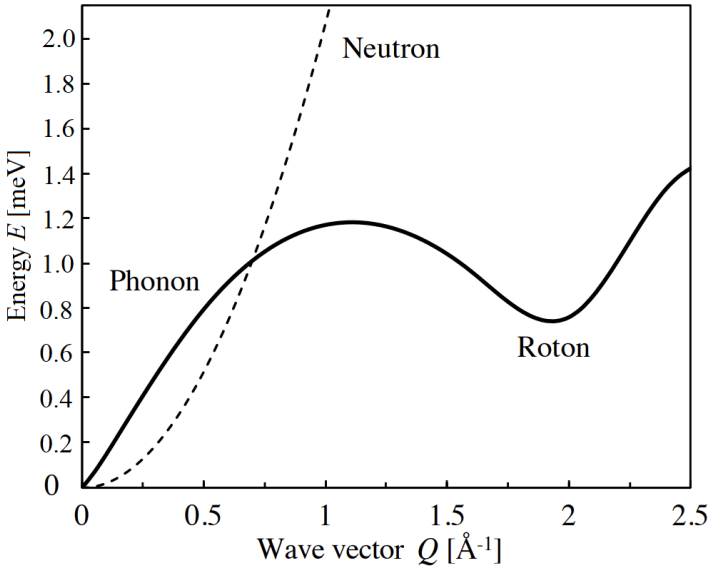

Figure 2.2: The dispersion curve He-II (solid) and of free neutrons (dashed)[39]. The wave vector is defined as $p/\hbar$.

The losses of UCN in superfluid ^{4}He is dominated by the 2-phonon upscattering rate, which goes as T^7, where T is the temperature of the superfluid [17, 40]. Having a lower temperature T for the superfluid is then vital to reduce losses. At $T = 1$ K, the loss rate is

$$\frac{1}{\tau_{\text{UCN}}} = \frac{1}{\tau_{\text{wall}}} + \frac{1}{\tau_{\text{up}}} + \frac{1}{\tau_{\text{abs}}} + \frac{1}{\tau_{\beta}} [40]. \tag{2.4}$$

Here τ_{wall} is the wall loss lifetime from the specific material and impurities and can range on the order of $10 - 10^2$ s. The term τ_{abs} is the loss lifetime in He due to ^{3}He capture from impurities, which with isotopically pure ^{4}He is around the order of 10^2. The term τ_{β} is the neutron lifetime $\tau_{\beta} = (878.4 \pm 0.4)$ s [16]. The term τ_{up} is from upscattering from phonons. The UCN loss rate is

dominated by 2-phonon upscattering rate and τ_{up}^{-1} is proportional to

$$\tau_{\text{up}}^{-1} = B \cdot \left(\frac{T}{1\ \text{K}}\right)^7 \tag{2.5}$$

where the coefficient of B can vary from $B = (4 - 16) \times 10^{-3}$ s$^{-}1$ [40]. With values of $B = (1.6 - 8 \times 10^{-3}$ s$^{-}1$ and with a wall loss lifetime between $(32 - 38)$ s the lifetime is 20 s [41].

This means two of the key challenges in using superfluid helium sources are in trying to keep the temperature low (T < 0.8 K), and in extracting the UCNs from the superfluid helium for experiments. Note that SNS is trying to solve the latter by doing the nEDM experiment in the source itself.

In comparison, the UCN loss lifetime in superthermal ^{4}He can be hundreds of seconds, while in sD_2 about 25 ms.

2.2.3 Doppler shifting

A Doppler shifter, or ultracold neutron turbine, makes use of elastic scattering of UCNs off a material surface. It gets its name because the process lowers the wave number of the incident neutron. When undergoing reflection off a moving surface the reflected neutron velocity is

$$\vec{v}_r = \vec{v} + 2|(\vec{v} - \vec{v}_m) \cdot \hat{n}|\hat{n}. \tag{2.6}$$

In this equation, the velocity vector of the reflected neutron is $\vec{v}_r$, the velocity vector of the neutron prior to the collision is $\vec{v}$, the velocity vector of the neutron mirror is $\vec{v}_m$, and the normal vector perpendicular to the mirror's surface is $\hat{n}$ [42].

Figure 2.3 shows a neutron mirror moving with velocity $\vec{v}_m$ in grey and an incident neutron with velocity $\vec{v}$ in dark blue. It shows how a neutron mirror with $\vec{v}_m = \vec{v}/2$ can reduce the neutron's reflected velocity to near zero only leaving the perpendicular velocity $\vec{v}_r$.

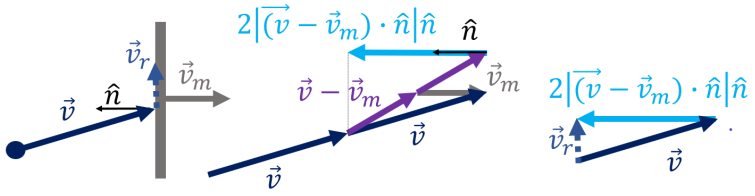

$$\vec{v}_r = \vec{v} + 2|\overrightarrow{(v} - \vec{v}_m)\cdot\hat{n}|\hat{n}$$

Figure 2.3: A neutron-mirror collision decelerates the neutron in the direction normal to the moving neutron mirror.

If the incident neutron had little to no transverse components, it would be reduced to zero velocity. However, this would only work for a rather limited range of velocities of neutrons in a beam. Multiple mirrors can be arranged on a spinning axis to decelerate a continuous cold neutron beam. This makes the apparatus have the appearance of a turbine. Instead of straight mirrors, curved mirrors can be used to avoid multiple collisions, so the UCN will have to travel only a short distance to escape being accelerated by the next mirror. This method is fundamentally limited by Liouville's theorem; the process cannot compress the phase space of the UCN, whereas superthermal sources can by carrying away momentum and energy using phonons. Thus, it is believed that superthermal sources will eventually win out over turbine sources. However, at this time, the UCN turbine at ILL is still competitive with the leading superthermal sources.

2.3 Survey of UCN sources worldwide

This section will present a few UCN sources, both historic and modern.

The ILL source is a nuclear reactor source that creates cold neutrons by using large guides with slight angles in reactors to guide higher energy neutrons towards their main moderation method to convert them to cold neutrons in liquid hydrogen or liquid deuterium [17, 43]. The resulting cold neutrons are converted to UCN using a UCN turbine (Fig 2.4). UCN exit the turbine via a port, and they exit perpendicular to the axis of the neutron turbine.

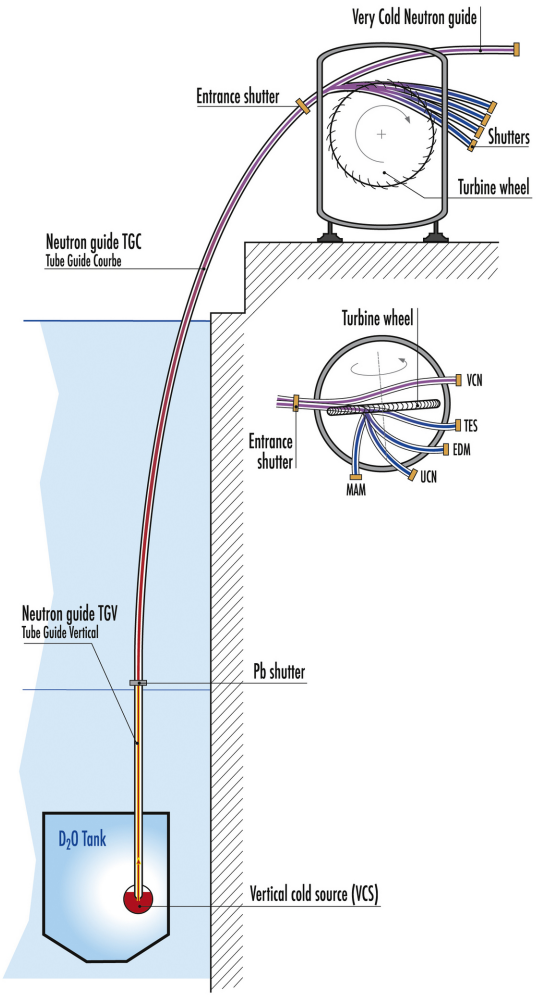

Figure 2.4: CN-VCN turbine source at ILL-Grenoble. The cold neutron deuterium source uses gravity for some cooling. But a less steep bend actually encourages the cold neutrons to enter the turbine at the correct angles. This turbine creates both very cold neutrons (VCNs) and UCNs [44] (source described in [43]).

The UCN source at the Paul-Scherrer Institute (PSI) (Fig. 2.5), uses a proton beam incident on a lead target. The resulting high-energy neutrons are moderated by liquid heavy water, followed by a solid deuterium converter, creating UCNs. The UCN extraction is into a vertical cryostat to store the UCNs before exiting to the West-1, West-2, or South UCN beam ports [45].

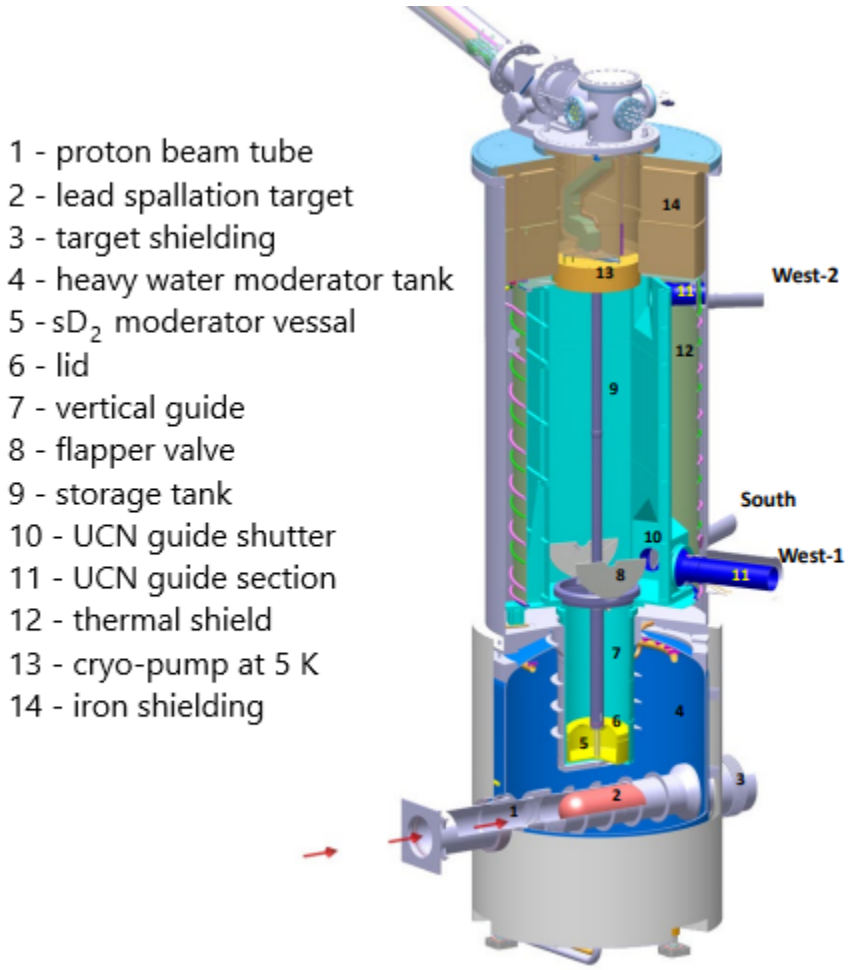

Figure 2.5: The PSI UCN source uses accelerator-driven spallation, and a sD_2 superthermal UCN converter [45].

In addition to the two UCN sources described previously in this section, there are several unique combinations of neutron production and UCN converters, as shown in Table 2.1. This more complete list of current UCN sources includes the method of neutron production as its main method of conversion of neutrons to UCN.

Table 2.1: World-wide UCN Sources and their statuses.

Experiment Group	Neutron Production	Converter	Status
ILL	Reactor, CN	Doppler shifter	running
J-PARC	Spallation	Doppler shifter	running
ILL SUN-2	Reactor, CN	Superfluid He	running
ILL SuperSUN	Reactor, CN	Superfluid He	
TUCAN	Spallation	Superfluid He	upgrading
PIK Reactor, Gatchina	Reactor	Superfluid He	development phase
LANL	Spallation	sD_2	recently upgraded
Mainz	Reactor	sD_2	running
PSI	Spallation	sD_2	running
NSCU Pulstar	Reactor	sD_2	installing
FRM-II	Reactor	sD_2	development stage

The Japan Proton Accelerator Research Complex (J-PARC) produces neutrons via spallation and uses a Doppler shifter to convert neutrons to UCNs. The SUN-2 Source at ILL is a cold neutron reactor that uses superfluid helium to produce UCNs, this source is being used to support the SuperSUN development, which is in the process of installation [46]. The PIK reactor (high-beam PIK reactor is an abbreviation of the names of the developers of the project Petrova and Konopleva) is in the development phase at Gatchina and will provide neutrons to a superfluid helium UCN source [33]. The UCN source at Los Alamos National Labratory (LANL) uses proton beam spallation followed by a solid deuterium moderation to produce UCN [47]. The pulsed TRIGA reactor at Mainz, Germany upgraded its solid deuterium ultracold neutron source in 2018 bringing their UCN density to 8.5/cm^3 [48]. Paul Scherrer Institute (PSI) uses a spallation-driven solid deuterium UCN source (Fig 2.5 [49]. The North Carolina State University (NCSU) Pulstar

reactor uses a pulsed neutron beam from a nuclear reactor and a solid deuterium superthermal moderator to produce UCNs. The FRM-II reactor (Germany) UCN source is in the development stage and plans to use a deuterium converter to produce UCN.

Each source complements the other, allowing research on neutron properties with UCN to be carried out worldwide. Each source has unique strengths and weaknesses. The goal of TUCAN is to surpass the UCN production of the currently running UCN sources. The unique combination of spallation and He-II makes the project compelling.

2.4 The TUCAN source

The results from this thesis are from the vertical He-II UCN source, shown in Figure 2.6. The vertical source was developed and previously operated at RCNP Osaka, Japan [50]. It operated at TRIUMF from 2017-2019. The TRIUMF Ultra-Cold Advanced Neutron (TUCAN) source is in the process of being upgraded. Once completed the new TUCAN source will use 40 μA of 500 MeV protons from the TRIUMF cyclotron to produce neutrons by spallation from a tungsten target.

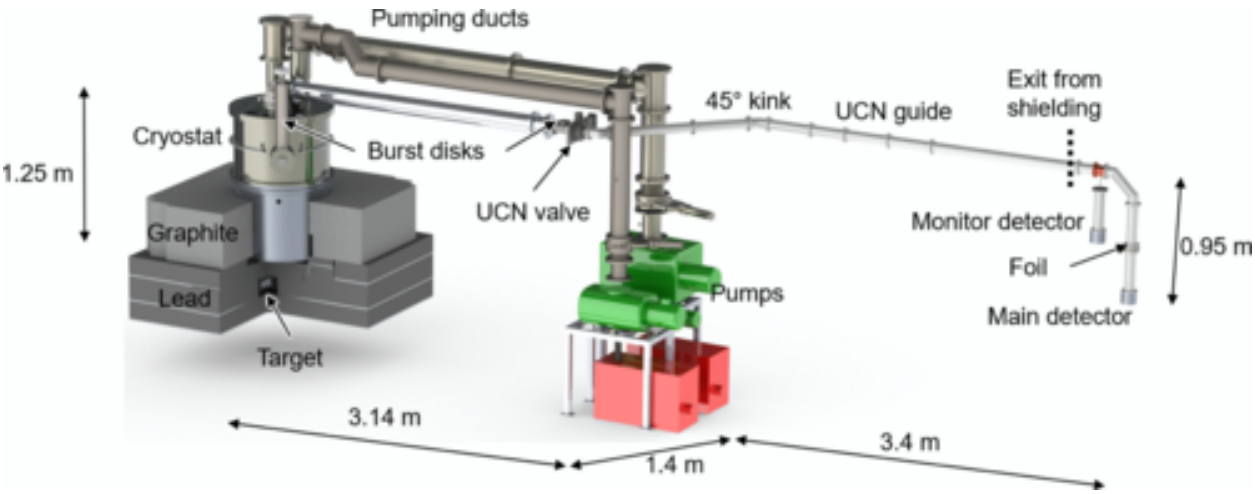

Figure 2.6: The vertical UCN crysostat source and guide layout of the UCN spallation source at UCN TRIUMF [51].

The proton beam is extracted from the main TRIUMF proton beamline with a kicker magnet [52] and directed by a series of collimators and magnets to the tungsten target [51]. The prototype vertical He-II UCN source could only accept 1 μA of proton beam current on the tungsten target before heating reduced the UCN production.The protons hitting the target created high energy neutrons.

The source used successive layers of neutron moderation to slow down free neutrons and eventually convert them to UCNs. The high energy neutrons quickly thermalized with the graphite, lead shielding, and liquid heavy water losing energy through elastic scattering, becoming thermal neutrons.

More elastic scattering in the cold solid heavy water occurred before ~ 1 meV neutrons whose energy is higher than the nickel coated bottle potential (256 neV) penetrated the bottle and reacted with the superthermal He-II near 1 K. The D_2O ice is used to slow the free neutrons down through thermal to cold temperatures.

When the CN traverse the superfluid helium, they scatter producing phonons causing them to lose energy. The 1 meV neutrons were converted into UCN in the bottle. It is at this point free neutrons downscatter according to the dispersion curve for elementary excitations in He-II, shown in Fig. 2.2. The newly converted UCN have a $\sqrt{E}$ energy spectrum (see equation 3.37 of [17]). The UCN are trapped in the nickel bottle with an exit in on the top connected to neutron guides.

The UCN whose energy is above 128 neV could overcome the gravitational potential to leave via the exit port in the top above the bottle 1.25 m above the bottom of the bottle (Fig. 2.6). UCN with energy below 125 neV are trapped in the bottle and either upscatter or decay, since they never leave the bottle. Once in the guide the UCN behaved as a heavy ideal gas. They traversed the 3.14 m of guide to make it to a 45° kink (Fig. 2.6). After another 1.4 m of guide the UCNs will see another kink before exiting the concrete shield to the exit port in 3.4 m (Fig. 2.6). The purpose of the kink is to eliminate high energy neutrons with low incident angles to the guide from reflecting along the guides and into the detector.

At the exit port, some UCN will be counted through a pinhole in a monitor detector, which

will be used to normalize the rates in the main detector to UCN actually produced. The source produced UCN with an energy spectrum of less than 90 neV [53]. The UCN from this source were used to test UCN guides and other components [51, 52].

2.4.1 Heating tests of the vertical cryostat

The heat added by the heater or by the proton beam flows throughout the liquid superfluid helium to reach the heat exchanger. The heat exchanger is located to the right, near the top of the level of the superfluid helium, as shown in Fig. 2.7.

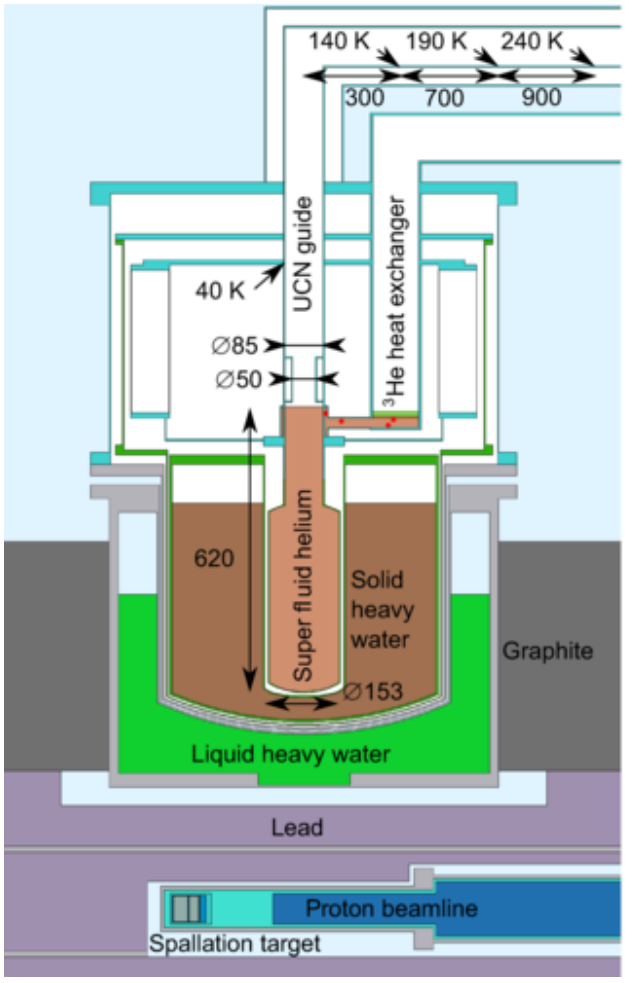

Figure 2.7: Drawing of a cross-section of the vertical cryostat (units in millimetres). The target is irradiated with protons, producing spallation neutrons. The red dots indicate the low temperature sensor locations. The temperature along the UCN guide is given as well. [41]

This heat flow has to travel through the narrow channels, and slits near the top of the bottle, which will seriously limit the heat flow. This is the geometry used in models and discussions in Chapter 4.

Florian Rehm's undergraduate thesis [54] studies temperature gradients in the temperature probes along the arm going from the source bottle to the heat exchanger. These temperature sensors were never calibrated precisely. To counter this, Rehm only looked at temperature differences and their change with heat load, rather than the absolute magnitude. Instead, here we are looking directly at the vapour pressure above the UCN bottle using a low pressure capacitance manometer gauge. Since pressure drops in the UCN guide are small, the vapour pressure is linked to the temperature of the He-II production volume [55]. Therefore, we are looking directly at the signal of the heat load on the UCN bottle where the neutrons would see it (see Fig 2.8).

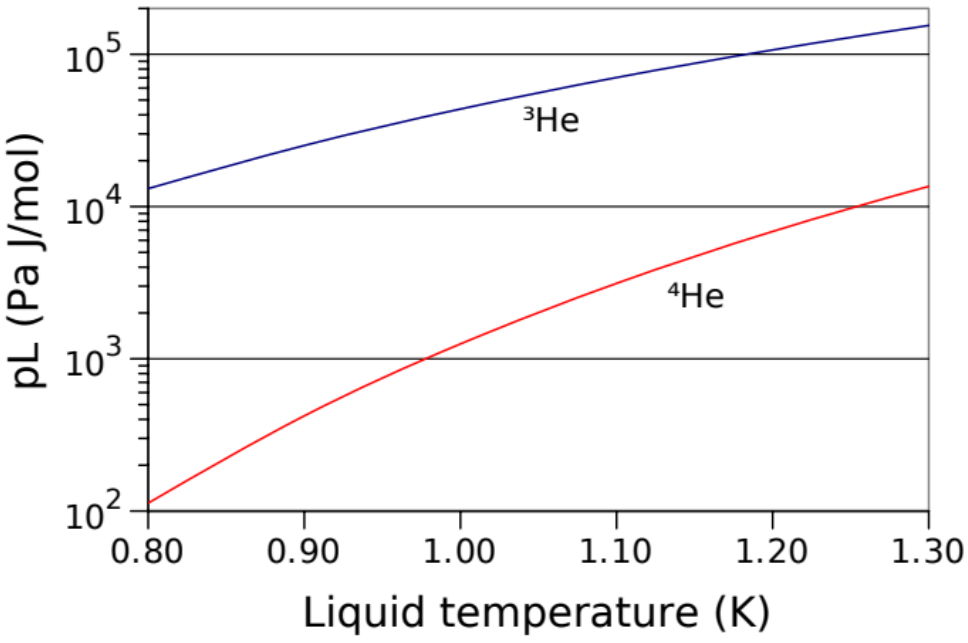

Figure 2.8: Product of latent heat and vapour pressure for liquid helium at different temperatures (figure taken from [55])

.

Figure 2.8 shows that the temperature of the ^{4}He is directly linked to the product of the pressure to the latent heat of vaporization. We can extract the temperature by measuring the pressure.

In this work, I focus on understanding this temperature heat flux through tiny gaps. Assuming the heat exchanger temperature does not change significantly, and that the heat flux is restricted to passing through the tiny gaps in the foil separating the He-II production volume from the heat exchanger. A chief result is that it takes a fairly long time ($\sim$100 s) for the heat to be transmitted to the heat exchanger, which can not be explained by phenomena like second sound (wave propagation of thermal excitations in superfluid helium) alone in this geometry.

The vertical source has a few issues with the heat load. Its primary problem is that its heat response is very slow and temperature rise very large, on the timescale of 15 minutes to reach equilibrium with an applied heat source. Therefore, plans were made for the new horizontal cryostat for a future source (Figure 8.2). There are many improvements to the vertical source to produce UCNs. The material potential of He-II is 18 neV, making for near horizontal extraction compelling; this potential corresponds to 16 cm in Earth's gravitational potential. Additionally, improvements to the moderators have been made. Instead of a direct heavy water ice moderator, there will be a liquid deuterium moderator, with a geometry optimized for the room temperature moderators. There will also be an increase in the He-II production volume, from 8 L to 33 L. Additionally, thinner walls of the UCN bottle will reduce heating from the shower of particles produced by spallation, primarily from beta particles and gamma rays.

The beam current will be increased from 1 μA to 40 μA . This increase requires improvements to the cooling power across all parts of the liquid helium cryostat. For example, bigger pumps are needed to cool the ^{3}He faster. An improvement on the heat conductance of the bottle is needed. This means no thin channels the superfluid needs to flow through in the vertical source, instead heat conduction is needed. A larger surface area heat exchanger with a direct connection to the He-II will be used to solve this deficiency (Figure 8.1). This last point is the basis of the superfluid portion of my thesis. I will directly measure the vertical cryostat's heat response and compare it with a model that can be used to benchmark the design of the horizontal cryostat. The new source's

cryostat needs to handle 10 W of heat deposited into the He-II, compared to the 300 mW maximum of the vertical cryostat.

All these improvements should combine to have a several hundred-fold increase in UCN delivered to experiments compared to the vertical source. The new horizontal source is currently being helium leak checked. Chapter 8 will discuss this future work in more detail. Several studies of the performance of the new cryostat have been completed, and installation will continue over the next year.

2.5 Concluding remarks

There are multiple methods of creating free neutrons and converting them to ultracold neutrons. The TUCAN collaboration is building a spallation-driven He-II UCN source. The upgrade of the TUCAN source from the vertical prototype to the horizontal source is underway over the next two years.

In TUCAN's source, protons hitting the high density tungsten target create spallation neutrons and other high energy particles. The neutrons are slowed in the surrounding layers of lead, liquid heavy water, heavy water ice, and finally in the superfluid helium (He-II). In Section 1.4 we discussed how the speed of the neutrons is related to the energy range. The UCNs, when their energy is below the Fermi potential of the nickel coated UCN bottle, are confined and directed via the guide to the experimental area.

The distinct properties of He-II will be discussed in more detail in the next chapter. The fact that He-II has a low upscatter cross-section and nearly negligible neutron capture cross-section make it ideal in creating a high density UCN source. Working near 1 K there are few excitations in the He-II, ready to accept heat and produce excitations from cold neutrons causing them to downscatter into the ultracold regime. Superfluid helium can upscatter neutrons of the UCN regime at a rate proportional to T^7. This T^7 UCN loss rate means that UCN production is extremely sensitive to temperature changes and that cooling the superfluid is vital to maintain large production rates for superfluid helium.

3. Properties of He-II

To understand the cryostat a brief discussion of the properties of liquid helium-II are presented in this chapter. Several unique properties of the superfluid liquid helium-II are discussed. Experimental evidence supporting a model with the existence of two distinct types of motion in the superfluid helium will be shown. This discussion will go over superfluid vortices and their associated experimental evidence and will briefly outline the connection between the two fluid model as related to Gorter-Mellink heat conduction, in particular mutual friction. This essential link is vital in understanding the time dependent Gorter-Mellink model of heat transport discussed in Chapter 4.

3.1 Liquid Helium-II

The boiling point of liquid helium is 4.2 K at atmospheric pressure. There are two phases of liquid helium. There is a warmer phase called liquid helium-I, and a colder phase called liquid helium-II. It is the colder phase that earns the title of a superfluid. The transition between the phases of liquid helium occurs at a temperature of 2.17 K and is called the lambda point. The lambda point gets its name from Figure 3.1, where the shape of the specific heat as a function of temperature looks like the Greek letter λ. These properties are for the stable isotope ^{4}He. The second stable isotope of helium is ^{3}He, for which the superfluid phase does not exist at atmospheric pressure (The superfluid phase of ^{3}He only exists at high pressure and exceedingly low temperature). The nucleus ^{4}He has an even number of neutrons and protons (spin-1/2 particles), and so has integer spin. This makes ^{4}He bosonic and able to form a Bose-Einstein condensate, while the ^{3}He nucleus is spin-1/2 and thus it is a fermion. The natural abundance of ^{3}He is rare compared to ^{4}He, with the ratio being $1{:}10^7$. While ^{4}He is created in the proton-proton chain, a set of nuclear reactions by which stars convert hydrogen into helium, ^{3}He is dominantly created through cosmic ray spallation, where a cosmic ray impacts heavier nuclei and fragments them.

Evaporative cooling may be used to cool the liquid helium through the transition temperature.

As the liquid's temperature nears the lambda point, boiling increases then stops entirely at the transition. The superfluid still evaporates, it just no longer boils, because density fluctuations are no longer possible due to the very high thermal conductivity of the superfluid.

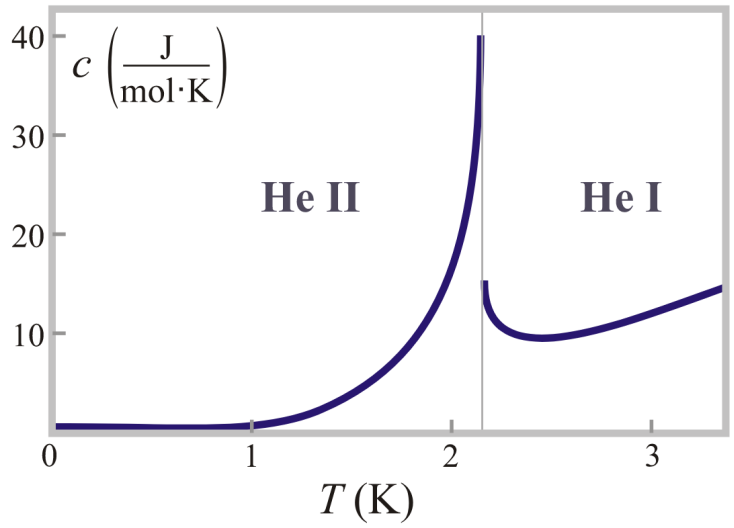

Figure 3.1: Plot of specific heat capacity versus temperature of liquid ^{4}He, showing the phase transition from He-I to He-II [56]

In Figure 3.1, the specific heat decrease with temperature in the He-I phase, but as it nears the lambda point it rises. At the transition, there is a discontinuity, which is evidence of a distinct phase change. The heat capacity of He-II starts higher than He-I at the transition, but rapidly falls to zero as the temperature approaches absolute zero. Pumping on He-II, it becomes increasingly harder to cool as it gets colder. For UCN, we will need to cool it to $\sim$1 K, and this leads to different cooling mechanism being used involving ^{3}He and a heat exchanger, see Chapter 4.

3.1.1 Superleak versus bulk flow viscosity

Helium-II is capable of two different kinds of motion with radically different viscous properties. The first is a superfluid flow, capable of perfect non-viscous flow that is thermodynamically reversible. The second is normal flow that both has viscosity, and is irreversible. To demonstrate

these properties we can look at the well-known phenomenon of superfluid flow. Superfluid flow occurs with little or no friction. Superfluid Helium-II will flow through microscopic capillaries which are too small to permit normal fluid to pass.

A superleak can be experimentally demonstrated by putting helium-II in a beaker which has an unglazed ceramic bottom (Figure 3.2 a). The unglazed ceramic has microscopic capillaries through which only a superfluid fluid with near zero viscosity can leak. In Figure 3.2 b Superfluid flow of liquid helium-II flowing in a thin film is collecting in a drop at the bottom of the container. The drop will fall when enough superfluid collects, and eventually all the superfluid will flow out of the container.

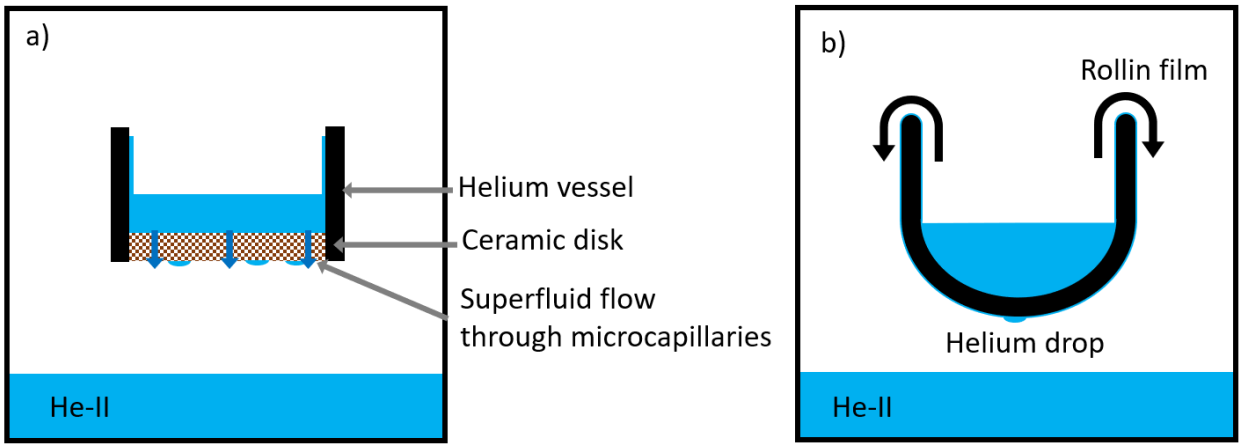

Figure 3.2: Diagram of a superleak and superflow of super fluid helium. a) The superfluid flows through a superleak in the ceramic bottom through the microscopic capillaries, since it has zero viscosity. b) Van der Waals forces and zero viscosity allow superfluid helium to form Rollin films that creep up the sides of the container and flow out of the vessel.

The superleak is noticeable just below the lambda point, but the rate of flow through the bottom of the vessel increases as the temperate decreases. This demonstrates that the small helium-II viscosity drops with temperature. Another effect that is related to the superleak is Rollin film. A superfluid can flow out of a container over its rim. It does this through a thin film called a Rollin film that travels up over the container's walls, collects and then drips off the bottom. Figure

3.2.b shows a diagram of this effect. It is only possible due to the incredibly low viscosity of the superfluid.

The viscosity of helium-II can also be measured using a rotating viscometer setup such as the one in Figure 3.3.

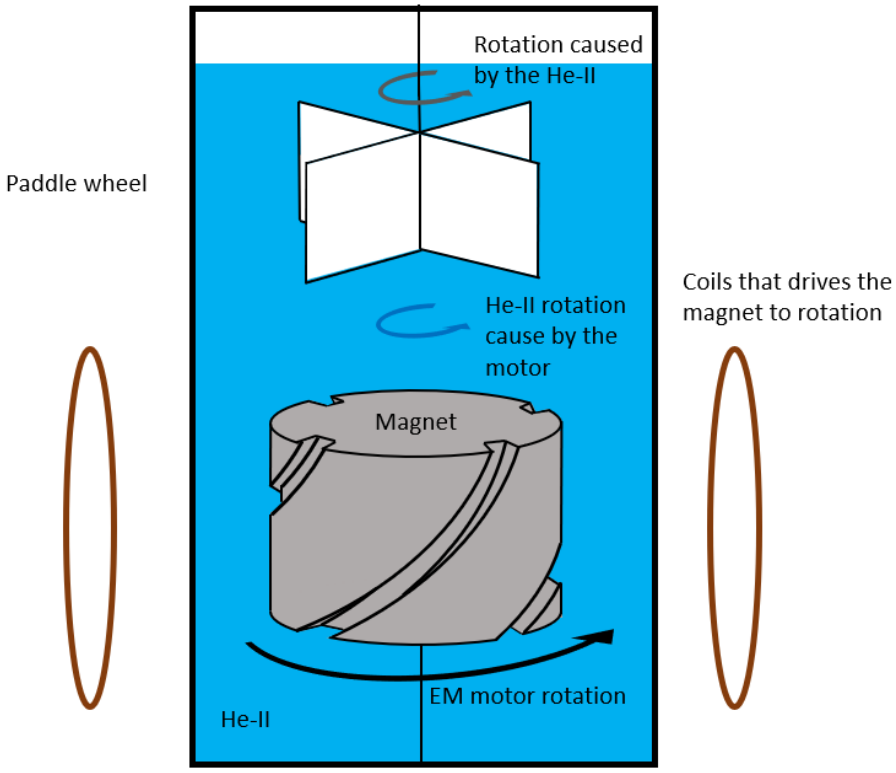

Figure 3.3: Schematic diagram showing the rotating cylinder experiment. The coils are electromagnetic motors that spin a magnetic cylinder in the superfluid. Above the cylinder is a paddle wheel that is suspended in superfluid helium.

The cylinder, submerged in liquid helium, is rotated via an EM motor. Suspended above the cylinder, also in the liquid helium, there is a paddle wheel. This wheel only moves if there is rotational motion of the fluid in the beaker and the fluid has some viscosity. Once the cylinder rotation is started, a short while later, the paddle wheel turns. This indicates that the fluid has viscosity. Viscosity is an interfluid force due to the van der Waals force, that manifests itself as an

attraction force that the liquid exerts on itself. A layer of liquid is attracted to the cylinder and is dragged along as the cylinder rotates. The van der Waals force allows this rotation to be transferred to the bounding layer of liquid helium which is not moving and so on for the bulk liquid. As the bulk liquid acquires rotational motion. The rotational motion then moves the paddle-wheel, much like a classical liquid would.

The rotating viscometer and superleak experiments demonstrate an apparent contradiction. The He-II seems to behave both as a classical liquid with viscosity and as a superfluid with no viscosity. The two distinct and incongruous viscosity properties suggest that there are two types of motion. These two types of viscosity are accounted for in the two-fluid model that will be presented in Section 3.1.2.

3.1.2 Two-Fluid Model

The two distinct types of flow present in helium-II are described by the two-fluid model. The helium-II is modelled as having two parts: a superfluid part, and a normal part. This model is successful in describing both heat and mass transport [57]. Fig. 3.4 shows the normalized density of the superfluid part (ρ_s/ρ) and the normal part (ρ_n/ρ) as a function of temperature.

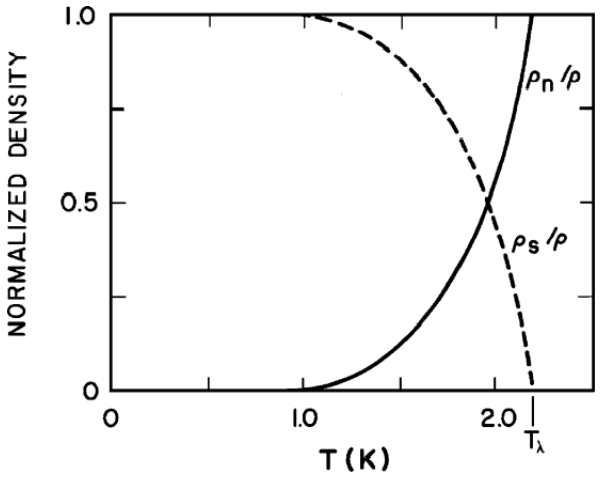

Figure 3.4: Ratio of the normal component and superfluid component part densities in Helium-II [57].

The density of helium-II (ρ) is assumed to be the sum of the two component densities:

$$\rho = \rho_s + \rho_n. \tag{3.1}$$

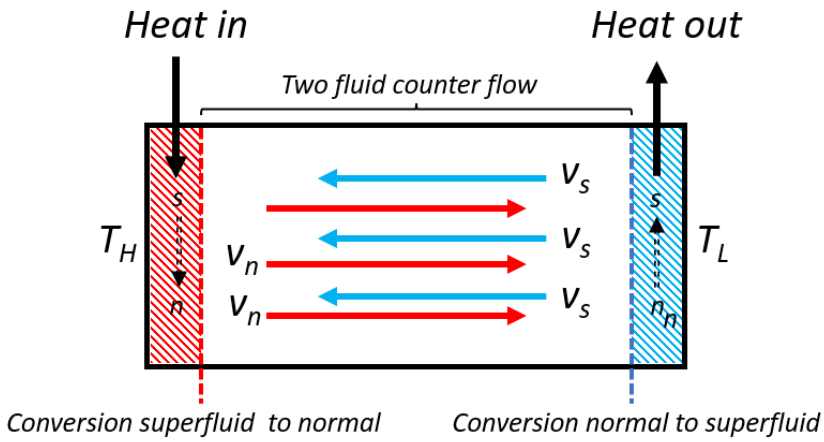

Figure 3.5: Transport of heat by a counter flow of the two fluid components, the superfluid component and the normal component, of He-II.

The existence of superleaks through capillaries and Rollin film provide evidence for a part of the fluid that has no entropy and no viscosity. The superfluid component in the two-fluid model contains no entropy, and the normal component would contain all the entropy and heat of the system.

Figure 3.5 shows the counter flow of the two fluid model. The normal component v_n flows as a classical liquid towards the low temperature region, T_L while the non-entropy containing superfluid component v_s flows as a superfluid counter the classical flow towards the heat input and high temperature region, T_H. The counter flow of the two-fluid model is the explanation for the fountain effect and why there is mass transfer.

3.1.3 Fountain Effect

The fountain effect is a surprising effect that only appears on liquid helium-II, and is counter to classical liquid behaviour. In Figure 3.6 the helium-II flows from the vessel through a superleak spontaneously towards the heater, through microscopic channels. Thermodynamics prohibits heat flow from areas of low heat towards areas of high heat. It is therefore concluded the helium that experiences this flow carry no heat.

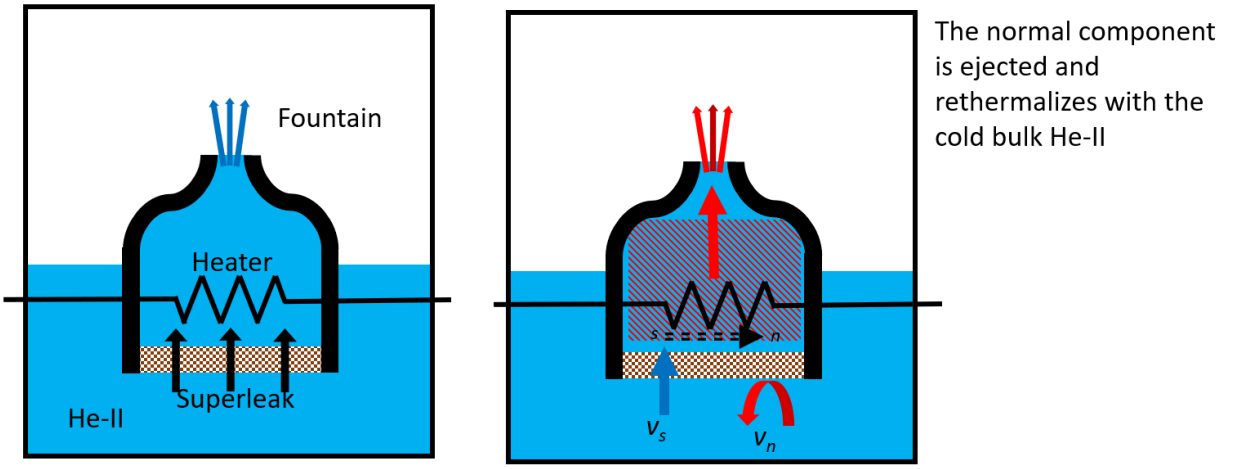

Figure 3.6: Diagram showing the fountain effect in superfluid helium. Heat is added by a heater causing a flow towards the heater in the reverse direction (right). The fountain effect can be understood with the two fluid model (right).

As the helium-II travels towards the heater it is warmed. In the two fluid model the superfluid component is allowed to enter the vessel through a superleak and is converted to the normal component at the heater (Fig. 3.6). It cannot re-enter the capillary channels due to its own larger viscosity. The red and blue arrows indicate the flow of the superfluid component, v_s, and the normal component v_n. As more of the normal component of the liquid helium builds up it then pumps the liquid helium out of the top of the vessel producing a fountain. The normal component then renormalizes with the bulk liquid through boil off.

3.1.4 Second sound

The property of second sound is a bit of a misnomer. It does not refer to the elastic nature of sound traversing through the liquid producing audible changes, instead refers to the conduction of heat via waves that propagate through the superfluid. It is a quantum mechanical phenomenon of heat transfer.

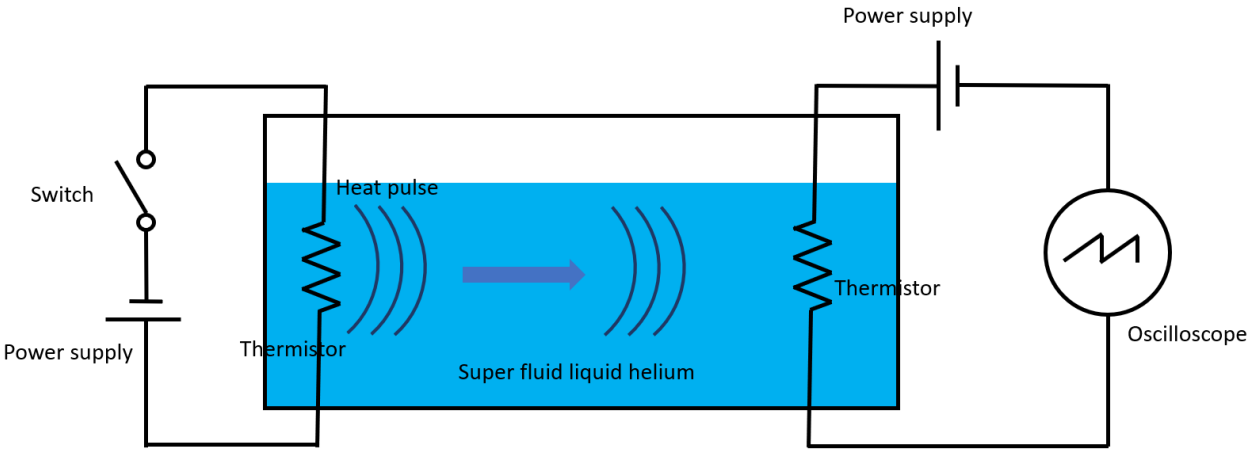

Figure 3.7: The experimental setup of second sound, two carbon resistors are submerged in liquid helium.

Like sound, the speed of the propagation of the wave can be measured. It can be measured using a setup similar to the once shown in Figure 3.7 [58]. This property is unique to helium-II, because in classical fluids the heat propagates via diffusion through the material. The sound propagates through a density of particle-like thermal excitations, phonons and rotons.

In Figure 3.7, two carbon resistors are placed inside a liquid helium vessel. The resistance of carbon near $\sim$0 K is dependent on its temperature. The helium is cooled to about 1 K. The left carbon resistor applies a 1 ms long pulse of current which heats superfluid. The heat does not diffuse, but instead propagates as a density wave of excitation. The right resistor has a constant voltage running across it. The heat pulse warms the second resistor slightly, which changes the voltage slightly. A current pulse is produced in the circuit, which goes through an amplifier to produce a

magnified voltage. This signal occurs after a delay, and the distance between the two resistors can be used to determine the speed of second sound, the thermal excitation wave propagation.

3.2 Quantum Vortices in He-II

Quantum vortex arrays, or vortices, are the means through which the superfluid component of He-II can also acquire viscosity. Vortices are quantized spin-carrying excitations in He-II.

There is experimental evidence that vortices exist. One of the first hints of their existence was in 1950 when Osborne looked at results that appeared to be a contradiction from the lack of viscosity in the superfluid component in the two fluid model [59]. By submerging a bucket and spinning it in He-II at temperatures below 1 K there is no normal component and therefore there should be no meniscus. Figure 3.8 outlines the experiment. Osborne found that the fractional abundances of the superfluid part helium did not effect the height of the parabolic meniscus, contrary to the expectations of a frictionless flow.

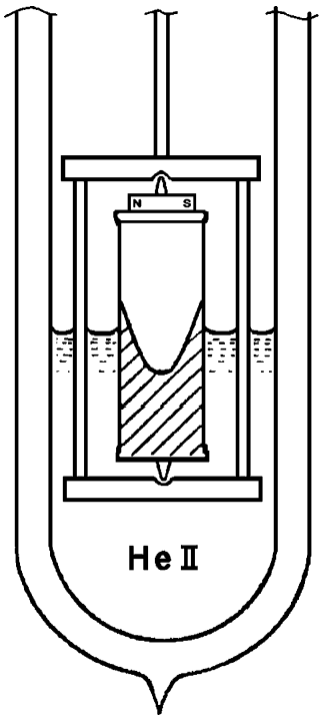

Figure 3.8: A simple rotating bucket inside a vessel containing He-II. The helium II acquires global rotation (figure from [57]) [59].

The explanation for the contradiction is vortices. Physically, what is happening in the experiment is the vortices allow the superfluid component to acquire rotation but cancel each other in the bulk fluid, except on the boundary. Thus, the superfluid component can acquire spin and form a meniscus under rotation.

More direct evidence is the imaging of vortex arrays exist, such evidence is visualization made from trapping electrons in superfluid He-II (Fig. 3.9). The electron bubbles are attracted to the rotations to minimize surface energy. After a time, the electrons were accelerated to strike a phosphorous paper, producing light.

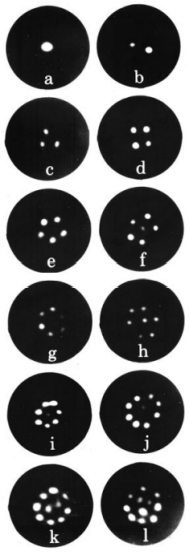

Figure 3.9: Photographic evidence of vortex line array in rotating He II. The labels (a) to (l) show increasing angular frequency (image from [57]) [60].

The vortex lines are quantized and their density n_0 is related to the frequency of angular momentum ω_0 that they carry. The quantized number density of vortex lines can be given by:

$$n_0 = \frac{2\omega_0 m}{h} \cong 20\omega_0 \text{ per mm}^2[57]. \tag{3.2}$$

The unit h/m is the quantized unit of circulation. For a vortex array each vortex core will have

h/m units of circulation.

3.3 Mutual Friction and heat conduction in turbulent superfluid

Mutual friction arises from the viscous-like drag between the two components: the normal component and the turbulent superfluid component with vortices. In the two-fluid model, heat is carried by the normal component. If the superfluid component is turbulent (vortices) then the normal component is impeded by the vortices, limiting heat transport.

The friction force can be calculated as [57]:

$$\vec{F}_{ns} = L_0\vec{f} = A_{GM}\rho_n\rho_s(\vec{v}_n - \vec{v}_s - \vec{v}_0)^2(\vec{v}_n - \vec{v_s}), \tag{3.3}$$

where ρ_n and ρ_s is the density of the normal and superfluid components. Similarly, $\vec{v_n}$ and $\vec{v_s}$ is the velocity of the normal and superfluid components, and $\vec{v}_0$ is the velocity of the bulk ^{4}He. The A_{GM} is called the Gorter-Mellink mutual friction coefficient. The line length of the vortex is given by L_0 and the line force per unit length of the vortex is $\vec{f}$.

At high heat fluxes, the normal component itself can excite vortices in the superfluid component. The steady-state heat transport in a one dimension channel containing He-II can be solved by considering the transport equation for the normal and superfluid component,

$$\frac{dT}{dx} = -\frac{\beta\mu_n v_n}{\rho s d^2} - \frac{A_{GM}\rho_n}{s}|\vec{v}_n - \vec{v}_s|^3. \tag{3.4}$$

Here the terms $\rho = \rho_s + \rho_n$ is the total density, the entropy is s, β is a numerical constant related the geometry, μ_n is the normal component viscosity, and d in the one dimensional channel diameter. If there is no net mass flow, and counterflow is the only important transport mechanism, then the temperature gradient becomes:

$$\frac{dT}{dx} = -\frac{\beta\mu_n q}{(\rho s)^2 d^2 T} - \frac{A_{GM}\rho_n}{\rho_s^3 s^4 T^3}q^3 \tag{3.5}$$

Here $q = \rho s T v_n$, is the heat flux (carried by the normal component) [57]. The second term

arises due to the mutual friction and varies as q^3, becoming dominant for high heat fluxes. Often the relation is fit to a phenomenological model, and the exponent can differ from 3. Usually it is near 3 for a broad range of physical states. The Gorter-Mellink coefficient is also temperature dependent. Equation 3.5 has a functional form that varies depending on which of the two terms dominate. At large q, rather than fitting this equation a power law relationship of

$$\frac{dT}{dx} = -f(T,p)q^m \tag{3.6}$$

is fit where m can differ from 3, and $f(T,p)$ is the thermal conductivity function and is also fitted to an empirical form.

3.4 Concluding remarks

Helium-II is a unique quantum phase of matter with many properties that are distinct from classical fluids. He-II can be thought of as having two distinct components with differing properties: a superfluid component with zero viscosity and a normal component with viscosity which carries heat.

Quantum vortices are carriers of angular momentum and can dominate the normal component for high heat flux. In order to understand high temperature heat loads in small channels the Gorter-Mellink thermal conductivity function is used.

Calculations of time-dependent heat flow in He-II in the vertical UCN source cryostat will be discussed in the next chapter, Chapter 4. Chapter 4 will also describe a model of heat transport in He-II which reproduces time-dependence of the temperature of the UCN production volume, which is based on the Gorter-Mellink regime of heat flow in He-II.

4. Temperature measurements of the He-II cryostat

This chapter will describe a model for transient heat response, and present a comparison of data to that model.

A vertical He-II cryostat was used in the TUCAN Fall 2018 and Fall 2019 runs for UCN production. To better understand the limitations of the vertical cryostat due to heating of the He-II due to a beam induced thermal load, a heater and a pressure gauge to measure the low $\sim$1 K He-II temperature were installed before the Fall 2019 run. Already at this time a new horizontal He-II cryostat was being designed that would improve the cooling power of the He-II, and allow for larger heat loads. In this chapter, the temperature measurements from Fall 2019 are compared to a simple model which helped us model the new horizontal He-II cryostat design.

4.1 Experimental Arrangement

The temperature heat response data I collected was from a heater test. The experimental arrangement is seen in Fig 4.1. A coil of wire is wrapped around the UCN bottle and is connected to a power supply. A newly installed low pressure gauge is installed downstream in vacuum, open to the surface of the bottle.

Applied heat is analogous to the beam power delivered, and is added to the ambient background heat. The heat load on the UCN bottle raises the temperature of the superfluid helium. The vapour pressure is detected in the pressure gauge PG9L according to Fig. 4.2. The Heat in the bottle travels through slits in the neck of the bottle down a small channel to the ^{4}He reservoir. Heat is conducted through a copper finned heat exchanger into the ^{3}He liquid, which is continuously cooled to a temperature of about 0.8 K.

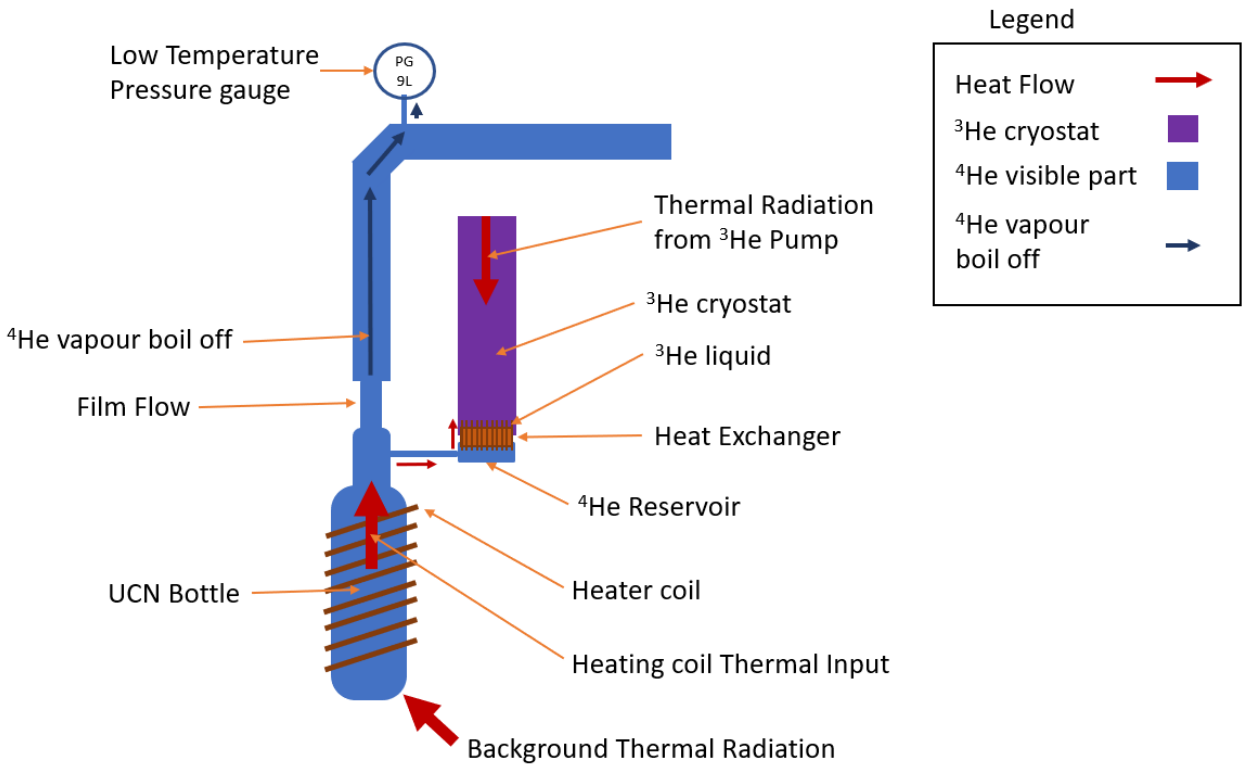

Figure 4.1: Experimental arrangement for the heat response tests of the vertical cyrostat.

In my heating experiments, I turned on the heater coil and watched the temperature and pressure gauges rise. Once the temperature rise stabilized (after several minutes) I then turned off the power to the heating coil. I did this with several applied heater powers, 25 mW, and 50 mW, 75 mW, 100 mW, 150 mW and 200 mW.

The UCN bottle holds the liquid helium superfluid and the vapour pressure P above the free He-II surface is related to the temperature T by is given by the numerical equation [61]:

$$\begin{aligned}\ln P(T) = {} & 4.6202 - 6.399/T + 2.541\log(T) + (0.00612/2)\cdot T^2 \\ & - 0.5197(7\cdot 14.14/(14.14^2+1) - 1/T)\arctan(7\cdot T - 14.14) \\ & - 7\cdot 0.5197/2/(14.14^2+1)\log(T^2/(1+(7\cdot T - 14.14)^2)) \quad (4.1)\end{aligned}$$

where P depends completely on the temperature of the He-II. Thus, the pressure is given by,

$$P(T) = \exp^{\ln(P(T))} . \tag{4.2}$$

I used a numerical solver in python to invert the function to solve for temperature T for a given vapour pressure P.

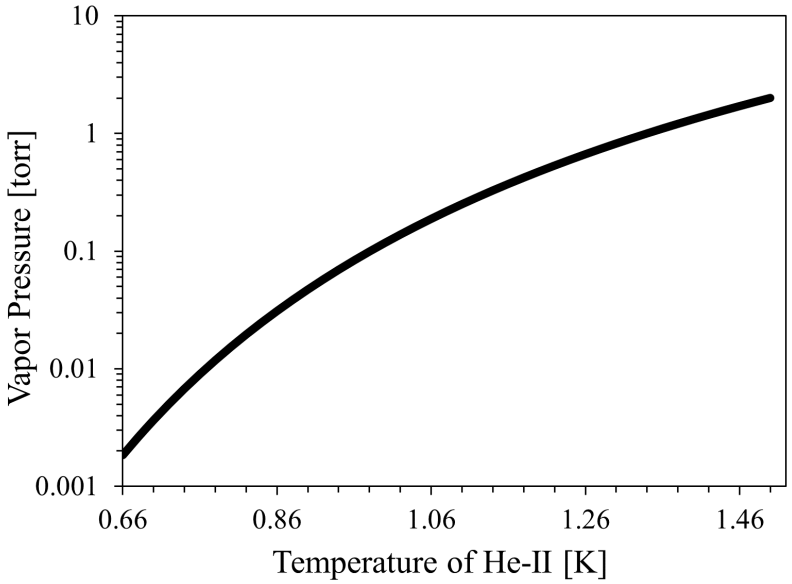

Figure 4.2: Plot of the empirical calculation for vapour pressure and temperature of He-II [61].

Figure 4.3 displays typical data from the heater test with the power of the coil. This figure is for the 200 mW applied power. What is being measured is the temperature of the He-II from the vapour pressure over time. At some point (at ≈ 3000 s) the heater coil turns on, delivering 200 mW to the He-II, after the temperature plateaus the heater is turned off. What is of interest is the slow heat response time of the liquid and the large T rise.The temperature changes looked exponential. I therefore fit a single exponential with background for both a heating and cooling cycle is given by the piece-wise function:

$$T(t) = \begin{cases} m(t-t_1)+b & t \le t_1 \\ m(t-t_1)+b+\Delta T_1(1-e^{\frac{-(t-t_1)}{\tau_1}}) & t_1 \le t \le t_2, \\ m(t-t_1)+b'+\Delta T_2 e^{\frac{-(t-t_2)}{\tau_2}} & t_2 \le t \end{cases} \tag{4.3}$$

$$b' = b + \Delta T_1(1-e^{\frac{-(t_2-t_1)}{\tau_1}}) - \Delta T_2 \tag{4.4}$$

where t is time, ΔT_i is the exponential limit, m is the slope of the background helium temperature, b is the constant part of the background temperature, and b' is the modified offset enforcing continuity, and finally t_1 is the start of the heater and t_2 is the heater time it was set off.

Table 4.1: Heater test where the temperature increases exponentially due to heating to a plateau then drops exponentially back to a sloped baseline, using equations 4.3 and 4.4 (refer to Appendix A.1 for fits).

Heat (mW)	ΔT_1 (K)	τ_1 (s)	m (K/s)	b (K)	t_1 (s)	t_2 (s)	ΔT_2(K)	τ_2 (s)
25	0.02265(3)	308(1)	$7.6(1)\times10^{-7}$	1.11881(1)	7242.3(6)	9686.1(6)	0.02292(4)	320.(1)
75	0.05928(4)	291.18(4)	$7.9(2)\times10^{-7}$	1.12548(2)	1314.7(2)	3827.9(2)	0.06001(4)	333.7(5)
100	0.07631(4)	280.0(3)	$8.8(1)\times10^{-7}$	1.12090(1)	3290.0(2)	5248.0(2)	0.07711(3)	343.0(3)
200	0.12850(1)	250.6(1)	$9.38(2)\times10^{-7}$	1.119390(7)	2985.63(8)	5321.2(1)	0.12998(1)	359.2(2)

The data collected that had a stable temperature increase were for 25, 75, 100, and 200 mW. Table 4.1 has the resulting fit data.

The linear background in the temperature is due to a slow period near linear raise in temperature due to the helium emptying from boil off before it is topped up during the cryostat filling cycle in the ^{3}He pot. It has a saw tooth periodicity at large time scales. At the end of Figure 4.3 near 13500 s the background temperature begins to fall due to ^{3}He filling in the heat exchanger, improving cooling.

The red line in Figure 4.3 is the fit to the data using Equation 4.3. Table 4.1 summarizes the

heater test data fit to a rising and falling exponential.

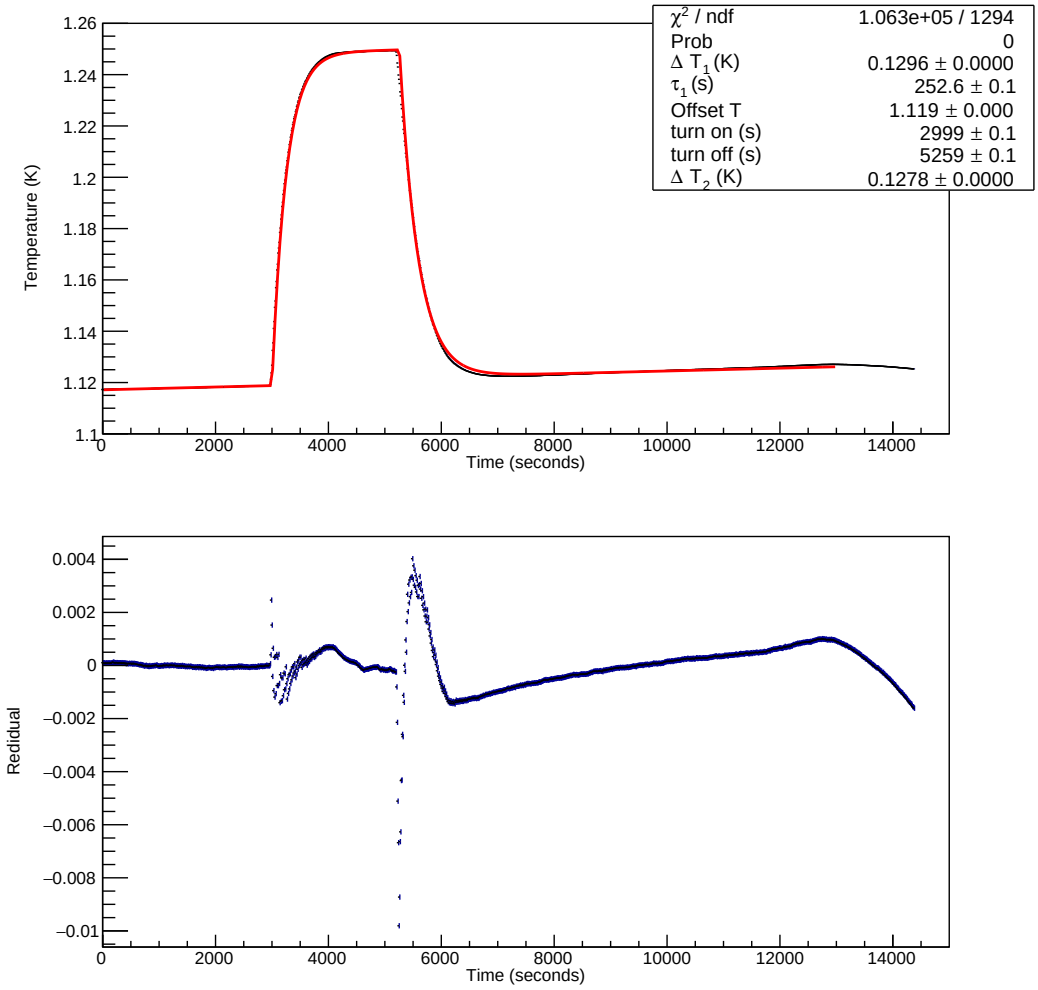

Figure 4.3: PG9L derived temperature versus time graph for a heater power of 200 mW fit with a piece-wise function defined in Eq. 4.3.

The statistical precision of the temperature was taken as the residual of the linear region for each plot. Figure 4.3 illustrates the s below the heat response. The plot is divided into three regions of interest. The first is the linear component with a slope, whose residual is purely statistical. The heater is then turned on, and an exponential is fit. In the plot of the residuals, this second region would benefit from the additional exponential. The third region is during cooling when the heater

is turned off. This third region would also fit better with the addition of a second exponential. The background is also not completely linear in this region. This suggests a more complete physical model them simple heating and cooling is required, one based on the properties of superfluid helium.

A second piece-wise function was used to fit only the cooling parts for all Heater Tests, and is defined:

$$T(t) = \begin{cases} m(t-t_2) + b + \Delta T_2 & t \leq t_2 \\ m(t-t_2) + b + \Delta T_2 e^{\frac{-(t-t_2)}{\tau_2}} & t_2 \leq t \end{cases} . \tag{4.5}$$

Here we have similar definitions of components, but it is used to fit a plateau then an exponential drop-off, to a sloped background temperature. This is a trivial extension of Equations 4.3 and 4.4. Figure A.9 illustrates the behaviour of this fit. There is a sloped background and an exponential drop-off as the heater is turned off.

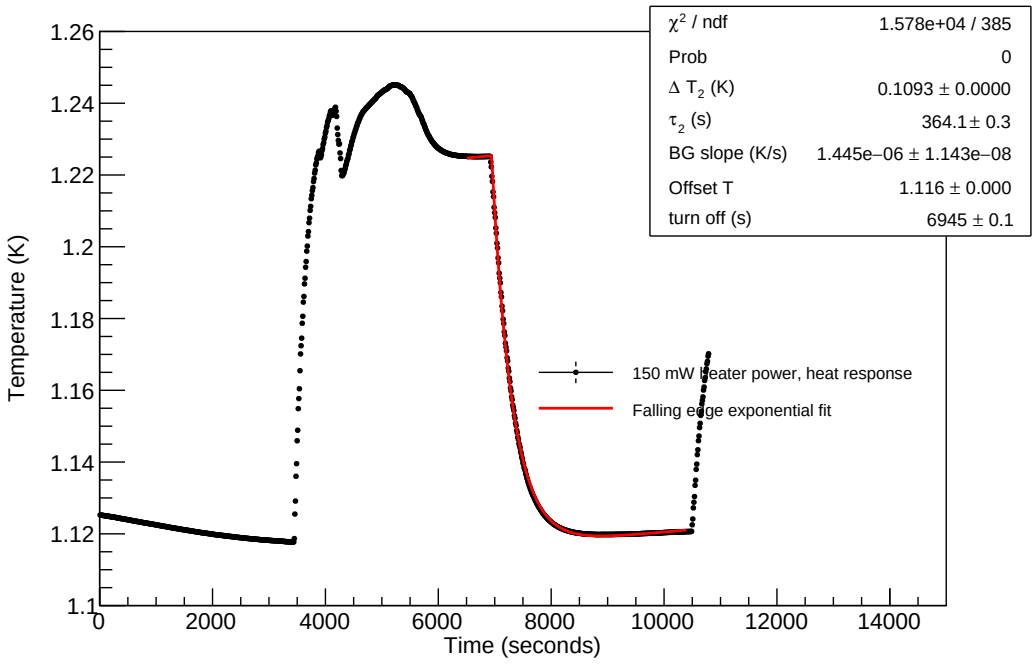

Figure 4.4: PG9L derived temperature versus time graph for a heater power of 150 mW fit with a piece-wise function defined in Eq. 4.5, for the falling cases.

Figure 4.4 temperature rise is jagged which resulted from the temperature running away and turning the heater off and then back on. This is due to a likely instability in the ^{3}He refrigerator used to cool the He-II

The data for 25, 75, 100, and 200 mW was the same, but includes unstable temperature rise, with a smooth temperature fall for 50 and 150 mW. Table 4.2 has the resulting fit data.

Table 4.2: Falling edge, heater test where the temperature starts at a plateau then drops exponentially back to a sloped baseline, using equation 4.5 (see Appendix A.2 for fits).

Heater (mW)	ΔT_2 (K)	τ_2 (s)	m (slope) (K/s)	b (K)	t_2 (s)
25	0.02325(6)	328(1)	9.4(3) $\times 10^{-7}$	1.12005(5)	9684.7(6)
50	0.04341(3)	322.4(6)	6.9(1) $\times 10^{-7}$	1.11899(3)	7554.0(3)
75	0.06107(7)	344.1(7)	14.1(3)$\times 10^{-7}$	1.12565(6)	3826.7(2)
100	0.08100(8)	366.0(5)	29.2(4)$\times 10^{-7}$	1.11834(7)	5243.1(2)
150	0.10929(3)	364.0(3)	14.4(1)$\times 10^{-7}$	1.11608(3)	6935.8(1)
200	0.12920(2)	361.3(2)	9.96(2)$\times 10^{-7}$	1.11973(1)	5233.7(1)

A third piece-wise function was used to fit only the raising edge of a temperature increase. Figure 4.5 illustrates the behaviour of the fit. There is a sloped background and an exponential rise.

$$T(t) = \begin{cases} m(t-t_1)+b & t \leq t_1 \\ m(t-t_1)+b+\Delta T_1(1-e^{\frac{-(t-t_1)}{\tau_1}}) & t_1 \leq t \end{cases}. \tag{4.6}$$

The definitions of each of the functions are similar, but it is used to fit a plateau then a temperature rise to a plateau. There is a sloped background temperature in all three exponential functions.

Table 4.3: Rising edge, heater tests where the temperature starts at stable temperature and then raises in an exponentially decaying way to a plateau, using equation 4.6 (see Appendix A.3 for fits).

Heater (mW)	ΔT_1 (K)	τ_1 (s)	m (slope) (K/s)	b (K)	t_1 (s)
25	0.02311(5)	318(1)	5.6(2) $\times 10^{-7}$	1.11870(1)	7238.5(6)
75	0.05976(5)	296.3(5)	5.5(2) $\times 10^{-7}$	1.12544(2)	1313.7(2)
100	0.07709(4)	283.4(5)	6.0(1) $\times 10^{-7}$	1.12065(5)	3287.8(2)
200	0.13015(2)	254.1(1)	4.05(6)$\times 10^{-7}$	1.11860(1)	2983.47(8)

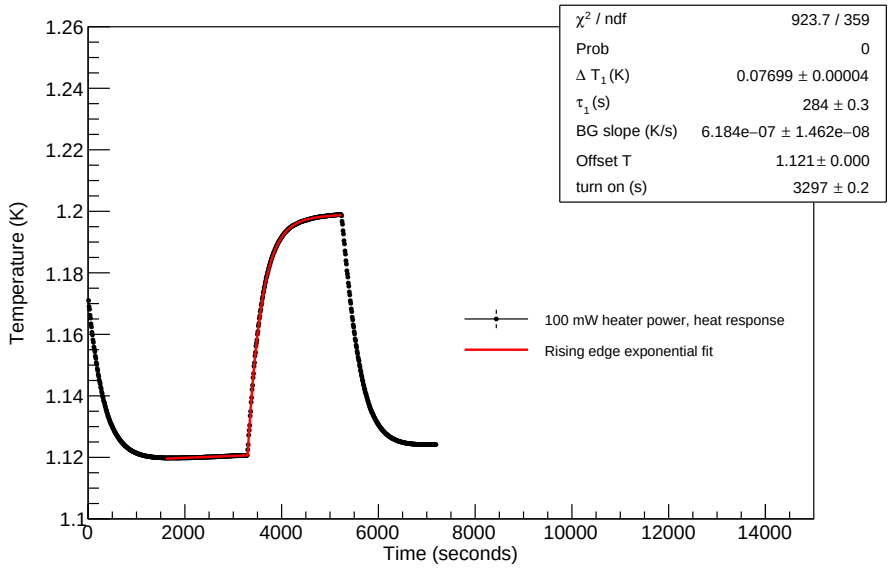

Figure 4.5: PG9L derived temperature versus time graph for a heater power of 100 mW fit with a piece-wise function defined in Eq. 4.6, for the rising temperature case.

The data collected that had temperature drops were the same as the total case, since it needed a well-behaved temperature increase, it needed to settle on a temperature and not run away due to He-3 boiling completely away during cooling. Table 4.2 has the resulting fit data.

Table 4.4: Heater test final results. The values were taken to be the average of the fit if available. The asterisk on the power * denotes only falling edge was used.

Heater	ΔT (K) for PG9L	τ (s)
25 mW	0.02300(2)	319(7)
50 mW*	0.04341(3)	322.4(6)
75 mW	0.0600(7)	320(20)
100 mW	0.078(2)	320(40)
150 mW*	0.10929(3)	361.3(2)
200 mW	0.129458(8)	300(50)

The results of Table 4.4 can be compared to a model to see if the model comes qualitatively close to predicting the data. In Table 4.4 values in brackets denote the statistical uncertainty in the final significant figure.Additionally, the final temps can be plotted as a function of temperature.

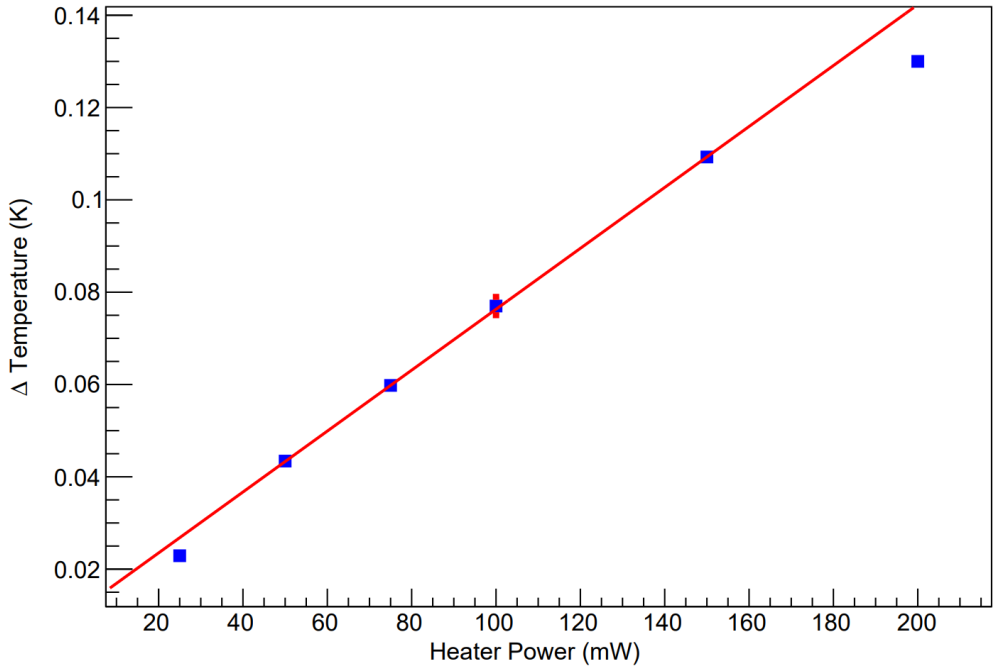

Figure 4.6: Change in temperature as a function of heater power, naive fit to the results in Table 4.4.

The red line on the plot was naively fit to a linear function $T(P) = mP + b$. With the terms $m = 0.000660(4)$ (K/mW) and $b = 0.01031(5)$ K. This is naive assumption, Figures 4.11 and 4.12 show that this trend can range from concave up to concave down according to the model presented in the next section.

4.2 One-dimensional model of vertical bottle cooling for the vertical cryostat

In Chapter 3, various unique properties of He-II were discussed and the Gorter-Mellink mutual friction heat conduction was introduced. In this section, a one-dimensional Gorter-Mellink (GM) model is developed to understand the bottle temperature as a function of time and applied heat [62]. This model was used to understand the slow temperature rise of the UCN bottle as heat migrated from the UCN bottle and its temperature plateau. The conceptual layout for the one-dimensional model for heat flow is shown in Fig. 4.7. In the model, the He-II in the UCN bottle is connected by a short channel of He-II, connecting it to a larger reservoir of He-II, referred to as the $bath$ in Fig 4.7. The $bath$ is connected by larger diameter channels to a large surface area heat exchanger with the ^{3}He in the refrigerator.

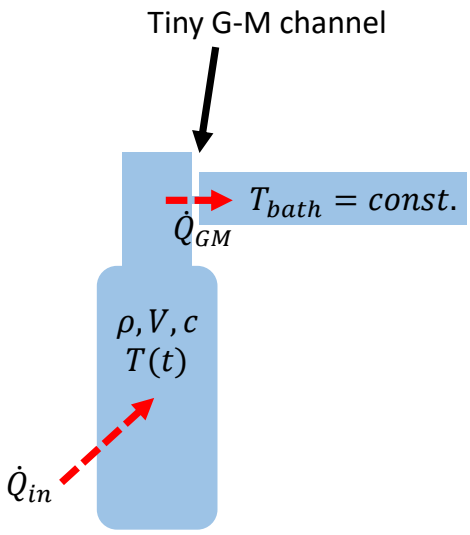

Figure 4.7: Conceptual layout of calculational model. Heat enters $\dot{Q}_{in}$ the vertical UCN source bottle from beam heating. Heat exits $\dot{Q}_{GM}$ via conduction in He-II through a tiny Gorter-Mellink channel. The temperature of the bottle as a function of time is $T(t)$, and the bath temperature T_{bath} is held constant. The calculation and other various quantities illustrated are described in the text.

Cooling through the single small channel is modelled to simulate the small holes and slits which in reality connect the bottle to the $bath$. The larger channel and heat-exchanger are modelled as a reservoir, which maintains the temperature $T_{\rm bath}$. Conduction of heat through the small channel is modelled by the Gorter-Mellink thermal gradient (Eq. 3.6).

Initially, before the heat $\dot{Q}_{\rm in}$ is applied, the temperature in the bottle is taken to be equal to the bath temperature:

$$T(t=0) = T_{\rm bath}. \tag{4.7}$$

After the heat $\dot{Q}_{\rm in}$ is applied, the temperature rises via

$$\rho V c \frac{dT}{dt} = -\dot{Q}_{\rm GM} + \dot{Q}_{\rm in}. \tag{4.8}$$

Here, ρ is the density of He-II, V is the volume of He-II in the bottle, and c is the specific heat capacity of the He-II. The input heat comes from either beam heating or the heater coil, and is typically below 300 mW.

The quantity $\dot{Q}_{\rm GM}$ represents the heat removed by conduction, which also depends on time. The temperature will reach an equilibrium value $T(\infty) > T_{\rm bath}$ when $\dot{Q}_{\rm in} = \dot{Q}_{\rm GM}$.

In a one-dimensional Gorter-Mellink channel, the temperature gradient dT/dx in the He-II is described by a power-law relationship with the heat flux along the channel q in Eq. 3.6 given by

$$dT/dx = -f(T,p)q^m, \tag{4.9}$$

where $f(T,p)$ is the thermal conductivity function [57]. The value of $f(T,p)$ is normally constrained by phenomenological fits. The exponent is normally taken to be $m = 3$, although some phenomenological fits adopt slightly larger non-integer values [55, 54]. Equation (4.9) can be rewritten in terms of the quantities on Fig. 4.7 as

$$\frac{T(t) - T_{\rm bath}}{\ell} = f(T_{\rm bath}, {\rm SVP}) \left(\frac{\dot{Q}_{\rm GM}}{A} \right)^m. \tag{4.10}$$

Here, the quantities ℓ and A are the channel length and area, respectively. The approximation that the channel be short and that $T(t) \approx T_{\rm bath}$ have been taken. The term SVP is meant to indicate that the He-II is near the saturated vapour pressure in this source, and so the thermal conductivity function should be evaluated near the saturated vapour pressure. Equation (4.10) can be solved for $\dot{Q}_{\rm GM}$ and applied to Eq. (4.8), giving:

$$\rho V c \frac{dT}{dt} = \dot{Q}_{\rm in} - A \left[\left(\frac{T(t) - T_{\rm bath}}{\ell} \right) f^{-1}(T_{\rm bath}, {\rm SVP}) \right]^{1/m}. \tag{4.11}$$

This equation can be solved for $T(t)$ subject to the initial condition (Eq. (4.7)).

The factor $f^{-1}(T,p)$ is strongly temperature dependent, so that in cases where $T(t) >> T_{\rm bath}$ the approximation taken in Eq. (4.10) is invalid. In such cases, a more valid approximation is

$$\int_{T_{\rm bath}}^{T(t)} dT' f^{-1}(T', {\rm SVP}) = \ell \left(\frac{\dot{Q}_{\rm GM}}{A} \right)^m. \tag{4.12}$$

In this more general case, Eq. (4.11) may be written as

$$\rho V c \frac{dT}{dt} = \dot{Q}_{\rm in} - A \left[\frac{1}{\ell} \int_{T_{\rm bath}}^{T(t)} dT' f^{-1}(T', {\rm SVP}) \right]^{1/m}. \tag{4.13}$$

This equation is solved numerically for $T(t)$.

4.3 Numerical Solution of the model

To solve Equation 4.13, numerical time steps Δt_i are taken and used to calculate the corresponding temperature step

$$\Delta T_i = \Delta t_i \left\{ \frac{(\dot{Q}_{in}/V)}{\rho c} - \frac{A}{\rho V c} \left[\frac{1}{\ell} \int_{T_{\rm bath}}^{T_i} dT' f^{-1}(T', {\rm SVP}) \right]^{1/3} \right\}. \tag{4.14}$$

The next temperature can then be calculated using$T_{i+1} = T_i + \Delta T_i$. The temperature step is then added back to the previous temperature in a running total. The integral in the brackets is evaluated

by a running Riemann sum at each time step:

$$\int_{T_{\text{bath}}}^{T_i} dT' f^{-1}(T', \text{SVP}) = \sum_{T_i} \Delta T_i f^{-1}(T_i, \text{SVP}) \tag{4.15}$$

where the total sum is kept and used to compute the next time step Δt_{i+1}.

The thermal conductivity function's inverse is used, and is given by Van Sciver [57] as:

$$f^{-1}(T, p) = g(T_\lambda)[t^{5.7}(1 - t^{5.7})]^3 \tag{4.16}$$

where $g(T_\lambda) = \rho^2 s_\lambda^4 T_\lambda^3 / A_\lambda$, $t = T/T_\lambda$, $s_\lambda = 1559$ J/(kg K), and $A_\lambda = 1450$ (m s)/kg are used. Additionally, the (constant) value of ρ from Table 4.5 and the value $T_\lambda = 2.17$ K are used.

The specific heat capacity c is also strongly temperature dependent. It was found that including this temperature dependence was important to reproduce the temperature dependence of time constants with similar trends as the measured data. The fit for $c(T)$ used was[57]

$$c(T) = \begin{cases} 20.4\, T^3, & \text{for } T < 0.6, \\ 108\, T^{6.7}, & \text{for } 0.6 < T < 1.1, \text{ and} \\ 117\, T^{5.6}, & \text{for } T > 1.1. \end{cases} \tag{4.17}$$

Here, c is expressed in units of J/(kg K) and T in units of K.

4.4 Sample Calculations

The integration was implemented in a python code which may be found at `https://github.com/shansenromu/transient_he-ii`. For the calculations presented here, the code `transients-bgheat.py` was used. Table 4.5 is used as input to evaluate the numerical solutions.

Table 4.5: Constants used in sample calculations.

Constant	Value	Unit
ρ	145	kg/m^3
V	0.0085	m^3
$T(0) = T_{\text{bath}}$	1	K
m	3	dimensionless
$\dot{Q}_{\text{in}}$	various	W

A sample calculation may be found in Fig. 4.8. In Eq. 4.13 the variables A and ℓ appear in the same term as $A\ell^{1/3}$. Thus, A and l can not be determined separately from the fit. We decided to use $\ell = \sqrt{A}$, envisioning a small cubic GM channel. This calculation assumes $\ell = \sqrt{A} = 0.005$ m. The bottle temperature can be seen to rise significantly for higher step heat inputs $\dot{Q}_{\text{in}}$. Furthermore, the time for the temperatures to reach equilibrium is well over 100 s.

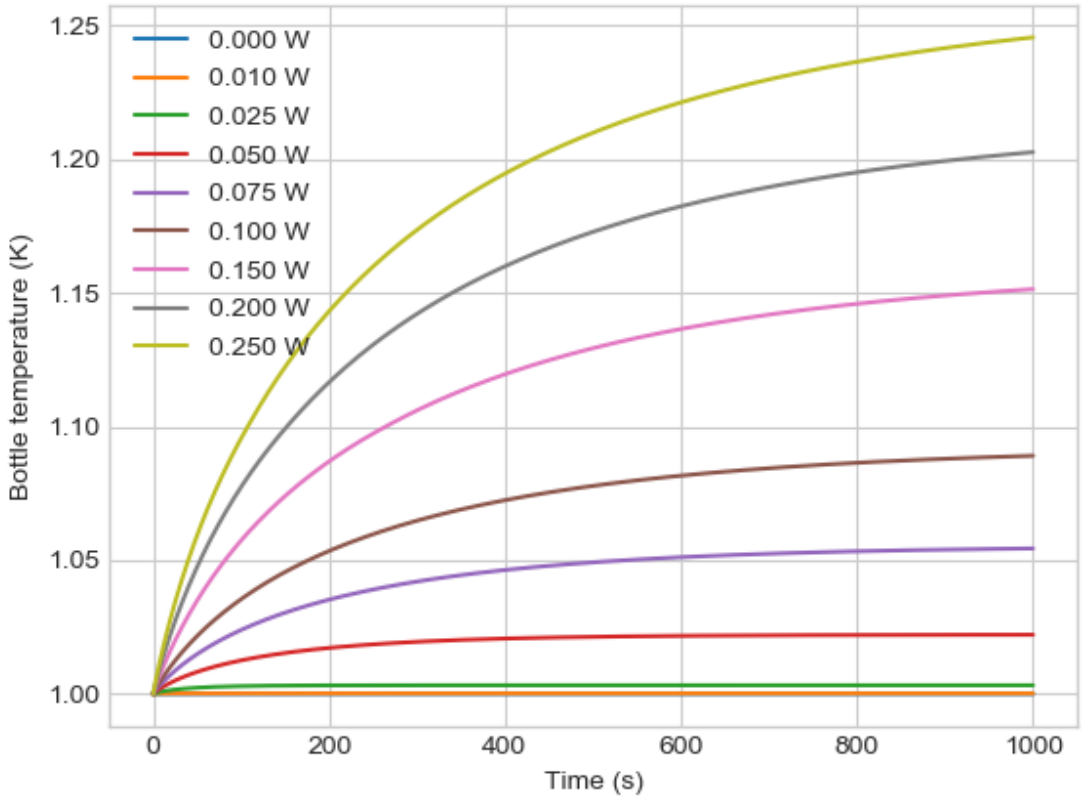

Figure 4.8: Sample calculations for a 1D Gorter-Mellink channel model heat response in temperature for various heat inputs and $\ell = \sqrt{A} = 0.005$ m.

Figure 4.9 shows the result if $\ell = \sqrt{A} = 0.01$ m is used. The temperatures for each heat input are seen to rise more quickly and ultimately do not reach as large of a final temperature value. This means that a greater thermal link is established through the channel as it gets larger, allowing the bottle to be more inline with the heat exchanger temperature.

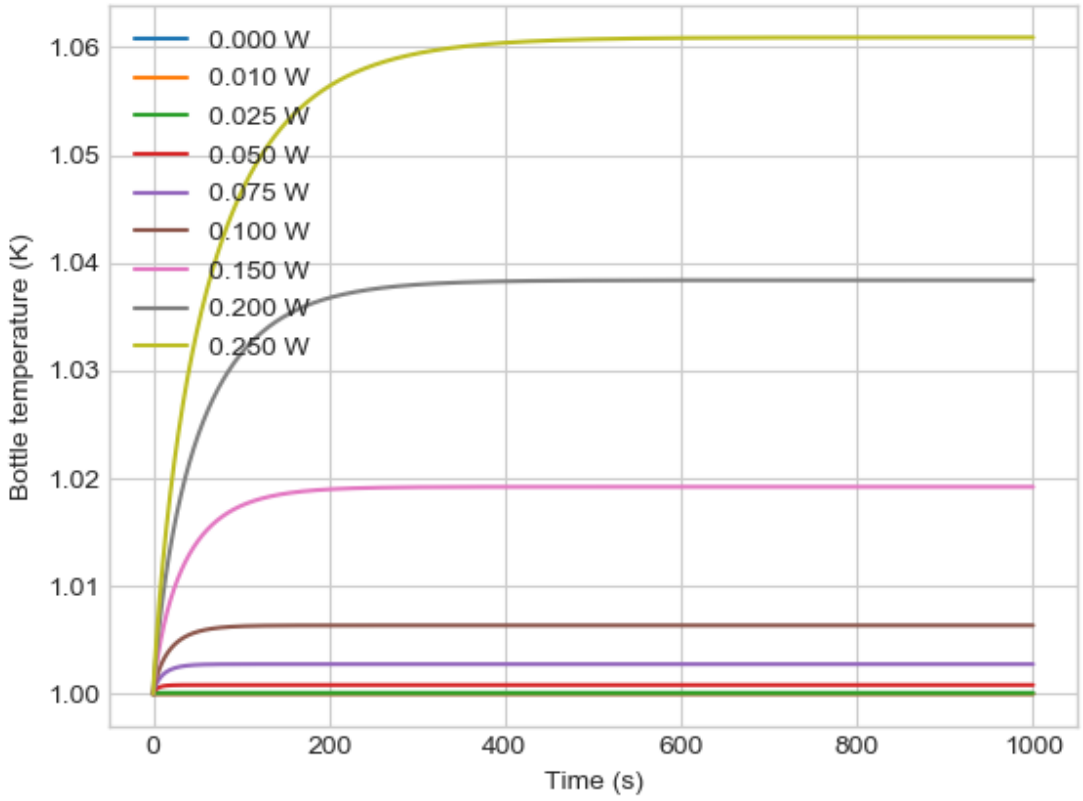

Figure 4.9: Sample calculations for a 1D Gorter-Mellink channel model for various heat inputs using and $\ell = \sqrt{A} = 0.01$ m.

The final temperature reached in the calculation can be compared with a static calculation where time derivatives are set to zero. This comparison is made in Figs. 4.10 and 4.11 for $\ell = 0.005$ m and $\ell = 0.01$ m, respectively. The values presented as "after 1000 s" are the final values of the time-dependent simulation. The value presented as "at infinity" are those calculated by solving for the time-independent case, where the time derivative in Eq. 4.13 has been set to zero. Good agreement is seen between both calculations. In cases where either the heat load is higher, or the channel dimension smaller, discrepancies can be seen where the final temperature might not reach its saturation value before the simulation is terminated.

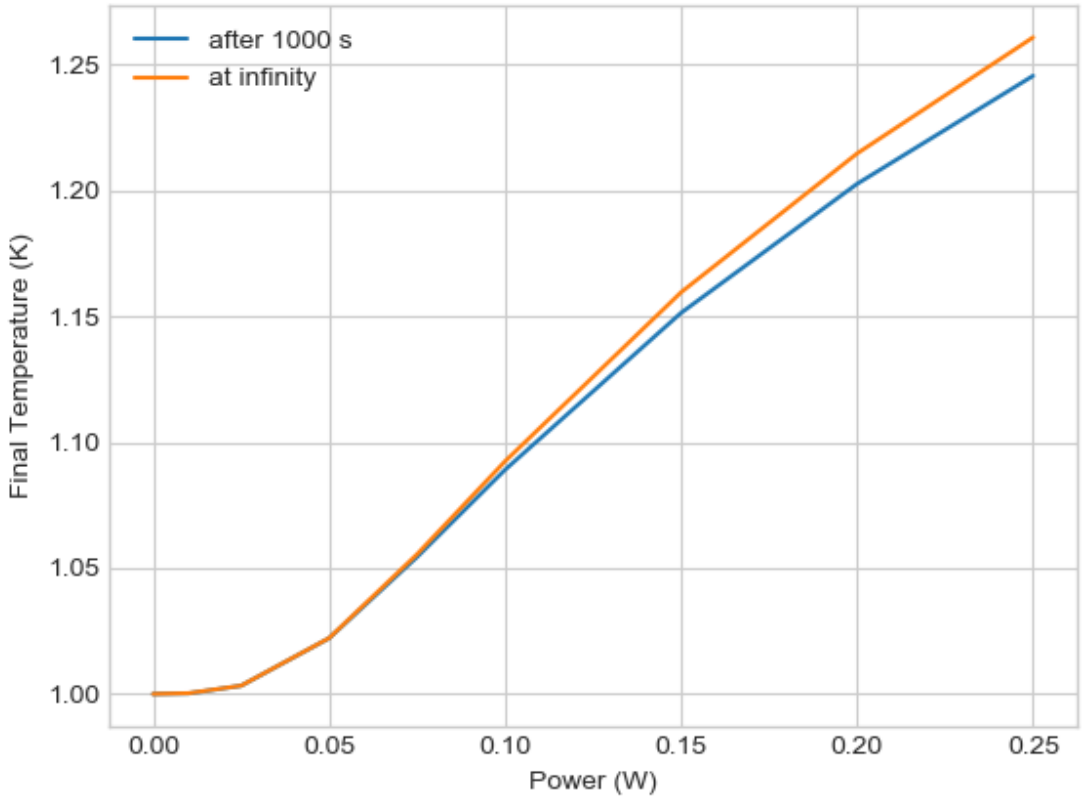

Figure 4.10: Final heat reached in the calculation compared with the value expected at $t = \infty$. Calculation assumes $\ell = \sqrt{A} = 0.005$ m.

For the weaker thermal link, in Fig. 4.10, the $\dot{Q}_{\text{in}}$ dependence can be seen to transition from a q^3 dependence to a more linear dependence. This is an effect of the thermal conductivity of the He-II becoming larger at the higher temperatures, so that $T(t) \approx T_{\text{bath}}$ is no longer valid and Eq. 4.10 must be replaced with Eq. 4.12, as was done for these simulations. For the $\ell = 0.01$ m case (Fig. 4.11), the q^3 dependence is more evident. This happens because the temperature rise is smaller, leading to $f^{-1}(T, p)$ being approximately constant.

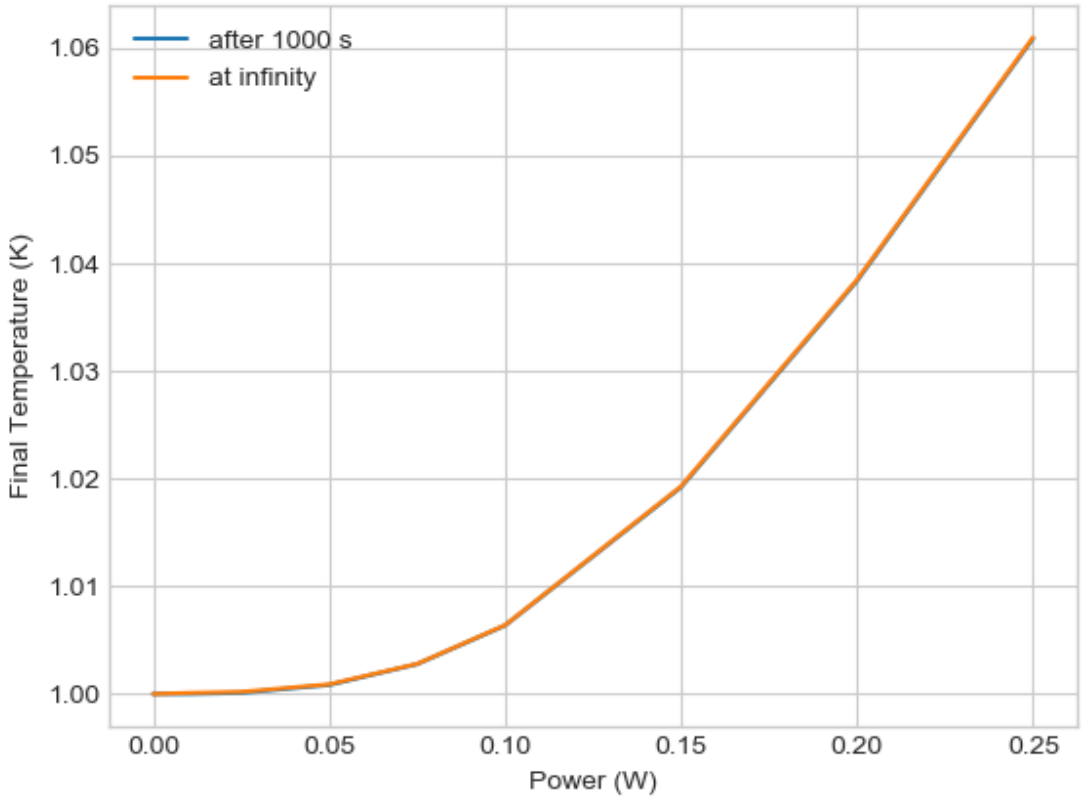

Figure 4.11: Final heat reached in the calculation compared with the value expected at $t = \infty$. Calculation assumes $\ell = \sqrt{A} = 0.01$ m.

4.4.1 Inclusion of background heat

The same calculations can be done with a constant background heat $\dot{Q}_{\rm bg}$ included for all times. It is known that for this source, there is an apparent background of order 150 mW [63, 54]. In this case, the temperature is assumed to be initially in equilibrium with heat flow through the GM channel, controlling the bottle temperature (i.e. $T(0) \neq T_{bath}$ as for Eq. 4.7). The additional heat $\dot{Q}_{\rm in}$ is then switched on at $t = 0$.

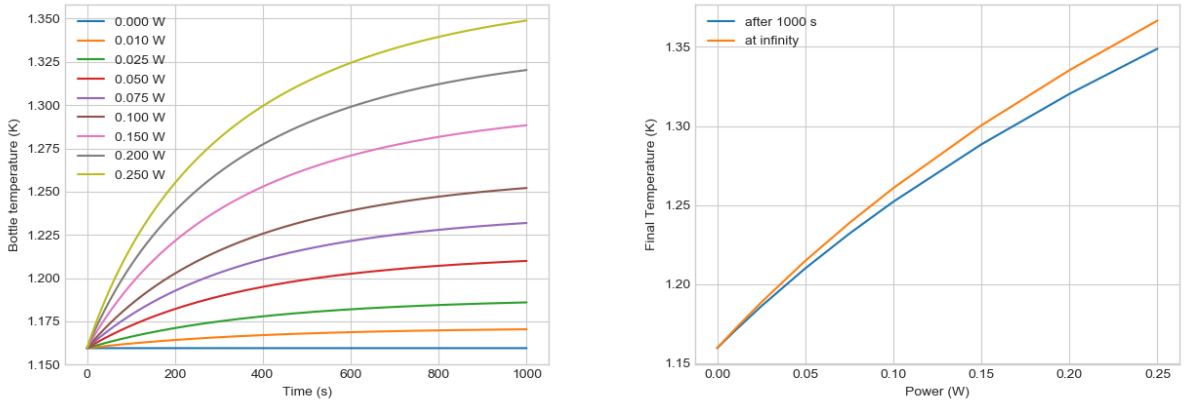

Figure 4.12: Left: time-dependence of temperatures for $\ell = \sqrt{A} = 0.005$ m with a background heat of 150 mW. Right: values at $t = \infty$ compared with final value from time-dependent calculation.

Results of this calculation are shown for an assumed background heat of 150 mW in Figs. 4.12 and 4.13, for channel dimension $\ell = 0.005$ m and 0.01 m, respectively. The background heat tends not to substantially affect the time constant of the temperature equilibration. It does tend to make the limiting temperature more linear in relation to the applied heater power rather than going as q^3 in the zero background condition.

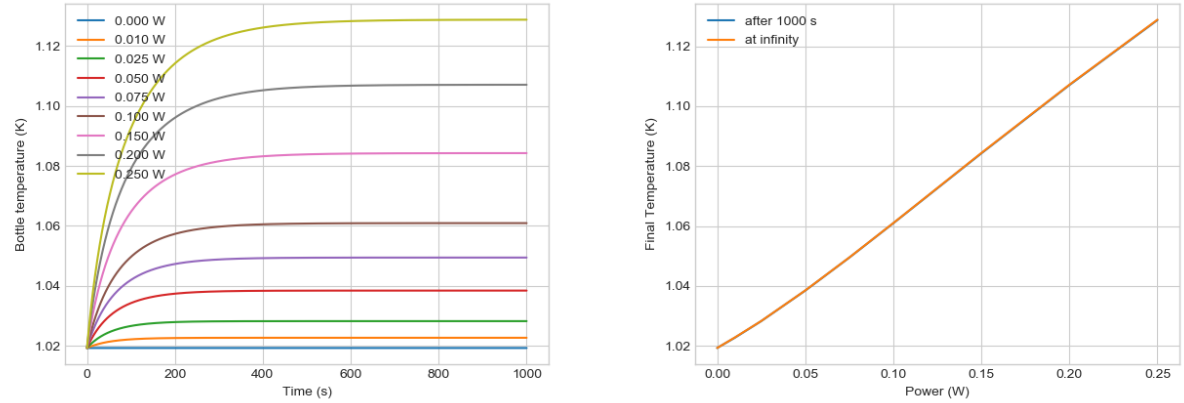

Figure 4.13: Left: time-dependence of temperatures for $\ell = \sqrt{A} = 0.01$ m with a background heat of 150 mW. Right: values at $t = \infty$ compared with final value from time-dependent calculation.

A similar effect was observed in F. Rehm's calculations for the channel connecting the bottle to the ^{3}He heat-exchanger. This trend in Fig. 4.12 looks similar to Fig 4.6 as well, nearly linear with a slight concave bend.

We can take the same exponential fits that we fit that data with and try to fit the model. Using different possible values for the background heat from 50 mW to 200 mW, Table 4.6 shows the fit results for single rising exponential fits for applied heating power of $\dot{Q}_{\rm BG} = 25, 75, 100$ and 200 mW.

In Table 4.6 the model used the same ℓ and T_{hex} to produce similar results as the data, then fit to exponential parameters form Equation 4.6. The resulting parameters from Table 4.6 can be compared to the fit results from Tables 4.1 and 4.2.

In Figure 4.14 I look at the temperature difference ΔT and not at absolute temperature due to the initial background temperatures being different from each other in the data, while being held constant in the theory. For each heat load the temperature difference ΔT of the data and the theory is fit with an exponential (see Table 4.6).

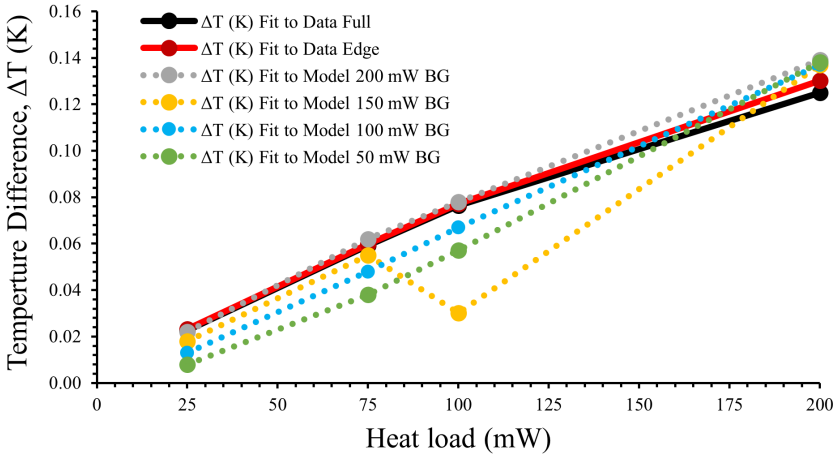

Figure 4.14: Change in temperature ΔT from exponential fits for applied heat loads, both the data (solid lines) and the model (dotted lines).

Table 4.6: Fit parameters from the exponential temperature model described in the text. Graphs of these fits appear in Appendix A, Fig. A.15 to A.18.

Heater Power (mW)	ΔT (K)	τ (s)	T_{start} (K)	$\dot{Q}_{\text{BG}}$ (W)
25	0.022	258	1.120	0.2
75	0.062	262	1.120	0.2
100	0.0779	263	1.120	0.2
200	0.139	269	1.120	0.2

Heater Power (mW)	ΔT (K)	τ (s)	T_{start} (K)	$\dot{Q}_{\text{BG}}$ (W)
25	0.018	253	1.122	0.15
75	0.055	252	1.122	0.15
100	0.073	262	1.122	0.15
200	0.137	285	1.122	0.15

Heater Power (mW)	ΔT (K)	τ (s)	T_{start} (K)	$\dot{Q}_{\text{BG}}$ (W)
25	0.013	251	1.128	0.10
75	0.048	252	1.128	0.10
100	0.067	275	1.128	0.10
200	0.137	322	1.128	0.10

Heater Power (mW)	ΔT (K)	τ (s)	T_{start} (K)	$\dot{Q}_{\text{BG}}$ (W)
25	0.008	267	1.124	0.05
75	0.038	236	1.124	0.05
100	0.057	278	1.124	0.05
200	0.138	262	1.124	0.05

The error bars in Figure 4.14 are smaller than the points, and the χ^2/ndf for the fits run from 10-100. Suggesting the purely statistical error gives an incomplete picture. At best, we can say the trend of rising temperature differences are in agreement, and are approximately the right order of magnitude.

Figure 4.15 shows the time constant τ of the applied heat load for the measured value and theoretical values fitted for an exponential.

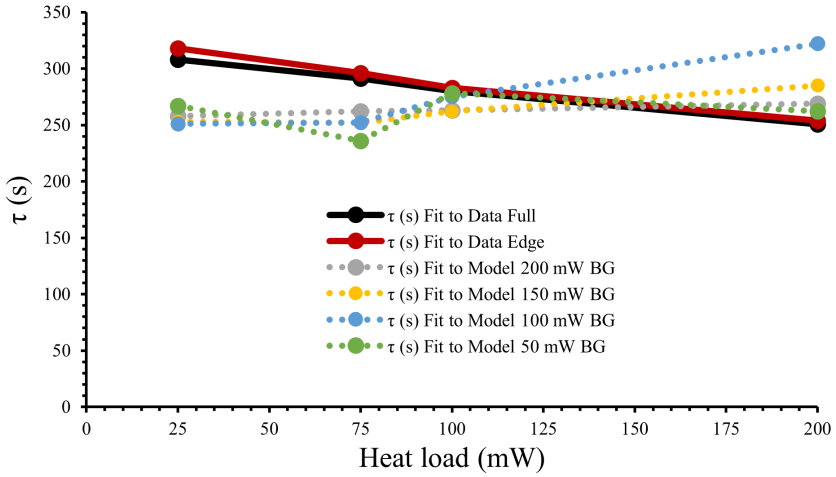

Figure 4.15: The exponential time constant τ for applied heat loads, both for the data and the model's exponential fit results.

A similar comment can be made about the error bars in Figure 4.15, as made for Figure 4.14. The purely statistical error is smaller than the points, and the χ^2/ndf for the fits run from 10-100. Here the large time scales are importantly qualitatively in agreement. They are approximately the right order of magnitude. The explanation for the disagreement is that the simple exponential fitting does not explain the model and the data. This is understood to be the case due to the heat capacity and thermal link changing as the temperature increases.

4.5 Fitting 1D Model to Data

I extended the model to fit the data directly. Solving the numerical integral for every point takes much too long, so the data is fit to a modified numerical solver. This solver computes the numerical integral for a subset of temperature data, every 10 s rather than every seconds. A total 300 points is calculated in the numeric solver and interpolated to the subset. These points are used to minimize the chi-square fitting for the model parameters: length of channel ℓ, and temperature of the heat-exchanger T_{hex}.

The time the heater is turned on and off are also fit, but is not a part of the 1D model. Before the heater is turned on, the equilibrium temperature is solved, it is only when the heat load is applied there is a heat response, and the numerical method of solving discussed in Section 4.3 is used.

The background heat flux input is held fixed when fitting. This is because $\dot{Q}_{\text{BG}}$ would sometimes be driven to nonphysically large values by the fit, it was felt to be better determined by the overall ^{3}He evaporation rate in the fridge, which implies the ≈ 150 mW values mentioned earlier. Looking at reasonable values of background heat, the model outputs the value of length of channel ℓ, and temperature of the heat exchanger T_{hex} of that fit.

In Figure 4.16, the time before the heater is turned on, the data is fit to a flat line which is the evaluation of the UCN bottle's temperature at equilibrium with ambient background heat, 200 mW in this fit. At the time approximately 5000 s into the run the 200 mW heating coil is turned on. After the coils turns on the 1D model's results are fit, and output a characteristic length $\ell = \sqrt{A} = 0.007 \pm 0.002$ m. The temperature of the heat exchanger is used for both the constant temperature and time evolving parts. This fit gives a value for the temperature of the heat exchanger (capthex) $T_{\text{hex}} = 1.0 \pm 0.2$ K for the temperature of the heat exchanger.

The data for 25, 75, 100 and 200 mW heating coil power were used to fit the 1D heating. This was due to the 50 mW and the 150 mW temperature rising and not reaching equilibrium during the heat test. This was due to the helium 3 pot being emptied, resulting in a runaway fridge temperature. Periodically, the helium 3 pot is filled because it empties below its fill threshold. If this happens during a temperature test, there is a chance that the temperature of the bottle increases

rapidly. For the short heat input from the neutron beam the cyrostat cools fast enough and stops, but for a steady state heat input the heat response can be non-exponential. The data is still useful since final values can still be used if the temperature manages to stabilize after the helium 3 pot fills, as well as the heat response after the applied heat is turned off.

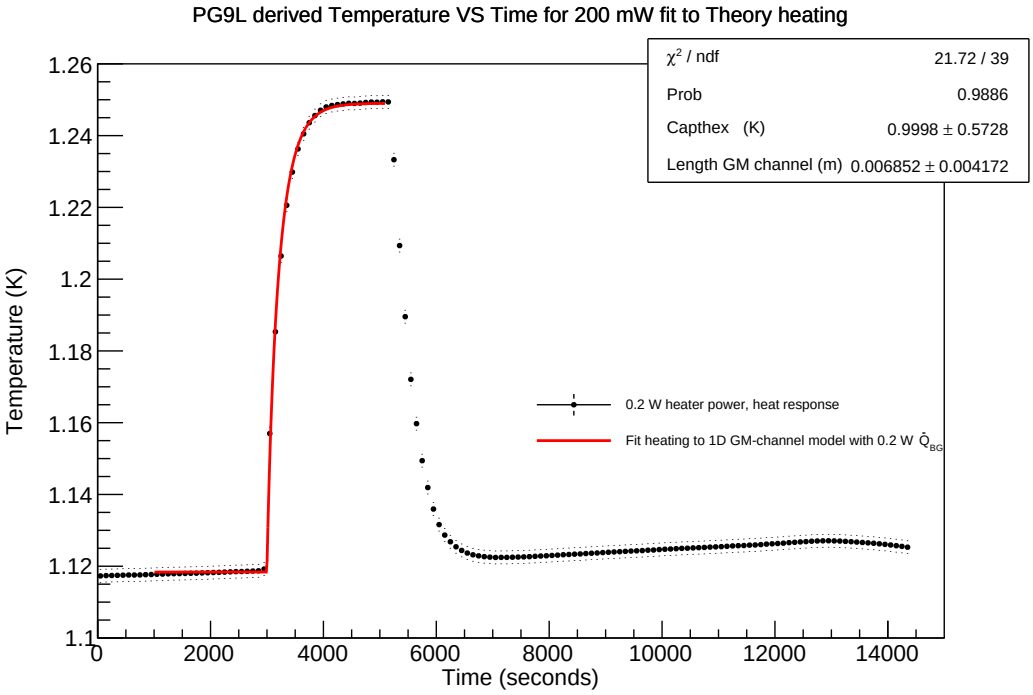

Figure 4.16: Heat response of the temperature of the UCN bottle for a heater power of 200 mW fit 1D model with $\dot{Q}_{\mathrm{BG}} = 200$ mW background heat

In Table 4.7 three different constant background heats $\dot{Q}_{\mathrm{BG}} =$ 100, 150, and 200 mW were used in the determining the fits. The fits for channel length ℓ and T_{hex} are presented. There is a subtle decrease in best fit for the heat exchanger temperature T_{hex} for higher background heat input. There is an increase in channel length ℓ fit to the data as we increase the assumed ambient background heat.

This means the model can explain the data. The error in temperature using the pressure gauge was found to be 0.0001 K by fitting a line to a large flat region and determined the standard

deviation. The standard deviation was found to be 0.00014 K. I treated the deviation from a straight background in the range of fitting as a statistical error.

Table 4.7: Theory parameters fit to the data for various background heat loads for the raising temperature. Fits from Appendix A, plots of fits are in Figure A.19-A.30

$\dot{Q}$ (mW)	Channel length, l (m)	T_{hex} (K)	$\dot{Q}_{\mathrm{BG}}$ (mW)
25	0.005(4)	1.1(4)	100
75	0.005(2)	1.1(5)	100
100	0.005(1)	1.1(6)	100
200	0.006(3)	1.1(2)	100

$\dot{Q}$ (mW)	Channel length, l (m)	T_{hex} (K)	$\dot{Q}_{\mathrm{BG}}$ (mW)
25	0.006(3)	1.0(5)	150
75	0.006(3)	1.1(5)	150
100	0.006(3)	1.1(6)	150
200	0.0063(5)	1.07(1)	150

$\dot{Q}$ (mW)	Channel length, l (m)	T_{hex} (K)	$\dot{Q}_{\mathrm{BG}}$ (mW)
25	0.0066(8)	0.9(6)	200
75	0.007(5)	1.0(4)	200
100	0.007(3)	0.9(6)	200
200	0.007(4)	1.0(6)	200

I mention it briefly here the chi-square/ndf of the fits were at best on the order 0.5 and at worst 1.2 for the heating 1D model. I increased the error on temperature by the average derivation from

a sloped line. This is to account for the systematic uncertainties in the fit model. The temperature of the heat exchanger was not a constant but oscillated over a long timescale due to the level of helium in the 4 K reservoir, which affects pre-cooling of the ^{3}He and its temperature in the ^{3}He pot. This oscillation meant the background temperatures appeared to be linear, since it slowly changed in time. The 1D model assumes that the ^{3}He pot is constant and that the temperature gradient in the channel reaches its equilibrium fast compared to the heat response.

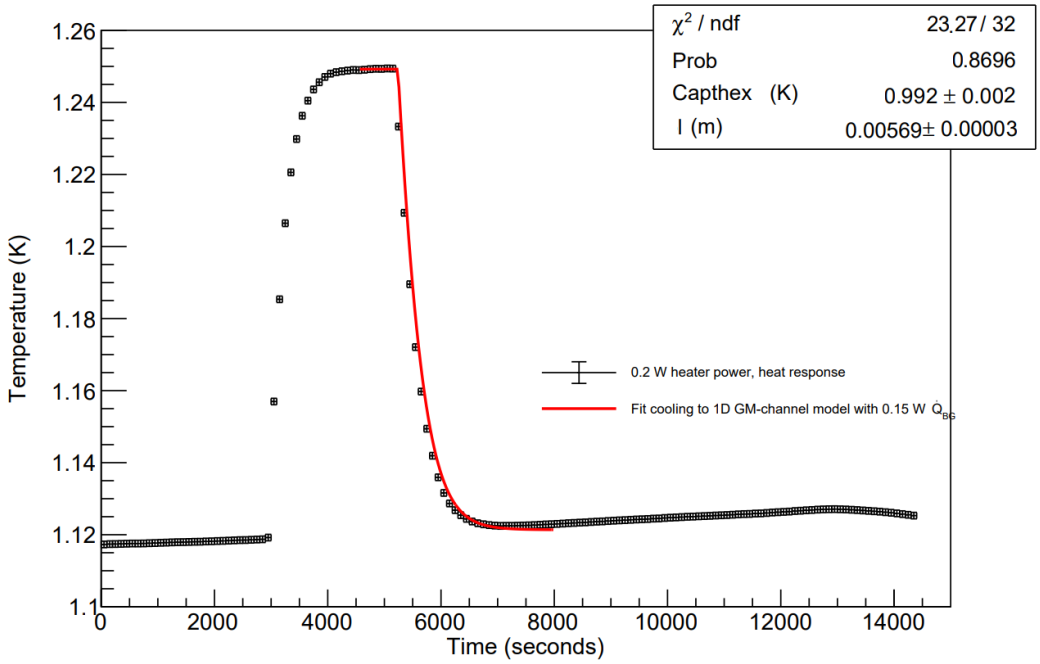

Figure 4.17: Heat response of the temperature of the UCN bottle for a heater power of 200 mW fit 1D model with $\dot{Q}_{\mathrm{BG}} = 200$ mW background heat for the cooling edge side

In Figure 4.17 the cryostat model is modified and used to calculate cooling. We see that before the heater is turned off at $t = 5440$ s, there is a constant value for temperature and after that what appears to an exponential, settling on a final temperature value. In this case, the equilibrium heat load is calculated to be $\dot{Q}_{\mathrm{BG}} + \dot{Q}_{\mathrm{in}}$ prior to turning off the heater. For heater powers of 100 and 200 mW a constant temperature was fit first, because the initial temperature results in the fit were not converging. These trials needed to have the heater on for a longer period of time to establish

the equilibrium. After the heater is turned off, the numerical solution is used, but with only the background heat $\dot{Q}_{\mathrm{BG}}$.

Table 4.8 is the collection of fit results from the numeric solutions using only the cooling edge of the data. Similarly to the heating case, the model fits for $\ell = \sqrt{A}$ and T_{hex}. Only 200 mW for the background heat $\dot{Q}_{\mathrm{BG}}$ is used.

Table 4.8: Fitting 1D Cryostat Model to Data for cooling. Fits from Appendix A. Plots of fits are in Figure A.31-A.36

Heater Power (mW)	Channel length, l (m)	T_{hex} (K)	$\dot{Q}_{\mathrm{BG}}$ (mW)
25	0.006(3)	0.8(2)	150
50	0.006(3)	1.1(6)	150
75	0.006(1)	1.1(6)	150
100	0.00578(2)	1.019(4)	150
150	0.0063(1)	1.07(7)	150
200	0.00569(3)	0.992(2)	150

When fitting to the model, the slightly non-exponential shape of the temperature rise curve seems to better account for the shape of heat response. This is likely due to the strong temperature and q dependence of the properties of He-II. For example, $f(T)^{-1}$ has a strong peak as T approaches 1.9 K, making the thermal conduction much stronger as T rises.

4.6 Concluding remarks

The numerical model discussed in Section 4.2 gives reasonable estimates for the channel length (and dimension of the square channel) of 6 ± 1 mm as well as the temperature of the helium-3 heat exchanger of 1 K. Taking the rising and falling data as a whole, the agreement is reasonable, given

the many approximations of the model. The model shows good qualitative agreement. The slow heat response lends credence to the idea that the cause of the heat response can be attributed to Gorter-Mellink heat transport. The exponential fits by themselves fail to capture heat response by the data by itself, since the sloped temperature of the ^{3}He effects on the ambient bottle temperature.

Part II

Using UCN to measure the neutron electric dipole moment

5. Simultaneous spin analyzer design

In order to measure an nEDM, we need to measure frequency differences in the Larmor precession in the presence of an electric field parallel and antiparallel to a magnetic field. The final polarization state is used to determine the frequency difference after a Ramsey sequence. This polarization measurement is crucial to measuring an nEDM and in fact a part of the statistical uncertainty embedded in the Ramsey visibility α.

The basic concept of the SSA is that the two spin states of the UCNs can be detected at the same time which increases the precision of the measurement since it limits losses. Both polarization states need to be detected for the points of interest in the Ramsey Fringe, in Figure 1.3. These four points can be measured in four experimental runs detecting only a single state each but that would be throwing away half of the neutrons. Only two experimental runs need to occur if both polarization states of the neutron can be detected at the same time. The SSA method was developed as an improvement from using a single arm spin analyzer. The single arm method has a spin flipper that changes which spin state it measures throughout the experimental run, optimizing the neutron count by minimizing losses through storage time above the analyzing foil. The use of a two-armed analyzer system with two spin flippers is superior to the single arm because it reduces the losses occurring when holding one polarization state of neutrons above the analyzer foil.

In Figure 5.1 one arm lets the neutrons through. The iron foil acts as a magnetic potential barrier to low field seekers. This is due to the magnetic field inside the foil being high ($\sim$2 T) thus only high-field-seeking UCNs can pass through. The coloured arrows label the initial state as either a high-field seeker or a low-field seeker. This is the polarization or spin of the UCN. It is useful to think of the polarization in this way to discuss the interaction of the UCN with the foil.

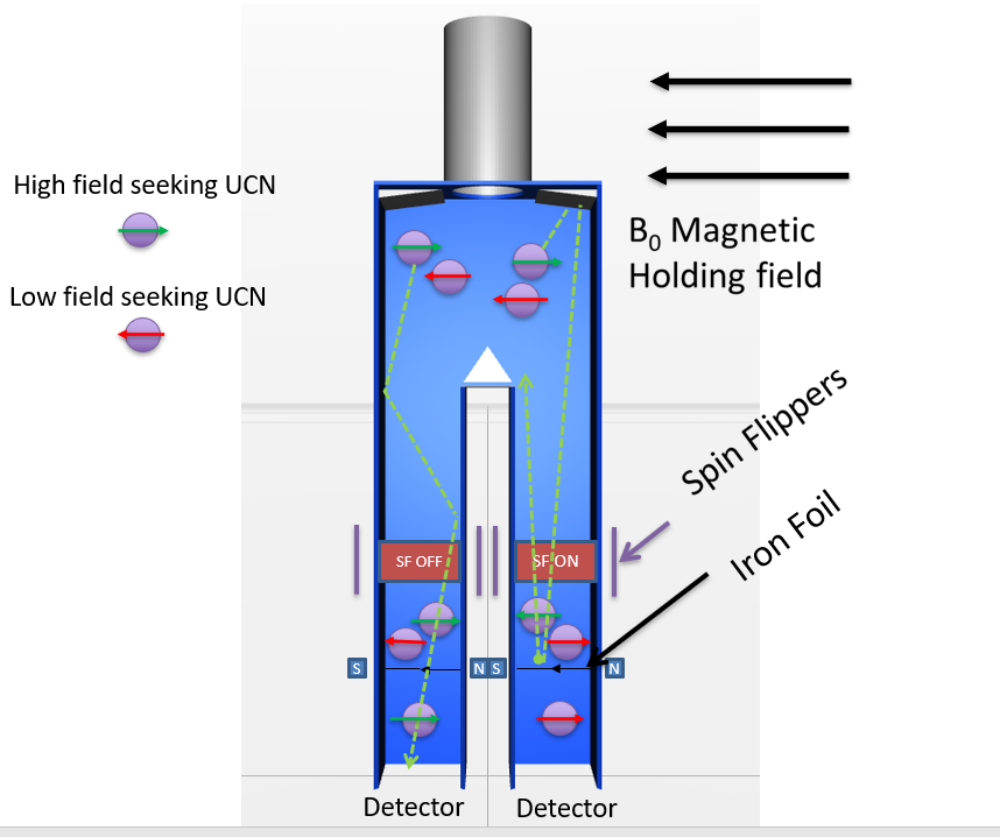

Figure 5.1: Pictorial concept of the simultaneous spin analyser illustrating the path of high field seekers.

The magnetic holding field B_0 aligns the polarized UCNs. There are two polarization states, those that are originally aligned to accelerate and gain energy in magnetic fields, and those that decelerate in magnetic fields, called high field seekers and low field seekers respectively. In the right arm of the SSA in Fig. 5.1 the original high field-seeking neutrons turn into low field-seeking neutrons and are reflected by the magnetic potential of the iron foil. Similarly, the original low field-seeking neutrons flip their polarization to the high field in the right arm and are then in the correct spin state to be counted. Thus the UCNs that were in the high field seeking state prior to entering the SSA (labeled green) are counted in the arm with the spin flipper off (left arm), while the low field seeking neutron are counted in the arm with the spin flipper on (right arm). Both arms have a spin flipper and different runs will be used with the spin flipper coils on and off to eliminate

directional preferences in that data from possible geometric asymmetries from fields.

Figure 5.2 illustrates the design of a prototype simultaneous spin analyzer with the fringe field of the analyzer foil acting as the gradient for the spin flipping coils. Each of the components of the design is modular and can be characterized independently. The rest of this chapter discusses the characteristics of the individual parts and how they work. While the next chapter, Chapter 6 characterization of the components' efficiency with UCNs is presented.

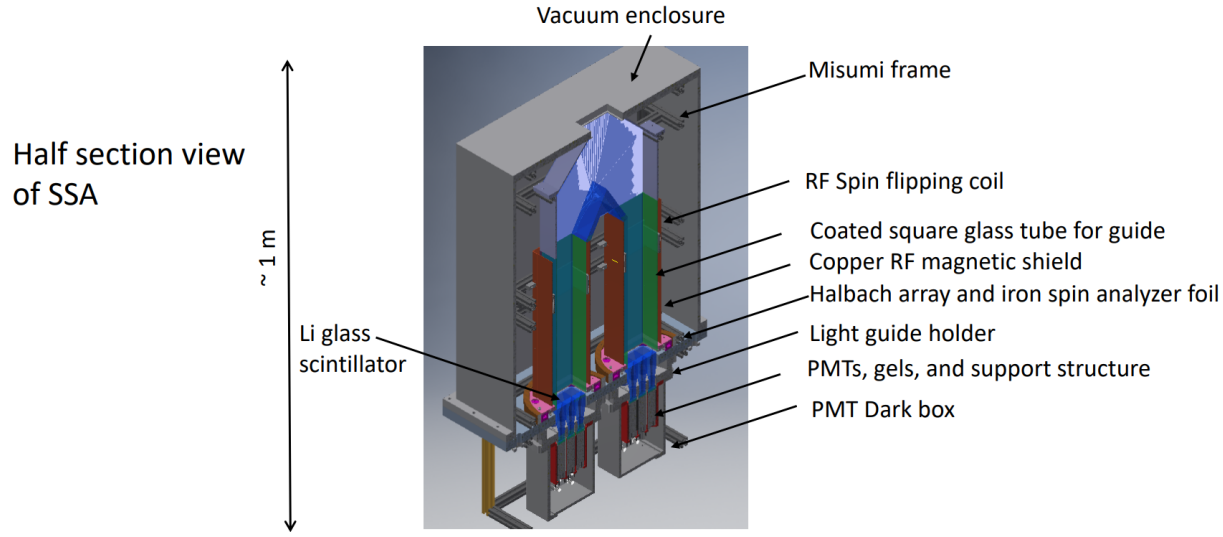

Figure 5.2: Simultaneous spin analyser 3D model

The main components of the SSA are the RF spin flipping coil, the magnetic shield, and the Halbach array with iron analyzer foil. These are the components whose performance is characterized in the next chapter. The RF coil is labelled as such since it is identical to the RF coil in nuclear magnetic resonance imaging machines, but since the magnetic field is lower, our frequency is below that of radio waves. Our typical frequency of the oscillating magnetic field was about 6-9 kHz and that of radio waves is 20 kHz to 300 GHz. The guide arms are glass to prevent eddy currents in a metallic guide from interfering with the oscillations. The arms are glass tubes with a square cross-section coated with a thin layer of nickel molybdenum (NiMo). The guides are square to

maximize the area for counting UCN in the detector's PMTs. There is a vacuum enclosure around the whole apparatus to ensure that the system is in a vacuum and allow the pressure on both sides of the foil to easily reach equilibrium, which would be more difficult if only the guides were kept in a vacuum.

In Victor Heláine's thesis, he suggests that the fringe field of a dual-arm can be from the iron foil itself and can provide the needed linear magnetic-field gradient [20]. This is because shorter arms may improve statistical uncertainty. Moving the spin flipper as close as possible to the iron foil will shorten the guide length of the arm. Approximately 90% of neutrons per meter will travel through a guide. The rest are lost via upscattering, decay, and other losses. Additionally, there would be a higher chance of moving from one arm to the next with shorter guides. This motivates us to use the fringe of the iron foil as the method of creating the necessary magnetic gradient for the spin flipping coils.

5.1 Geant4 Studies of SSA

To determine the geometry of the SSA I used a UCN simulation package included in Geant4. Geant4 is a high-energy particle physics software package for a Monte Carlo simulation. I use an existing low-energy UCN physics package specifically tailored for UCN to study geometry in a future SSA. I used the internal geometry volumes of Geant4 to parameterize the various dimensions of the design. Each of the labelled dimensions in Figure 5.3 can be changed with an input script, where you tell the program what each of the volume's dimensions will be in millimeters.

The size of the square pipe guide was chosen to maximize the resolution of the detector, being 90×90 cm, to optimally match the detector size. The arm length was fixed to 50 cm, which is approximately the size of the copper shield (see Figure 5.11). Additionally, the wedge thickness was kept to a minimum of 10 cm, which is the minimum distance of two magnetic arrays holders (see Figure 5.6), so that we can use the ones we designed and tested.

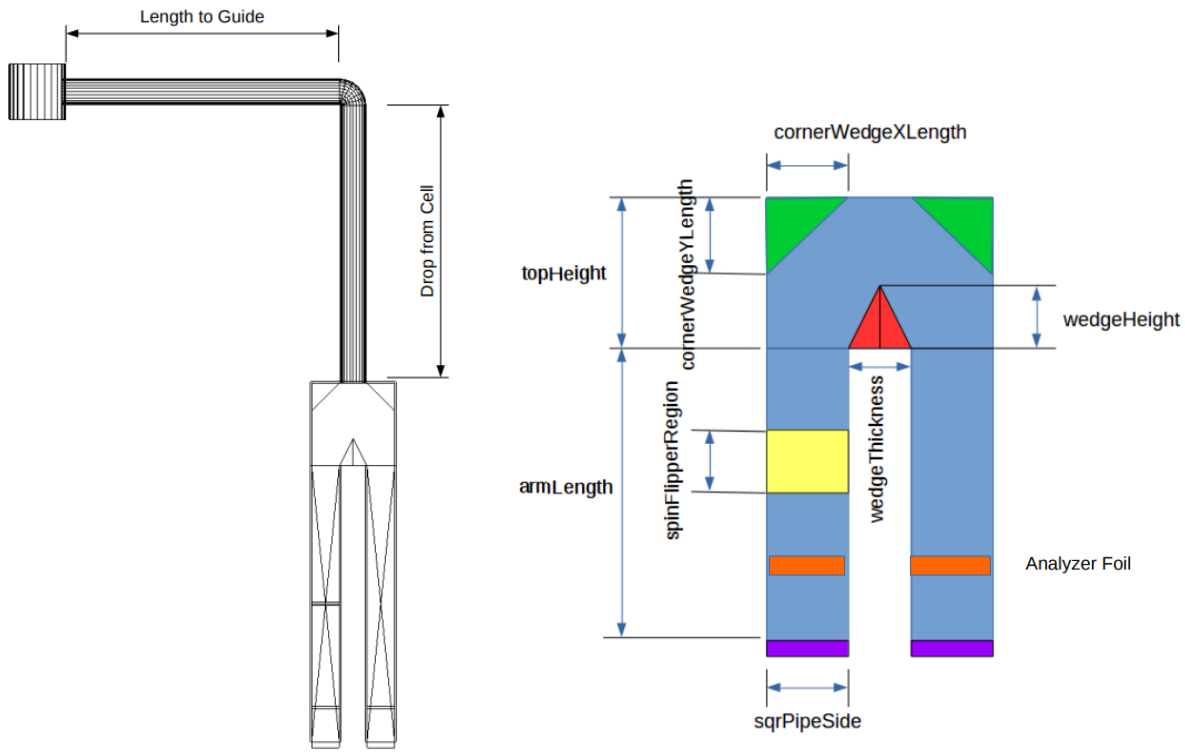

Figure 5.3: Geant4 geometry for a UCN Monte Carlo simulation for the SSA showing an approximate setup for an nEDM measurement with holding cell (left), and fully labeled SSA volumes (right).

The corner wedge length was chosen to produce the minimal distance between the input guide to reduce the ceiling area. The top height, corner wedge height (or Y length), and center wedge height are the three parameters to optimize. For the geometry scans 10000 UCNs were simulated at each scan point, originating from just above the SSA with an initial direction of travel preferentially downwards towards the SSA. The position distribution was randomized on a disk. Figure 5.4 shows the results of a geometry scan for a fixed top height of 40 cm. The UCN were initially simulated as completely polarized in one direction and efficiency is defined as the number of UCN detected over the number of UCN created.

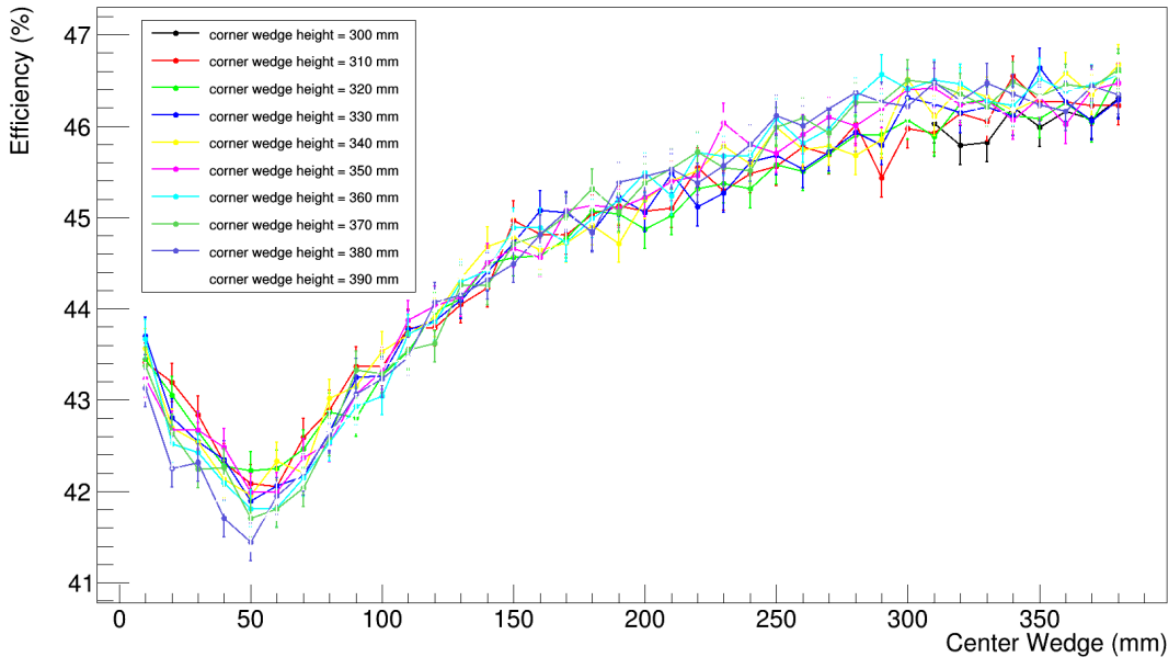

Figure 5.4: Parameter sweep for a Geant4 simulated UCN SSA geometry looking at the center wedge height and corner wedge height.

5.2 Polarizing foil details

Figure 5.5 illustrates the potential barrier modified by the magnetic field. Both the material effective potential and the magnetic potential add. In a thin iron foil at its saturation point the internal magnetic field is approximately 2 T. At 2 T this magnetic flux acts as a spin-dependent gate for any UCNs between 90 neV and 330 neV, since the effective effective potential then is:

$$\begin{aligned} V_{eff} &= V_{\mathrm{F}} \mp \mu B \\ &= V_{\mathrm{F,iron}} \mp \mu_{\mathrm{n}}(2\ \mathrm{T}) \\ &= 210 \mp 120\ \mathrm{neV} \end{aligned} \tag{5.1}$$

This magnetic effective potential lets one spin state through because of a reduced potential for that state and increased potential for the other. The dashed line in Fig. 5.5 illustrates an example

UCN with kinetic energy above the effective potential for iron, $V_F = 210$ neV. It would normally be transmitted through the foil, however if its spin state was low field seeking, it would experience an effective potential of $V_{eff} = 330$ neV which would prevent it from traversing the foil.

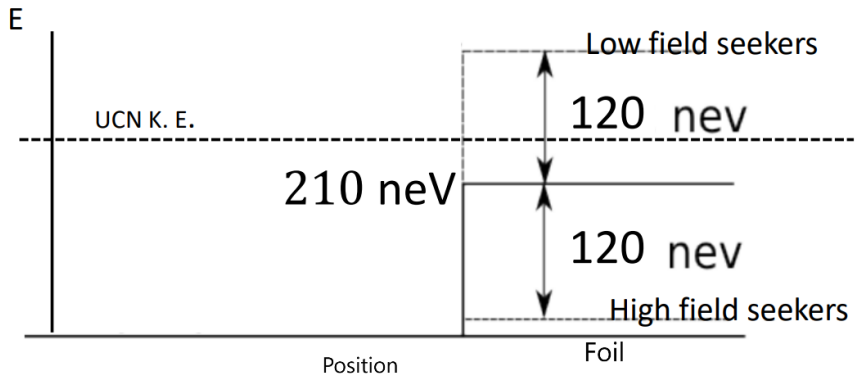

Figure 5.5: Polarization dependent potential energy of a magnetized thin iron foil. The magnetized iron foil acts as a polarizing gate, only letting in the high field seeking polarization state. The dashed line is an example UCN kinetic energy.

The polarizing foil tested in the Fall 2018 run was an iron coating on an Al foil, which was to be magnetized to $\sim$2 T with a Halbach array of permanent magnets designed to have a 14 mT (140 Oe) at its centre. Further details on the foils can be found in Chapter 7. The design of the Halbach array was carried out in OPERA, an electromagnetic finite element analysis program [64]. These results were checked with Comsol, which is a second finite element analysis program [65]. The Halbach array consisted of sixteen 12.7 mm cube neodymium magnets (N52). The magnets were held in place with an aluminum frame that was 181.4 mm diameter, and with its lid was 25.4 mm thick. A drawing of the plan view of the magnet holder is shown in Fig. 5.6 along with a 2019 design that uses larger permanent magnets.

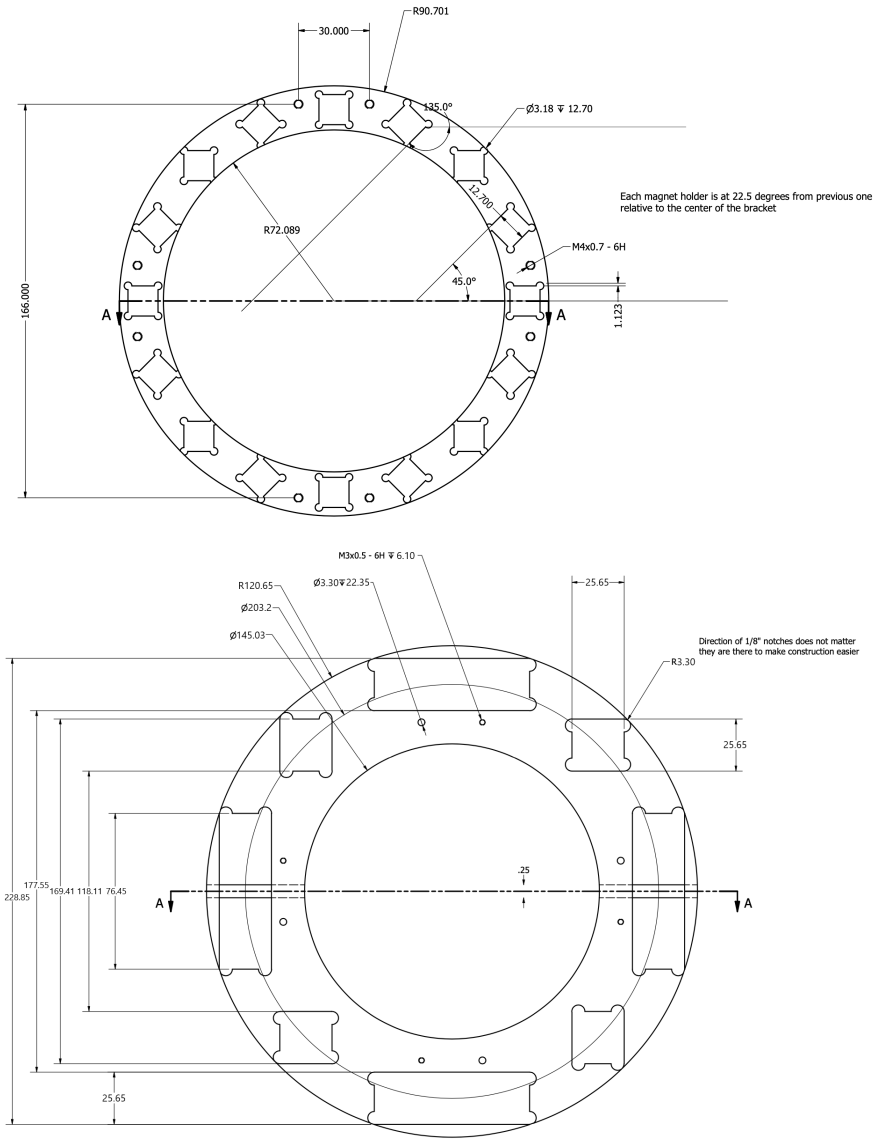

Figure 5.6: Fall 2018 Halbach array magnet frame plan view with dimensions in mm (top), and 2019 Halbach array magnet frame with dimensions in mm (bottom)

Surrounding the Halbach array a stack of 30 iron rings with total thickness 25.4-mm surrounds the return yoke to allow two Halbach arrays with return yokes could be placed next to each other on the arms of the SSA.

The magnetic field produced by the Fall 2018 Halbach array was about 12 mT (120 Oe) at its center, and the fringe field was generally of the same shape simulated. Measurements of the magnetic field along the axis of the Halbach array are shown in Fig. 5.7.

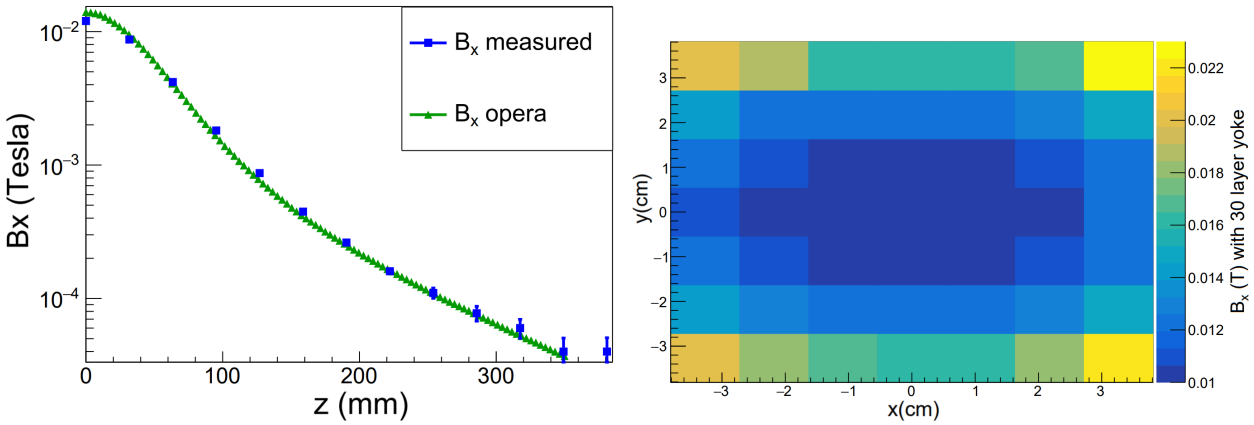

Figure 5.7: Fall 2018 Halbach array magnetic field along the z-axis from both simulation and measurement with a hall probe (left), and as measured with the hall probe in the central plane (right).

After discovering a lower than expected polarization of UCN traversing the foils (as discussed next in Chapter 6), a new Halbach array with larger permanent magnets was designed. The new 2019 Halbach array was designed to reach a central magnetic field of 28 mT (280 Oe), which should be sufficient to fully magnetize the foils. For this design 1x0.75x0.5 inch magnets polarized along the 0.5 inch direction were stacked, using a total of 32 magnets were used, and because of the force required to place the final central magnets, a special jig was built to place the magnets in the holder. The simulated magnetic field for the 2019 Halbach array is shown in Fig. 5.8.

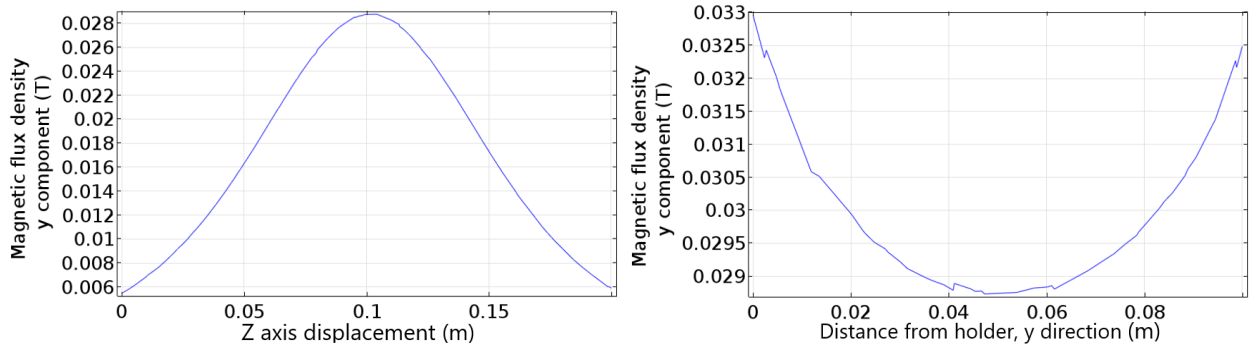

Figure 5.8: Fall 2019 Halbach array magnetic field along the z-axis from simulation with the center at 0.1 m (left), and along the y-axis in the plane of the magnets starting at the inner edge of the foil holder (right).

I conducted magnetization studies of the iron foils used in the 2018 measurements and as well as new foils developed for future tests. These studies look at the internal magnetization of the foils in the presence of an external magnetic field. These studies were conducted at the University of Winnipeg's condensed matter lab using a vibrating sample magnetometer (VSM). The results of the studies are shown in figure 5.9. The LeBow foils are identical to the foils inside the UCN polarizer used in the 2018 test, and are made up of a 400 nm Fe layer deposited on a 25 μm layer of $AlMg_3$ aluminum foil. The Movetec foils were produced for future tests, and are made of 150 nm Fe layer deposited on a 25 μm layer of $AlMg_3$ aluminum foil. The original polarizer Halbach array produced a 1.2 mT (12 Oe) applied magnetic field at its center. To magnetize both types of foils a higher magnetic field is needed. We found that an 0.012 T applied field (H) would not sufficiently polarize the Movetec foils since the area inside the hysteresis curve in Figure 5.9 has an internal magnetic field, B, of -0.5 T to 1 T. The LeBow foil was magnetized but not saturated. This means that the applied field does not guarantee a strong magnetic internal field in the direction of the background field. The background field was used as a holding field that the spins would follow and was produced by the fringe field of TRIUMF's cyclotron's main magnet.

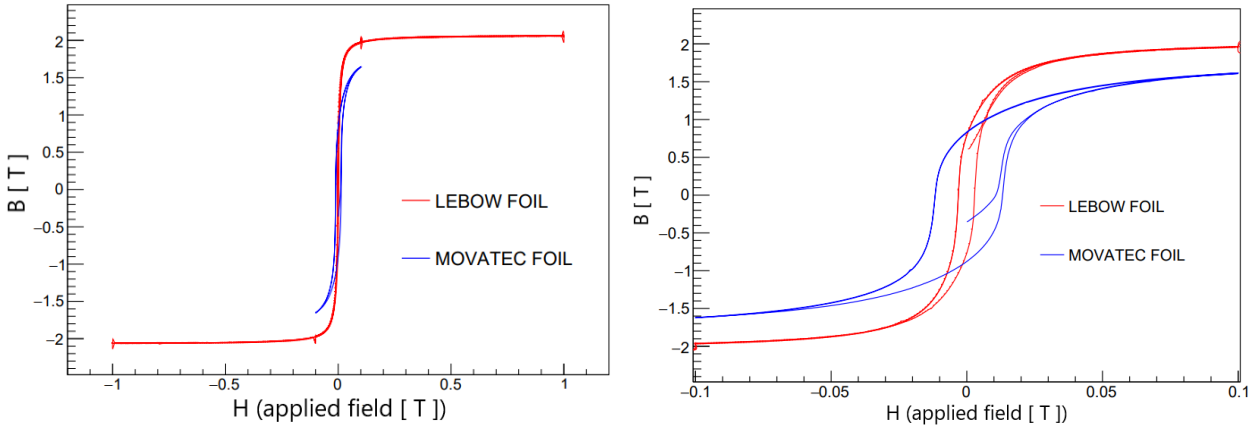

Figure 5.9: Mass normalized hysteresis curve showing the magnetic field in iron of the foil samples measured using a VSM. The red curve is the LeBow foil (400 nm Fe layer deposited on a 25 μm layer of $AlMg_3$ aluminum foil) and the blue curve is the Movatex foil (150 nm Fe layer deposited on a 25 μm layer of $AlMg_3$ aluminum foil). The LeBow foil was used in the 2018 polarizer measurements.

New studies of the foil magnetization have been made in Japan by Takashi Higuchi for iron foils on Al and Si substrates [66]. He has shown that for foils on Si a 20 Oe field is sufficient to fully magnetize the foil, while for foils on Al 50 Oe is required (but that 20 Oe could be sufficient for holding the magnetization of pre-polarized foils). The hysteresis plots generated by vibrating sample magnetometry (VSM) are shown in Fig. 5.10.

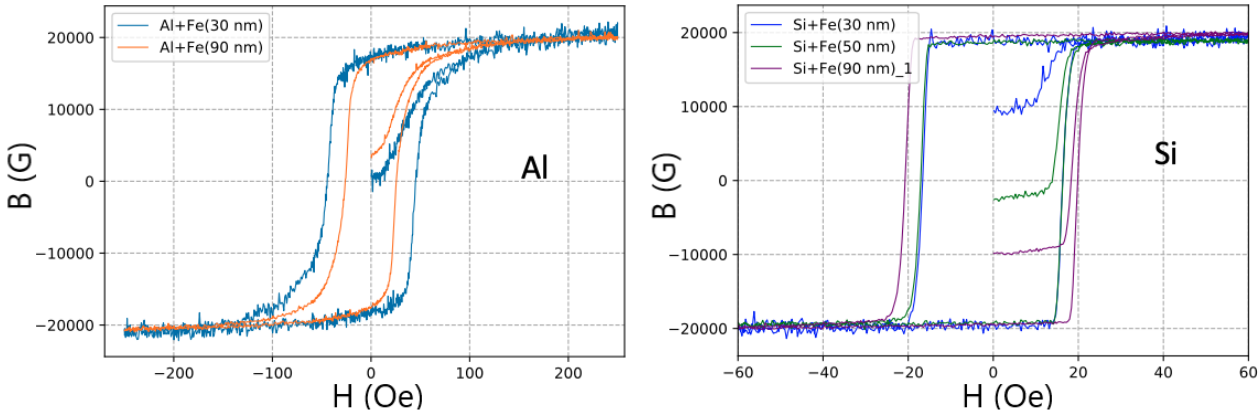

Figure 5.10: Hysteresis curve showing magnetic field in the iron foil (30 nm thick and 90 nm thick) on Al substrate as a function of applied field in Oe (left), and on Si substrate right (right). Figures courtesy of Takashi Higuchi [66].

Based on my observations and those made by the Japan group, the thicker the iron layer deposited on aluminum foil, the lower magnetic field is required to saturate it. However, depositing thin layers on silicon was able to saturate at lower fields overall.

5.3 Spin flipper coils

The spin flipper operates by a method called Adiabatic Fast Passage (AFP) described in this section. If the Adiabatic Slow Passage (ASP) condition is met, the spin of the UCN follows a slowly changing holding field $B_0(t)$. The ASP condition is given by

$$\frac{dB_0}{dt} \ll \omega_{\text{Larmor}} B_0. \tag{5.2}$$

The Larmor frequency is the frequency of rotation that the spins precess around a stationary B_0 magnetic field. If you introduce a magnetic field perpendicular to the holding field, that is oscillating at frequency ω, then the total magnetic field is

$$\begin{aligned}\vec{B} &= \vec{B_0} + \vec{B_1} \\ &= B_0\hat{k} + B_1\cos(\omega t)\hat{i} + B_1\sin(\omega t)\hat{j}.\end{aligned} \tag{5.3}$$

In the rotating frame, with angular velocity ω The effective magnetic field becomes

$$\vec{B}_{\text{eff}} = \Big(B_0(t) - \frac{\omega}{\gamma}\Big)\hat{k} + B_1\hat{i}. \tag{5.4}$$

In the rotating frame the UCN do not see an oscillating field and thus only needs to satisfy the ASP condition. Using a coordinate transform back out of the rotating frame the AFP condition arises and is given by:

$$\frac{dB_{\text{eff}}}{dt} \ll \omega_{\text{Larmor}} B_{\text{eff}}, \text{ and} \tag{5.5}$$

$$\frac{d}{dt}\Big|\Big(B_0(t) - \frac{\omega}{\gamma}\Big)\hat{k} + B_1\hat{i}\Big| \ll \omega_{\text{Larmor}}\Big|\Big(B_0(t) - \frac{\omega}{\gamma}\Big)\hat{k} + B_1\hat{i}\Big|. \tag{5.6}$$

The only time varying component in this frame is $B_0(t)$, and therefore the AFP condition is

$$\frac{dB_0(t)}{dt} \ll \omega_{\text{Larmor}}\Big|\Big(B_0(t) - \frac{\omega}{\gamma}\Big)\hat{k} + B_1\hat{i}\Big|. \tag{5.7}$$

An even more stringent condition is when the right-hand side is at a minimum. This occurs when on resonance with the holding field, $\omega = \gamma B_0$, and we can write

$$\frac{dB_0(t)}{dt} \ll \omega_{\text{Larmor}} B_1. \tag{5.8}$$

Here, the Larmor frequency at this point in time and frame is only due to B_1, and, therefore,

$$\frac{dB_0(t)}{dt} \ll \gamma B_1^2. \tag{5.9}$$

The AFP method allows us to flip the spin to measure different spin states, in the same run. The spin flipper coil was designed to use the fringe field of the analyzer foil holding field for the gradient. At a distance of 35 cm from the center of the Halbach array, the magnetic field from the Opera simulation was $B_x = 0.4$ gauss, and the gradient $B_x/dz = 0.04$ gauss/cm. When used at TRIUMF there was a large external magnetic field from the cyclotron, and B_x of the Halbach array was oriented to align with the cyclotron field (vertical) which when added to the Halbach array field produced about 2.7 gauss. At this magnetic field, it was found that the spin flipper coil operated at 8.2 kHz worked well to flip the neutron spins.

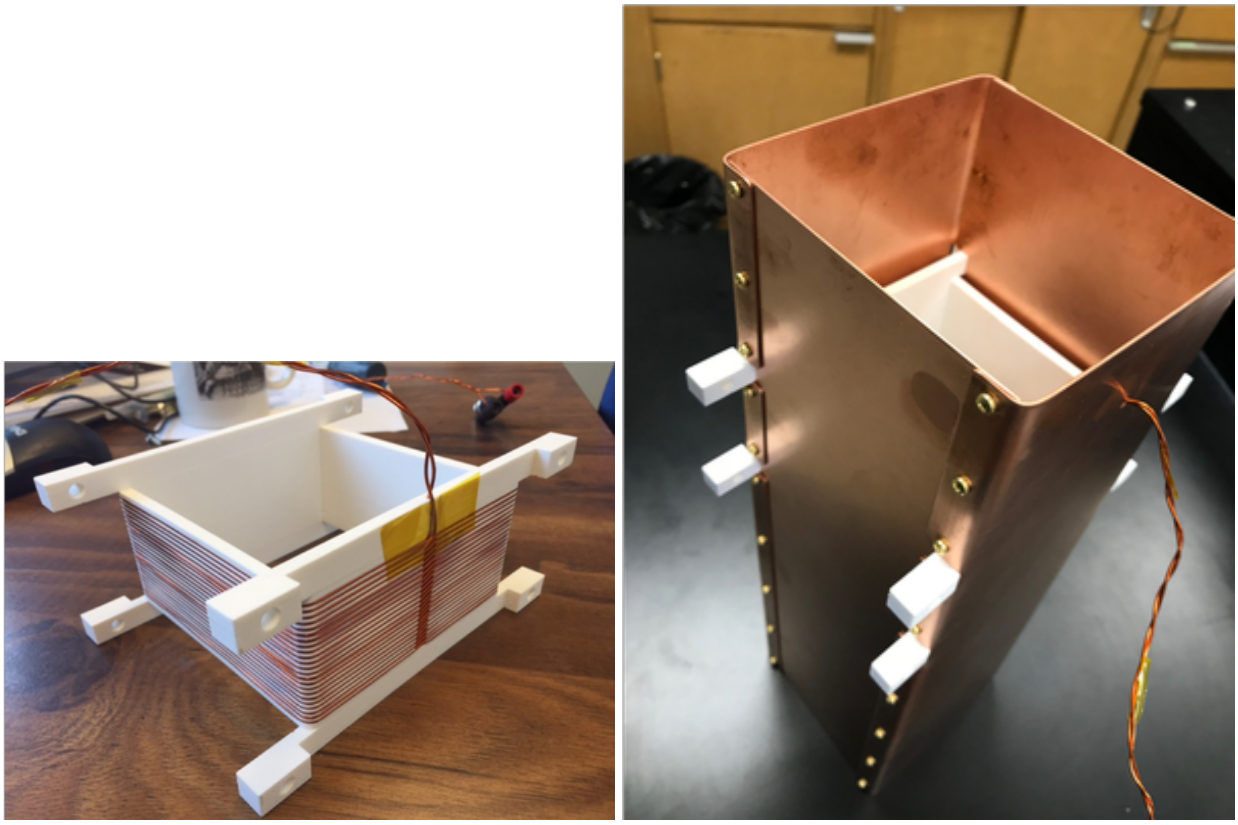

Figure 5.11: Photos of the spin flipper coil. The left photo is without the shielding copper, and the right is with the shielding copper

The spin flipper coil holder was 3D printed with polylactic acid filament (PLA), a widely used thermo plastic filament used in 3D printing. The spin flipper coil holder has 22 windings over a

10 cm region and with 10 cm by 10 cm aperture. The coil, has a resistance of 0.23 Ohms, and when it is outside of the copper shielding has an inductance of 78.2 ± 0.2 μH. With the copper shielding, the effective inductance of the coil becomes 27.7 ± 0.2 μH. With the copper shielding the magnetic field produced at the center of the coil is about 78 μT/A. Therefore, to produce about 100 μT magnetic field, about 1.3 A of current is required. A picture of the RF coil is shown in Fig. 5.11. A square coil was chosen to minimize the footprint around square UCN guides. A table of the coil impedance for different frequencies is in Table 5.1. For the spin flipper coil that is used in the SSA, a different material for the coil holder will be needed that is vacuum compatible.

Table 5.1: Inductive reactance, and overall impedance of the spin flipper coil when in the copper shield.

f (Hz)	ω (rad/s)	X_L (Ω)	Impedance (Ω)
1000.0	6283.2	0.2	0.3
3000.0	18849.6	0.5	0.6
5000.0	31415.9	0.9	0.9
7000.0	43982.3	1.2	1.3
9000.0	56548.7	1.6	1.6
11000.0	69115.0	1.9	2.0
13000.0	81681.4	2.3	2.3
15000.0	94247.8	2.6	2.7
17000.0	106814.2	3.0	3.0
19000.0	119380.5	3.3	3.4

In order to produce the 1.3 Amps AC current to drive each of the spin flipper coils, an Agilent function generator is used to generate the waveform, and an audio amplifier (Studio Art Pro) is used as a current amplifier. Since the audio amplifier expects 4 Ω speakers, an additional 3 Ω

power resistor and heatsink is added in series with each coil. To check the current, the voltage across the 3 Ω power resistor is measured (V_2). The circuit diagram showing the connection of the function generator, to one of the two input channels, and the output to one of the spin flipper coils is shown in Fig. 5.12.

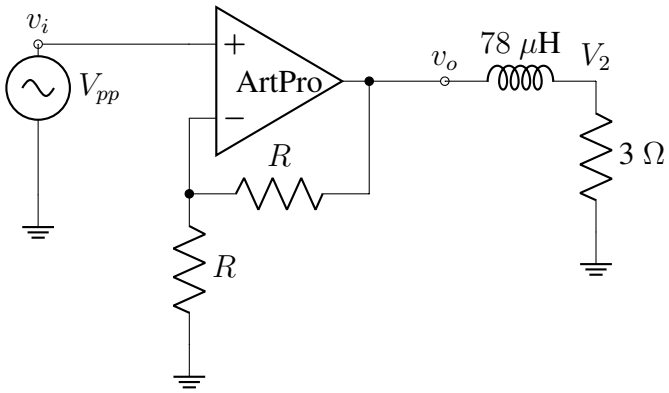

Figure 5.12: Circuit diagram for the spin flipper coil current generation. Note that the ArtPro power amplifier box terminals are at v_i and v_o, and that it acts as a non-inverting buffer to allow a larger current to be drawn than the supply V_{pp}

To set the output from the current amplifier, the attenuation is put to a maximum and slowly lowered until V_2 has 5 V_{pp}, meaning that just over 1.3 A of current is going through the coil and the 3 Ω resistor.

Each component works together to form the basis of the SSA. In the upcoming chapter, we plan on using two polarizing foils and two spin flipping coils to characterize the polarizing power of the iron foils and the efficiency of the spin flipping coils.

5.4 Future Studies

I propose that upgrading the Halbach array to be more powerful will fix the problem with the foil magnetization being too small to fully polarize the UCN.

I also propose using a method of testing the SSA with a similar spin-flipper sequential switching method as the single armed spin analyzer uses to achieve higher statistics measurements of

UCN. In this method, a single spin analyzer in a single arm detector has to alternate the spin flipper on and off during the cycle to count UCNs of both spin states. A future test could be to study if there are any gains in switching the spin flipping coils while using the the dual arm, since there is only a 50% chance that a UCN in the wrong arm can make it over to the correct arm to be counted. This new procedure could allow an increase in N that is large enough to offset any decreases to α and result in a more statistically significant measurement.

5.5 Concluding remarks

We started using a concept of the U-shaped simultaneous analyzer developed for PSI [67]. The major difference being that I wanted to use the fringe field of the Halbach array as the gradient of the spin flipper coil to shrink the arm length to reduce losses. We needed to test if this concept could work to reduce arm size.

Geant4 was used to model of the two arm spin analyzer and input our geometry via script to study the dimensions to determine what geometry was optimal.

A future simultaneous spin analyzer (SSA) was designed as modules that could be individually tested. We wanted the capability to be able to upgrade each component, as well as characterize each component outside the SSA. In the upcoming chapter, we test and simulate the experiments carried out on these modular components.

6. Tests of simultaneous spin analysis components with ultracold neutrons

In this chapter I will discuss the experiments done to characterize the performance of polarizer magnets, the adiabatic spin flippers as well as the performance of the Super Conducting Magnet (SCM). We measure the UCN count rate with various power states of spin flippers. Using the count rate it is possible to characterize the polarization power of the analyzer foils and the spin flipping efficiency of the spin flippers. In order to produce UCNs a new primary proton beamline at TRIUMF is used which can deliver up to 40 μA of 480 MeV protons to the tungsten target [68]. During the runs with the prototype vertical UCN Source described in Chap. 3, the beamline's current was set to 1 μ A. There is a 60-second period with the VAT valve closed during the proton beam on period, where UCN build up in volume from the source up to a gate valve, produced by the VAT company. After 60 s the valve is opened and UCNs are delivered to the experiment. During the UCN buildup phase, the ^{3}He monitor detector counts can be used to normalize the UCN produced during this stage.

Experiments at the vertical UCN source at TRIUMF in 2018 were performed in a series of cycles, due to the beam being pulsed. Each cycle can be separated in periods, during which time UCN storage valves and spin flippers can be set to different states. The first period is the irradiation period, where the tungsten target is irradiated with protons from the beamline and UCNs are produced.

6.1 Characterizing the analyzer foils and the spin flipper coil

The experimental setup for the analyzer foil measurement is shown in Figure 6.1. In this experiment, there are two polarizer foils (a polarizer and an analyzer), and two spin flippers. A sequence of four measurements are made with different settings of the spin flippers, which allows separate efficiencies for the spin-flip probabilities, and the polarizer efficiencies to be measured.

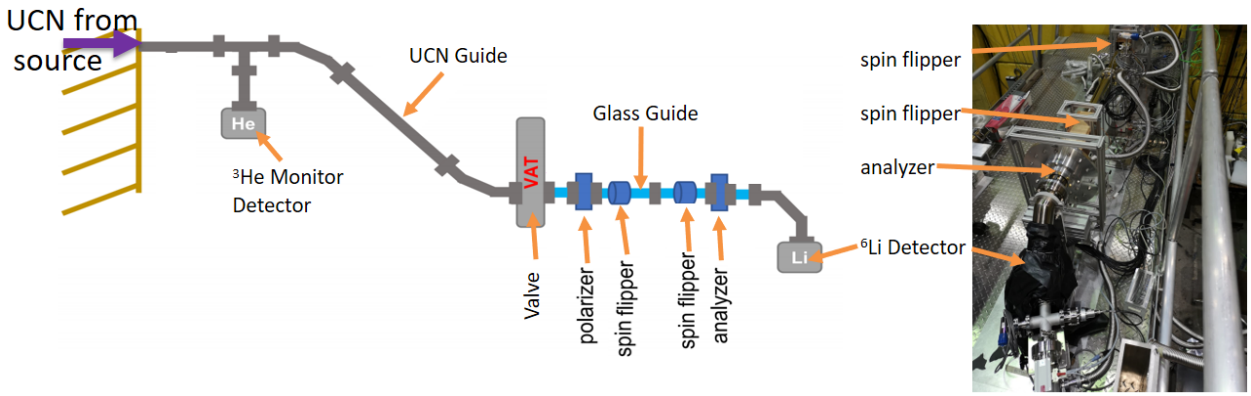

Figure 6.1: The geometry used to perform the spin flipper and iron foil polarizing efficiency measurements.

In each measurement, the power states of the spin flippers is chosen, during the counting period. After that build-up period, the VAT valve, labelled as VAT in Fig. 6.1, is opened, allowing UCN to traverse through the experiment with different probabilities depending on their spin state. The opening of the VAT valve happens at $t = 60$ s and remains open until $t = 180$ s. Thus, the ^{6}Li-detector will only count UCNs from 60-180 s during a cycle. In order to study systematic effects, and to build up statistics, the sequence of four measurements was repeated several times, as will be detailed in the next subsection.

The count rate for the differing power state are given by N_{ij}, where the subscript i refers to the second spin flipper and j refers to the first spin flipper. The values of i, j is either 0 (off) or 1 (on). There are four power state for the two spin flippers for the experiment depicted in Fig 6.1. They are with both spin flippers off (N_{00}), both spin flippers on (N_{11}), with only the first spin flipper on (N_{01}), and with only the second spin flipper on (N_{10}).

To characterize the polarizer, spin flipper, and SCM the transmission matrix formalism can be used [69], to check the solutions presented by Wolfgang Schreyer in his thesis [70].

The polarization of UCN can be described by a vector with two components. The first component is the number of UCN which are attracted to high field and the second component is the number of UCN attracted to low magnetic field. To start, the incident beam is defined as a vector

and is assumed to have some initial intensity i_0. The UCN beam in an unpolarized beam which is defined as

$$I = \begin{pmatrix} i_0 \\ i_0 \end{pmatrix}. \tag{6.1}$$

The detector efficiency with efficiency det is defined as a row vector under this formalism:

$$D = \begin{pmatrix} det & det \end{pmatrix}. \tag{6.2}$$

The polarizing power of the polarizer and analyzer matrix is assumed to be the same and is:

$$P = \begin{pmatrix} t_{hfs} & d_{lfs} \\ d_{hfs} & t_{lfs} \end{pmatrix} \tag{6.3}$$

where t_{hfs} is the probability of transmission of high field seeking spins, where d_{hfs} is the probability of depolarization of high field seeking spins. Similarly, t_{lfs} is the probability of transmission of low field seeking spins, where d_{lfs} is the probability of depolarization of low field seeking spins. The lfs and hfs are labels given to particles whose spin states gain energy in high or low magnetic field.

Under this formalism, the probability of spinflipping from a spin flipper is given by s_i in the spin flipping matrix S_i:

$$S_i = \begin{pmatrix} (1 - s_i) & s_i \\ s_i & (1 - s_i) \end{pmatrix} \tag{6.4}$$

here the subscript denotes if it is the first or second (1 or 2) spin flippers.

The available observable is the count rate under a spin flipper power state. The counts rate N is then defined as:

$$N_{00} = D \cdot P \cdot P \cdot I \tag{6.5}$$

$$N_{01} = D \cdot P \cdot S_1 \cdot P \cdot I \tag{6.6}$$

$$N_{10} = D \cdot P \cdot S_2 \cdot P \cdot I \tag{6.7}$$

$$N_{11} = D \cdot P \cdot S_2 \cdot S_1 \cdot P \cdot I \tag{6.8}$$

Where the subscripts denote the power state of the spin flipper.

To characterize the polarizer/analyzer a polarizing power p_A is defined by:

$$p_A = \frac{\begin{pmatrix} 1 & -1 \end{pmatrix} \cdot P \cdot I}{\begin{pmatrix} 1 & 1 \end{pmatrix} \cdot P \cdot I} = \frac{t_{hfs} + d_{lfs} - t_{lfs} - d_{hfs}}{t_{hfs} + d_{lfs} + t_{lfs} + d_{hfs}} \tag{6.9}$$

The polarizing power is given by a linear combination of the terms from Eq. 6.5-6.8 under a few assumptions (see Appendix B for the full solutions). There are 8 potential equations that solve for the polarization power, but they come in equivalent pairs. For identical polarizers $P_1 = P_2 = P$, with symmetric depolarization $d_{lfs} = d_{hfs}$, and perfect spin flipper efficiency the polarization is given by

$$p_{A1} = \sqrt{\frac{N_{00} - N_{01}}{N_{00} + N_{01}}}, \tag{6.10}$$

and

$$p_{A2} = \sqrt{\frac{N_{00} - N_{10}}{N_{00} + N_{10}}}. \tag{6.11}$$

Under these assumptions Eq. 6.10 is equivalent to Eq 6.11 and therefore $p_{A1} = p_{A2}$.

For identical polarizers $P_1 = P_2 = P$, with perfect polarizer $l_{lfs} = d_{lfs} = 0$, and perfect spin flipper efficiency the polarization is given by:

$$p_{A3} = \frac{N_{00} - N_{01}}{N_{00} + N_{01}}, \tag{6.12}$$

and

$$p_{A4} = \frac{N_{00} - N_{10}}{N_{00} + N_{10}}. \tag{6.13}$$

Under these assumptions Eq. 6.22 is equivalent to Eq 6.13 and therefore $p_{A3} = p_{A4}$.

For identical polarizers $P_1 = P_2 = P$, with symmetric depolarization $d_{hfs} = d_{lfs}$, and identical spin flipper efficiencies $s_1 = s_2 = s$ the polarization is given by:

$$p_{A5} = \sqrt{\frac{(N_{00} - N_{01})^2}{N_{11}N_{00} + N_{10}^2}}, \tag{6.14}$$

and

$$p_{A6} = \sqrt{\frac{(N_{00} - N_{10})^2}{N_{11}N_{00} + N_{01}^2}}. \tag{6.15}$$

Under these assumptions Eq. 6.14 is equivalent to Eq 6.15 and therefore $p_{A5} = p_{A6}$.

For identical polarizers $P_1 = P_2 = P$, with perfect polarization $l_{lfs} = d_{lfs} = 0$, and identical spin flipper efficiencies $s_1 = s_2 = s$ the polarization is given by:

$$p_{A7} = \frac{(N_{00} - N_{01})^2}{N_{11}N_{00} + N_{10}^2}, \tag{6.16}$$

and

$$p_{A8} = \frac{(N_{00} - N_{10})^2}{N_{11}N_{00} + N_{01}^2}. \tag{6.17}$$

Under these assumptions Eq. 6.16 is equivalent to Eq 6.17 and therefore $p_{A7} = p_{A8}$.

Equation 6.16 and 6.17 is important since in simulation we simulate symmetric depolarization, with imperfect polarizers.

Solving Eq. 6.5-6.8 for the spin flipping probabilities gives:

$$s_1 = \frac{1}{2}\left(1 + \frac{N_{11} - N_{01}}{N_{00} - N_{10}}\right), \tag{6.18}$$

and similarly it follows that:

$$s_2 = \frac{1}{2}\left(1 + \frac{N_{11} - N_{10}}{N_{00} - N_{01}}\right). \tag{6.19}$$

These spin flipper probabilities is the spin flipper efficiency. We can define a term f called the flipper efficiency:

$$f_1 = \frac{N_{11} - N_{01}}{N_{00} - N_{10}} = 2s_1 - 1 \tag{6.20}$$

$$f_2 = \frac{N_{11} - N_{10}}{N_{00} - N_{01}} = 2s_2 - 1 \tag{6.21}$$

This term is related to the spin flipper efficiency and is used in the following equation:

$$p_{A5} = \frac{N_{00} - N_{01}}{f_1 N_{00} + N_{01}}, \tag{6.22}$$

This is identical to Eq. 6.14 but would only need a single known spin flipper efficiency to account for an imperfect spin flipper.

6.1.1 Experimental Data for the spin analyzer and spin flipper measurements

A total of sixty-six 180 s cycles of UCN production were used for the experiment for the analyzer foil polarizing power and spin flipper efficiency measurements. The setting of the spin flipper coils was changed before each cycle, following a pattern with both spin flippers off (N_{00}), then spin flipper 1 on and 2 off (N_{10}), then with spin flipper 1 off then 2 on (N_{01}), and then both spin flippers on were used (N_{11}). This pattern of four cycles was repeated for a total of 66 cycles. Fig. 6.2 shows the raw counts in the ^{6}Li detector. Between runs 10 and 30 there was an issue with the primary proton beam intensity causing the total number UCN counted during those cycles to be much lower.

The TUCAN collaboration uses standard cuts for treatment of all the data collected during the runs. The first was a treatment of the raw detector data. The Li^6 detector uses a pulse shape discrimination, PSD, based on the pulse of the event and a value called charge long, Q_{long}, which is the total number of charge collected in the photomultiper tube during a 200 ns counting window after an event trigger [**?**]. If the Q_{long} is high, then the event has the characteristic long scintillation time of a neutron. Also, the PSD generally has to be large as well.

$$PSD > 0.3 \tag{6.23}$$

and

$$Q_{long} > 2000. \tag{6.24}$$

The ^{3}He detector has a relatively short charge characteristic of a neutron. For the event to be considered a neutron the charge collected after an event in 80 ns, Q_{short} the event must satisfy

$$Q_{short} > 300. \tag{6.25}$$

The following cuts were applied to the data:

- the beam current dropped below 0.1 μA
- the beam current fluctuated by more than 0.02 μA
- the last period does not contain any ^{6}Li events, thus the run was aborted at some point during this cycle
- IV1 never opened, therefore no UCNs delivered to experiment
- ion gauge IG5 read a pressure between 10^-7 torr and 10^-2 torr, meaning that this gauge was on causing additional background in the ^{6}Li detector
- the ^{6}Li detector averaged a counting rate below 10 Hz during the counting period
- the ^{6}Li detector detected a large background rate above 10 Hz during the irradiation period
- the ^{3}He detector detected less than 300 UCN during counting

In total, 7 cycles out of 67 were excluded from the analysis. Cycles 22, 60, 61, 62, 63, and 64 were cut because the beam dropped below 0.1 μA. Cycle 67 was cut because the last period does not contain any ^{6}Li events.

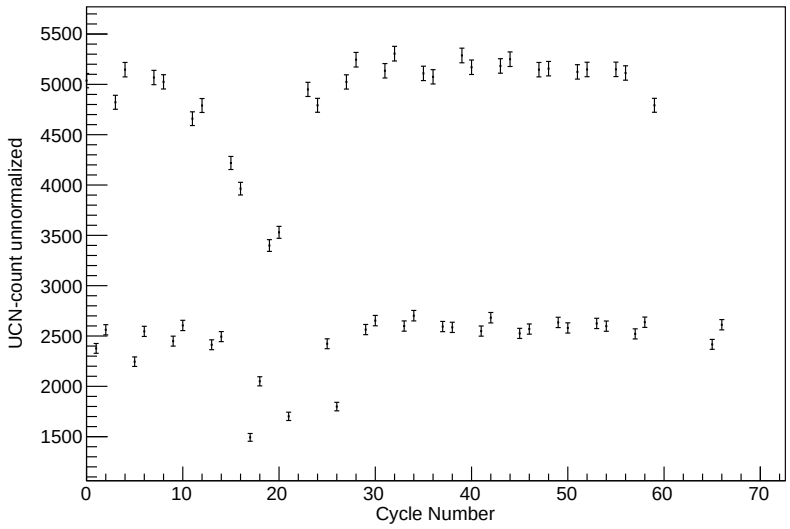

Figure 6.2: UCN count in the ^{6}Li detector without normalization to illustrate beam instability, particularly between cycle number 10 and 30.

We know that there is a characteristic to the run cycles of N_{00}, N_{01}, N_{10} and N_{11}, that repeats. We separate the data into the four groups. We then calculate the ^{3}He detector count rate in period 1, the irradiation period. This will act as a normalization, so that we can divide this rate into the final ^{6}Li detector during the final period to get a ratio of UCN detected to UCN produced, which normalizes the data.

To counteract the beam instability, a pre-holding time of 10 seconds was established, during which the ^{3}He detector counts a small sample of the created UCN. The ratio between the UCN counted in the final detector and the number of UCNs in the monitor detector will account for fluctuations in UCN production from beam instabilities. Figure 6.3 graphs the ratio of the ^{6}Li detector to the ^{3}He normalization detector.

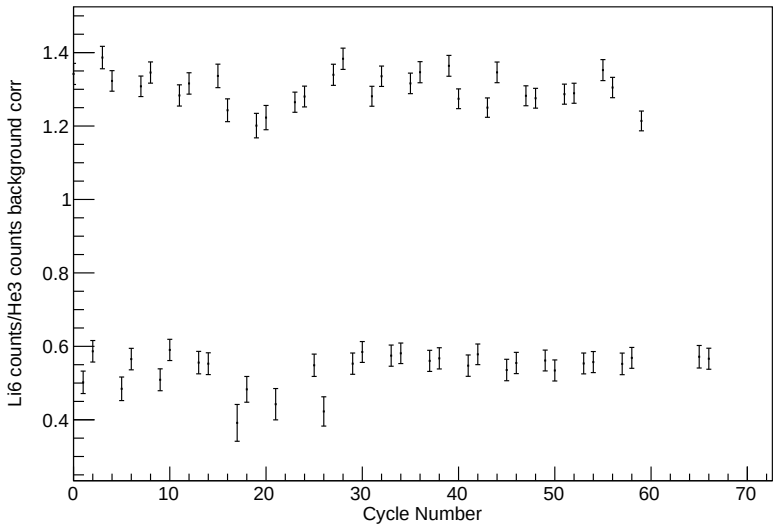

Figure 6.3: UCN counts in the ^{6}Li detector normalized to the helium monitor detector during filling. Illustrating the correction of the beam instability between cycle number 10 and 30.

The background rate in the ^{6}Li detector is 5.83 ± 0.04 /s. The normalization process eliminated the beam instability from the data, resulting in a flat line between identical settings.

Table 6.1: UCN counts in the detectors for different power states N_{ij}.

Spin flipper power states (N_{ij})	Number of cycles	^{6}Li detector counts	^{3}He monitor detector counts	Ratio ($^6\text{Li}_{\text{BG corrected}}$ /^{3}He)
N_{00}	15	63900 $\pm$ 300	48300 $\pm$ 200	1.310 $\pm$ 0.008
N_{01}	15	27900 $\pm$ 200	48900 $\pm$ 200	0.555 $\pm$ 0.004
N_{10}	16	27900 $\pm$ 200	50600 $\pm$ 200	0.532 $\pm$ 0.004
N_{11}	15	63300 $\pm$ 300	48200 $\pm$ 200	1.297 $\pm$ 0.008

The initial look at the statistical uncertainty of the analyzing efficiency, over time, is separated into bins, with edges at $[60., 62., 62.5, 63., 64., 67., 70., 74., 80., 100., 180.]$ s. The bins were chosen

so that the number of counts in each bin were the same. Fig. 6.4 shows the polarization over time of the analyzer foil set-up.

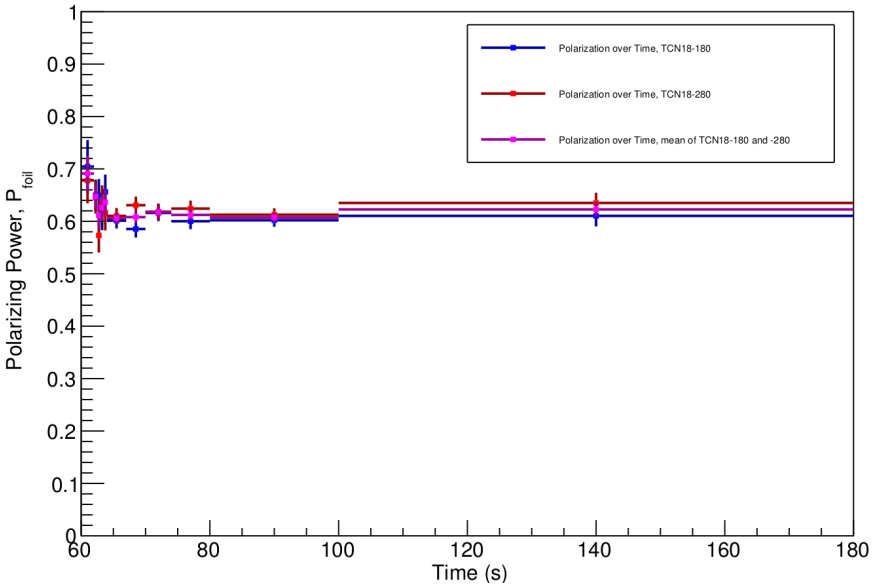

Figure 6.4: Measured polarization power, P_{foil}, as a function of time in TCN18-180 using Eq 6.14. The bins were chosen, so the statistical errors were roughly the same.

We can get an overall measure of the polarization power if we calculate p for all time, using Eq. 6.16 and 6.17, we get $p_{A7} = 0.64 \pm 0.01$ and $p_{A8} = 0.66 \pm 0.01$. This agrees with Fig. 6.4 for the polarization power over time plot (p vs t).

Similarly, the probability of spin flipping using Eq. 6.18 and 6.19 we get $s_1 = 0.977 \pm 0.009$ and $s_2 = 1.007 \pm 0.009$.

6.1.2 PENTrack Polarization Simulations Test

In order to run a thorough analysis on the spin flipper and analyzer foil, we need to be able to track spins within a full physics simulation. In order to accomplish this, I tested new code for PENTrack [71]. PENTrack is a Monte Carlo simulation of ultracold neutrons (UCNs) and this simulation has been modified to study the performance of the spin polarizer/analyzer. This

simulation's performance needed to be checked to ensure that the UCNs are behaving correctly in simulation. This section will describe those tests.

A material property for the internal magnetization, in units of Tesla (T) is an input to the simulation. This parameter functions as a volume magnetization, which modifies the effective potential of the material along the direction parallel to the spin. The spin dependent UCN's effective potential, $V_{\mathrm{F}}(\mathrm{spin})$ becomes

$$V_{\mathrm{F}}(\mathrm{spin}) = V_{\mathrm{F}} \pm \vec{\mu}_N \cdot \vec{B}_{\mathrm{int.}}, \tag{6.26}$$

where the unmodified effective potential is given by V_{F}, the magnetic moment of the neutron is given by $\vec{\mu}_N = \mu\vec{S}$, which lays in the direction of the spin $\vec{S}$, and the internal magnetic field of the material is given by $\vec{B}_{\mathrm{int.}}$.

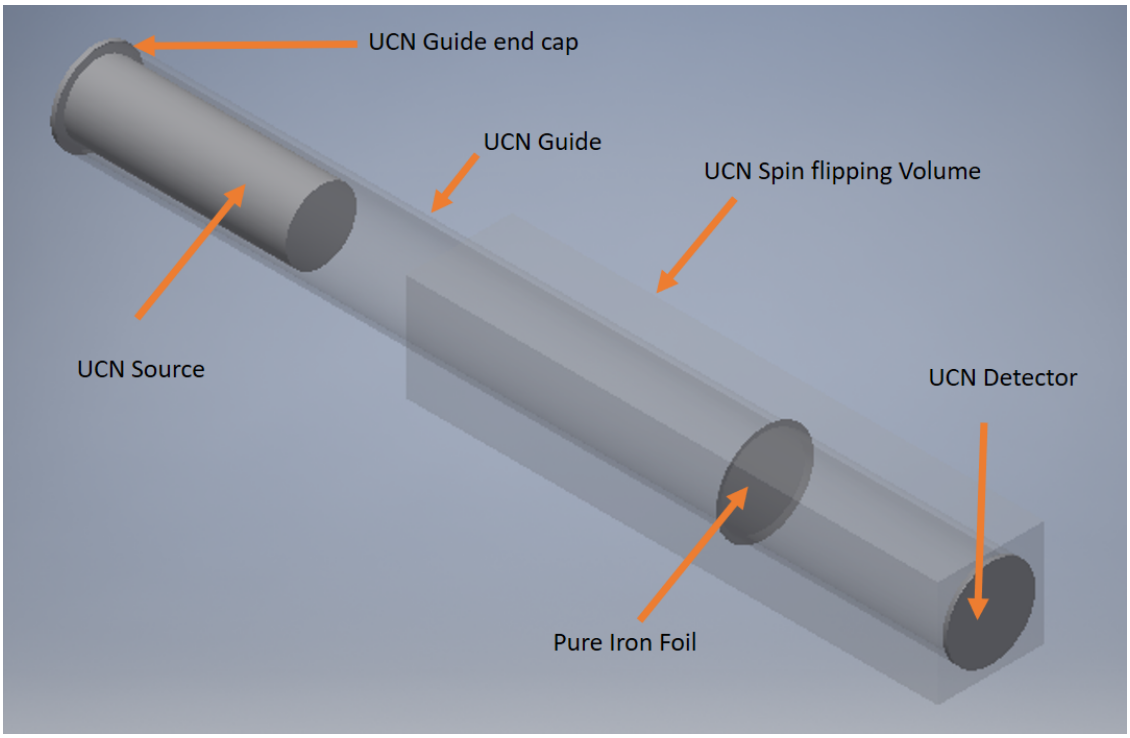

Figure 6.5: The geometry used to perform these tests was generated from AutoDesk Inventor. The coloured arrows label the different parts of the simple model one foil model.

Fig. 6.5 shows the geometry used to test the simulation. In Fig. 6.5 the cylinder is a 1-meter-long ideal UCN guide without any wall losses or depolarization. The rectangular box is the UCN spin flipping region which in the drawing is semi-transparent so that the UCN guide end cap, the UCN source, spin analyzing pure iron foil and the UCN detector can be seen.

The UCNs are simulated to start in the UCN source and travel down the guide and are detected with 100% efficiency at the UCN Detector. If they start with the correct spin state, then they will pass through the pure iron foil without losses. If the neutrons are of the opposite spin states, they see a higher effective potential and so will reflect from the pure iron foil, resulting in no UCN detected at the detector.

Similarly, the spin flipper simulation is done by flipping the spins of neutrons that enter or leave the spin flipping volume. This spin flipping effect is tested using UCN starting in one of the spin states, and seeing whether they all reach the detector, or are all contained in the region before the analyzer foil.

I performed checks to see if PENTrack was properly handling a spin dependent effective potential. In particular, I simulated enough neutrons so that we can determine if the polarization is working and that all edge cases can be seen, while keeping the run time relatively short. The checks included looking at the final spin states and the number of spin-flips that a UCN would undergo in simulation, to see if it lined up with expectations. The energy spectrum has a $\sqrt{E}$ distribution from 0 to 400 neV. The test of the simulation's ability needs to access edge cases as well, so we chose a value of neutron energy much higher than the material potential, and much higher than we will be using in simulations of the experiments.

We can artificially split the data into UCNs with starting spin state, or polarization (Pol.), of -1 or 1. If we select to only look at one spin state of the starting neutron, it is equivalent to an initially polarized collection of neutrons of that state. Thus, we can use the information from a single simulation to see if the polarization power of the foil is working without the need for spin flipper, by treating each of the spin states as a separate measurement that counts the number of UCN detected N for each spin state as Eq. 6.27 dictates.

The polarization power p is

$$p = \frac{N\uparrow - N\downarrow}{N\uparrow + N\downarrow}, \tag{6.27}$$

where N is the UCN counts of a particular spin state which has subscripts to indicate the spin state of the UCN, ± 1, denoted with arrows.

We would expect, if the potential is being modified correctly, one state to be preferentially reflected from the foil, while the other passes through the foil to the detector. An indication that the simulation is working, is that different numbers of UCN of each of the starting spins are detected, as summarized in Table 6.2. We can conclude that the iron foil is being modified correctly. Of the total 5000 UCN that were simulated for each spin state, they were not all detected. There are UCNs being lost to upscattering, and decay. Additionally, I simulated neutrons up to 400 neV, at which energy they can leave the simulated volume directly. However, if their initial trajectory was such that they would end up in the counting volume, they would be counted even if they had a higher energy than the effective potential of the guides. Note that in these tests the spin flip on bounce is still kept on the order of 10^{-5}/bounce, meaning that there is no depolarization being added into the system by the foils, it is only the higher energy neutrons that get counted from the wrong spin state.

Table 6.2: Table of UCNs detected in the counting volume of the simple geometry test in Figure 6.5 with stainless steel guide and a square root power energy distribution from 0 to 400 neV. This is a subset of data, uncounted data is not included in this table.

Spin flipper power state	Pol. Start = 1	Pol. Start = -1	Polarization Power
SF On	1777	133	0.86
SF Off	126	1753	0.86

The PENTrack simulation is setting the internal magnetic field of the spin flipping coil by simply having a parameter to alter the effective potential the UCN sees at the surface according to

Eq. 6.26. The polarizing power of the foil is calculated to be 0.86 ± 0.02. The polarization power in this check is expected to be 1.0 for UCN. However due to edge case checks I simulated neutrons up to 400 neV, and the high energy neutrons are able to overcome the effective potential of the magnetized iron foil regardless of their spin state.

Table 6.3 shows the results from an idealized simulation with no spin depolarization on any surface, where the initial energy of the UCNs has a maximum of 260 neV, instead of 400 neV. Additionally, the internal magnetic potential was set to an unrealistic number of 3 T. This idealized case was simulated to ensure that the polarization is modifying the UCNs in the correct way. The simulated polarization observable was 1.00 ± 0.02. We simulated 10 000 UCNs of a single spin state, that would be counted only if the spin flipper was working. This was to make sure the spins flipper code and volumes worked as expected. Nearly 10% of the neutrons did not get counted as they continued to bounce around in the guide, not having been detected in the length of time simulated.

Table 6.3: Simulation results of the simple geometry test in Fig. 6.5 with perfectly non-absorbing guide with 20% diffuse reflection and a 1/2-power energy distribution from 0 to 260 neV, with the internal effective potential set to 3 T. 10000 UCNs were thrown of a single polarization state. The unrealistic case to prove that the foil is working correctly.

Spin flipper power state	Counts in Detector	Decayed	Did not finish
SF On	9038	2%	8%
SF Off	0	20%	80%

PENTrack's new polarization handling of the internal magnetization is done by adding a material property that allows simulating spin flippers and spin analyzer foils. This allows the simulation to test the experiments that were performed at TRIUMF to characterize the SSA components.

The modified PENTrack was able to track spin, using a model that records the neutron spin as aligned parallel or antiparallel to the magnetic field. This means that we can use spin depolar-

ization probabilities and large number of neutrons to simulate the spin response of neutrons to the materials used to guide and store the UCN. The simulation can be used to do material property scans to predict what depolarization change is due to the foil and what is due to spin flips on materials. Figure 6.8 depicts the scan through the spin-flip probabilities of the foil and the neutron polarization that is observed.

6.1.3 PENTrack Polarizer and Spin flipper Simulation Simulations

In the fall of 2018 UCN beam run we tested the polarizer foils and spin flipper coils. Fig. 6.5 shows the geometry used in the simulation to understand the real data and to assist with the analysis. The model consists of over 120+ parts. The simulation mimics the data taking, where a cycle time of 190 seconds after initial irradiation is considered.

The UCN are simulated by injecting neutrons at the centre position of the UCN bottle, located in the bottom left of Fig. 6.5. The valves, located just before and after the spin analyzers at the end of the green section in Fig. 6.5 open after 60s after the irradiation period.

The UCN bottle is stainless steel ($V_F = 188$ neV) as well as most of the guides up until the first VAT valve. The valve is aluminum ($V_F = 54$ neV). The glass UCN guides are coated with nickel-molybdenum ($V_F = 220$ neV). Upstream towards the UCN bottle, where there are no polarizing components, the coating is either stainless steel or nickel. Down stream in the experiment where the polarizing components are located, we use Nickel molybdenum, NiMo. NiMo is better at preserving the polarization than stainless steel. NiMo has depolarization probability per bounce of 10^{-5}. Stainless steel has a depolarization probability per bounce of 10^{-3}.

There are several other loss mechanisms for the UCN aside from upscattering as well. There is a possibility of wall losses as UCN are stored or travel in guides. Typically, the wall loss probability is on the order of 10^{-5} per bounce. Ultimately, neutrons can be lost by decay as well. All this is included in simulation.

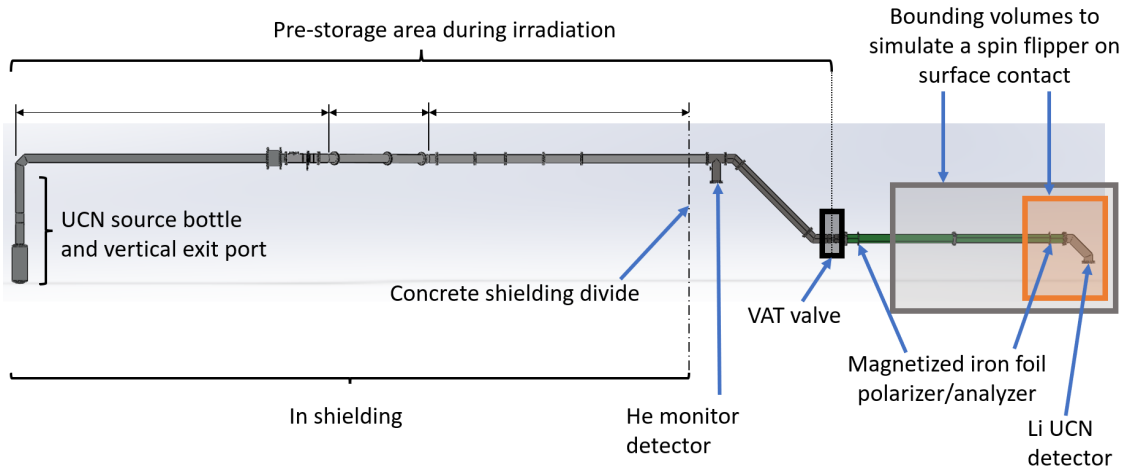

Figure 6.6: Geometry of source and SSA component test experiment in simulation.

The grey and orange rectangles define the regions of the spin flippers in the simple model used for the simulation. The boundary of the box that intersects with the neutron path will undergo a spin flip, according to the material parameters set for the enclosing volume. In this way, we can simulate a simple spin flipper efficiency. What is important is that there is only one surface that UCN will go through. The first surface of the two spin flipper volumes will be representative of spin flipper 1 (SF1). The second will be representative of the second spin flipper.

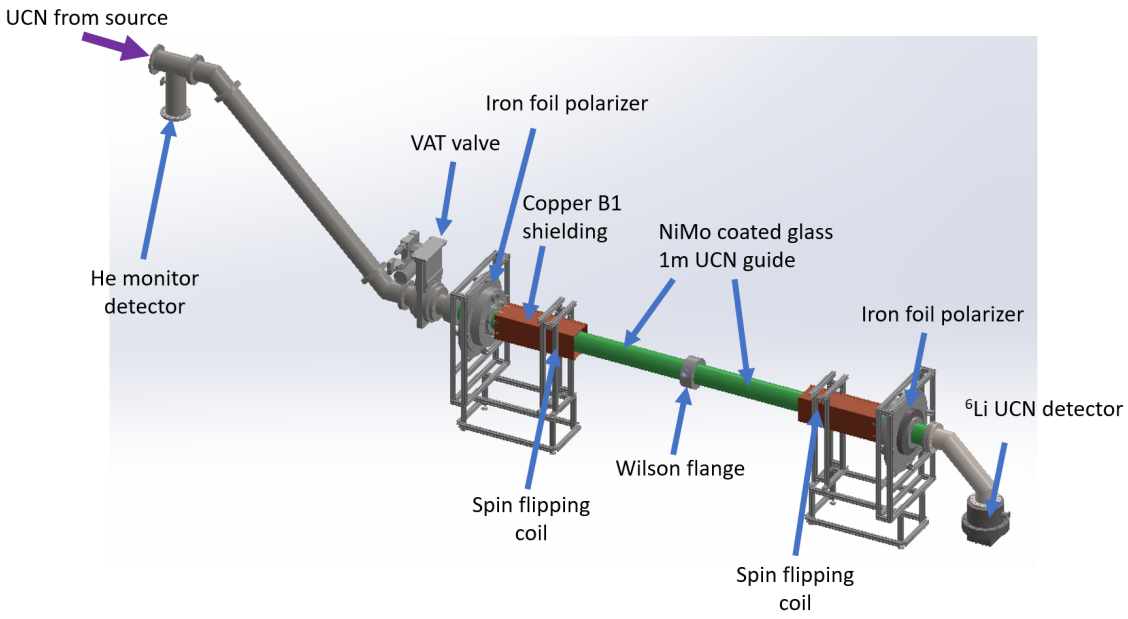

Figure 6.7: The geometry that this simulation follows the polarization experiment of the Fall 2018. The VAT valve is closed for the first 60 s of the experiment and the valve is open for the remainder of the experiment. The green guides are nickel-molybdenum glass coated UCN guides.

The setup of the spin analyzer and spin flippers is shown in Figure 6.7 that is a magnified view of Figure 6.1, of the experiment section. The experiment consists of a valve at the entrance to the components under test, a spin analyzer, followed by two spin flippers, and finally an identical spin analyzer. The analyzer and polarizer at two magnetized iron foils. This experiment setup assumes identical polarizing power of the analyzer and the polarizer analytically as discussed in the text surrounding Equation 6.10, therefore I will use identical properties for parameter sweeps for the magnetized foils in simulation.

The polarization power of the foil can be affected by depolarization in the guides. The effect is small for realistic estimates of depolarization for polarizing preserving materials such and NiMo or NiP, nickel molybdenum and nickel phosphorus respectively. The probability of spin flipping per bounce for NiMo or NiP, less than 10^-5/bounce. Therefore, the main contributing factor will be depolarization in the foil, or due to the spin flippers themselves. We can test the assumption that the depolarization in the foil is the largest effect by changing it in the simulation, and seeing how that

affects the observable. Figure 6.8 illustrates the effect that depolarization in the foil would have on the polarization power as determined in the simulation. Here the compared polarization power observable is determined using Eq. 6.14 and UCNs reaching the detectors, while the polarization power is calculated based on the simulated material properties.

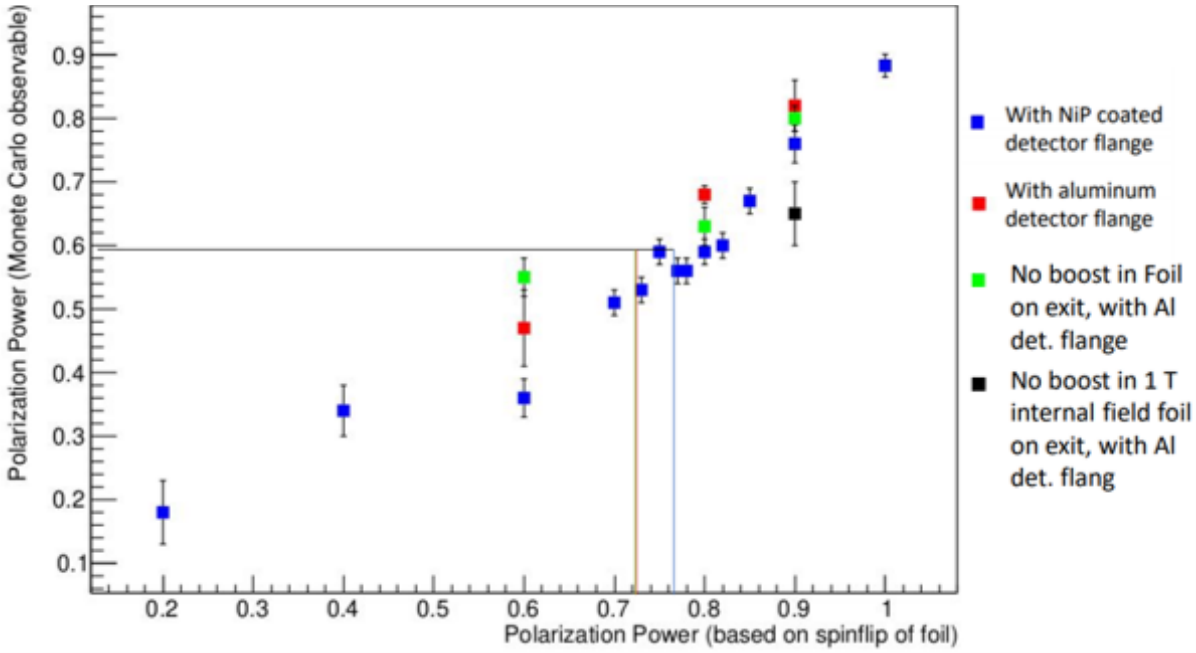

Figure 6.8: Simulated polarization power observable as a function of calculated individual foil depolarization for the analyzer foil experiment in Fig. 6.6.

The error bars in Figure 6.8 are only statistical, simulated from UCN loss per bounce, neutron decays, and other loss channels. The black horizontal line at 0.6 represents the polarization observed in the experimental data. The vertical lines indicate a plausible region of uncertainty in the simulated spin-flip probability that gives us the polarization observed in the data.

6.1.4 Concluding remarks for the analyzer foils and spin flipper characterization

The polarizer, comprised of an iron foil magnetized by a Halbach array, was found to have a polarizing power calculated with Eq. 6.16 and 6.17, of $p_{A7} = 0.64 \pm 0.01$ and $p_{A8} = 0.66 \pm 0.01$.

The spin flipper efficiencies from Eq. 6.18 and 6.19 were found to be $s_1 = 0.977 \pm 0.009$ and $s_2 = 1.007 \pm 0.009$.

Extensive offline analysis revealed that the foil's internal magnetization was likely not saturating. Details of some of the foil measurements are presented in the following Chapter. This could mean that magnetic domains were unaligned, resulting in an overall depolarization as the UCN pass through the foil. Additionally, scans through of the adiabatic fast passage revealed that in some conditions it is possible to have the UCN double spin-flip. This is qualitative, since we don't have a full 3D map along the guide, but do have a map in the plane of the UCN guide. There might exist trajectories in the magnetic field that the UCNs can spin-flip twice.

6.2 Experiment for the superconducting magnet neutron polarization measurement

The experimental setup for the superconducting magnet (SCM) neutron polarization measurement is shown in Fig. 6.9. In this experiment, the polarizer is the SCM, followed by a spin flipper coil, and an analyzer foil. Only two measurements are needed in this case, one with the spin flipper off, and one with the spin flipper on. In both cases the same 60-second beam on period, followed by 120-second measurement period, is used.

In this experiment the spin flippers had to be placed closer to the analyzer foils which required the copper RF coil shielding to be removed and the plastic RF magnetic field generating coil holder was affixed to the glass UCN guide with tape.

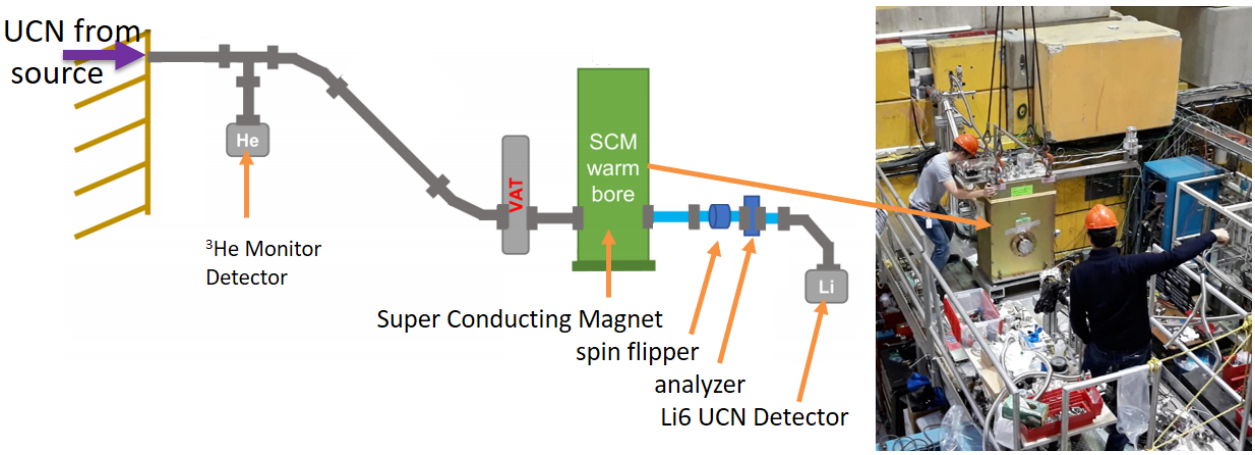

Figure 6.9: The geometry used to perform the super conducting magnet polarizing efficiency measurement, internally labelled as experiment TCN18-070.

To measure the SCM polarization power p_{SCM} we divided out the polarization power of the analyzing foil, 0.64 ± 0.01, measured during the TCN18-180 setup depicted in Fig. 6.1 by the asymmetry of the of this experimental setup.

$$p = \frac{N0 - N1}{N0 + N1} = p_{SCM} \times p_{foil} \tag{6.28}$$

where p is the asymmetry of polarization for the SCM measurement, and p_{SCM} is the polarization power of the SCM, p_{foil} is the polarization power measured in Sec. 6.1.1. Here, $N0$ and $N1$ represent count rate of UCN in the ^{6}Li detector with the spin flipper off $N0$ and with the spin flipper on $N1$. So in this experiment, a 2 cycle repeating pattern is used during data collection.

6.2.1 Data for the superconducting magnet polarizing power measurement

For this experiment, we also are able to change the current being delivered to the SCM. So we did a number of runs of differing SCM current. We did a run for 0 A, 50 A, 100 A, 150 A, 175 A and 200 A. Each run consisted of a minimum of 20 cycles.

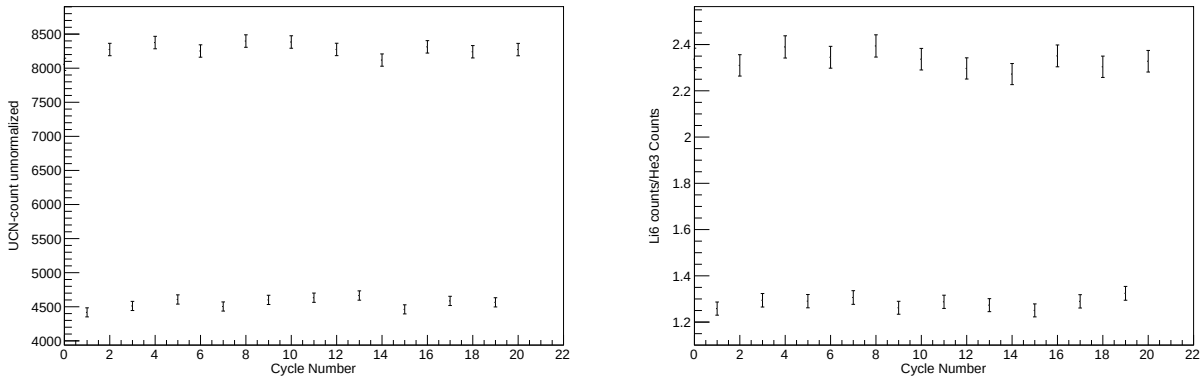

Figure 6.10: Data for a typical SCM polarization run, for SCM current 200 A. Raw UCN counts in ^{6}Li detector (left). Normalized ^{6}Li count rate to the ^{3}He monitor detector during irradiation (right).

All the currents expect 100 A had only their last cycle cut, because of the run being aborted during that cycle.

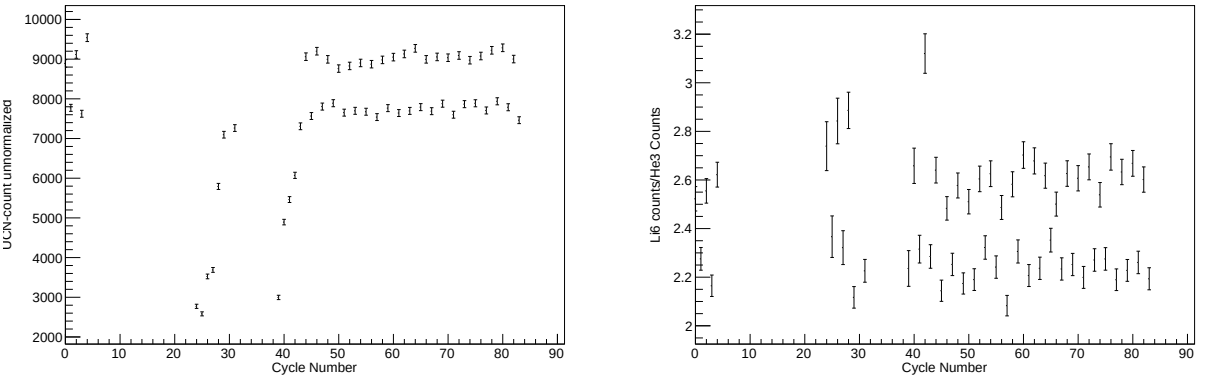

Figure 6.11: Data for 100 A SCM polarization run, which had proton beam instabilities. Raw UCN counts in ^{6}Li detector (left). Normalized ^{6}Li count rate to the ^{3}He monitor detector during irradiation (right).

During the 100 A SCM current test, the proton beam current dropped to zero twice, this lead to a total of 87 cycles. This is to ensure that enough data would be taken even with cuts. There were a total of 28 cycles cut because the beam current was less than $0.1\ \mu A$, and 3 cycles cut as a result of less than 1000 UCN counted in the ^{3}He monitor detector.

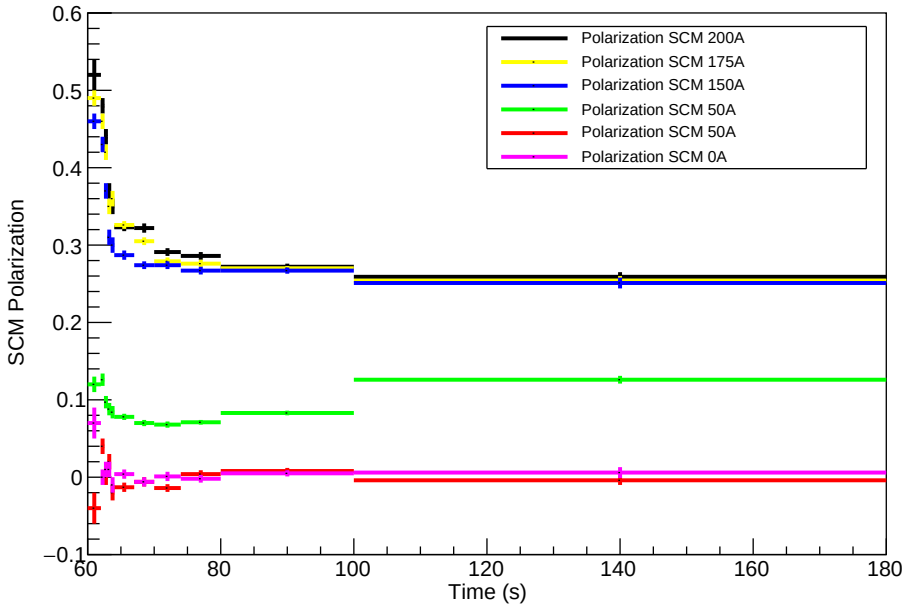

Figure 6.12: Polarization power, p, as a function of time for experiment TCN18-070. Eq. 6.27 was used to calculate p, by dividing out, the polarization of the polarization foil determined from TCN18-180.

In Fig. 6.12 the polarization of the SCM drops in the first few seconds of the valve opening for the currents of 150 A, 175 A and 200 A. Below 150 A the SCM doesn't provide a large enough magnetic field to stop one of the neutron spin states from passing into the experiment (i.e. it doesn't polarize the neutrons).

6.2.2 Calculating the Adiabatic Fast Passage parameter for the SCM guides

During the setup of the super conducting experiment, a coarse magnetic field measurement was made just outside the guide to the top and bottom. This field map, combined with the expected oscillating field of the spin flipper coils, was used to check the adiabatic parameters via equation 5.9.

To illustrate the adiabatic conditions in a graphical way, a plot of the adiabatic parameter k as defined in equation 5.2 as a function along the path length of the guide is made.

$$1 \ll \frac{\omega_{\text{Larmor}} B_0}{dB_0/dt}, \text{ becomes} \tag{6.29}$$

$$1 \ll k. \tag{6.30}$$

Similarly, for the AFP case (spin flipping via an applied oscillating field) the following condition must hold.

$$1 \ll \frac{\gamma B_1^2}{dB_0(t)/dt}, \text{ and} \tag{6.31}$$

$$1 \ll k'. \tag{6.32}$$

The path of the neutron has to be simulated. Magnetic field data was only obtained along the top and the bottom of the UCN guide. The simulation linearly interpolated this coarse magnetic holding field, while calculating the oscillating field from the RF coil via Biot-Savart, and modulating that amplitude with a cosine function. The SCM's field was added as an independent field and was taken from a magnetic simulation outputting a fine magnetic field map.

The UCNs positions were determined by using the time of flight for 8 m/s neutrons. If the adiabatic check holds for this worst-case speed, then it will hold for slower-moving neutrons.

The Bloch equations are a set of macroscopic equations that are used to calculate the time dependent evolution of the ensemble of nuclear magnetization (or average magnetic spin), $\mathbf{M(t)} = (M_x(t), M_y(t), M_z(t))$, in the presence of a time evolving magnetic field that is constant around the z-axis $\mathbf{B}(t) = (B_x(t), B_y(t), B_z)$, noting that $B_z(t) = B_z$ since it is constant;

$$\frac{dM_x(t)}{dt} = \gamma_n(\mathbf{M}(t) \times \mathbf{B(t)})_x - \frac{M_x}{T_2}, \tag{6.33}$$

$$\frac{dM_y(t)}{dt} = \gamma_n(\mathbf{M}(t) \times \mathbf{B(t)})_y - \frac{M_y}{T_2}, \text{ and} \tag{6.34}$$

$$\frac{dM_z(t)}{dt} = \gamma_n(\mathbf{M}(t) \times \mathbf{B(t)})_z - \frac{M_z - S_0}{T_1}. \tag{6.35}$$

Here the spin ensemble has relaxation times T_1 and T_2.

These equations are in the stationary lab frame, and our magnetic field doesn't remain only in

the z-direction. We can make an approximation to help us find a solution when the field is changing direction when the relaxation times T_1 and T_2 are large such that the equations become symmetric:

$$\frac{dS_x(t)}{dt} = \gamma_n(\mathbf{M}(t) \times \mathbf{B(t)})_x, \tag{6.36}$$

$$\frac{dS_y(t)}{dt} = \gamma_n(\mathbf{M}(t) \times \mathbf{B(t)})_y, \text{ and} \tag{6.37}$$

$$\frac{dS_z(t)}{dt} = \gamma_n(\mathbf{M}(t) \times \mathbf{B(t)})_z. \tag{6.38}$$

These equations do not account for depolarization due to wall interactions. They only calculate the misalignment of the ensemble of spins due to the magnetic field. A numerical integrator solves for the average spin vector of the neutron ensemble with small-time steps, updating the spin components that resulted in a changing magnetic field in that small time. The neutron ensemble is following a linear path and are mono energetic.

6.2.3 Simulation of AFP parameters

I simulated the Bloch equations for the magnetic field of the SCM and analyzer foil. This is to see if there are regions that can depolarize the UCNs completely, failing to flip the spin, or if the UCNs can traverse through the region as expected.

I wrote the code and am able to check the adiabatic conditions and calculate the expected spin ensemble direction for a group of neutrons. For a full simulation, the magnetic fields need to be measured, and then the Bloch equations can be solved. This allows for full spin evolution, but is too computationally intensive to be implemented in the full simulation. Only a few paths will be solved, to illustrate a potential problem between the analyzer foil characterization measurement and the polarization power of the SCM. The SCM is a powerful magnet, and therefore can change the magnetic field of the system because its fringe field extends far away. The spin tracking simulation yields spin flips for the few test tracks when the spin flipper is in the default position. When it is offset 20 cm closer to the SCM, still more than 1.5 meters away, the spin flipper fails.

I calculated the adiabatic parameters along the bottom of the guide, in the centre and along the

top of the guide, trying to seek places where depolarization could occur.

For these simulations on the magnetic field, I calculate offsets to the B_1 field compared to the holding field B_0. This is to try and compensate for the fact that there is limited magnetic field data in that region. I am constrained to be in the plane for the holding field. An offset of zero corresponds to the SF coil's default position with the copper shield of the spin flipper coil is bolted directly to the analyzer foil, leaving a 30 cm between the foil and the centre of the SF coil.

In the left panel of Fig. 6.13 the pink line is the adiabatic slow passage condition, k from Equation 6.30, it indicates that the holding field, B_0, satisfies the adiabatic slow passage condition since the value of k is large. The yellow line in the left panel shows that for a small region around the spin flipper, the AFP condition k' from Equation 6.32 holds as well. This means that the spin will follow the B_0 holding field until it reaches the spin flipper oscillating B_1 coil and then will undergo a spin flip at that region, and then follow the B_0 holding field afterwards.

The only other check is that the frequency of oscillating field B_1 field matches the critical Larmor frequency for the total $B = \omega/\gamma_n$ in the region of the spin flipper coil; or to put it simply, if the black line in Fig. 6.13 crosses the cyan midpoint of oscillation in the right panel. In the right panel of Fig. 6.13 the black line represent the magnetic field that is the spin flipper is absolutely tuned to $B_{crit} = \omega/\gamma$. We can see that for this calculation the black line does indeed cross the midpoint of the oscillations, or the total holding field B_0 when the k_{AFP} or k' is large.

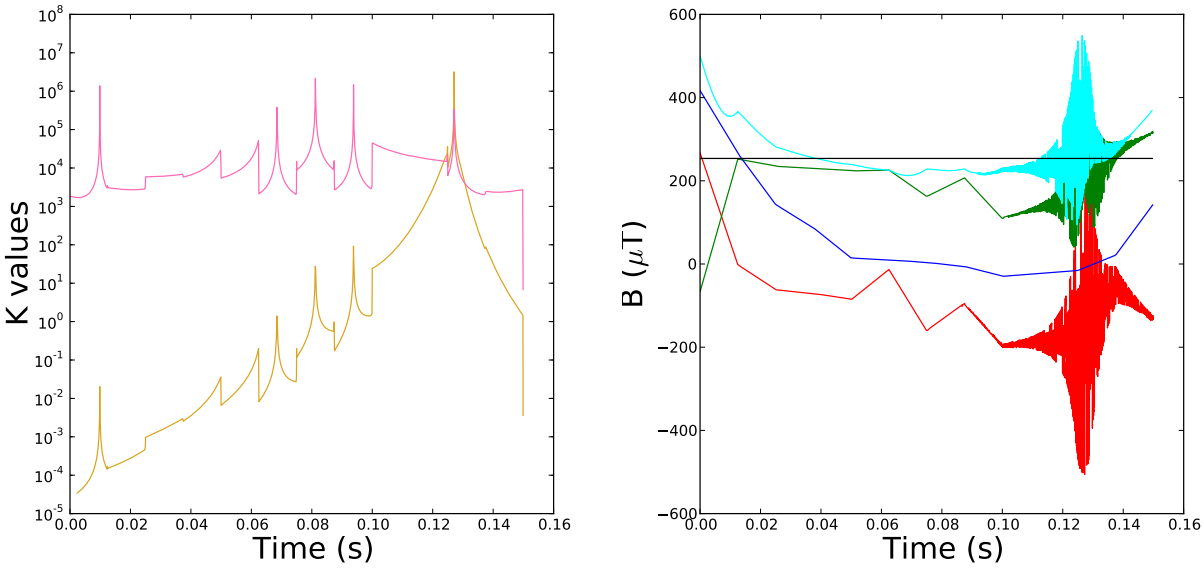

Figure 6.13: Adiabatic conditions check along the bottom of the guide with a straight trajectory. The left panel shows a direct comparison between the adiabatic condition to follow just a holding field k_{ASP} in pink and the AFP condition k_{AFP} in yellow with the oscillating B1 field from (Eq. 5.2 and 5.9. The right show magnetic components of the holding field B0 and B1 coils combined B_{tot} in cyan with its components (red, green, blue) and the critical magnetic field that frequency of the SF coil is set to μT in black.

The magnetic fields satisfy the previous metrics for the adiabatic conditions, both in the holding field and for spin flipping via AFP. We can benchmark these metrics to a Bloch equation solver, which solves the equations of motion for the spin ensemble of UCNs in a specific magnetic environment. The Bloch equations in Eq. 6.36 show the average magnetization (spin) of the ensemble of UCNs. Simulated in Fig 6.14 is the Bloch equation solved with the changing magnetic field. We can compare Fig 6.14 with Fig 6.13 to see if the simple adiabatic parameters are enough to ensure that there is a spin flip. The yellow line in Fig. 6.14 is the cosine of the angle between the static holding field and the average spin magnitude **M**, which is related to the polarization.

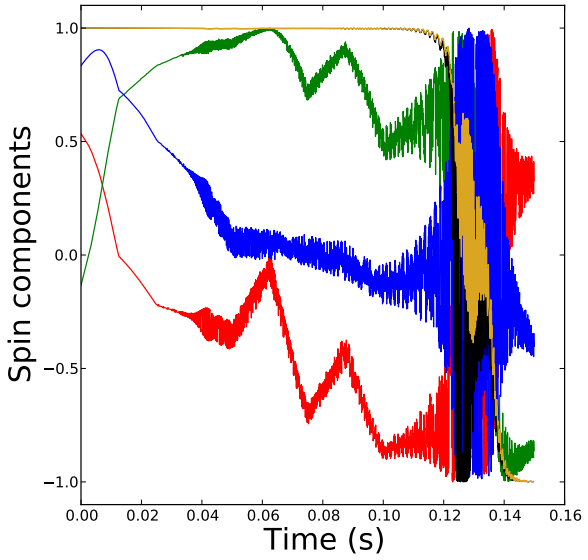

Figure 6.14: Average Spin Components with cosine of the angle between the spin vector to the magnetic field vector long the Y-4 cm straight trajectory with no offset between spin flipper mount and analyzer foil flange. Yellow is the cosine of the angle between $\vec{B}_0$ and $\vec{M}$, black is the cosine of the angle between $\vec{B}_{tot}$, and (red, green, blue) is the spin components of $\vec{M}$

We see that the polarization flips direction relative to the holding field in Fig. 6.14. i.e. in the times between 0.12 s and 0.14 s the average spin, indicated by the yellow line, goes from +1 to pointing in the opposite direction at -1.

6.2.3.1 Along the Bottom of the Guide with B1 offset

Introducing an offset to the spin flipper magnetic field in the direction upstream away from the polarizer is a way of changing the holding field we calculate, as we cannot look at the magnetic field transverse to the direction of the guide.

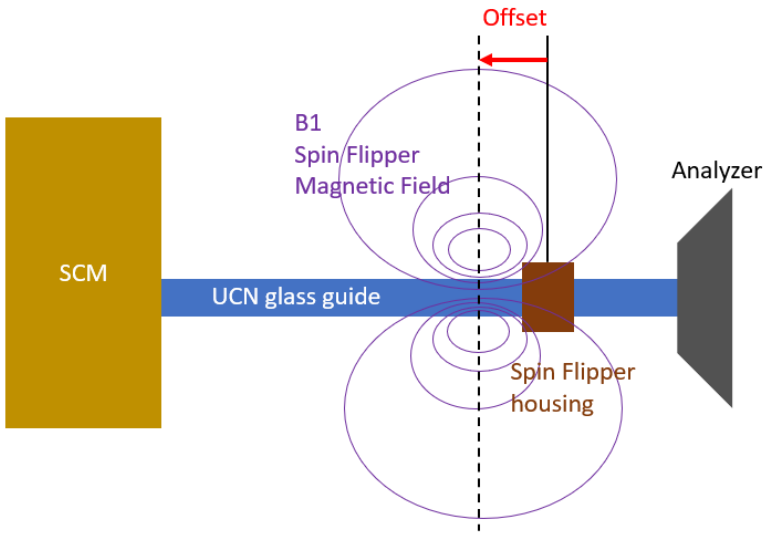

Figure 6.15: A schematic diagram of the experiment, illustrating what direction the B1 magnetic filed offset moves during simulations that include offset.

To ensure spin flipping in the region of interest in the plane central to the B_1 coil, we can move the spin flipper's central location to sample different magnetic character to get a qualitative feel for how sensitive the holding field is to the spin flipping coils location. Figure 6.15 shows the B_1 field moving in simulation by an offset to sample a new holding B_0 field. Note that the field gradients are weaker in this direction than nearer to the analyzer foil, due to its proximity to the Halbach array. Moving transversely nearer to the analyzer has larger effects for the B_0 magnetic field.

Similar to the case with a perfectly aligned UCN guide and magnetic field, Fig. 6.16 shows that the adiabatic parameters are still satisfied along this offset trajectory. The frequency that the spin flipper is tuned to (shown in pink) is close to, but not equal to $B_{tot} = \omega/\gamma$, for the non-oscillating total magnetic field. In the right of figure of Fig 6.16 the holding field, B_0, plus the oscillating field B_1 is shown as the centre of the Black, B_{tot}.

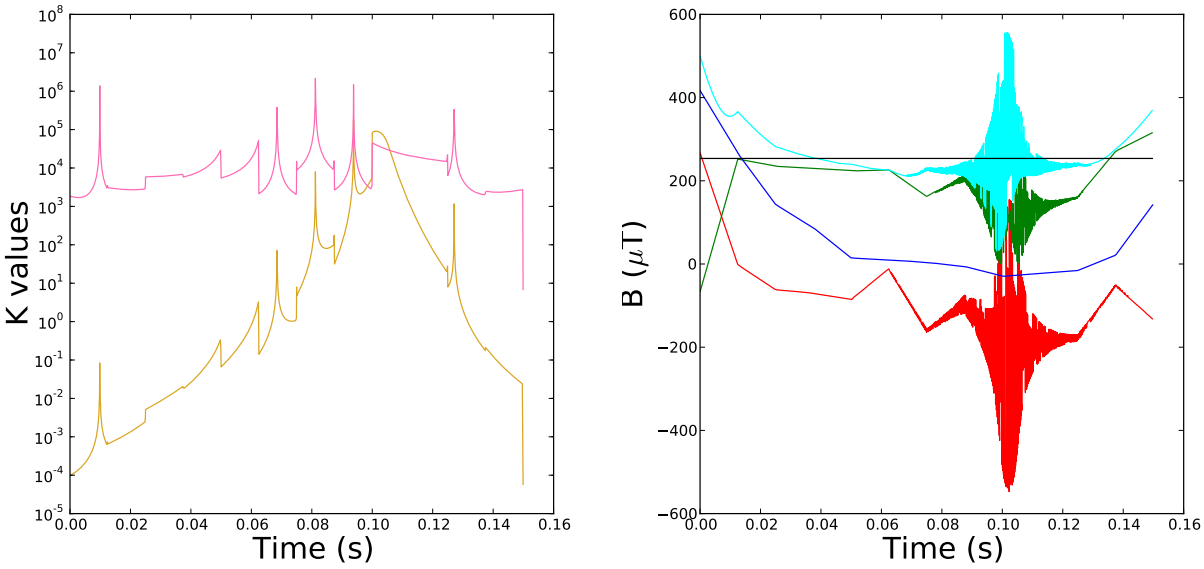

Figure 6.16: Adiabatic conditions check along the bottom of the guide in a straight trajectory with 20 cm offset between spin flipper mount and analyzer foil flange. The left panel shows a direct comparison between the adiabatic condition to follow just a holding field k_{ASP} in pink and the AFP condition k_{AFP} in yellow with the oscillating B1 field from (Eq. 5.2 and 5.9. The right show magnetic components of the holding field B0 and B1 coils combined B_{tot} in cyan with its components (Bx, By, Bz) = (red, green, blue) and the characteristic magnetic field of the frequency, $B = \omega/\gamma_n$, of the oscillating field in black.

The adiabatic conditions check are satisfied in the left panel of Fig 6.16. Both the yellow line k' and the pink line k are sufficiently large to ensure spin flipping according to Equations 6.30 and 6.32.

It is the additional check that fails in this case. The magnetic field that the oscillating B_1 frequency is tuned to, $B = \omega/\gamma_n$ fails to cross the midline of the B_{tot} (shown right in cyan in Fig. 6.16), or fails to cross the holding field B_0.

We can proceed with the calculation of the Bloch equations to see if in simulation the results are different.

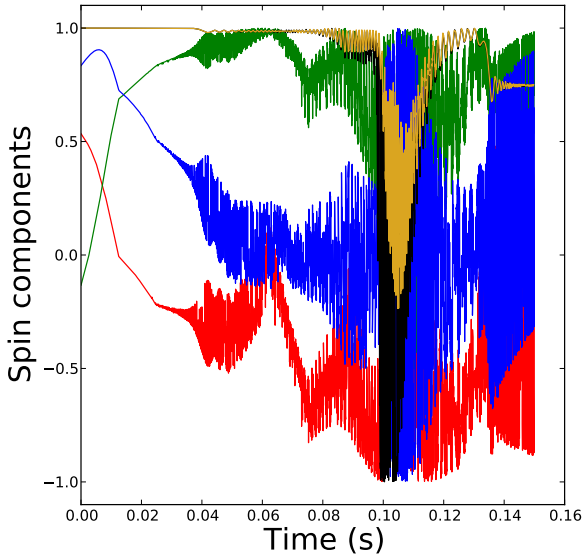

Figure 6.17: Spin Components with cosine of the angle between the spin vector and the magnetic field vector long the Y -4 cm straight trajectory with 20 cm offset between spin flipper mount and analyzer foil flange.

In Fig. 6.17 the cosine of the angle between the average spin vector and the magnetic field (the yellow line) shows the that the sign goes from +1 to 0.75 in the end, failing to flip the spin, slightly depolarizing the magnetization. The angle between the average spin polarization and the magnetic field is 41°.

The polarization doesn't change from 1 to -1 through the simulation for all values, and thus the spin flipper fails to change the polarization. As shown in Table 6.4, the spin flipper succeeds at flipping the spin along the top of the guide when there is an offset, illustrating that depending on the magnetic character of the holding field, the spin flipper can both succeed for some neutron trajectories and fails for others.

Table 6.4: Adiabatic Fast Pass Bloch equations calculator for various straight trajectories.

Region	Offset (cm)	Final Polarization
Top	0	-1.0
Centre	0	-1.0
Bottom	0	-1.0
Top	20	-0.9
Centre	20	-0.25
Bottom	20	0.75

Along the centre trajectory with a 20 cm offset the spin flipping coil depolarizes the neutrons and along the bottom it does not flip the polarization. This lends credibility to the fact that the spin flipper might not work efficiently in this setup where the holding field isn't being controlled. The simulation can both depolarize completely, and fails completely to change the polarization at all, as shown in Figure 6.14 and Figure 6.17 respectively.

6.2.4 Experimental analysis for the SCM polarization experiment

I simulated the super conducting magnetic (SCM) measurement, with a single spin flipping coil and analyzer foil, in PENTrack. The geometry was identical to the SCM polarization characterization discussed in Sec. 6.2. This simulation will test the depolarization in the analyzer foil or near the analyzer foil, as well as attempt to explain the discrepancy of the expected value of polarization by testing the assumption of an efficient spin flipper. This assumption was used before since in this setup characterizing the foil was impossible.

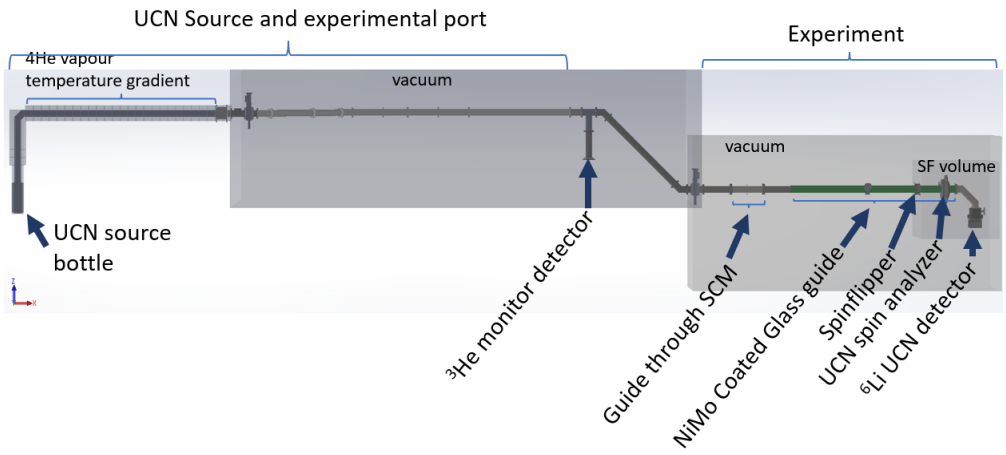

Figure 6.18: Geometry for the source and SCM polarization measurement PENTrack simulation, made in SolidWorks. The geometry includes the UCN source and SCM parts.

The diagram in Fig. 6.18 illustrates the full experimental setup in the simulation, as well as the source volume. The simulation includes a temperature/vacuum gradient of the vapour from the ^{4}He from the UCN source bottle.

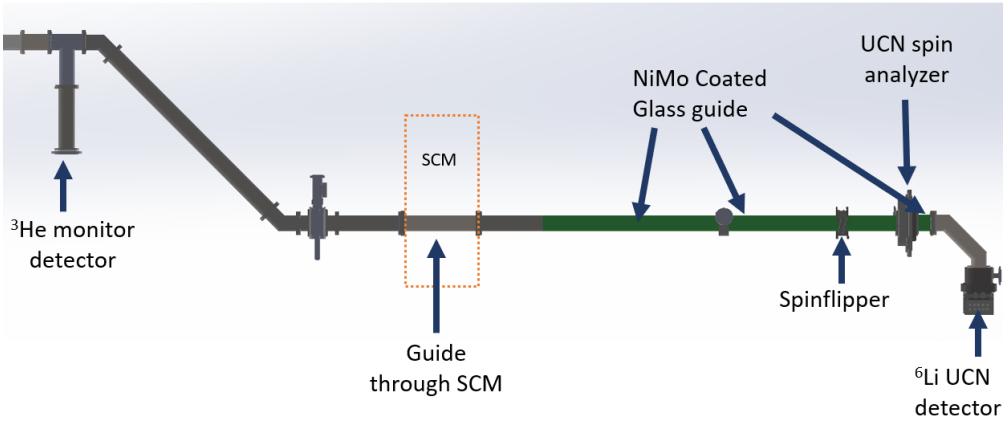

Figure 6.19: Geometry for the SCM polarization measurement PENTrack simulation, made in SolidWorks. Zoomed into the experimental portion.

The diagram in Fig. 6.19 illustrates only the experimental portion, which does not include the UCN production volume and associated guides. This is a simulation of UCN transport and

includes a full magnetic simulation for the SCM for polarization purposes, excluding any spin flipping caused by oscillating magnetic fields. The spin flipper is instead modelled as a surface that has a depolarization per interaction that mimics the spin flipper efficiency, making this a toy model in the respect that it is not a full spin flipping simulation.

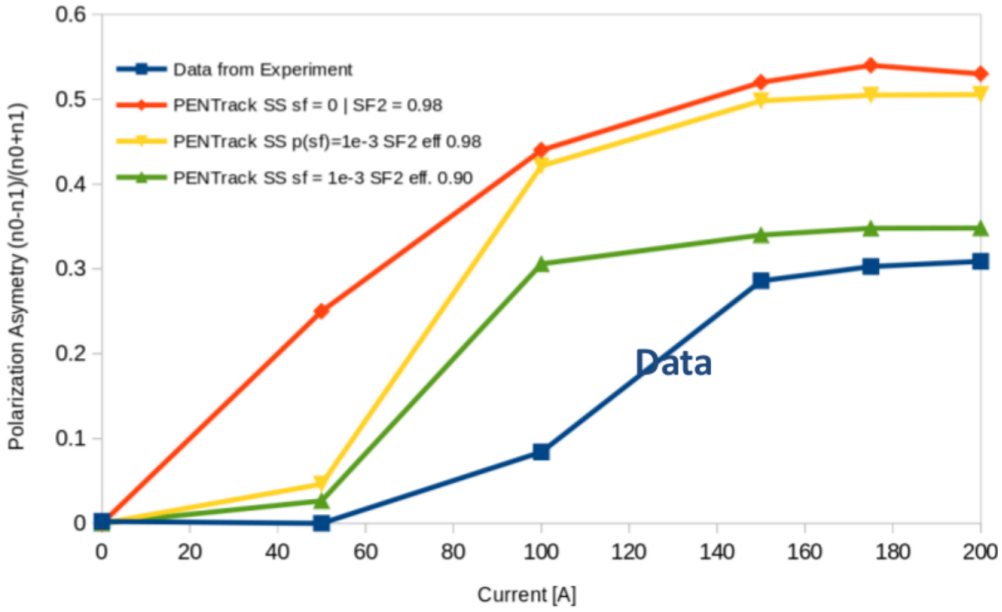

Figure 6.20: Polarization Asymmetry for different current settings for the super conducting magnet polarizer. Showing data from experiment as well as simulated data with various settings.

In Figure 6.20 the current of the superconducting magnet (SCM) was swept from 0 A to 200 A at intervals, to get an idea of the dependence of polarizing ability for different SCM magnetic fields. Simulating the data was done with in PENTrack again. A parameter sweep was conducted to try and explain the discrepancy of the expected value of polarizing power of the SCM expected to be near 1, with the data. The sweep of reasonable stainless steel probability of spin flipping parameters was taken from 0 to 10^{-3}. This probability of spin flipping affects the low current polarizing asymmetry the most. A sweep of the spin flipper 2 (SF2) efficiency was conducted in simulation, and it suggests that a value of 0.90 for the spin flipper efficiency of the SF coil combined with a spin flip per bounce of $10^{-}3$ the stainless steel SCM guide can explain the high

depolarization seen in this experiment. There are low current discrepancies between simulation and experimental data, but the number of neutrons were too low for a proper tuning of the spin flipper. It is therefore a strong possibility that during the low current SF was tuned much lower than a 90% efficiency and therefore the data not aligning with the simulation for low current has minimal impact on the validity of the simulation.

6.2.5 Concluding remarks for the SCM measurement

The polarizing power of the Super Conducting Magnet (SCM) was measured to be around $p_{\text{SCM}} = 55 \pm 2\%$, much lower than the expected near 100%. This discrepancy could be due to magnetic interference of the SCM on the holding field gradient of the spin flipping coil. Additionally, it could be due to increased wall collisions and a relatively high spin-flip per bounce on the internal guide of the SCM.

I suggest more UCN be counted during tuning of the SF coils and during the run, to get a more precise measurement. Furthermore I suggest (if space allows) that two spin flippers be used after the SCM, to allow for a characterization of the SF during the run.

These experiment suggest that more careful control of the gradient magnetic field in the spin-flipper is necessary in the future. For the SCM, a stronger polarizing field, and less depolarizing guide materials are needed to fully polarize the UCNs.

6.3 Conclusion

To conclude, the polarization power measured for the spin analyzers was 0.650 ± 0.003 and 0.630 ± 0.003 with the polarizer foils having a spin flipping efficiency of 0.977 ± 0.008 and 1.007 ± 0.008, assuming symmetric polarizers and spin flippers. In simulation, this measured asymmetry reflects a simulated polarizing power of 0.78 ± 0.08.

The polarization power measured for the SCM was 0.55 ± 0.02 with the assumption that polarizer foils polarization power is 0.64 and the spin flippers have a spin flipping efficiency of 0.99. In simulation, this measured asymmetry reflects a simulated polarizing power of the SCM of nearly 0.86 (if the inner bore was coated with polarizing preserving coating) if the spin flipper efficiency

was 0.90, which can qualitatively be explained by the fringe of the analyzer increasing its gradient in the spin flipper region with the presence of the SCM. Additionally, there was no polarizing preserving coating in the SCM inner bore, leading to large depolarization for low currents.

7. Measurements of analyzer foil magnetization

There are several potential causes for the depolarization observed in the characterization of the SSA components experiment. The reason we suspect the foil for causing the majority of the UCN depolarization in the experiment is two-fold. The measurements of the spin flipping efficiency yielded nearly 100 percent efficiency, $(97.7 \pm 0.8)\%$ and $(100.7 \pm 0.8)\%$, which leads us to believe the main effect is due to the analyzer foil not being fully magnetized. This means the foil let in the wrong spin state or depolarized spins into the opposite spin state as UCN travelled through the iron foil. The polarized domains of the iron the foil were not aligned to the magnetic field outside the foil which can cause a large depolarization [72].

The principle of operation of the polarizer foils is discussed in chapter 6. The foil consists of a thin aluminum foil coated with a layer of iron. Figure 7.1 shows the foil in its mounting ring. The magnetization can be directly measured by measuring the field outside the foil in a magnetic shield. To characterize the internal magnetization, Fabian Piermaier and I took measurements of the magnetic field using a fluxgate above the foil. He analyzed the results in his Bachelor thesis, where he fit the results to the model of a magnetized cylinder in free space [73].

Figure 7.1 shows an aluminum foil covered with iron. It is in an aluminum ring that can be mounted inside the spin analyzer magnet array with non-magnetic brass screws. There is a piece of tape indicating the direction of the polarizing magnetic field, to indicate direction, that will be kept consistent throughout the measuring. The measurement is conducted in along a straight line and the magnetization of the foil can have miss alignment for this direction so a parameter, ϕ is used to denote the angle of miss alignment.

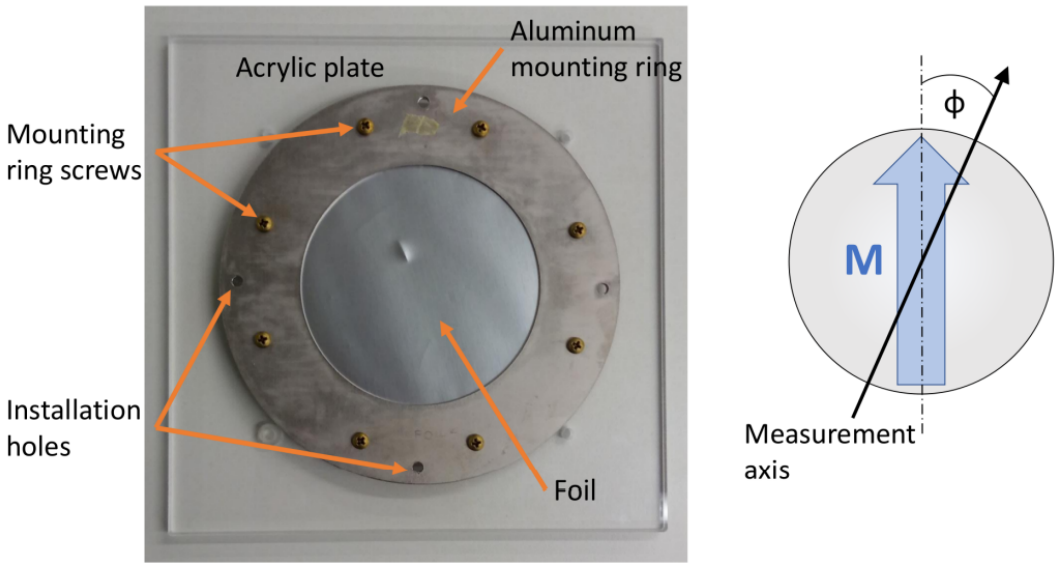

Figure 7.1: An aluminum foil coated with iron, shown in its mounting ring (left). It lies on an acrylic plate ready to measure the magnetization, M. The magnetization can be offset by an angle Φ, shown right [73].

The measurement was taken along the line between the installation holes, which may differ from the angle of magnetization Φ. The analytical solution of a homogeneously magnetized cylinder was used as a model [74]. The full analytical solution that was fit can be found in Appendix C.

The analytical solution of a magnetized cylinder was used to predict what the magnetic flux density is outside the cylinder, which in turn determines its total internal magnetization, M [73]. Figure 7.2 shows the analytical solution for the magnetic flux density of a foil measured 3 cm above of a homogeneously magnetized cylinder.

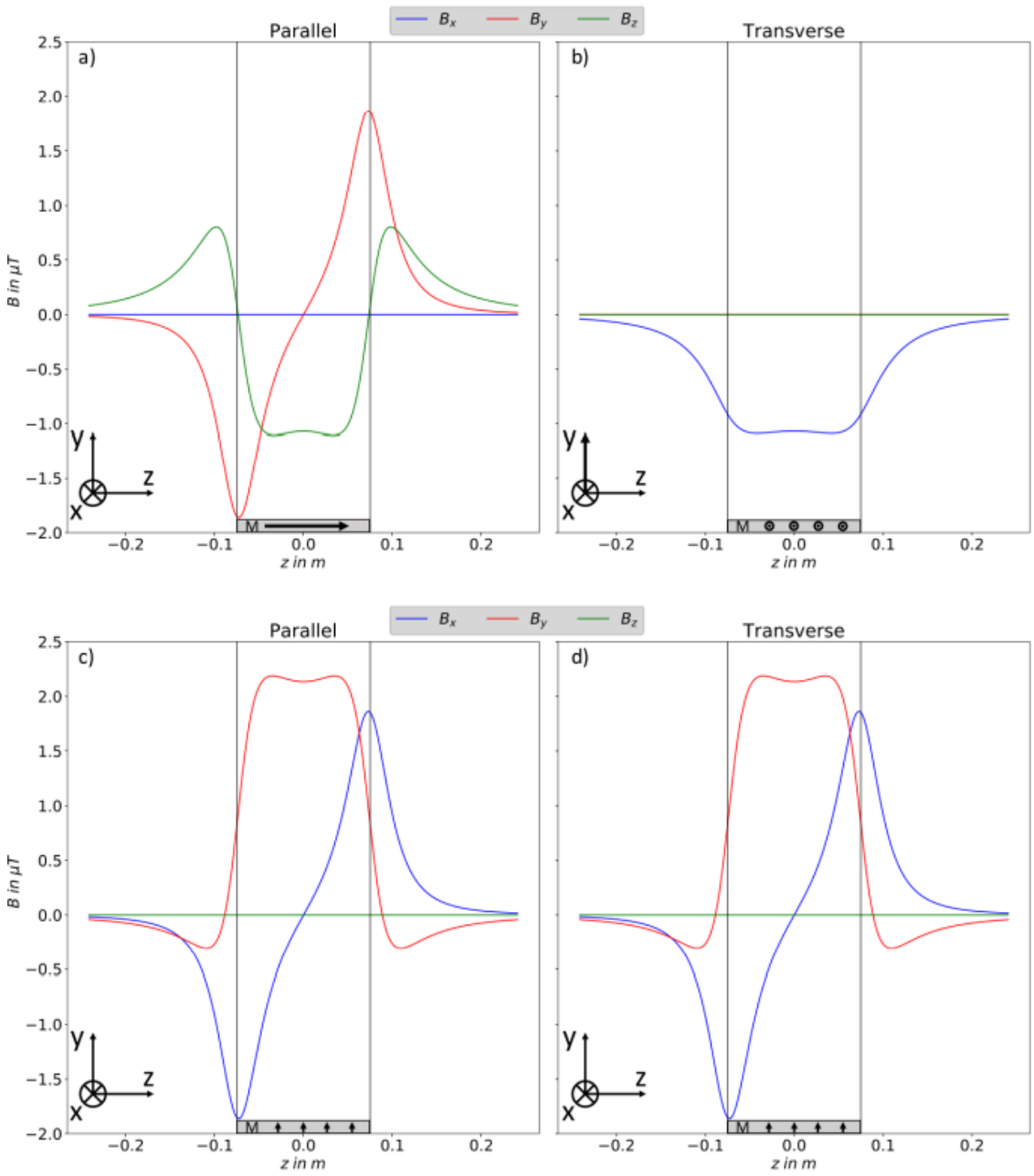

Figure 7.2: Magnetic flux solution to the homogeneously magnetized cylinder used to fit the data. Graphs show the solution for the magnetic field above the foil for a uniformly magnetized foil with the direction of magnetization shown in a rectangle subset below each plot. a) and b) shows the magnetization perpendicular to the cylindrical axis. c) and d) shows magnetization along the direction of the cylindrical axis. [73]

To characterize the internal magnetization, we measured the external flux along a line to compare to the analytic solution of a uniformly magnetized cylinder. Figure 7.3 shows a schematic

diagram of the experiment. In order to accomplish this measurement a low ambient magnetic field is needed. To accomplish this we used a long mu-metal shield to suppress the ambient magnetic field in the room. A fluxgate was attached to an aluminum track that it could smoothly slide along. The apparatus took measurements at regular intervals along the linear guide.

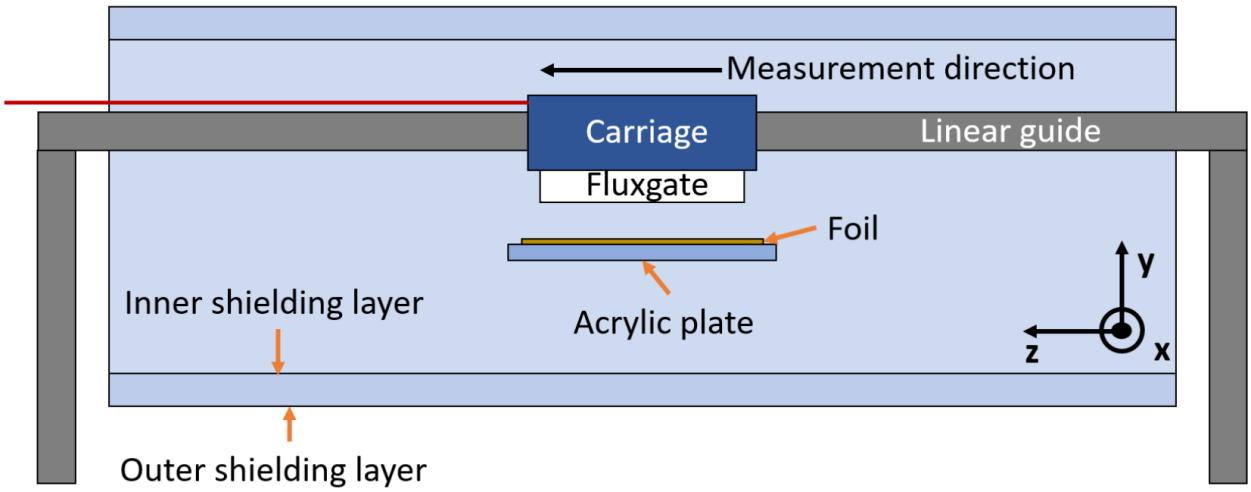

Figure 7.3: Foil magnetization measurement schematic [73]. The foil was placed in the center of a cylindrical mu-metal shield on an acrylic plate 29 $\pm$ 1 mm below the center of the 3 axis fluxgate. The fluxgate is attached to a carriage that is pulled along a linear guide by an external rope.

The raw data was a series of points that needed to be processed. The fluxgate records magnetic flux density in the x, y and z directions. Figure 7.4 shows measurement data for foil 1, one of the foils in the 2018 UCN run. Even with just the raw data, a few points can be made. One is that it is not a uniformly magnetized cylinder in the transverse direction only, as evidence by the off axis components of the B_y and B_z. This means that the magnetization direction is different from the direction of the magnetic array in the analyzer foil.

Figure 7.4 shows two distinct measurements of the same foil. One measurement is with the suspected magnetization inline with the measurement line (left) and the other where the magnetization direction is transverse to the measurement direction. The origin here is defined in terms of

the fluxgate coordinates at the start of the mu-metal shield. Therefore, the measurement direction is along the $-x$ axis.

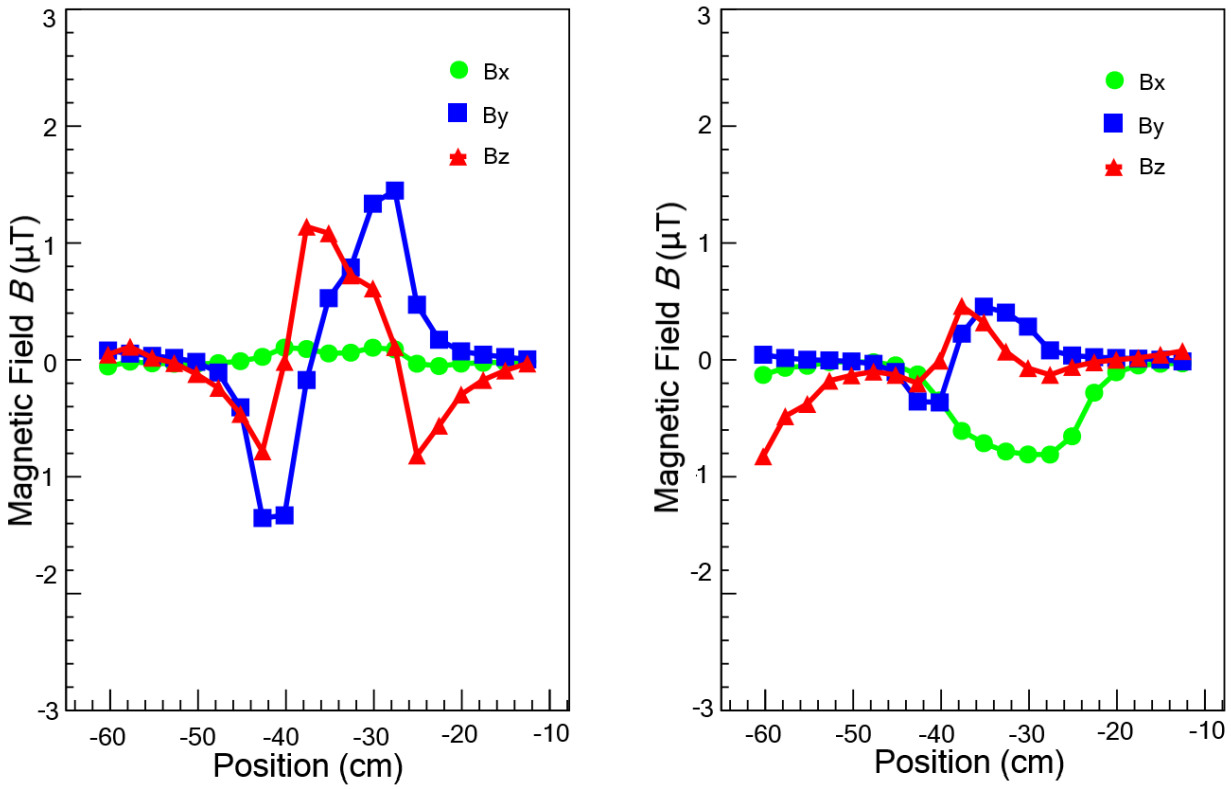

Figure 7.4: Magnetization of FOIL1 directly out of POL1 during the 2018 TUCAN UCN fall run, as measured by a fluxgate 28 mm above the foil center. The left graph shows the magnetization vector of the foil when the position is moving along the direction of magnetization. The right graph shows the case when the magnetization is perpendicular to the measurement position axis.

Piermaier conducted the analysis of the raw data to characterize the internal magnetization and fit the uniformly magnetized cylinder to the output with parameters of rotational offset [73]. Figure 7.5 shows the measurement of foil 4 as points being fit to the model of the uniformly magnetized cylindrical disk as the dashed lines.

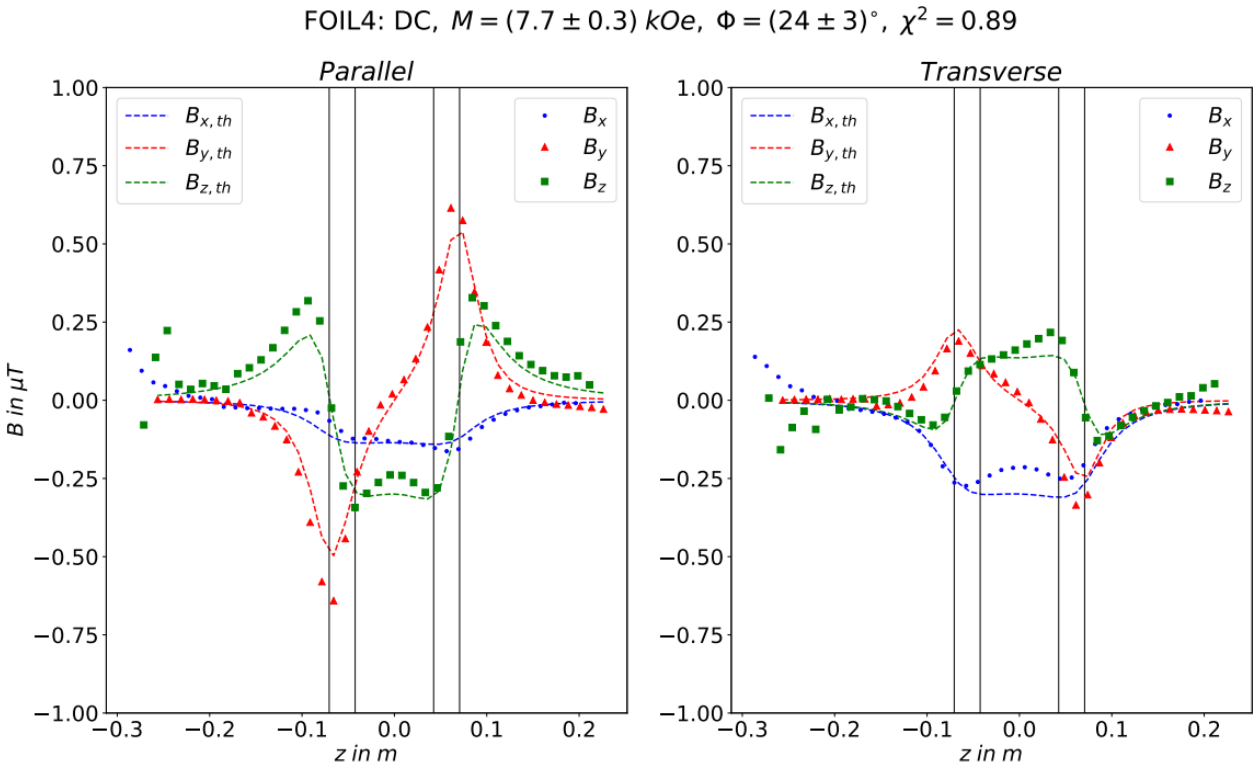

Figure 7.5: The results of the fit of Foil 4 [73]. The dots represent the measurements and the fit of the analytical solution of a uniformly magnetized cylinder is the dashed lines

A summary of the results can be found in Table 7.1. Foils 1 and 2 were inside the Halback array during the Fall 2018 bream time, and were in the polarizer foil holders during the tests.

All foils are composed of a 25 um aluminum foil on which a pure iron layer is deposited. A 150 nm iron layer was deposited on the Movatec foils and a 400 nm iron layer was deposited on the LeBow foils. The diameter of the polarizer foil is 141.40 mm in its final holder and the ring used for the sputtering is 162.00 mm diameter.

We wanted to compare the foils we used (LeBow) to new foils that were ordered (Movatec).

Table 7.1: Results of the foil magnetization measurements, from Fabian Piermaier [73]. AF stands for ambient field of the experimental hall.

Foil Number	Manufacturer	Test	M [kOe]	ρ [°]	χ^2
4	Movatec	DC	7.7 ± 0.3	24 ± 3	0.89
4	Movatec	173 A	9.2 ± 0.4	-7 ± 3	1.4
3	Movatec	100 A	9.2 ± 0.3	-19 ± 2	1.08
6	LeBow	DC	6.0 ± 0.4	2 ± 4	13.33
1	LeBow	POL1, 2018	7.1 ± 0.4	-3 ± 4	5.28
2	LeBow	POL2, 2018	10.7 ± 0.4	-2 ± 3	15.4
6	LeBow	100 A	8.6 ± 0.3	4 ± 3	7.44
6	LeBow	-100 A	8.7 ± 0.3	0 ± 3	8.55
1	LeBow	100 A	8.7 ± 0.3	2 ± 3	8.4
2	LeBow	100 A	11.2 ± 0.4	-1 ± 2	9.14
5	LeBow	Before AF	6.3 ± 0.4	5 ± 4	6.4
5	LeBow	After AF	6.0 ± 0.3	1 ± 3	3.41

In Table 7.1, AF in test the test column refers to the ambient magnetic field in the Meson Hall at TRIUMF. The test refers to what we did prior to measuring the field above the foil. Here, DC refers to the initial condition from the manufacturer. It is seen that direct from the manufacturer the magnetization has the greatest rotation misalignment between the expected foil magnetization and the measured. It is interesting to note that both foil 1 and foil 2 magnetization M increased when put in a large magnetic coil signifying that each foil was not completely magnetized during operation as a polarizing foil.

One of the Movatec foils, foil 3 or foil 4, was put in a 20 Gauss coil at the University of Winnipeg during an attempt to measure the flux captured during magnetization, in a sort of magnetization measurement.

One of the original LeBow foils, either foil 1 or foil 2 was placed into one of the polarizers and taken out before being shipped to make sure the foil holder would fit into the polarizer. It was then later placed back into one of the polarizers with the direction of magnetization not being tracked.

Foil 1 and foil 2 were only placed into the polarizer a day before being moved onto the platform. There was therefore only a day to a day-and-a-half time in the polarizer before being tested.

7.1 Concluding remarks

In order to explain the high depolarization, we measured the magnetic field around the foil and compared it to the analytical magnetic field of a cylindrical magnetization. To further study the effects of the foils on UCN polarization measurement a stronger magnetic Halbach array was built, that was never tested due to an unforeseen shutdown of the Fall 2019 UCN source at TRIUMF. There is a known relationship between the depolarization and the angle by which the internal magnetization mismatches the external field [72].

$$p = \frac{n_+ - n_-}{n_+ + n_-} \approx \cos(\theta) \tag{7.1}$$

Here p is the polarizing power of the foil, n_+ is the fraction of neutrons leaving the foil without the spins flipping due to depolarization, n_- is the fraction of neutrons whose spins flip due to depolarization, and θ is the angle between the internal and external magnetic fields. To explain our polarization of $p_{A7} = 0.64 \pm 0.01$ and $p_{A8} = 0.66 \pm 0.01$. 0.60 ± 0.03 the difference would have to be 50° and 48°. This angle value in nearly is greater than a 45° rotation. At first this number appears too large and the relationship between the misalignment of the internal magnetic field to the external holding field can not explain the depolarization of the UCN, but perhaps it can explain a significant portion. On the scale of the magnetic domains, the depolarization effect could be even worse than the average, and could explain the misalignment of the polarization. Using the value of polarization of 0.78 read off the graph in Fig. 6.8 from the simulated polarization power corresponding to the observable $p_{A7} = 0.64 \pm 0.01$ the misalignment would be 39° rotation.

8. Conclusions

The research presented in this thesis contributes to a future nEDM experiment at TRIUMF (the TUCAN nEDM experiment). The experimental goal of the TUCAN nEDM experiment is to measure the nEDM with a $10^{-27} e \cdot$ cm

The current nEDM experiments are statistically limited due to the relatively small samples of UCN that can be produced. To improve the statistics, our new source provides improved cooling power. To create a large number of UCNs higher power must be provided to the UCN cryostat, that has to be kept at $\sim$1 K.

Additional to the large number of UCN, we want to efficiently determine the spin state of the UCNs with minimal losses to the number of UCNs after the nEDM measurement. In this thesis a modular set of spin manipulation and analysis components were designed and tested with UCNs at TRIUMF.

8.1 Conclusion of He-II temperature measurements

We discussed UCN production in superfluid helium. The UCN upscattering rate in the He-II is proportional to T^7, where T is the temperature. Superfluid helium has a strong temperature dependence, and therefore correctly modelling the heat response of cryostats for superfluid helium is important.

The vertical UCN source had a serious limitation to its cooling power. The heat had to be conducted through tiny holes and slits to a large area heat exchanger. This design fails at higher heat loads because the conduction enters a region where the thermal conduction term is proportional to q^3, where q is this heat flux. This regime of heat conduction, known as the Gorter-Mellink regime, arises due to quantum turbulence in the He-II. By using a time-dependent 1D model involving Gorter-Mellink heat conduction, I was able to understand quantitatively the temperature rises in the He-II observed in the vertical source, and their previously unexplained timescales, where the temperature is observed to rise and fall over hundreds of seconds. The only fit parameters in

the model are the channel dimensions and the background heat load. These were found to have reasonable values based on the known typical sizes of the holes and slits. This information gives confidence that the Gorter-Mellink model is relevant to this kind of spallation-driven UCN source, where a large amount of heat is deposited into the He-II. By benchmarking the model of heat flow to the data we can rely on calculations to demonstrate that the new source can withstand the power input necessary to attain the new UCN requirement.

8.1.1 Future Work

Based in part on these results, the future UCN source upgrade at TRIUMF will not use the same heat exchanger strategy. A large-area heat exchanger will still be used, but it will not be hidden from the UCN by tiny holes and slits. Instead, the heat exchanger will have a tubular design (see Fig. 8.1).

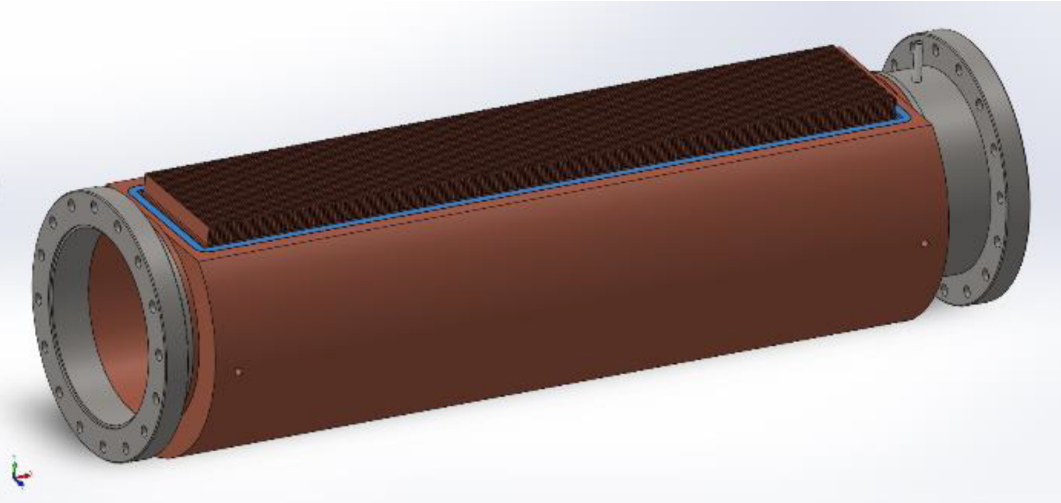

Figure 8.1: Design of heat exchanger (HEX1) for the new horizontal UCN source [75]. HEX1 will be machined from Cu, and will be coated in the inner surface with Ni plating, for UCN compatibility. He-II contained within the central volume will exchange heat through the Cu heat exchanger with colder ^{3}He which will be in contact with the fins seen on the upper surface. Figure courtesy of the TUCAN collaboration.

UCN will pass through the tube, and will be contained by the inner surface, which will be the

same surface as that used for heat exchange. The inner surface is 15 cm in diameter and 60 cm long, to give enough surface area for heat to exchange. On the top exterior surface, fins will still be used for contact with ^{3}He. The ^{3}He side will be in a nucleate boiling regime to promote efficient heat transfer with minimal temperature rise. In this way, it is estimated that the He-II within the heat exchanger will be maintained at a temperature of 1.0 K. Gorter-Mellink heat conduction will limit the heat flow from the UCN production volume to the heat exchanger, which will now be through a long horizontal channel of He-II, 15 cm in diameter and 3 m long (see Fig. 8.2). The temperature at the far end, in the UCN production volume, is expected to be 1.1 K, for the design heat load of 10 W. Time-dependent simulations of the temperature rise, which are based on the same equations used in my simulation, have been conducted, and predict a much faster time dependence because of the larger channel dimensions used [76].

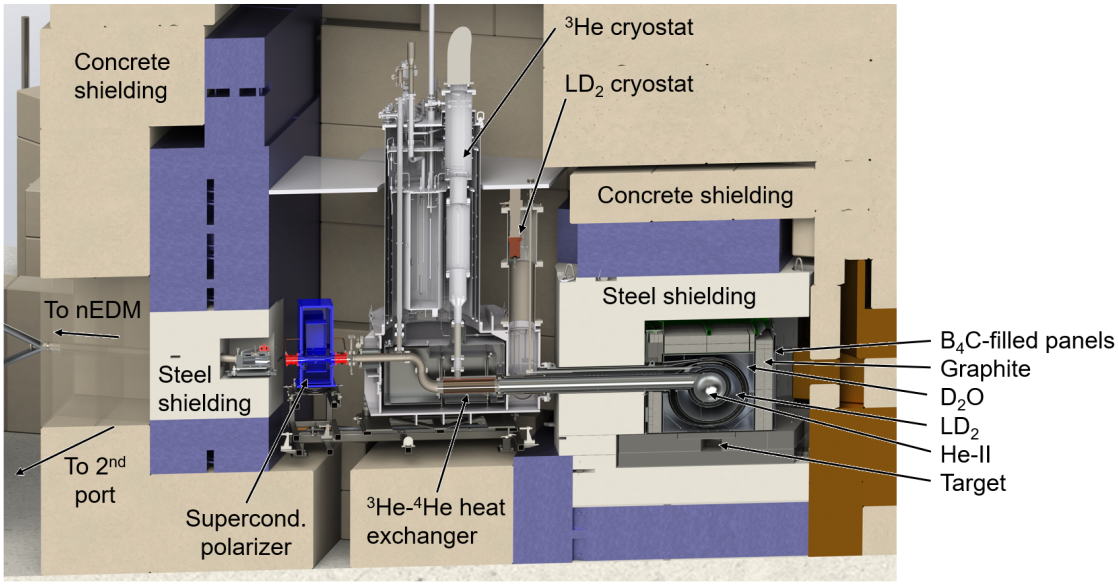

Figure 8.2: The horizontal UCN source upgrade for the TUCAN experiment [77] Heat deposited in the He-II production volume is transported through a long horizontal column of He-II to the ^{3}He-^{4}He heat exchanger. Further detail of the heat exchanger may be found in Fig. 8.1. Figure courtesy of the TUCAN collaboration.

One of the highest priority measurements that will be done with the new He-II cryostat system

and tail section is a measurement of the temperature distribution in the He-II using temperature sensors distributed along the UCN guide (cite S. Vanbergen). The time-dependence of the sensors will also be a very interesting cross-check of the Gorter-Mellink prediction.

8.2 Conclusion on the polarization measurements

This thesis reports some of the first measurements done at TRIUMF involving polarized UCN. By conducting measurements with polarizing foils and spin flippers, I was able to show that the polarizing foils did not seem to provide a large polarization of UCN. The measured adiabatic fast-passage spin flipper had a spin flipping efficiency of 0.977 ± 0.008 and 1.007 ± 0.008, and the spin-analyzer had a polarizing power of 0.650 ± 0.003 and 0.630 ± 0.003. The simulations of the analyzer show that the single pass polarizing power of the foil is 0.78 ± 0.08, whereas other groups had achieved around $(89.7 \pm 4.3)\%$ for single pass polarization power[67]. Under the assumption of no transmission of the wrong spin state through the SCM, the polarizing power of the SCM was measured as 0.57 ± 0.05. This led to many offline tests of the foils including VSM measurements and scans over the foils with fluxgate magnetometers. Both measurement techniques seemed to indicate that the foils might not be fully saturated in the field generated by the permanent magnets used in the experiment. My results also indicate that bad magnetic field distributions in the neighbourhood of the spin flippers could have led to an apparent poor polarization when used with the superconducting magnet. The results clearly indicate that the UCN guiding field in the region of the spin flippers must be designed very carefully with one crossing of the resonance condition occurring in the spin flipper region. Otherwise, multiple spin flips can be induced which could worsen the polarization.

8.2.1 Future work

These experiments have led to a large push among the TUCAN collaboration to produce and understand polarizing foils. Our Japanese collaborators (T. Higuchi et al.) have begun collaborating with a group at the Kyoto University Institute for Integrated Radiation and Nuclear Science (KURNS), developing in-house coating capabilities for producing iron films on aluminum and sil-

icon substrates. The techniques I developed (VSM, fluxgate scans, and UCN measurements) are now being used by the same group. Experiments using the new foils have recently been conducted using the Doppler shifter UCN source at J-PARC, and show promising results [34]. The development of guiding fields and spin flippers is being done by a group at TRIUMF, and will build on the results presented in my thesis. Another idea for future work is that the spin-flipper states being switched in the SSA after a time, in a similar manner as the sequential spin analysis, which could improve the statistical precision of the nEDM experiment. It could increase the number of counts, since wrong-state neutrons that go into an arm of the SSA are less likely to be counted in the correct arm. As long as the visibility α would be maintained, switching the SSA to count these unfortunate neutrons would give a statistical improvement. It would follow a similar method as the sequential switch in a single arm, but for both arms of the SSA.

REFERENCES

[1] J. Martin, B. Franke, K. Hatanaka, et al. The TRIUMF UltraCold Advanced Neutron Source. *Nuclear Physics News*, 31(2):19–22, 2021.

[2] S. Afach, G. Ban, G. Bison, et al. A device for simultaneous spin analysis of ultracold neutrons. *Eur. Phys. J. A*, 51(11), 2015.

[3] M. Pospelov and A. Ritz. Electric dipole moments as probes of new physics. *Annals of Physics*, 318(1), 2005.

[4] V. Cirigliano, E. Mereghetti, and P. Stoffer. Non-perturbative renormalization scheme for the c p -odd three-gluon operator. *J. High Energ. Phys*, 94, 2020.

[5] D. Andreev, D. G. Ang, D. DeMille, and others (ACME Collaboration). ACME Collaboration. Improved limit on the electric dipole moment of the electron. *Nature*, 562, 2018.

[6] A. Crivellin and F. Saturnino. Correlating tauonic B decays with the neutron electric dipole moment via scalar leptoquark. *Phys. Rev. D*, 100, 2019.

[7] W. Dekens, J. de Vries, M. Jung, and K.K. Vos. The phenomenology of electic dipole moments in models of scalar leptoquarks. *J. High Energ. Phys.*, 69, 2019.

[8] V. Cirigliano, A. Crivellin, W. Dekens, et al. CP Violation in Higgs-Gauge Interactions: From Tabletop Experiments to the LHC. *Phys. Rev. Lett.*, 123, 2019.

[9] R. Gupta, B.Y. Bhattacharya, V. Cirigliano, et al. Flavor diagonal tensor charges of the nucleon from $(2 + 1 + 1)$-flavor lattice QCD. *Phys. Rev. D.*, 98, 2018.

[10] Kaori Fuyuto, Xiao-Gang He, Gang Li, and Michael Ramsey-Musolf. cp-violating dark photon interaction. *Phys. Rev. D*, 101, 2020.

[11] Nicole F. Bell, Tyler Corbett, Michael Nee, and Michael J. Ramsey-Musolf. Electric dipole moments from postsphaleron baryogenesis. *Phys. Rev. D*, 99, 2019.

[12] Y. Mimura, R. Mohapatra, and M. Severson. Grand unified parity solution to the strong CP problem. *Phys. Rev. D.*, 99, 2019.

[13] Marcela Carena, Da Liu, Jia Liu, Nausheen R. Shah, Carlos E. M. Wagner, and Xiao-Ping Wang. ν solution to the strong cp problem. *Phys. Rev. D*, 100, 2019.

[14] D. Morrissey and M. Ramsey-Musolf. Electroweak baryogenesis. *New J. Phys.*, 14, 2012.

[15] A. Sakharov. Violation of cp invariance, c asymmetry and baryon asymmetry of the universe. *JETP Letters (USSR)*, 5, 1967.

[16] R. L. Workman et al. Review of Particle Physics. *PTEP*, 2022:083C01, 2022.

[17] R. Golub, D. Richardson, and S. K. Lamoreaux. *Ultra-Cold Neutrons*. Taylor Francis Group, LLC, 1991.

[18] Norman F. Ramsey. A molecular beam resonance method with separated oscillating fields. *Phys. Rev.*, 78, 1950.

[19] P. Harris. The neutron edm experiment. *Phys. Rev. Lett.*, 0709, 2007.

[20] V. Hélaine. *Mesure du moment dipolaire électrique du neutron: analyse simultanée du spin et analyse préliminaire du données*. PhD thesis, Université de Caen Basse-Normandie, 2014.

[21] C. Abel, S. Afach, N. J. Ayres, et al. Measurement of the permanent electric dipole moment of the neutron. *Phys. Rev. Lett.*, 124(8), 2020.

[22] nEDM Mat. PSI. The history of neutron edm limits including the latest best result published 2020 by the nedm collaboration at psi. 2021.

[23] T. Chupp. The Los Alamos neutron elctric dipole moment experiment. Presented at the nEDM2021 conference online session (talk), 2021.

[24] W. Korsch. Overview of the nEDM@SNS Project. Presented at the nEDM2021 conference online session (talk), 2021.

[25] H. Filter. PanEDM status and overview. Presented at the nEDM2021 conference online session (talk), 2021.

[26] D. Wurm, D. Beck, T. Chupp, et al. The PanEDM neutron electric dipole moment experiment at the ILL. *EPJ Web of Conferences*, 219:512, 2019.

[27] S. Degenkolb. Updates on the PenEDM experiment and future outlook. Presented at ETCstar (talk), 2022.

[28] V. Bondar. Design of the n2EDM experiment at PSI. Presented at the nEDM2021 conference online session (talk), 2021.

[29] N. J. Ayres, G. Ban, Bienstman, et al. The design of the n2EDM experiment. *Eur. Phsy. J. C*, 81, 2021.

[30] Jacob Thorren. The neutron BeamEDM experiment. Presented at the nEDM2021 conference online session (talk), 2021.

[31] E. Chanel, Z. Hodge, D. Ries, et al. The pulsed neutron beam EDM experiment. *EPJ Web Conferences*, 219, 2019.

[32] Florian M. Piegsa. New concept for a neutron electric dipole moment search using a pulsed beam. *Phys. Rev. C*, 88, 2013.

[33] A. Serebrov. Source of UCN using superfluid helium at the PIK reactor of pnpi nrc ki: Physics of fundamental interactions with neutrons and neutrinos, at pik reactor. Presented at the nEDM2021 conference online session (talk), 2021.

[34] T. Higuchi. Prospects towards a neutron EDM measurment with an advanced ultracold neutron source at TRIUMF. Presented at the nEDM2021 conference online session (talk), 2021.

[35] C. Abel, N. Ayres, Ban G., et al. nedm experiment at psi: Data-taking strategy and senstivity of the dataset. *EPJ Web of Conferences*, 219:02001, 2019.

[36] C. L. Morris, J. M. Anaya, and T. J. others Bowles. Solid deuterium surface degradation at ultracold neutron sources. *Eur. Phys. J. A*, 54, 2018.

[37] A. Anghel, T. L. Bailey, G. Bison, et al. Measurements of ultracold-neutron lifetimes in solid deuterium. *Phys. Rev. Lett.*, 89:272501, 2002.

[38] E. Korobkina, R. Golub, Wehring B. W., and Young A. R. Production of ucn by downscattering in superfluid he^4. *Physics Letters A*, 301(5), 2002.

[39] T. Higuchi. Prospects for a neutron edm measurement with an advanced ultracold neutron source at triumf, 2021.

[40] K. K. H. Leung, S. Ivanov, F. M. Piegsa, et al. Ultracold-neutron production and up-scattering in superfluid helium between 1.1 k and 2.4 k. *Phys. Rev. C*, 93, 2016.

[41] S. Ahmed, E Altiere, T. Anadalib, and others (including S. Hansen-Romu). First ultracold neutrons produced at TRIUMF. *Physics Review C*, 99:025503, 2019.

[42] S. Imajo, K. Mishima, M. Kitaguchi, et al. Pulsed ultra-cold neutron production using a Doppler shifter at J-PARC. *Progress of Theoretical and Experimental Physics*, 2016.

[43] A. Steyerl, H. Nagel, F.-X. Schreiber, et al. A new source of cold and ultracold neutrons. *Physics Letters A*, 116(7), 1986.

[44] ILL PF2 Ultracold neutron facility. Instrument layout, 2022.

[45] B. Lauss and B. Blau. UCN, the ultracold neutron source – neutrons for particle physics. *SciPost Phys. Proc.*, 2021.

[46] David Wurm, Douglas Beck, Tim Chupp, et al. The panedm neutron electric dipole moment experiment at the ill. *EPJ Web of Conferences*, 219:02006, 2019.

[47] D. Wong. Ultra cold neutrons transport for the Neutron Electric Dipole Moment Search at Los Alamos National Laboratory. Presented at the nEDM2021 conference online session (talk), 2021.

[48] J. Kahlenberg, D. Ries, K. U. Ross, et al. Upgrage of the ultracold neutron source at the pulsed reactor TRIGA Mainz. *Eur. Phys. J. A*, 53(226), 2017.

[49] I. Rienäcker. The PSI ultracold neutron source: UCN production and extreaction from the solid dueterium moderator. Presented at the nEDM2021 conference online session (talk), 2021.

[50] Y. Masuda, T. Kitagaki, K. Hatanaka, et al. Spallation ultracold-neutron production in superfluid helium. *Phys. Rev. Lett.*, 89, 2002.

[51] S. Ahmed, T. Andalib, M.J. Barnes (including Sean Hansen-Romu), et al. A beamline for fundamental neutron physics at triumf. *Nuclear Instruments and Methods in Physics Research Section A: Accelerators, Spectrometers, Detectors and Associated Equipment*, 927:101–108, 2019.

[52] S. Ahmed, E. Altiere, T. (including Sean Hansen-Romu) Andalib, et al. Fast-switching magnet serving a spallation-driven ultracold neutron source. *Phys. Rev. Accel. Beams*, 22:102401, 2019.

[53] R. Matsumiya. Study of he-ii spallation ucn source. *Osaka University*, 2013.

[54] R. Florian. Heat conductivity in superfluid helium and ultracold neutron source cryogenics. Master's thesis, University of Coburg, Germany, 2018.

[55] W. Schreyer. Towards tucan's search for the neutron electric dipole moment. *Talk presented at CIPANP2018*, 10 2018.

[56] Mpfiz. Own work. published under creative commons 1.0 universal, 2011.

[57] Steven W. Van Sciver. *Helium cryogenics; 2nd ed.* International cryogenics monograph series. Springer, New York, NY, 2012.

[58] D. Osborne. Determination of the velocity of propagation of the second sound in he ii. *J. Phys. (USSR)*, 10, 1946.

[59] D. Osborne. The rotation of liquid helium ii. *Proc. Phys. Soc.*, A63, 1950.

[60] E. J. Yarmchuk and R. E. Packard. Photographic studies of quantized vortex lines. *J. Low Temp. Phys.*, 46, 1982.

[61] J. R. Clement, J. K. Logan, and J. Gaffney. Liquid helium vapor pressure equation. *Phys. Rev.*, 100, 1955.

[62] J. Martin. Time-dependent heat flow in he-ii, 2019.

[63] R. Matsumiya. "private communication".

[64] Dassault Systems. Opera.

[65] COMSOL. Comsol multiphysics ac/dc module.

[66] Hiroaki Akatsuka, Takashi Higuchi, Sean Hansen-Romu, et al. Study of Thin Iron Films for Polarization Analysis of Ultracold Neutrons. In *24th International Symposium on Spin Physics*, 7 2022.

[67] S. Afach, G. Ban, G. Bison, et al. A device for simultaneous spin analysis of ultracold neutrons. *The European Physical Journal A*, 51, 2015.

[68] S. Ahmed, T. Andalib, M.J. (including Sean Hansen-Romu) Barnes, et al. A beamline for fundamental neutron physics at triumf. *Nucl. Instr. and Meth. Phys. Res. A*, 927, 2019.

[69] A. Serebrov, A. Aldushchenkov, M. Lasakov, et al. New method for precise determination of neutron beam polarization. *Nuclear Instruments and Methods in Physics Research Section A: Accelerators, Spectrometers, Detectors and Associated Equipment*, 357(2), 1995.

[70] W. Schreyer. *Magnets, polarizers, systematics, and optimizations of the neutron-lifetime experiment PENeLOPE*. PhD thesis, Technischen Universität München, 2016.

[71] W. Schreyer. Pentrack - a simulation tool for ultracold neutrons, protons and electrons. https://github.com/wschreyer/PENTrack/tree/polarizers, 2019.

[72] V. K. Ignatovich. Depolarization of ultracold neutrons in refraction and reflection by magnetic-film surfaces. *Pis'ma Zh. Eksp. Teor. Fiz*, 28, 1978.

[73] Fabian Piermaier. Measurement of the magnetic background field and characterization of spin analyzer foil for the neutron electric dipole moment experiment at triumf. Master's thesis, Coburg University of Applied Sciences, Germany, 2020.

[74] A. Caciagli, R. Baars, A. Philipse, and B. Kuipers. Exact expression for the magnetic field of a finite cylinder with arbitrary uniform magnetization. *J. Magn. Magn. Mater.*, 456, 2018.

[75] S. Kawasaki. Hex1 design update, 2022.

[76] S. Stargardter. Time-dependent thermal modeling for the TUCAN source. Presented at the CAP2021 conference (talk), 2021.

[77] W. Schreyer and Tucan Collaboration Team. *The TRIUMF UltraCold Advanced Neutron source*, volume 2021 of *APS Meeting Abstracts*. 2021.

APPENDIX A

TEMPERATURE HEAT STUDIES

A.1 Fits with Independent Parameters

Figures A.1-A.4 are heat response plots for He-II bottle temperature over time fit to Eq. 4.3 with independent parameters.

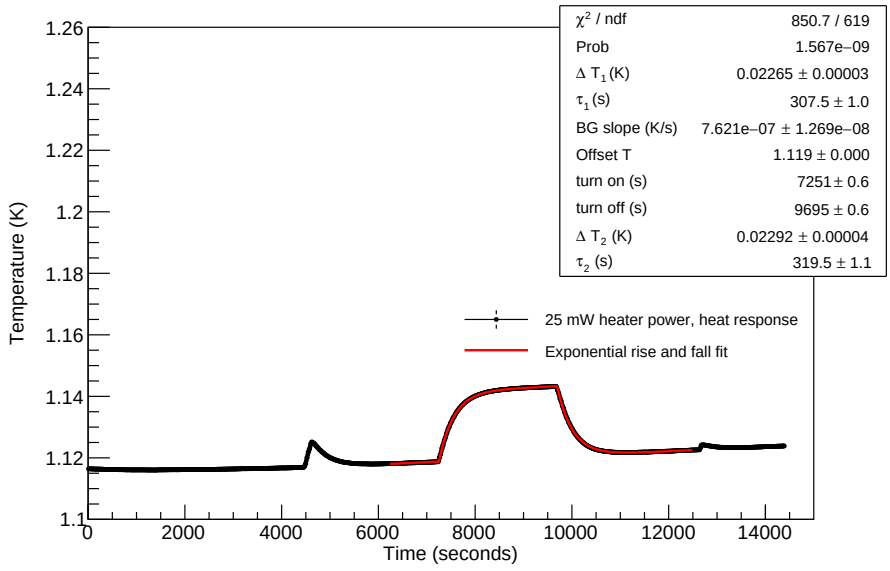

Figure A.1: PG9L derived Temperature versus time graph for a heater power of 25 mW fit with a piece-wise function defined in Eq. 4.3, a rising and falling exponetial.

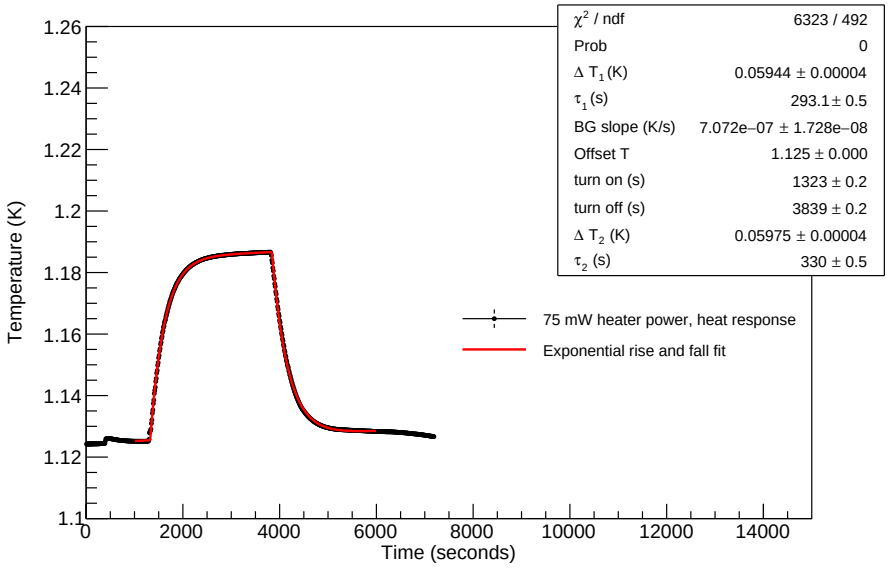

Figure A.2: PG9L derived Temperature versus time graph for a heater power of 75 mW fit with a piece-wise function defined in Eq. 4.3, a rising and falling exponetial.

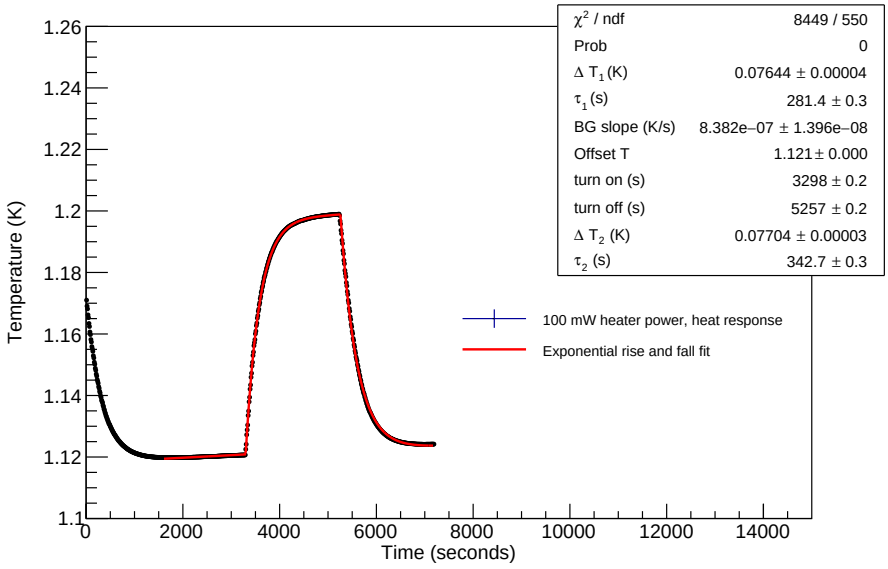

Figure A.3: PG9L derived Temperature versus time graph for a heater power of 100 mW fit with a piece-wise function defined in Eq. 4.3, a rising and falling exponential.

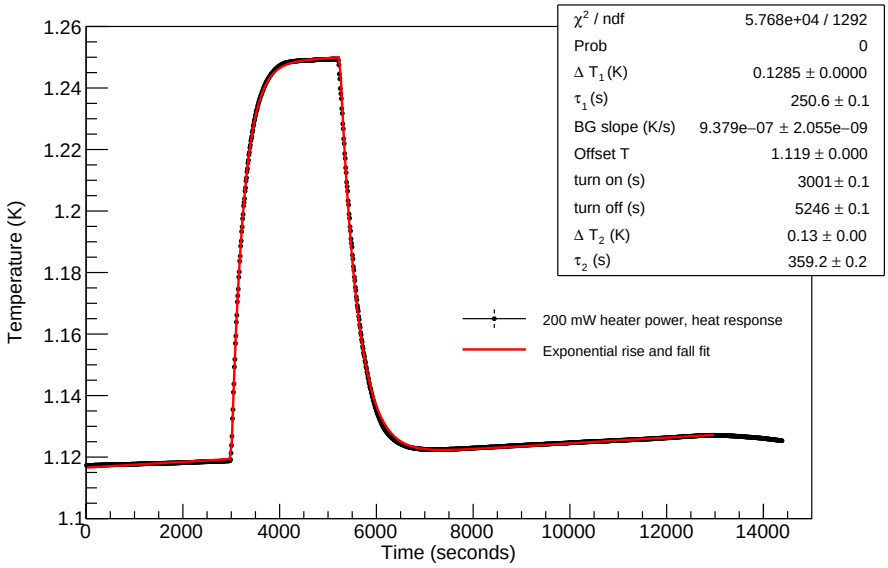

Figure A.4: PG9L derived Temperature versus time graph for a heater power of 200 mW fit with a piece-wise function defined in Eq. 4.3, a rising and falling exponetial.

A.2 Falling Edge Fit

Figures A.5-A.10 are heat response plots for He-II bottle temperature over time fit to Eq. 4.5 with independent parameters. This fits a falling exponential in time with a sloped background to temperature.

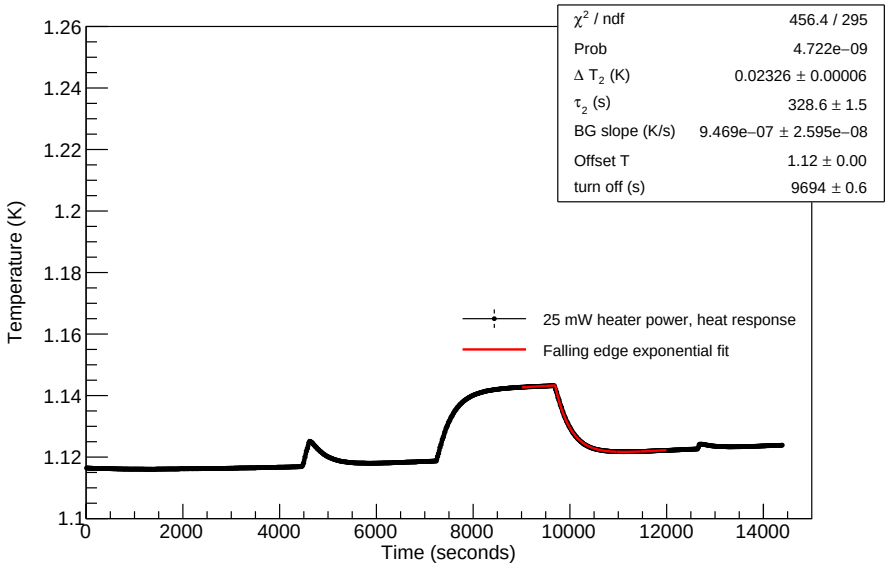

Figure A.5: PG9L derived Temperature versus time graph for a heater power of 25 mW fit with a piece-wise function defined in Eq. 4.5, a falling exponential only.

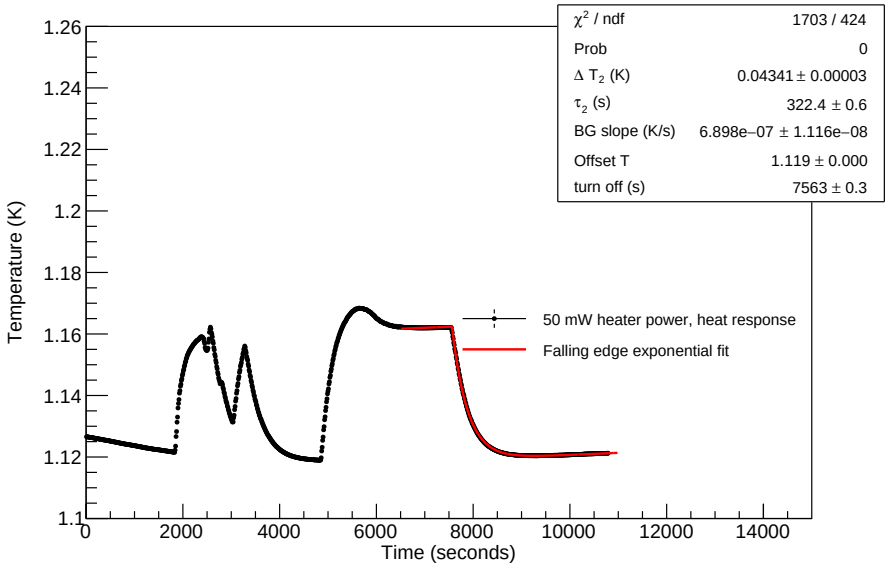

Figure A.6: PG9L derived Temperature versus time graph for a heater power of 50 mW fit with a piece-wise function defined in Eq. 4.5, a falling exponential only.

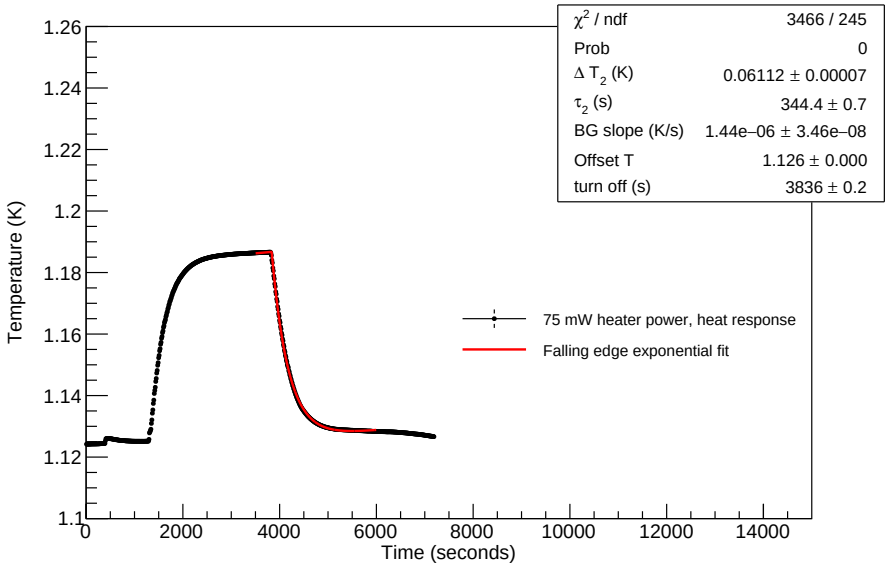

Figure A.7: PG9L derived Temperature versus time graph for a heater power of 75 mW fit with a piece-wise function defined in Eq. 4.5, a falling exponential only.

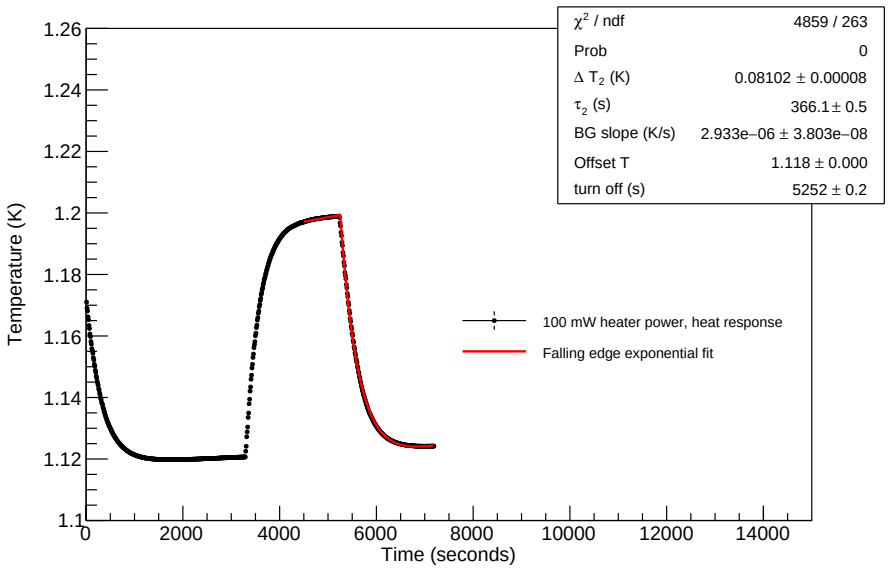

Figure A.8: PG9L derived Temperature versus time graph for a heater power of 100 mW fit with a piece-wise function defined in Eq. 4.5, a falling exponential only.

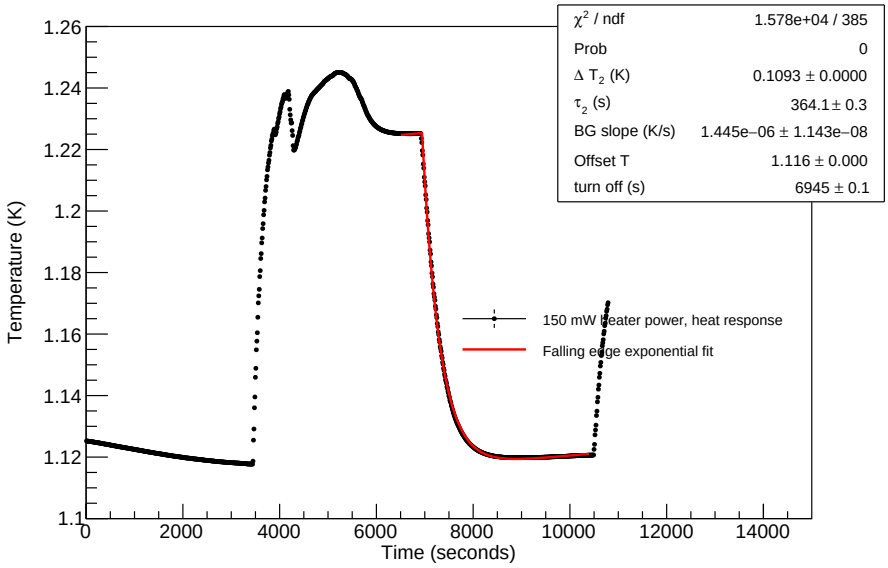

Figure A.9: PG9L derived Temperature versus time graph for a heater power of 150 mW fit with a piece-wise function defined in Eq. 4.5, a falling exponential only.

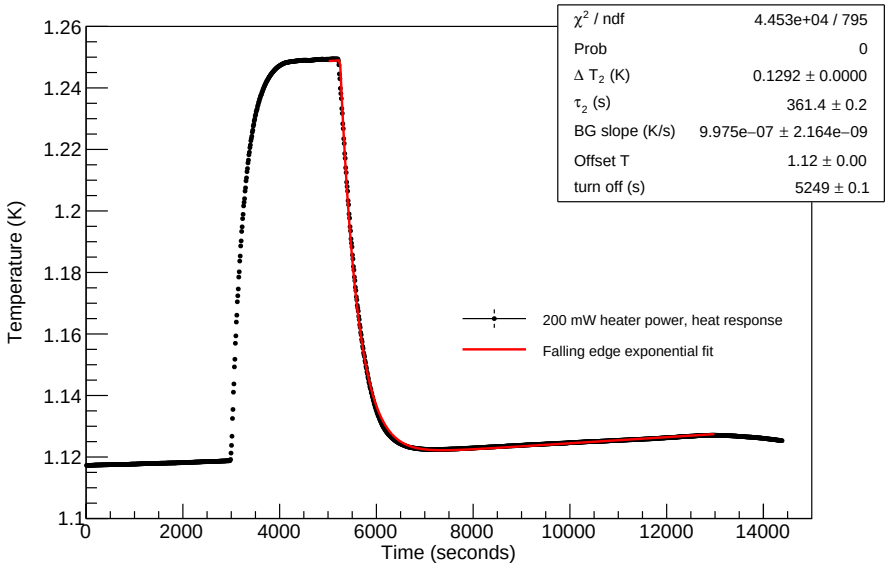

Figure A.10: PG9L derived Temperature versus time graph for a heater power of 200 mW fit with a piece-wise function defined in Eq. 4.5, a falling exponential only.

A.3 Rising Edge Fit

Figures A.11-A.14 are heat response plots for He-II bottle temperature over time fit to Eq. 4.6. This fits a rising exponential in time with a sloped background to temperature.

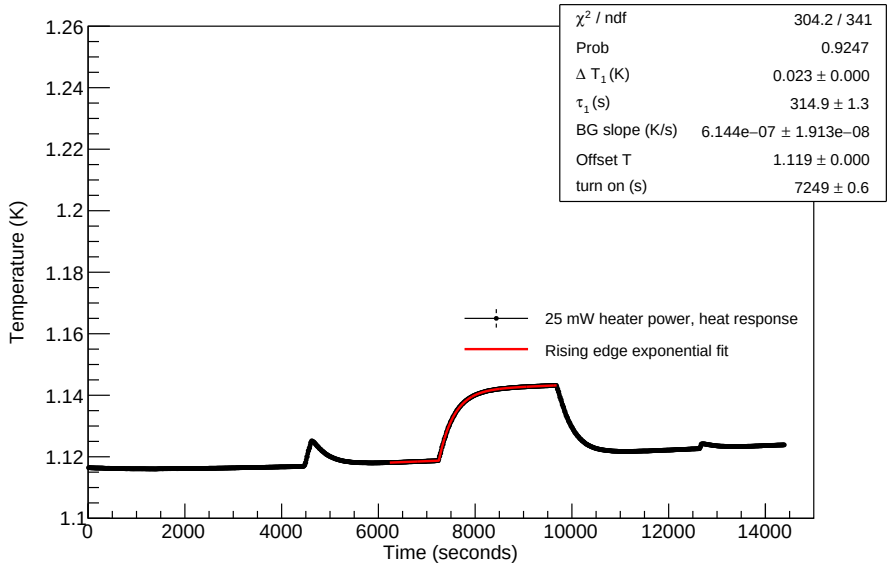

Figure A.11: PG9L derived Temperature versus time graph for a heater power of 25 mW fit with a piece-wise function defined in Eq. 4.6, only a rising exponential.

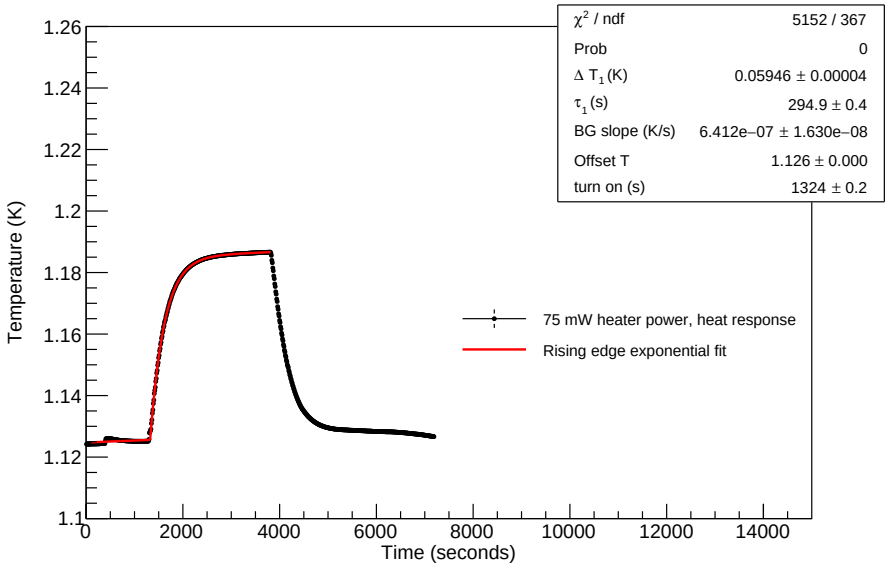

Figure A.12: PG9L derived Temperature versus time graph for a heater power of 75 mW fit with a piece-wise function defined in Eq. 4.6, only a rising exponential.

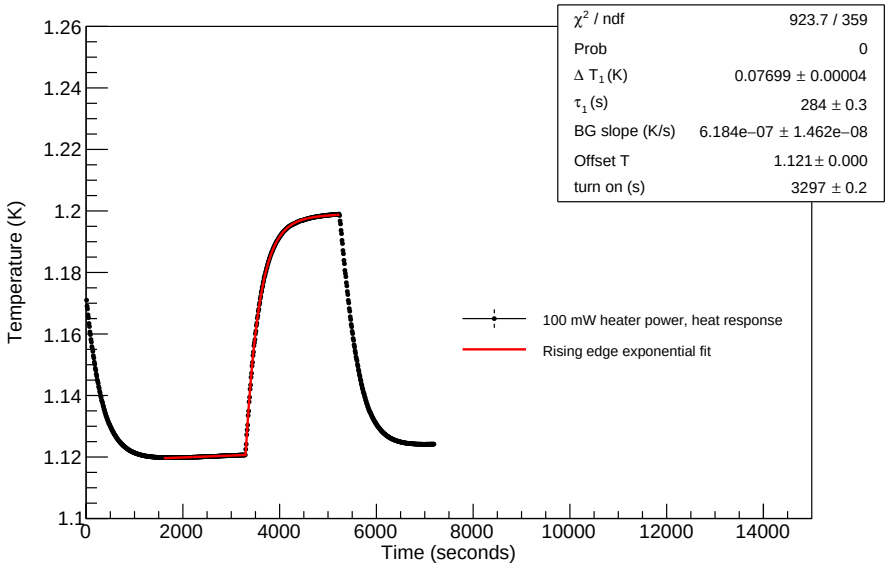

Figure A.13: PG9L derived Temperature versus time graph for a heater power of 100 mW fit with a piece-wise function defined in Eq. 4.6, only a rising exponential.

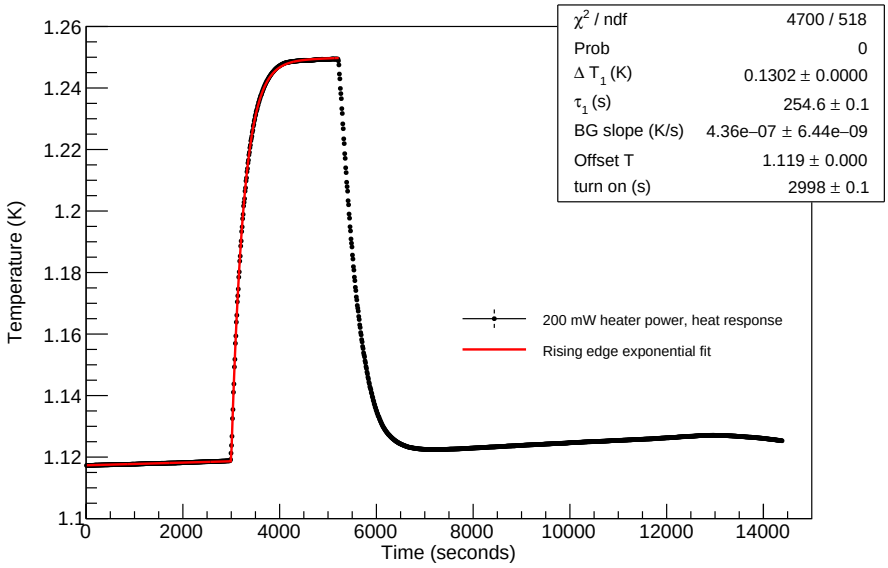

Figure A.14: PG9L derived Temperature versus time graph for a heater power of 200 mW fit with a piece-wise function defined in Eq. 4.6, only a rising exponential.

A.4 Fits with $\Delta T_1 = \Delta T_2$

Figures A.15-A.18 are heat response plots for He-II bottle temperature over time fit to Eq. 4.3 with temperature rise and fall made to be equal ($\Delta T_1 = \Delta T_2$).

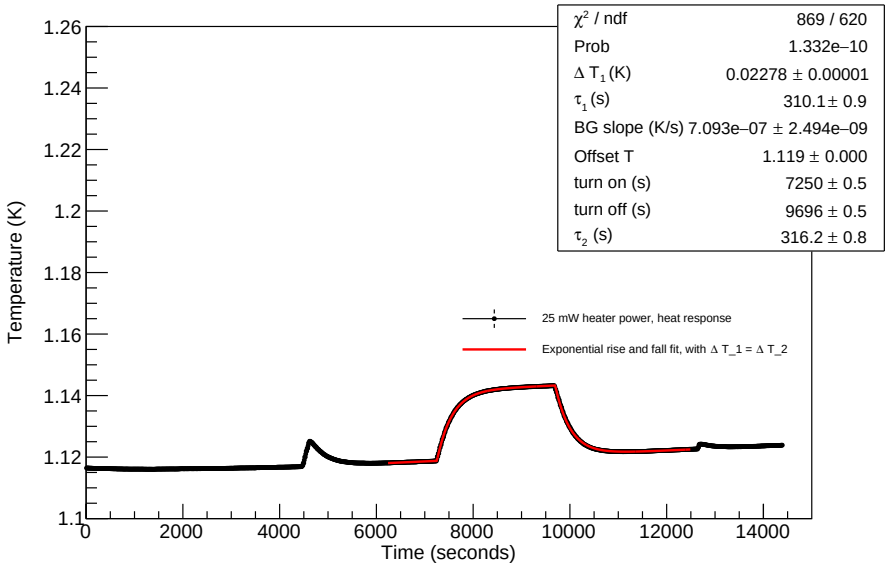

Figure A.15: PG9L derived Temperature versus time graph for a heater power of 25 mW fit with a piece-wise function defined in Eq. 4.3, a rising and falling exponential with $\Delta T_1 = \Delta T_2$

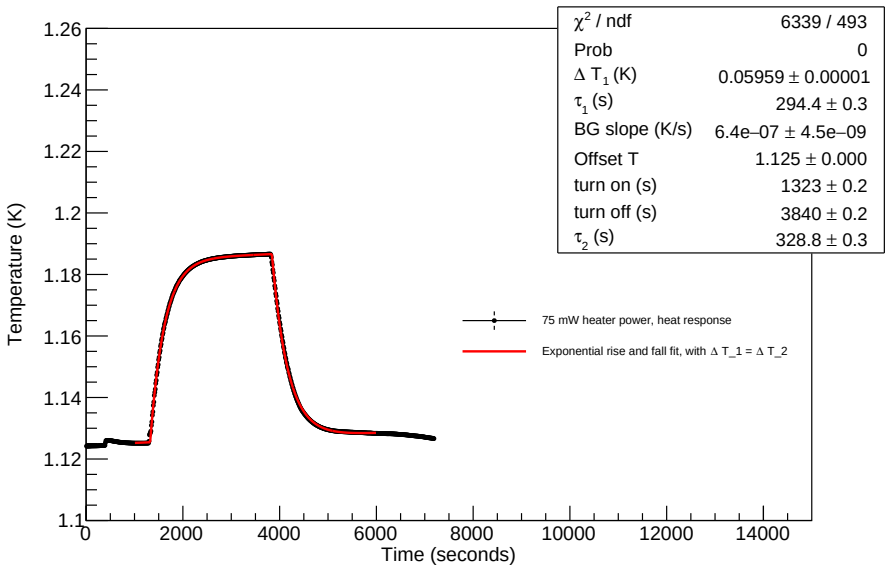

Figure A.16: PG9L derived Temperature versus time graph for a heater power of 75 mW fit with a piece-wise function defined in Eq. 4.3, a rising and falling exponential with $\Delta T_1 = \Delta T_2$

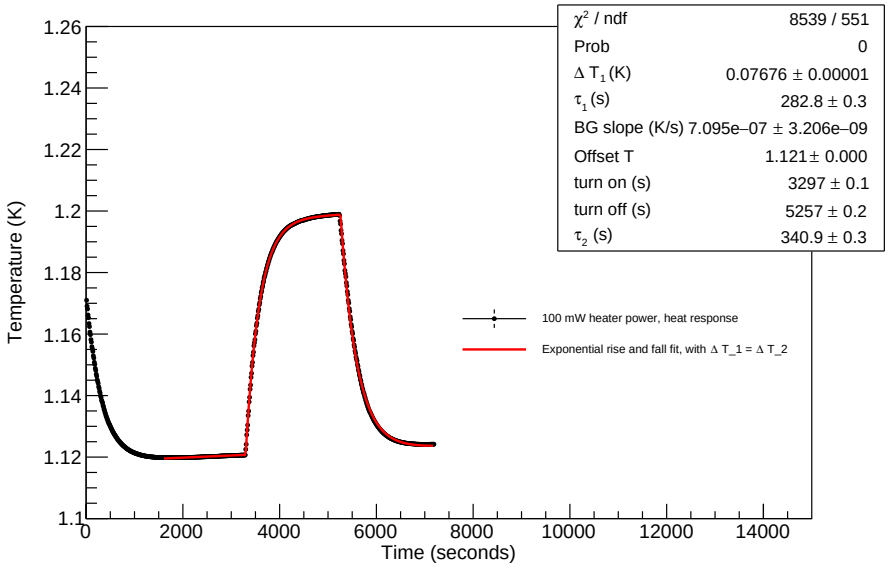

Figure A.17: PG9L derived Temperature versus time graph for a heater power of 100 mW fit with a piece-wise function defined in Eq. 4.3, a rising and falling exponential with $\Delta T_1 = \Delta T_2$

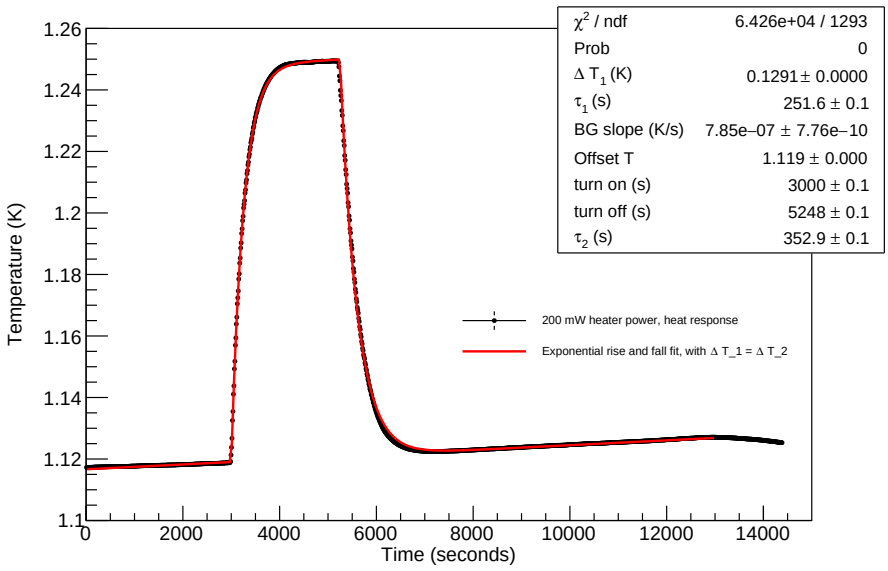

Figure A.18: PG9L derived Temperature versus time graph for a heater power of 200 mW fit with a piece-wise function defined in Eq. 4.3, a rising and falling exponential with $\Delta T_1 = \Delta T_2$

A.5 Fitting heat Response to theory: Heating

Figures A.19-A.30 are heat response plots for He-II bottle temperature over time fit to the 1D GM-model described in Chap 4. The data was fit to constant background heats, $\dot{Q}_{\mathrm{BG}} = 100, 150$ and 200 mW.

A.5.1 100 mW constant background heat $\dot{Q}_{\mathrm{BG}}$

Figures A.19-A.22 are heat response plots for He-II bottle temperature over time fit to the 1D GM-model with constant background heats, $\dot{Q}_{\mathrm{BG}} = 100$ mW.

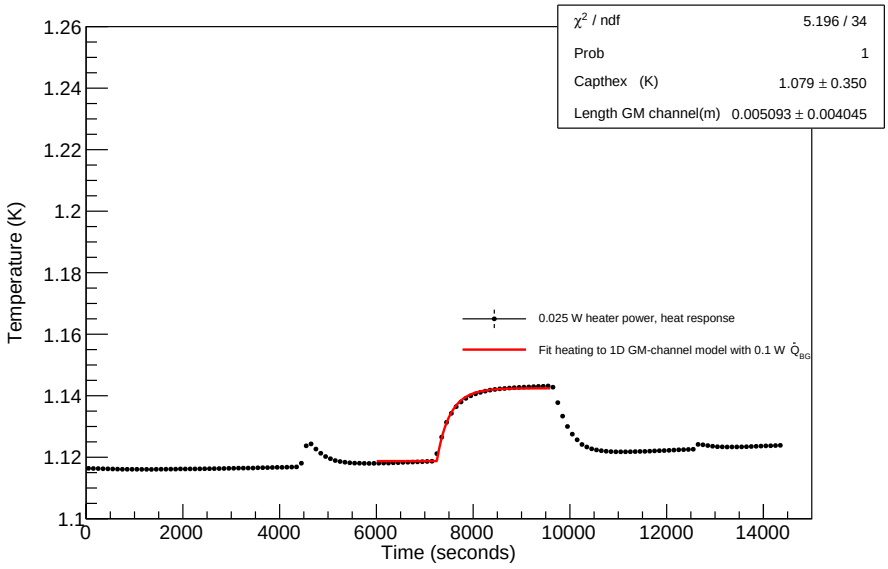

Figure A.19: Heat response of the temperature of the UCN bottle for a heater power of 25 mW fit 1D model with $\dot{Q}_{\mathrm{BG}} = 100$ mW background heat

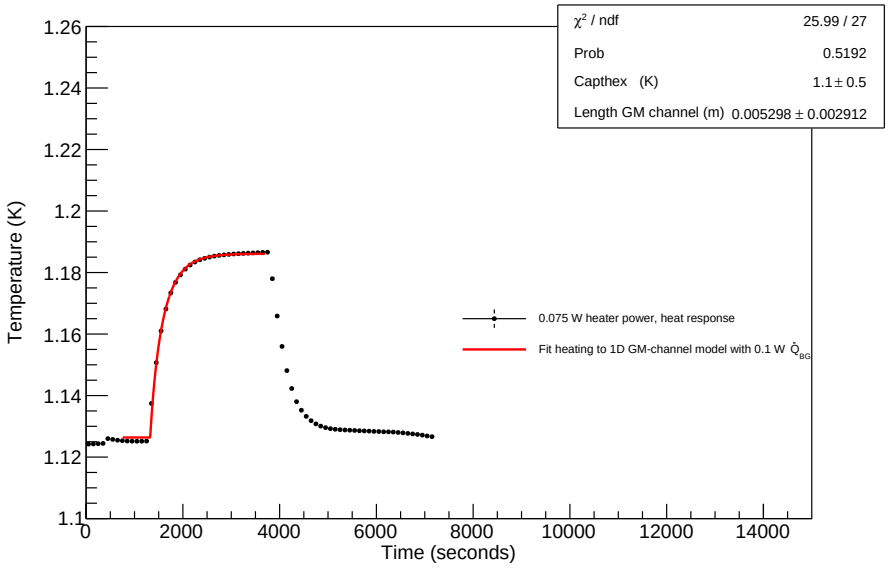

Figure A.20: Heat response of the temperature of the UCN bottle for a heater power of 75 mW fit 1D model with $\dot{Q}_{\mathrm{BG}} = 100$ mW background heat

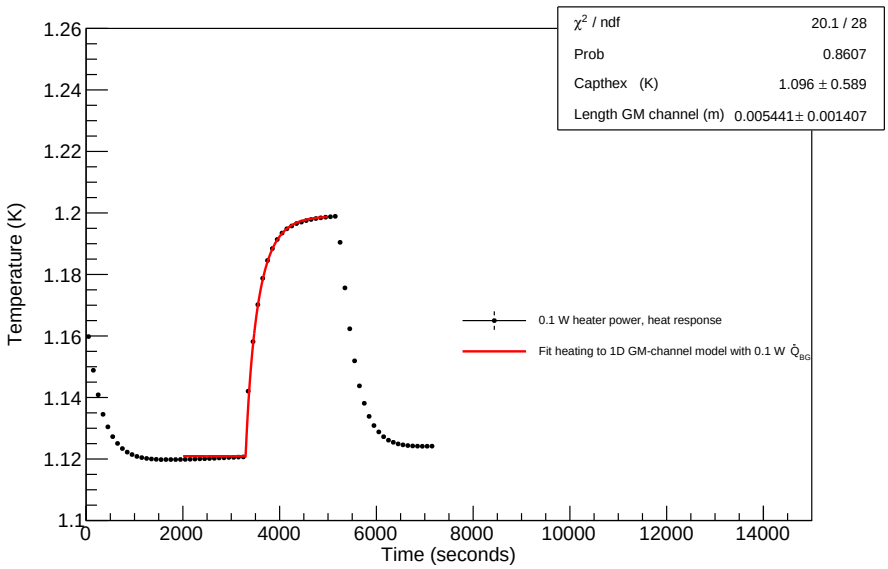

Figure A.21: Heat response of the temperature of the UCN bottle for a heater power of 100 mW fit 1D model with $\dot{Q}_{\mathrm{BG}} = 100$ mW background heat

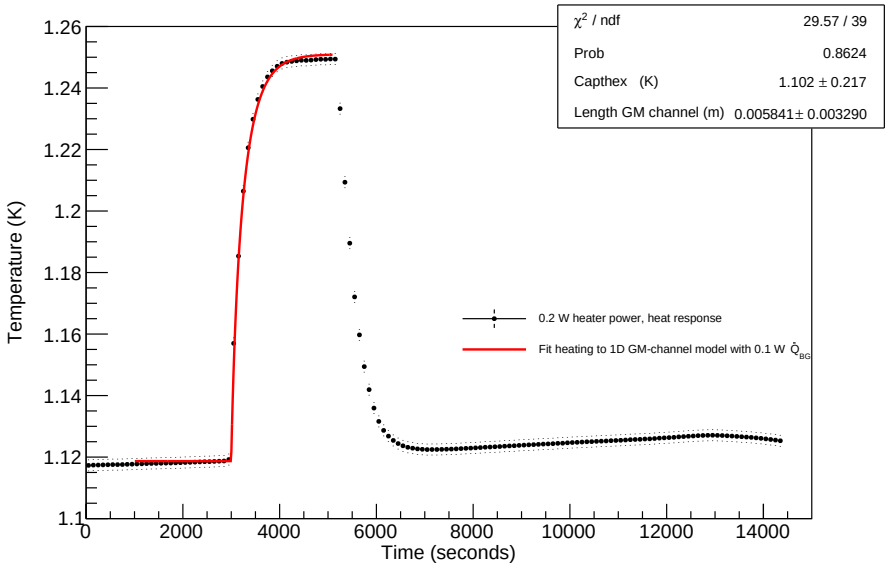

Figure A.22: Heat response of the temperature of the UCN bottle for a heater power of 200 mW fit 1D model with $\dot{Q}_{\mathrm{BG}} = 100$ mW background heat

A.5.2 150 mW constant background heat $\dot{Q}_{\mathrm{BG}}$

Figures A.23-A.26 are heat response plots for He-II bottle temperature over time fit to the 1D GM-model with constant background heats, $\dot{Q}_{\mathrm{BG}} = 150$ mW.

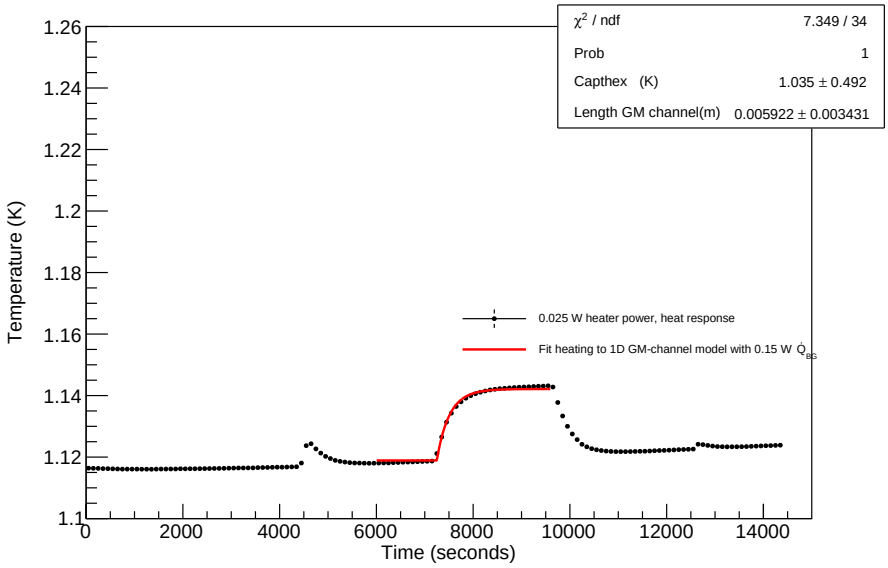

Figure A.23: Heat response of the temperature of the UCN bottle for a heater power of 25 mW fit 1D model with $\dot{Q}_{\mathrm{BG}} = 150$ mW background heat

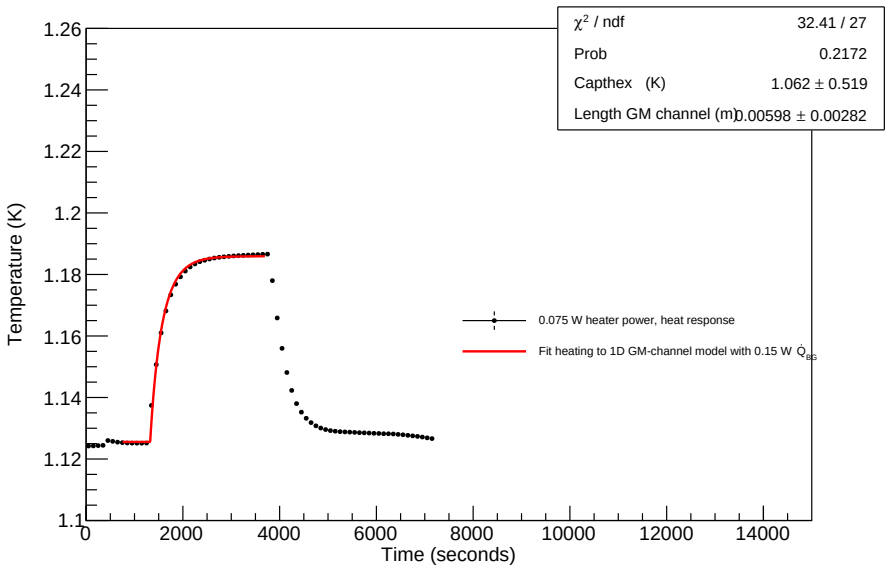

Figure A.24: Heat response of the temperature of the UCN bottle for a heater power of 75 mW fit 1D model with $\dot{Q}_{\mathrm{BG}} = 150$ mW background heat

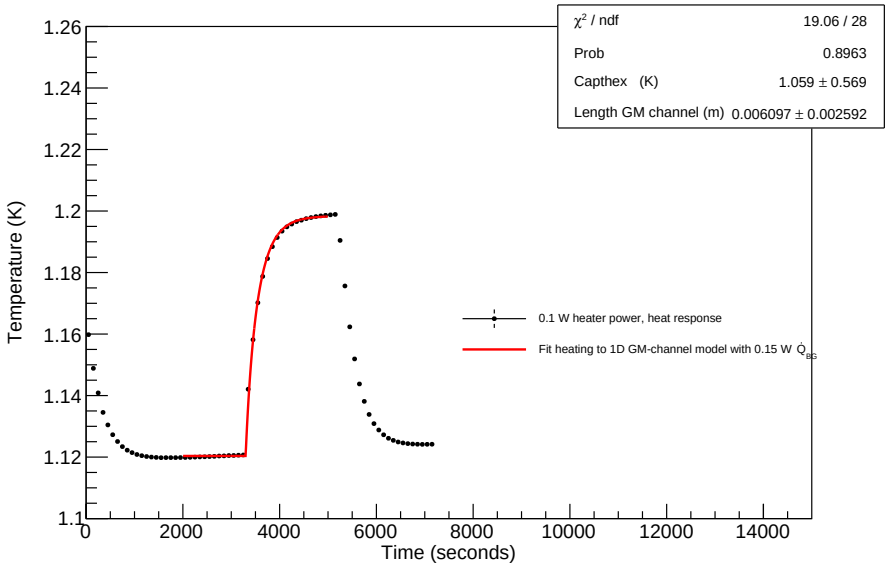

Figure A.25: Heat response of the temperature of the UCN bottle for a heater power of 100 mW fit 1D model with $\dot{Q}_{\mathrm{BG}} = 150$ mW background heat

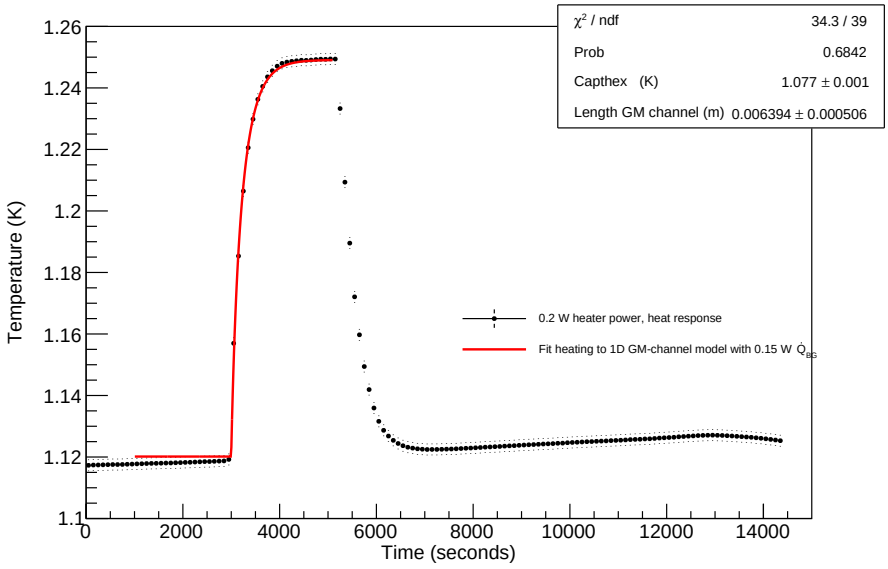

Figure A.26: Heat response of the temperature of the UCN bottle for a heater power of 200 mW fit 1D model with $\dot{Q}_{\mathrm{BG}} = 150$ mW background heat

A.5.3 200 mW constant background heat $\dot{Q}_{\mathrm{BG}}$

Figures A.27-A.30 are heat response plots for He-II bottle temperature over time fit to the 1D GM-model with constant background heats, $\dot{Q}_{\mathrm{BG}} = 200$ mW.

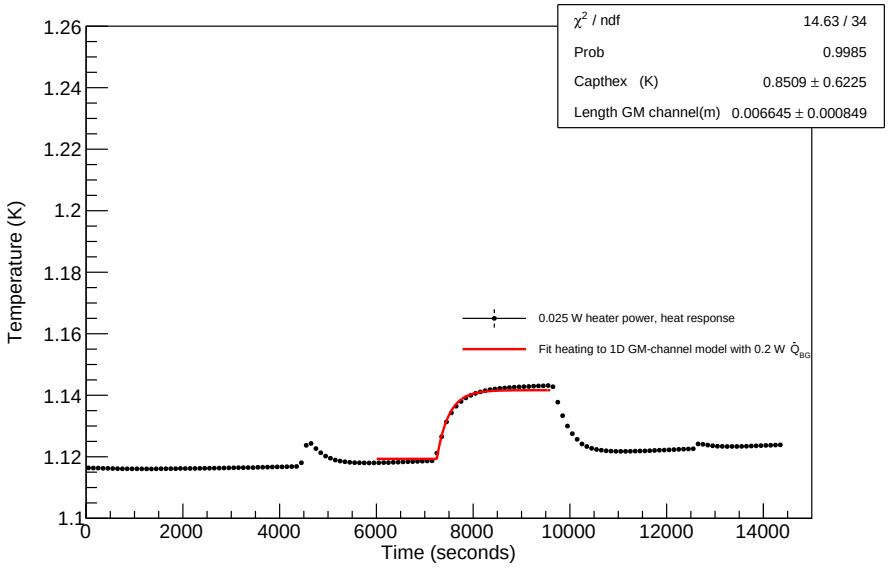

Figure A.27: Heat response of the temperature of the UCN bottle for a heater power of 25 mW fit 1D model with $\dot{Q}_{\mathrm{BG}} = 200$ mW background heat

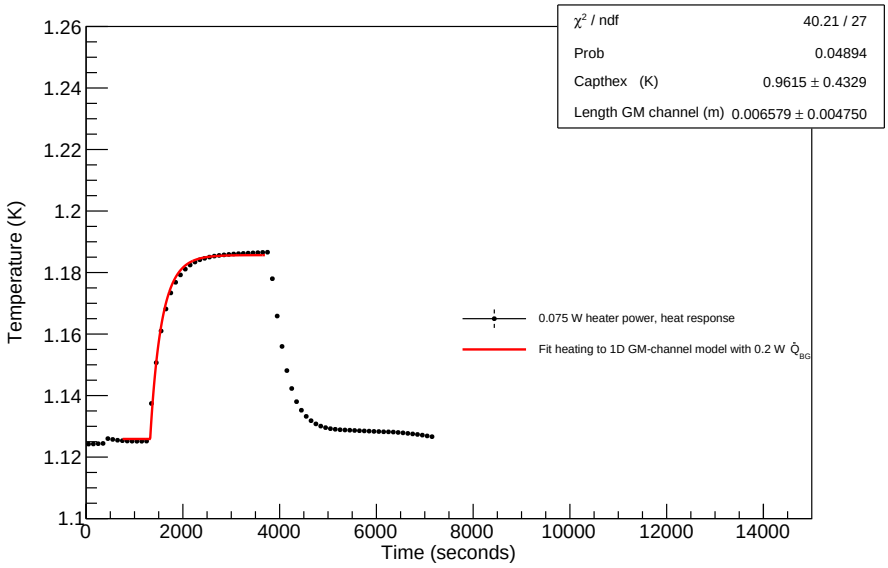

Figure A.28: Heat response of the temperature of the UCN bottle for a heater power of 75 mW fit 1D model with $\dot{Q}_{\mathrm{BG}} = 200$ mW background heat

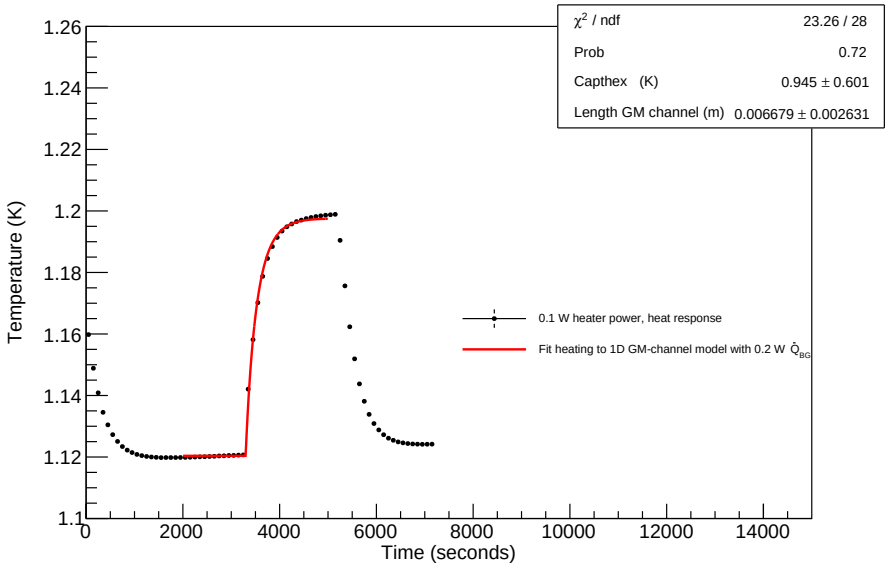

Figure A.29: Heat response of the temperature of the UCN bottle for a heater power of 100 mW fit 1D model with $\dot{Q}_{\mathrm{BG}} = 200$ mW background heat

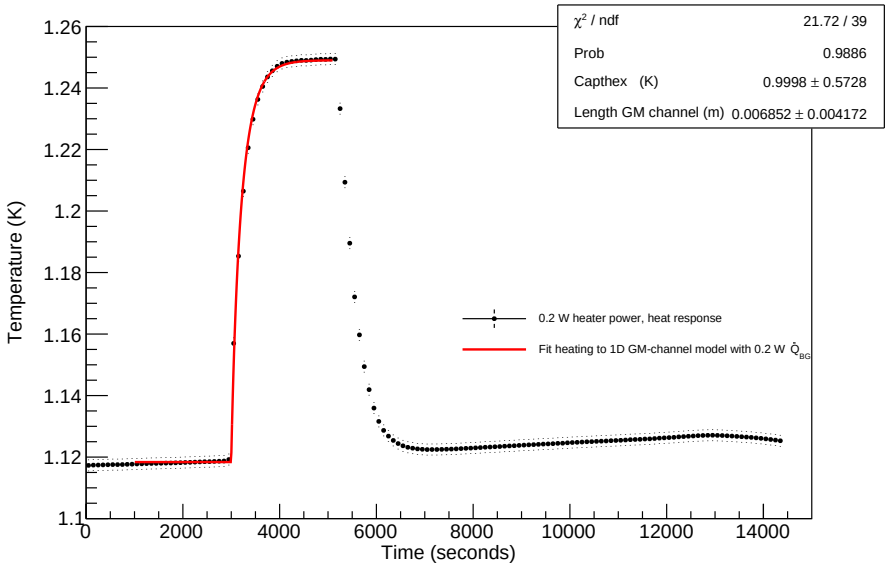

Figure A.30: Heat response of the temperature of the UCN bottle for a heater power of 200 mW fit 1D model with $\dot{Q}_{\mathrm{BG}} = 200$ mW background heat

A.6 Fitting heat response to theory: Cooling

Figures A.31-4.17 are heat response plots for He-II bottle temperature fit to the 1D model for cooling for constant background heat, $\dot{Q}_{\mathrm{BG}} = 150$ mW.

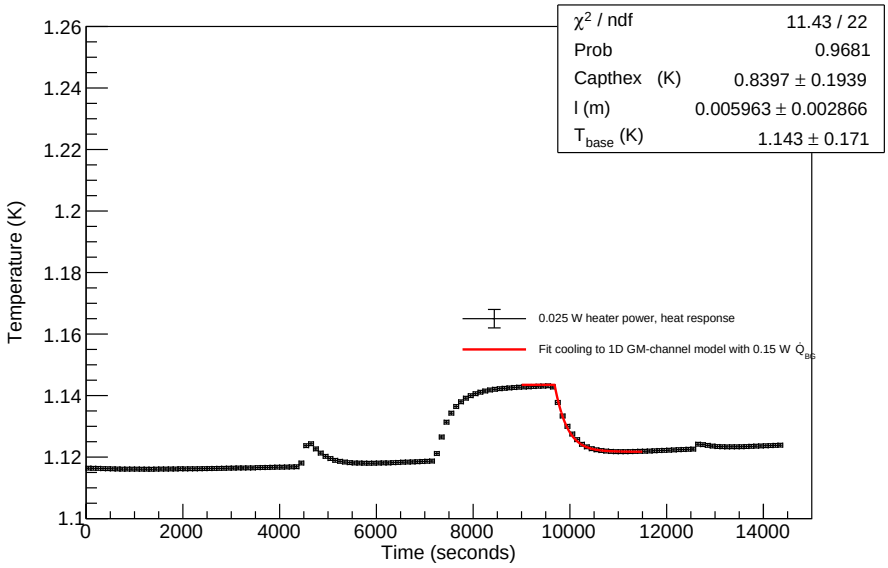

Figure A.31: Heat response of the temperature of the UCN bottle cooling after a heater power of 25 mW heat input fit 1D model with $\dot{Q}_{\mathrm{BG}} = 150$ mW background heat for the cooling edge side.

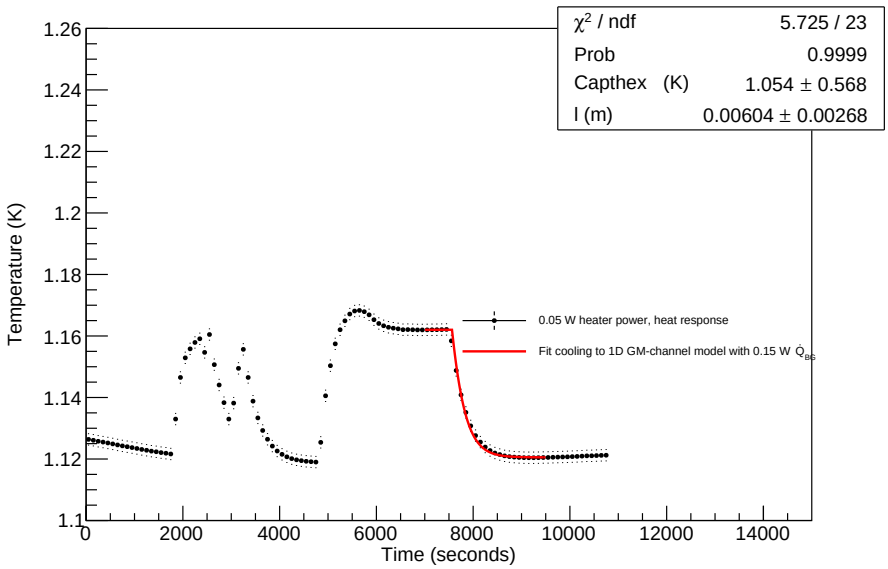

Figure A.32: Heat response of the temperature of the UCN bottle cooling after a heater power of 50 mW heat input fit 1D model with $\dot{Q}_{\mathrm{BG}} = 150$ mW background heat for the cooling edge side.

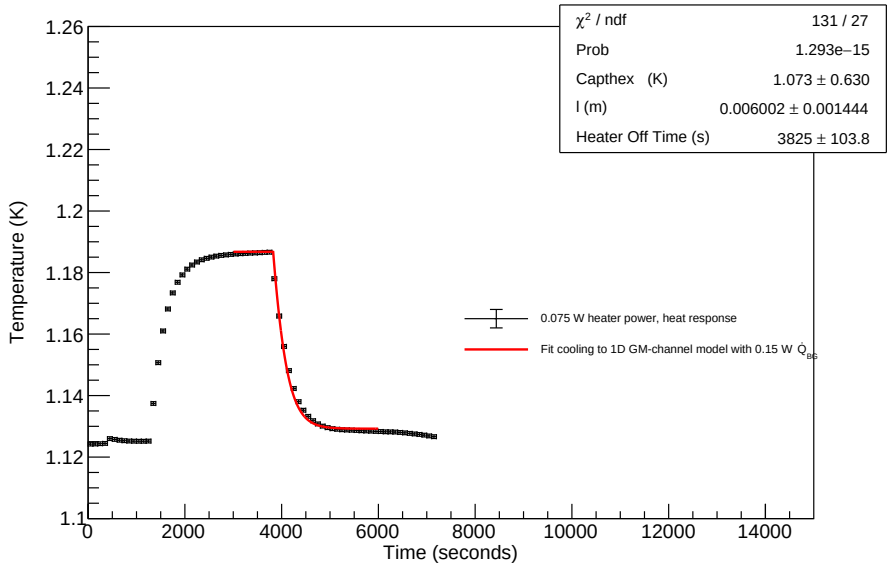

Figure A.33: Heat response of the temperature of the UCN bottle cooling after a heater power of 75 mW heat input fit 1D model with $\dot{Q}_{\mathrm{BG}} = 150$ mW background heat for the cooling edge side.

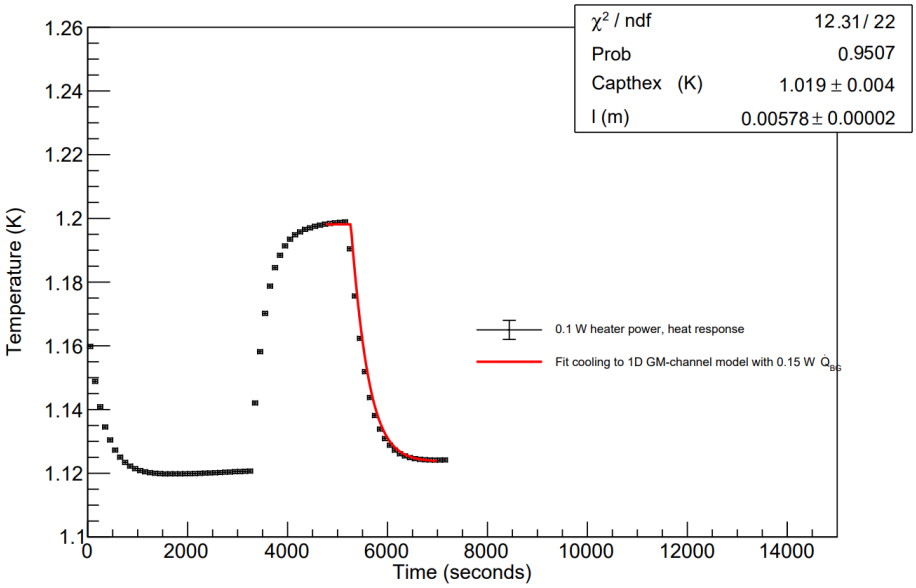

Figure A.34: Heat response of the temperature of the UCN bottle for a heater power of 100 mW fit 1D model with $\dot{Q}_{\mathrm{BG}} = 150$ mW background heat for the cooling edge side

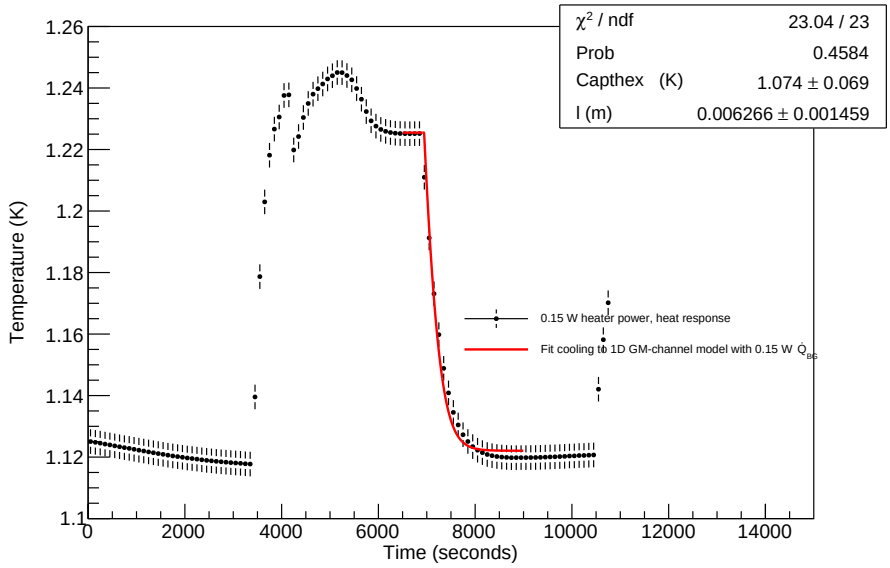

Figure A.35: Heat response of the temperature of the UCN bottle for a heater power of 150 mW fit 1D model with $\dot{Q}_{\mathrm{BG}} = 150$ mW background heat for the cooling edge side

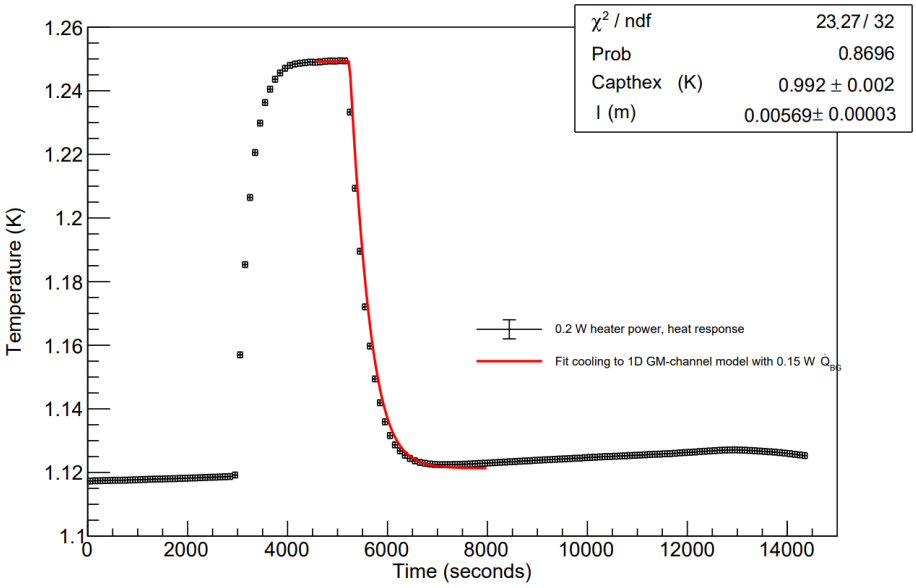

Figure A.36: Heat response of the temperature of the UCN bottle for a heater power of 200 mW fit 1D model with $\dot{Q}_{\mathrm{BG}} = 150$ mW background heat for the cooling edge side

APPENDIX B

Polarization and Spin flipper efficieny

To characterize the polarizer, spin flipper, and SCM in Chapter 6 the transmission matrix formalism can be used [69], to check the solutions presented by Wolfgang Schyerer in his thesis [70].

B.1 Defining the polarization power

The polarization of UCN can be described by a vector with two components. The first component is the number of UCN which are attracted to high field and the second component is the number of UCN attracted to low magnetic field. To start, the incident beam is defined as a vector and is assumed to have some initial intensity i_0. The UCN beam in an unpolarized beam which is defined as

$$I = \begin{pmatrix} i_0 \\ i_0 \end{pmatrix}. \tag{B.1}$$

The detector efficiency with efficiency det is defined as a row vector under this formalism:

$$D = \begin{pmatrix} det & det \end{pmatrix}. \tag{B.2}$$

The polarizing power of the polarizer and analyzer matrix is assumed to be the same and is:

$$P = \begin{pmatrix} t_{hfs} & d_{lfs} \\ d_{hfs} & t_{lfs} \end{pmatrix} \tag{B.3}$$

where t_{hfs} is the probability of transmission of high field seeking spins, where d_{hfs} is the probability of depolarization of high field seeking spins. Similarly, t_{lfs} is the probability of transmission of low field seeking spins, where d_{lfs} is the probability of depolarization of low field seeking spins. The lfs and hfs are labels given to particles whose spin states gain energy in high or low magnetic

field.

Under this formalism, the probability of spinflipping from a spin flipper is given by s_i in the spin flipping matrix S_i:

$$S_i = \begin{pmatrix} (1 - s_i) & s_i \\ s_i & (1 - s_i) \end{pmatrix} \tag{B.4}$$

here the subscript denotes if it is the first or second (1 or 2) spin flippers.

The available observable is the count rate under a spin flipper power state. The counts rate N is then defined as:

$$N_{00} = D \cdot P \cdot P \cdot I \tag{B.5}$$

$$N_{01} = D \cdot P \cdot S_1 \cdot P \cdot I \tag{B.6}$$

$$N_{10} = D \cdot P \cdot S_2 \cdot P \cdot I \tag{B.7}$$

$$N_{10} = D \cdot P \cdot S_2 \cdot S_1 \cdot P \cdot I \tag{B.8}$$

Where the subscripts denote the power state of the spin flipper.

To characterize the polarizer/analyzer a polarizing power p_A is defined by:

$$p_A = \frac{\begin{pmatrix} 1 & -1 \end{pmatrix} \cdot P \cdot I}{\begin{pmatrix} 1 & 1 \end{pmatrix} \cdot P \cdot I} = \frac{t_{hfs} + d_{lfs} - t_{lfs} - d_{hfs}}{t_{hfs} + d_{lfs} + t_{lfs} + d_{hfs}} \tag{B.9}$$

B.2 polarization power with perfect spin flipper efficiency

With the following substitution $s_1 = 1$ and $s_2 = 1$ Since we always deal with ratios of counts we can make the follwoing substitutions

where the vector u is defined as:

$$I \longrightarrow u = \begin{pmatrix} 1 \\ 1 \end{pmatrix} \tag{B.10}$$

and

$$D \longrightarrow u^{\dagger} = \begin{pmatrix} 1 & 1 \end{pmatrix} \tag{B.11}$$

and S is the perfect spin flipping matrix:

$$S = \begin{pmatrix} 0 & 1 \\ 1 & 0 \end{pmatrix} \tag{B.12}$$

For simplicity I will make the following substitutions:

$$P = \begin{pmatrix} t_{hfs} & d_{lfs} \\ d_{hfs} & t_{lfs} \end{pmatrix} = P = \begin{pmatrix} h & d \\ p & l \end{pmatrix} \tag{B.13}$$

Thus

$$u^{\dagger} \cdot P \cdot P \cdot u = \begin{pmatrix} 1 & 1 \end{pmatrix} \begin{pmatrix} h & d \\ p & l \end{pmatrix} \begin{pmatrix} h & d \\ p & l \end{pmatrix} \begin{pmatrix} 1 \\ 1 \end{pmatrix} \tag{B.14}$$

$$u^{\dagger} \cdot P \cdot P \cdot u = h^2 + 2dp + hd + ld + hp + lp + l^2 \tag{B.15}$$

Similarly

$$u^{\dagger} \cdot P \cdot S \cdot P \cdot u = \begin{pmatrix} 1 & 1 \end{pmatrix} \begin{pmatrix} h & d \\ p & l \end{pmatrix} \begin{pmatrix} 0 & 1 \\ 1 & 0 \end{pmatrix} \begin{pmatrix} h & d \\ p & l \end{pmatrix} \begin{pmatrix} 1 \\ 1 \end{pmatrix} \tag{B.16}$$

$$u^{\dagger} \cdot P \cdot S \cdot P \cdot u = \begin{pmatrix} 1 & 1 \end{pmatrix} \begin{pmatrix} d & h \\ l & p \end{pmatrix} \begin{pmatrix} h & d \\ p & l \end{pmatrix} \begin{pmatrix} 1 \\ 1 \end{pmatrix} \tag{B.17}$$

$$u^{\dagger} \cdot P \cdot S \cdot P \cdot u = dh + hp + d^2 + 2hl + p^2 + dl + lp \tag{B.18}$$

The inner part

$$\frac{N_{00}-N_{10}}{N_{00}+N_{10}}=\frac{(h^2+2dp+hd+ld+hp+lp+l^2)-(dh+hp+d^2+2hl+p^2+dl+lp)}{(h^2+2dp+hd+ld+hp+lp+l^2)+(dh+hp+d^2+2hl+p^2+dl+lp)} \tag{B.19}$$

which becomes:

$$\frac{N_{00}-N_{10}}{N_{00}+N_{10}}=\frac{h^2+2dp+l^2-p^2-d^2-2hl}{p^2+2lp+2hp+2pd+l^2+2hl+2dl+h^2+2dh+d^2} \tag{B.20}$$

Which simplifies to:

$$\frac{N_{00}-N_{10}}{N_{00}+N_{10}}=\frac{((h+d)-(l+p))((h-d)-(l-p))}{((h+d)+(l+p))^2} \tag{B.21}$$

here if we make the assumption of perfect polarizers which only transmit high field seekers or $l=d=0$ which was $t_{lfs}=0$ and $d_{lfs}=0$ and bring back the substitutions we get if the analyzer and polarizer have either no depolarization or symmetric depolarization with respect to high field seekers or low field seekers, $d=p$ which is $d_{hfs}=d_{lfs}$

$$\frac{N_{00}-N_{10}}{N_{00}+N_{10}}=\frac{((h+p)-(l+p))((h-p)-(l-p))}{((h+p)-(l+p))^2}=\frac{((h+p)+(l+p))^2}{((h+p)+(l+p))^2} \tag{B.22}$$

which is p^2.

Thus, under the assumption of symmetric depolarization with respect to high field seekers or low field seekers $d=p$ which is $d_{hfs}=d_{lfs}$ and perfect spin flippers we have the following definition of the polarization:

$$p_A=\sqrt{\frac{N_{00}-N_{01}}{N_{00}+N_{01}}} \tag{B.23}$$

and

$$p_A=\sqrt{\frac{N_{00}-N_{10}}{N_{00}+N_{10}}} \tag{B.24}$$

If the first polarizer perfectly polarizes the beam then

$$N_0 = u^\dagger \cdot P \cdot P_0 \cdot u = \begin{pmatrix} 1 & 1 \end{pmatrix} \begin{pmatrix} h & d \\ p & l \end{pmatrix} \begin{pmatrix} 1 & 0 \\ 0 & 0 \end{pmatrix} \begin{pmatrix} 1 \\ 1 \end{pmatrix} \tag{B.25}$$

$$N_0 = \begin{pmatrix} h+p & d+l \end{pmatrix} \begin{pmatrix} 1 \\ 0 \end{pmatrix} = h + p \tag{B.26}$$

And

$$N_1 = u^\dagger \cdot P \cdot S \cdot P_0 \cdot u = \begin{pmatrix} 1 & 1 \end{pmatrix} \begin{pmatrix} h & d \\ p & l \end{pmatrix} \begin{pmatrix} 0 & 1 \\ 1 & 0 \end{pmatrix} \begin{pmatrix} 1 & 0 \\ 0 & 0 \end{pmatrix} \begin{pmatrix} 1 \\ 1 \end{pmatrix} \tag{B.27}$$

$$N_1 = \begin{pmatrix} 1 & 1 \end{pmatrix} \begin{pmatrix} h & d \\ p & l \end{pmatrix} \begin{pmatrix} 0 \\ 1 \end{pmatrix} \tag{B.28}$$

$$N_1 = d + l \tag{B.29}$$

Thus under a perfectly polarized initial beam:

$$\frac{N_0 - N_1}{N_0 + N_1} = \frac{h + p - d - l}{h + p + d - l} = \frac{t_{hfs} + d +_{lfs} - t_{lfs} - d_{hfs}}{t_{hfs} + d +_{lfs} + t_{lfs} + d_{hfs}} = p_A \tag{B.30}$$

Similarly, if there is no depolarization of low field seeking spin flipper and there is no transmission of the wrong spin state (perfect polarizers) both $t_{lfs} = 0$ and $d_{lfs} = 0$ we can start from Eq. B.32 and get:

$$\frac{N_{00} - N_{10}}{N_{00} + N_{10}} = \frac{((h + d) - (l + p))((h - d) - (l - p))}{((h + d) + (l + p))^2} \tag{B.31}$$

with $d = 0$ and $l = 0$.

$$\frac{N_{00} - N_{10}}{N_{00} + N_{10}} = \frac{((h - p)(h + p))}{(h + p)^2} = \frac{h - p}{h + p} = \frac{t_{hfs} - d_{hfs}}{t_{hfs} + d_{hfs}} = p_A \tag{B.32}$$

since both $t_{lfs} = 0$ and $d_{lfs} = 0$.

B.3 Defining the spin flipping probability

If instead of perfect spin flipping matrices S we had a spin flipping probability s_1 is the spin flipping matrix:

$$S_1 = \begin{pmatrix} (1-s_1) & s_1 \\ s_1 & (1-s_1) \end{pmatrix} \tag{B.33}$$

$$N_{00} = u^{\dagger} \cdot P \cdot P_0 \cdot u = \begin{pmatrix} 1 & 1 \end{pmatrix} \begin{pmatrix} h & d \\ p & l \end{pmatrix} \begin{pmatrix} h_0 & d_0 \\ p_0 & l_0 \end{pmatrix} \begin{pmatrix} 1 \\ 1 \end{pmatrix} \tag{B.34}$$

$$N_{00} = \begin{pmatrix} h+p & d+l \end{pmatrix} \begin{pmatrix} h_0+d_0 \\ p_0+l_0 \end{pmatrix} \tag{B.35}$$

$$N_{00} = (h+p)(h_0+d_0) + (d+l)(p_0+l_0) \tag{B.36}$$

$$N_{01} = u^{\dagger} \cdot P \cdot S_1 \cdot P_0 \cdot u = \begin{pmatrix} 1 & 1 \end{pmatrix} \begin{pmatrix} h & d \\ p & l \end{pmatrix} \begin{pmatrix} 1-s_1 & s_1 \\ s_1 & 1-s_1 \end{pmatrix} \begin{pmatrix} h_0 & d_0 \\ p_0 & l_0 \end{pmatrix} \begin{pmatrix} 1 \\ 1 \end{pmatrix} \tag{B.37}$$

$$N_{01} = \begin{pmatrix} h+p & d+l \end{pmatrix} \begin{pmatrix} 1-s_1 & s_1 \\ s_1 & 1-s_1 \end{pmatrix} \begin{pmatrix} h_0+d_0 \\ p_0+l_0 \end{pmatrix} \tag{B.38}$$

$$N_{01} = \begin{pmatrix} h+p & d+l \end{pmatrix} \begin{pmatrix} 1-s_1 & s_1 \\ s_1 & 1-s_1 \end{pmatrix} \begin{pmatrix} h_0+d_0 \\ p_0+l_0 \end{pmatrix} \tag{B.39}$$

$$N_{01} = \begin{pmatrix} (h+p)(1-s_1)+(d+l)s_1 & (h+p)s_1+(d+l)(1-s_1) \end{pmatrix} \begin{pmatrix} h_0+d_0 \\ p_0+l_0 \end{pmatrix} \tag{B.40}$$

$$N_{01} = ((h+p)(1-s_1) + (d+l)s_1)(h_0+d_0) + ((h+p)s_1 + (d+l)(1-s_1))(p_0+l_0) \quad \text{(B.41)}$$

$$N_{01} = ((h+p)(1-s_1) + (d+l)s_1)(h_0+d_0) + ((h+p)s_1 + (d+l)(1-s_1))(p_0+l_0) \quad \text{(B.42)}$$

$$N_{01} = (h+p)(h_0+d_0)[(1-s_1)] + (d+l)(h_0+d_0)[s_1] + (h+p)(p_0+l_0)[s_1] + (d+l)(p_0+l_0)[(1-s_1)] \quad \text{(B.43)}$$

$$N_{10} = u^\dagger \cdot P \cdot S_2 \cdot P_0 \cdot u = \begin{pmatrix} 1 & 1 \end{pmatrix} \begin{pmatrix} h & d \\ p & l \end{pmatrix} \begin{pmatrix} 1-s_2 & s_2 \\ s_2 & 1-s_2 \end{pmatrix} \begin{pmatrix} h & d \\ p & l \end{pmatrix} \begin{pmatrix} 1 \\ 1 \end{pmatrix} \quad \text{(B.44)}$$

$$N_{01} = (h+p)(h_0+d_0)[(1-s_2)] + (d+l)(h_0+d_0)[s_2] + (h+p)(p_0+l_0)[s_2] + (d+l)(p_0+l_0)[(1-s_2)] \quad \text{(B.45)}$$

$$N_{11} = u^\dagger \cdot P \cdot S_2 \cdot S_1 \cdot P_0 \cdot u$$
$$= \begin{pmatrix} 1 & 1 \end{pmatrix} \begin{pmatrix} h & d \\ p & l \end{pmatrix} \begin{pmatrix} 1-s_2 & s_2 \\ s_2 & 1-s_2 \end{pmatrix} \begin{pmatrix} 1-s_1 & s_1 \\ s_1 & 1-s_1 \end{pmatrix} \begin{pmatrix} h_0 & d_0 \\ p_0 & l_0 \end{pmatrix} \begin{pmatrix} 1 \\ 1 \end{pmatrix} \quad \text{(B.46)}$$

$$N_{11} = \begin{pmatrix} (h+p)(1-s_2) + (d+l)s_2 & (h+p)s_2 + (d+l)(1-s_2) \end{pmatrix} \cdot \begin{pmatrix} 1-s_1 & s_1 \\ s_1 & 1-s_1 \end{pmatrix} \begin{pmatrix} h_0+d_0 \\ p_0+l_0 \end{pmatrix} \quad \text{(B.47)}$$

$$= \begin{pmatrix} (h+p)(1-s_2)+(d+l)s_2 & (h+p)s_2+(d+l)(1-s_2) \end{pmatrix} \begin{pmatrix} (h_0+d_0)(1-s_1)+(p_0+l_0)s_1 \\ (h_0+d_0)s_1+(p_0+l_0)(1-s_1) \end{pmatrix} \quad \text{(B.48)}$$

$$= [((h+p)(1-s_2)+(d+l)s_2)((h_0+d_0)(1-s_1)+(p_0+l_0)s_1)] + [((h+p)s_2+(d+l)(1-s_2))((h_0+d_0)s_1+(p_0+l_0)(1-s_1))] \quad \text{(B.49)}$$

$$= (h+p)(1-s_2)(h_0+d_0)(1-s_1)+(h+p)(1-s_2)(p_0+l_0)s_1+(d+l)s_2(h_0+d_0)(1-s_1) + (d+l)s_2(p_0+l_0)s_1+(h+p)s_2(h_0+d_0)s_1+(h+p)s_2(p_0+l_0)(1-s_1) + (d+l)(1-s_2)(h_0+d_0)s_1+(d+l)(1-s_2)(p_0+l_0)(1-s_1) \quad \text{(B.50)}$$

$$= (h+p)(h_0+d_0)[(1-s_2)(1-s_1)+s_2s_1]+(h+p)(p_0+l_0)[(1-s_2)s_1+s_2(1-s_1)] + (d+l)(h_0+d_0)[s_2(1-s_1)+(1-s_2)s_1]+(d+l)(p_0+l_0)[s_2s_1+(1-s_2)(1-s_1)] \quad \text{(B.51)}$$

Thus

$$N_{11}-N_{01} = (h+p)(h_0+d_0)[(1-s_2)(1-s_1)+s_2s_1]+(h+p)(p_0+l_0)[(1-s_2)s_1+s_2(1-s_1)] + (d+l)(h_0+d_0)[s_2(1-s_1)+(1-s_2)s_1]+(d+l)(p_0+l_0)[s_2s_1+(1-s_2)(1-s_1)] - [(h+p)(h_0+d_0)[(1-s_2)]+(d+l)(h_0+d_0)[s_1] + (h+p)(p_0+l_0)[s_1]+(d+l)(p_0+l_0)[(1-s_1)]] \quad \text{(B.52)}$$

$$N_{11} - N_{01} = (h+p)(h_0+d_0)[(1-s_2)(1-s_1) + s_2 s_1 - (1-s_2)]$$
$$+ (h+p)(p_0+l_0)[(1-s_2)s_1 + s_2(1-s_1) - s_1]$$
$$+ (d+l)(h_0+d_0)[s_2(1-s_1) + (1-s_2)s_1 - s_1]$$
$$+ (d+l)(p_0+l_0)[s_2 s_1 + (1-s_2)(1-s_1) - (1-s_1)] \quad \text{(B.53)}$$

$$N_{11} - N_{01} = (h+p)(h_0+d_0)[2s_2 s_1 - s_2] + (h+p)(p_0+l_0)[-(2s_2 s_1 - s_2)]$$
$$+ (d+l)(h_0+d_0)[-(2s_2 s_1 - s_2)] + (d+l)(p_0+l_0)[2s_2 s_1 - s_2] \quad \text{(B.54)}$$

$$N_{11} - N_{01} = [2s_2 s_1 - s_2][(h+p)(h_0+d_0) - (h+p)(p_0+l_0)$$
$$+ (d+l)(p_0+l_0) - (d+l)(h_0+d_0)] \quad \text{(B.55)}$$

Also

$$N_{00} - N_{10} = (h+p)(h_0+d_0) + (d+l)(p_0+l_0) - [(h+p)(h_0+d_0)[(1-s_2)]$$
$$+ (d+l)(h_0+d_0)[s_2] + (h+p)(p_0+l_0)[s_2] + (d+l)(p_0+l_0)[(1-s_2)]] \quad \text{(B.56)}$$

$$N_{00} - N_{10} = (h+p)(h_0+d_0) - (h+p)(h_0+d_0)[(1-s_2)] + (d+l)(p_0+l_0)$$
$$- (d+l)(p_0+l_0)[(1-s_2)]] - (d+l)(h_0+d_0)[s_2] - (h+p)(p_0+l_0)[s_2] \quad \text{(B.57)}$$

$$N_{00} - N_{10} = s_2[(h+p)(h_0+d_0) - (h+p)(p_0+l_0) + (d+l)(p_0+l_0) - (d+l)(h_0+d_0)]$$
$$\text{(B.58)}$$

Hence

$$\frac{N_{11}-N_{01}}{N_{00}-N_{10}} = \frac{[2s_2s_1-s_2][(h+p)(h_0+d_0)-(h+p)(p_0+l_0)+(d+l)(p_0+l_0)-(d+l)(h_0+d_0)]}{s_2[(h+p)(h_0+d_0)-(h+p)(p_0+l_0)+(d+l)(p_0+l_0)-(d+l)(h_0+d_0)]} \tag{B.59}$$

$$\frac{N_{11}-N_{01}}{N_{00}-N_{10}} = 2s_1-1 \tag{B.60}$$

Thus

$$s_1 = \frac{1}{2}\left(1+\frac{N_{11}-N_{01}}{N_{00}-N_{10}}\right) \tag{B.61}$$

and similarly it follows that:

$$s_2 = \frac{1}{2}\left(1+\frac{N_{11}-N_{10}}{N_{00}-N_{01}}\right) \tag{B.62}$$

B.4 Solving for the polarization for inefficient spin flippers

We start by defining a term called the flipper efficiency f (this is often called spin flipper efficiency, some people make the distinction [69]):

$$f_1 = \frac{N_{11}-N_{01}}{N_{00}-N_{10}} = 2s_1-1 \tag{B.63}$$

$$f_2 = \frac{N_{11}-N_{10}}{N_{00}-N_{01}} = 2s_1-1 \tag{B.64}$$

Starting from

$$\frac{(N_{00}-N_{10})^2}{N_{11}N_{00}-N_{01}^2} = \frac{(N_{00}-N_{10})^2}{N_{11}N_{00}+(N_{01}N_{00}-N_{01}N_{00})-N_{01}^2} \tag{B.65}$$

$$= \frac{(N_{00}-N_{10})^2}{(N_{11}-N_{01})N_{00}+N_{01}(N_{00}-N_{10})} \tag{B.66}$$

$$= \frac{N_{00}-N_{10}}{N_{00}-N_{10}}\frac{N_{00}-N_{10}}{\frac{N_{11}-N_{10}}{N_{00}-N_{01}}N_{00}+N_{01}} \tag{B.67}$$

Subbing f_2 in:

$$\frac{(N_{00}-N_{10})^2}{N_{11}N_{00}-N_{01}^2}=\frac{N_{00}-N_{10}}{f_2N_{00}+N_{01}}. \tag{B.68}$$

Similarly we get

$$\frac{(N_{00}-N_{01})^2}{N_{11}N_{00}-N_{10}^2}=\frac{N_{00}-N_{01}}{f_1N_{00}+N_{10}}. \tag{B.69}$$

Now we can solve the much simpler $\frac{N_{00}-N_{01}}{f_1N_{00}+N_{10}}$ by splitting up it into the denominator and the numerator. Looking at $N_{00}-N_{01}$ we see that we solved it before, but we can simplify it:

$$N_{00}-N_{01} = s_1[(h+p)[(h_0+d_0)-(p_0+l_0)]-(d+l)[(h_0+d_0)-(p_0+l_0)] \tag{B.70}$$

$$N_{00}-N_{01}=s_1[(h+p)-(d+l)][(h_0+d_0)-(p_0+l_0)] \tag{B.71}$$

The numerator of Equation B.69 is

$$f_1N_{00}+N_{10}=(2s_1-1)[(h+p)(h_0+d_0)+(d+l)(p_0+l_0)]$$
$$+[(h+p)(h_0+d_0)[(1-s_2)]+(d+l)(h_0+d_0)[s_2]+(h+p)(p_0+l_0)[s_2]+(d+l)(p_0+l_0)[(1-s_2)]] \tag{B.72}$$

$$f_1N_{00}+N_{10}=(h+p)(h_0+d_0)[(2s_1-1)+(1-s_2)]+(d+l)(p_0+l_0)[(2s_1-1)+(1-s_2)]$$
$$+(d+l)(h_0+d_0)[s_2]+(h+p)(p_0+l_0)[s_2] \tag{B.73}$$

$$f_1N_{00}+N_{10}=(h+p)(h_0+d_0)[(2s_1-s_2)]+(d+l)(p_0+l_0)[(2s_1-s_2)]$$
$$+(d+l)(h_0+d_0)[s_2]+(h+p)(p_0+l_0)[s_2] \tag{B.74}$$

$$f_1 N_{00} + N_{10} = (h+p)[(h_0+d_0)(2s_1 - s_2) + (p_0+l_0)(s_2)] + (d+l)[(p_0+l_0)(2s_1 - s_1) + (h_0+d_0)(s_2)] \quad \text{(B.75)}$$

The assumption of identical spin flippers $s_1 = S_2 = s$ is needed for the following to hold true:

$$f_1 N_{00} + N_{10} = (h+p)[(h_0+d_0)(s) + (p_0+l_0)(s)] + (d+l)[(p_0+l_0)(s) + (h_0+d_0)(s)] \quad \text{(B.76)}$$

$$f_1 N_{00} + N_{10} = s[(h+p)((h_0+d_0) + (p_0+l_0)) + (d+l)((p_0+l_0) + (h_0+d_0))] \quad \text{(B.77)}$$

$$f_1 N_{00} + N_{10} = s[((h+p) + (d+l))((h_0+d_0) + (p_0+l_0))] \quad \text{(B.78)}$$

with the denominator of Equation B.69 becoming,

$$N_{00} - N_{01} = s[(h+p) - (d+l)][(h_0+d_0) - (p_0+l_0)] \quad \text{(B.79)}$$

Thus under the assumption of identical spin flippers $s_1 = s_2 = s$ Equation B.69 becomes:

$$\frac{(N_{00} - N_{01})^2}{N_{11}N_{00} - N_{10}^2} = \frac{s[(h+p) - (d+l)][(h_0+d_0) - (p_0+l_0)]}{s[((h+p) + (d+l))((h_0+d_0) + (p_0+l_0))]}. \quad \text{(B.80)}$$

$$\frac{(N_{00} - N_{01})^2}{N_{11}N_{00} - N_{10}^2} = \frac{(h+p) - (l+d)][(h_0-p_0) - (l_0-d_0)}{((h+p) + (d+l))((h_0+p_0) + (l_0+d_0))}. \quad \text{(B.81)}$$

With symmetric depolarization in the first polarizer ($p_0 = d_0$) this becomes:

$$\frac{(N_{00} - N_{01})^2}{N_{11}N_{00} - N_{10}^2} = \frac{((h+p) - (l+d))((h_0+p_0) - (l_0+p_0))}{((h+p) + (d+l))((h_0+p_0) + (l_0+p_0))}. \quad \text{(B.82)}$$

$$\frac{(N_{00}-N_{01})^2}{N_{11}N_{00}-N_{10}^2}=\frac{(h+p)-(l+d)}{(h+p)+(d+l)}\frac{(h_0+p_0)-(l_0+p_0)}{(h_0+p_0)+(l_0+p_0)} \tag{B.83}$$

$$\frac{(N_{00}-N_{01})^2}{N_{11}N_{00}-N_{10}^2}=p_A\times p_0 \tag{B.84}$$

Additionally, for a perfectly polarized beam $h_0=1$ and $p_0=d_0=l_0=0$:

$$\frac{(N_{00}-N_{01})^2}{N_{11}N_{00}-N_{10}^2}=p_A \tag{B.85}$$

Finally, for identical ($P=P_0=P_A$) with perfect polarizers $d=l=0$:

$$\frac{(N_{00}-N_{01})^2}{N_{11}N_{00}-N_{10}^2}=\frac{(h+p)(h-p)}{(h+p)(h+p)}=\frac{(h-p)}{(h+p)}=p_A. \tag{B.86}$$

APPENDIX C

Solution to a magnetized cylinder

The solutions for the uniformly magnetized cylinder magnetized in an arbitrary direction [74]. This calculation was used to fit foil magentization in Chapter 7.

Start be defining the direction of the magnetization vector

$$\vec{M} = M_l\hat{z} + M_t\hat{\rho} \tag{C.1}$$

Use this to find the general relation of the magnetic field $\vec{H}$, the magnetic flux density $\vec{B}$ and the permeability of vacuum

$$\vec{B} = \mu_0(\vec{H} + \vec{M}) \tag{C.2}$$

To get the arbitrary magnetic field of the cylinder, we must define the auxiliary functions:

$$P_1(k) = K - \frac{2}{1-k^2}(K-E) \tag{C.3}$$

$$P_2(k) = \frac{\gamma}{1-\gamma^2}(P-K) - \frac{1}{1-\gamma^2}(\gamma^2 P - K) \tag{C.4}$$

$$P_3(k) = \frac{1}{1-k^2}(K-E) - \frac{\gamma^2}{1-\gamma^2}(P-K) \tag{C.5}$$

$$P_4(k) = \frac{\gamma}{1-\gamma^2}(P-K) + \frac{\gamma}{1-\gamma^2}(\gamma^2 P - K) - P(k)_1 \tag{C.6}$$

The following shorthand notation has been used:

$$\xi_{\pm} = z \pm L \tag{C.7}$$

$$\alpha_{\pm} = \frac{1}{\sqrt{\xi_{\pm}^2 + (\rho + R)^2}} \tag{C.8}$$

$$\beta_{\pm} = \xi_{\pm}\alpha_{\pm} \tag{C.9}$$

$$\gamma = \frac{\rho - R}{\rho + R} \tag{C.10}$$

$$k_{\pm}^2 = \frac{\xi_{\pm}^2 + (\rho - R)^2}{\xi_{\pm}^2 + (\rho + R)^2} \tag{C.11}$$

and the symbols K, E, and P are used to indicate the evaluation of the complete elliptic integrals of the first second and third kind as follows,

$$K = K(\sqrt{1-k^2}) = \int_0^{\pi/2} \frac{d\theta}{\sqrt{1-(1-k^2)\sin^2\theta}} \tag{C.12}$$

$$E = E(\sqrt{1-k^2}) = \int_0^{\pi/2} d\theta \sqrt{1-(1-k^2)\sin^2\theta} \tag{C.13}$$

$$P = \Pi(1-\gamma^2, sqrt1-k^2) = \int_0^{\pi/2} \frac{d\theta}{(1-(1-\gamma^2)\sin^2\theta)\sqrt{1-(1-k^2)\sin^2\theta}} \tag{C.14}$$

The magnetic filed expression then is

$$H_{\rho} = \frac{\partial\Phi}{\partial\rho} = \frac{MRcos\phi}{2\pi\rho}[\beta_+ P_4(k_+) - \beta_- P_4(k_-)] \tag{C.15}$$

$$H_{\phi} = -\frac{1}{\rho}\frac{\partial\Phi}{\partial\phi} = -\frac{MR\sin\phi}{\pi\rho}[\beta_+ P_3(k_+) - \beta_- P_3(k_-)] \tag{C.16}$$

$$H_z = -\frac{\partial\Phi}{\partial z} = \frac{MRcos\phi}{\pi}[\alpha_+ P_1(k_+) - \alpha_- P_1(k_-)] \tag{C.17}$$